University College London

Faculty of Mathematics and Physical Sciences

Department of Physics and Astronomy

Robotic process to accelerate large optics fabrication

Thesis submitted for the Degree of Doctor of Philosophy of the University College London (UCL)

by

Hsing-Yu Wu

August 2016

I, Hsing-Yu Wu, confirm that the work presented in this thesis is my own. I confirm that the information derived from other sources has been indicated in this thesis.

Table of Contents

List of Figures

List of Tables

Abstract

The manufacture of metre-scale optics for the next generation of extremely large telescopes (and many other applications) poses a number of unique challenges. For the primary mirror of the European Extremely Large Telescope, each of its 1.45 m segments will need to be completed with nanometre scale accuracy. This demands an unprecedented combination of hybrid fabricating technology to process nearly 1000 segments before the year 2024.

One important aspect in improving the current state-of-the-art manufacturing developments is adding an efficient smoothing process that can achieve a faster, and less expensive, manufacturing process-chain. The current process to finish a prototype segment using CNC grinding and CNC polishing takes approximately 1-2 months, and a significant contributing factor in this is the excessive processing times needed to correct the local grinding marks. In this study, therefore, grolishing, an intermediate process between grinding and polishing, is adopted to smooth the part and reduce the overall manufacturing time.

This PhD work serves to advance the development of effective robotic grolishing processes (RGP) by the following achievements: (1) to propose the specification and

achieve the requirements; (2) to design tools and establish a mechanism for grolishing; (3) to investigate and propose experimental methods to reduce process times while still achieving high performance, reliability and quality surfaces; (4) to establish the RGP and demonstrate that this process can smooth the errors from grinding and provide superior surfaces for polishing to speed up the current process; (5) to develop prototype metrology systems and algorithms to measure grolished surfaces; and, (6) to investigate an innovative proposed method to control mid-spatial frequencies on complex surfaces by using rotating rigid tools.

These novel achievements describe the newest fabrication technology, and anticipate the evolution of the process-chain for future high-quality imaging systems for use in astronomy, space-research and laser physics.

Acknowledgements

To begin with, the author wishes to thank his dissertation advisor, Professor David Walker, for his support, guidance and many enlightening discussions, despite the demands of his own research work. He is a profound researcher, an inspiring motivator, a wonderful teacher, and even a best friend. I feel fortunate to be his student.

I am also happy to work with such wonderful colleagues at the National Facility for Ultra Precision Surfaces (OpTIC) in the UK. I would like to take this opportunity to thank all the team members in the R&D groups who have made the institute and north Wales more fun to work in. Special mention should be made of Dr Guo-Yu Yu, who has provided much helpful advice, not limited purely to engineering problems, but also on daily life. Special mention should also be given to Professor Paul Rees and Dr Chun-Liang Kuo, for their willingness to share their knowledge in metrology and statistical problems.

The author wants to express his gratitude to the many friends and colleagues who have encouraged and shared their knowledge during these 14 years in optical engineering. With their time and discussion, the author has learnt something every day. Special acknowledgement is given to Miss Huang, Professor Chin-Tim Hsiao, Professor Horng

Chang, and Professor Gerd Keiser. Without their encouragement, the author would never have had the chance pursuing this PhD research abroad.

The author would like to acknowledge financial support from the MOE Technologies Incubation Scholarship from Ministry of Education, Taiwan. He also wants to thank his supervisor's grant support from the UK Engineering and Physical Sciences Research Council, the Science and Technology Facilities Council, Innovate-UK (previously called Technology Strategy Board). Financial support from Glyndwr University and Welsh Government, both in respect to the prototype segment and robot projects is gratefully acknowledged. It was only through this mix of funding that the research presented in this thesis could be realised.

In particular, the author wants to thanks his wife and family. The completion of this dissertation is supported by your endless love.

List of Abbreviations

Abrasive size	AS
Artificial intelligence	AI
Analysis of variance	ANOVA
Charge-coupled devices	CCD
Complementary metal-oxide-semiconductors	CMOS
Computer controlled grinding	CCG
Computer controlled polishing	CCP
Computer numerical control	CNC
Confidence interval	CI
Degree of freedom	DOF
Design of experiments	DOE
Device 1	D1
Device 2	D2

List of Abbreviations

DT/10/P Feather Touch	DFT
European Extremely Large Telescope	E-ELT
European Southern Observation	ESO
Extended Range Form Talysurf	ERFT
Extremely Large Telescopes	ELT
Field of View	FOV
Finite element method	FEM
Fluid jet polishing	FJP
Full-factorial design	FFD
Giant Magellan Telescope	GMT
High spatial frequency	HSF
Higher is better	HB
Influence function	IF
Infrared	IR

List of Abbreviations

Ion beam figuring	IBF
Kilogram	Kg
Load	L
Low spatial frequency	LSF
Lower is better	LB
Magnetorheological finishing	MRF
Mid spatial frequency	MSF
Modulation transfer function	MTF
Newton	N
Normal is better	NB
Orthogonal array	OA
Overhang	OH
Peak-to-Valley	PV
Point spread function	PSF

List of Abbreviations

Power spectrum density	PSD
Primary mirror	M1
Response surface methodology	RSM
Revolutions per minute	Rpm
Robotic grolishing process	RGP
Scanning electron microscope	SEM
Slurry density	SD
Spindle speed	S
Statistical quality control	SPC
Sum of squares	SS
Thirty Metre Telescope	TMT
Tool path generator	TPG
Tool travel feed	TF
Track space	TS

Peak-to-valley wavefront	PVW
Variance	V
Volumetric removal rate	VRR
Wavefront error	WFE

Chapter 1 Introduction

"We find them smaller and fainter, in constantly increasing numbers, and we know that we are reaching into space, farther and farther, until, with the faintest nebulae that can be detected with the greatest telescopes, we arrive at the frontier of the known universe."[1]

Edwin Powell Hubble (1889-1953)

1.1 Introduction

When Galileo Galilei published his belief in Copernicus' theory that the Sun revolves around the Earth, the Pope had him accused of heresy and he was put on trial by the Inquisition in Rome and forced to recant [2, 3]. Although his findings were prohibited at that time, many European astronomers used astronomical telescopes to observe the solar system and other planets in the universe, steadily developing the knowledge of astronomy.

Until the 1920s, many people did not realise that the Milky Way was not the entire universe, until Edwin Hubble used the 100-inch telescope at Mount Wilson to demonstrate that other galaxies existed [4, 5]. This second revolutionary discovery expanded our view of the universe to show that the heavens were not static, but expanding and changing over time [6]. It has since been recognised by astronomers that the universe was created 13.8 billion years ago [7], and that the observable universe has more than 100 billion galaxies [8]. The Earth, at about 4.54 billion years

old [9], is just one planet that orbits around its sun (i.e. star), among the approximately 300 billion stars that compose the Milky Way alone [10].

Finding evidence of life on so-called "extrasolar" planets would be one of the greatest of human discoveries. In addition, a huge number of other fascinating questions are waiting to be answered in 21st-century astronomy. For example, (1) How the first galaxies formed? (2) How dark matter and dark energy function and comprise our universe? (3) How the Big Bang led to the current universe? (4) What is the fate of the universe?

Answering these questions requires a new generation of telescopes. Just as with the 100-inch Mount Wilson telescope that Hubble used, the new generation of extremely large telescopes (ELTs) (e.g. the Giant Magellan Telescope (GMT), Thirty Meter Telescope (TMT), and the European Extremely Large Telescope (E-ELT)) have the potential to make discoveries that cannot yet be imagined. The great light collecting areas (aperture size: 25 m ~ 40 m) and powerful diffraction-limited resolutions (> 30 arcsec diameter field of view provided with active and adaptive optics [11]) of the ELTs, working from the near-infrared to the visible region, will be the best ever achieved.

The manufacture of these giant new telescopes projects raises many challenges, however. For example, the E-ELT will be composed of 798 hexagonal segments [12], with each segment being required to be manufactured in an average of 2-3 days, which is beyond the capabilities of current manufacturing technologies. Improvements in processing technologies are, therefore, essential for the successful

construction of the next generation of powerful telescopes to discover the mysteries of the universe.

In this context, this thesis focuses on a new processing technology, namely the robotic grolishing process (RPG); a procedure that lies between grinding and polishing to improve the overall processing speed in the production of mirrors. Before introducing the technical details, it is useful to review the history of telescopes to understand the case for large telescopes and the value of the RGP in the current process chain.

1.2 The history of the telescope

The history and evolution of large ground-based telescopes dates back to the seventeenth century. The Englishman, Thomas Harriott, is recognised as the first astronomer to use a telescope, when he made drawings of the Moon on 26 July 1609 [13]. Galileo did the same four months later, and also used his telescope to observe Jupiter's moons, leading him to postulate, controversially, that the Earth may not be the centre of the universe. Since the seventeenth century, we have seen huge advances in the evolution of telescopes. While both Harriot's and Galileo's telescopes utilised glasses just a couple of centimetres in diameter, in the 400 years since, the focusing elements have steadily increased in size so as to be able to gather light from fainter and more distant objects in the universe [14]. Moreover, in these 400 years, the astronomical telescope has gradually evolved from a manual device for visual observation to a huge computer-controlled instrument outputting digital images.

The size of refractive telescopes is limited to only about 1 metre in diameter, with the main limiting factors being that: (1) the lens can be supported only around its edge, (2) larger lenses can be distorted by their own weight, (3) a metre-scale lens is less cost-effective since the lens must maintain its homogeneous refractive index for the whole aperture, and (4) the lens has diverse refractive indices for various wavelengths (i.e. dispersion), which produces rings of false colour around stars and planets, referred to as chromatic aberrations (CAs). Even though these CAs can be corrected, more lenses are required to correct the error, which leads to a heavier structure and a higher system price. The larger the refractive lens, the more the CA correction. As refracting telescopes become larger, therefore, the benefits of their greater light-capturing ability become very marginal.

Although reflecting telescopes solve the issue of CAs, this is at the price of much more stringent polishing requirements for the glass compared to refractive surfaces. Historically, this has been a key limitation in the size of the mirror used in reflecting telescopes but modern processing technologies are now able to produce surfaces to an accuracy of a few nanometres (details of these recent processing techniques are reviewed in Section 2.4). In addition, since the 1960s, the need for more metre-scale telescopes has become more increasingly evident, as active and adaptive optics, built into telescopes, have been used to correct environmental and atmospheric disturbances in order to produce sharper images [15]. The utilisation of active and adaptive optics in telescopes has pushed the ability of observation further. Details of active and adaptive optics will be discussed further in Section 2.6. Another advantage of reflecting telescopes is that the mirror can be supported from the back,

thus limiting potential bending and distortion due to the mirror's weight. These are the reasons why the vast majority of metre-scale and large telescopes today are reflectors (i.e. using mirrors).

Following the 5 m Hale telescope in 1948 [16], and the 6 m Bolshoi telescope in 1975 [17], newer manufacturing technologies, such as spin-casting technology, have been devised to fabricate lightweight monolithic mirrors [18]. At present, the largest single mirror telescope is the Large Binocular Telescope [19], which has two effective apertures of up to 8.4 m. Astronomical telescopes in the 8 m to 10 m class are today's largest optical/infrared telescopes.

Before 1990, therefore, the primary mirror of metre-scale telescopes was constructed as a monolithic mirror. Based on the experience of completing many metre plus-scale monolithic primary mirrors, however, primary monolithic mirrors in excess of 8.4 m diameter are considered impractical [20, 21] for a variety of reasons, including: (1) the flexibility of the mirror requires heavy and strong support systems, (2) to compensate surface distortion (i.e. low order aberrations) due to gravity is challenging, (3) mid-spatial frequencies produced by sub-aperture tooling are difficult to remove, (4) it is expensive to transport such a mirror, and the limitation of infrastructures (e.g. shipping and the limited capacity of the road).

To achieve primary mirrors in excess of 8.4 m, therefore, segmentation is now used. The first segmented telescope ― the twin Keck telescopes, was initially developed under the leadership of Dr Jerry Nelson at Lawrence Berkeley National Laboratory and the University of California in the 1980s. The mirrors of the Keck telescopes

equate to a primary mirror of 10 m in diameter, comprised of 36 smaller hexagonal mirrors that operate as one, proving the concept of the segmented telescope as being viable [22]. Subsequent to the development of the Keck telescopes, the concept of the segmented telescope spread worldwide to the point that future large telescopes are primarily segmented [23, 24].

The next revolution in mirror technology will increase the primary size up to 20-40 m in diameter, referred to as extremely large telescopes (ELTs). As listed in Table 1-1, there are currently three world-leading projects expected to be completed in the 2020s [25-27]. From the design phases, the E-ELT and TMT will have 798 and 492 of 1.45 m hexagonal mirrors to compose 39.3 m and 30 m apertures, while the GMT will have seven 8.4 m diameter mirrors to compose a 24.5 m aperture. All three ELTs will support scientific goals of observing earth-like planets in the habitable zone, the discovery of alien life, the measurement of the first stars and galaxies at distances of tens of billions of light-years to help understand the evolution of our galaxy as well as to answer questions regarding supermassive black holes, dark matter and dark energy [28-31]. Although the technologies for the GMT project are most likely to be realised during the 2020s, all astronomers hope that all three telescopes will be operating in the next decade.

Table 1-1: ELTs in the next decade

Current ELT Projects	Aperture (m)	Segments	First light
European Extremely Large Telescope (E-ELT)	39.3	798 hexagons (about 1.45m corner-to-corner)	2024
Thirty Metre Telescope (TMT)	30	492 hexagons (about 1.44m corner-to-corner)	2022
Giant Magellan Telescope (GMT)	24.5	7 circular segments (each 8.4 m)	2021

1.3 The E-ELT project in OpTIC

The revolutionary 39.3 m European Extremely Large Telescope (E-ELT) from the European Southern Observation (ESO) will be the largest optical/infrared ground-based telescope in the world. The E-ELT is an 11-year, 1083 million Euro (M€) project [32], with the expected completion for the first phase being in 2024. This project challenges the state-of-the-art in its science, technology and engineering.

OpTIC Technium (hosting the National Facility for Ultra Precision Polishing) has been awarded a contract by the ESO to polish four prototype primary segments for the E-ELT, namely SPN04, SPN01, SPN03, and SPN06. The segments are illustrated in Figure 1-1. The four segments are different from one another, although each segment has a concave surface of radius of 69 m with a spherical departure of about 50 μm. The technique to polish a segment in the OpTIC facility is based on

"Precessions" polishing technology (details are discussed in Chapter 2), which was originally developed at UCL and then commercialised by Zeeko Ltd. since 2000 [33-36]. This process is combined with Computer Numerical Control (CNC) machines to polish surfaces and correct measured form errors (i.e. 'corrective polishing').

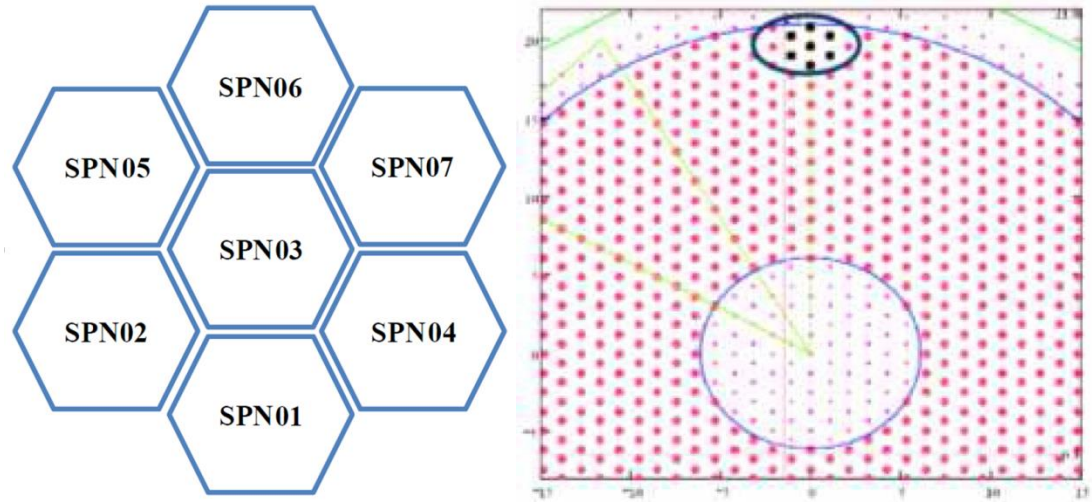

Figure 1-1: Seven prototype segments and their locations

The first hexagonal prototype, E-ELT segment SPN04, was certified as fully conformant by ESO on 15th October 2013, as shown in Figure 1-2. The following three segments SPN01, SPN03, and SPN06 were completed in 2015, demonstrating that the facility has developed a technology to process ultra-precision optics in the metre-scale dimension compliant with the specification.

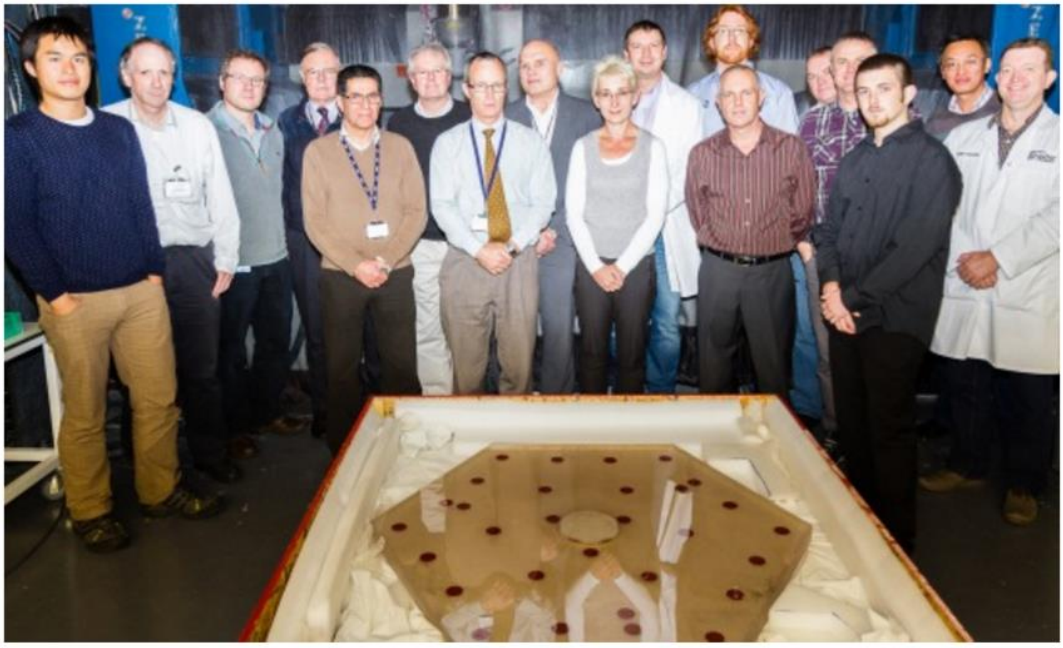

Figure 1-2: SPN04 was certified by ESO on 15th October 2013

From the experience of polishing the above four prototype segments, it was recognised that the polishing process is slower if an input surface has more local errors. For example, tooling marks (i.e. mid-spatial frequencies, MSF) left by the CNC grinding process were identified as time-consuming to correct [37, 38]. A potential method to polish out the MSF errors is to use hard tools, such as pitch pads, but this would increase the polishing time and further decrease the overall efficiency, potentially meaning that the primary mirror for the E-ELT may not be achievable by 2024.

It has been proposed by Prof Walker that a much faster intermediate process (so-called "grolishing") may be introduced between grinding and polishing, so as to speed up the overall manufacturing process. Grolishing can ease the pressure on the polishing process by removing the local tooling signatures from the grinding,

resulting in a reduction in the time and cost involved in polishing to remove local grinding marks. This research plays a key role in the development of a "Robotic Grolishing Process (RGP)" to improve a surface after grinding. The RGP seeks to enhance the overall processing efficiency in order to accelerate the production of large optics and can potentially be used to process the large optics for E-ELT or TMT segmented mirrors.

1.4 Motivation for developing the RGP, and contributions

As introduced in Section 1.3, grolishing is a process lying between grinding and polishing, and this research concentrates on developing the RGP as a candidate step in the manufacture of 1.4 m prototype segments for the 39.3 m E-ELT. Considering the high specifications and the nearly 1000 segments needed for the E-ELT project (please refer to Section 2.3.3), the main challenge is to complete the fabrication of the required 1.45 m segments within their stringent specifications, before the year 2024.

In order to meet the requirements of the E-ELT project, enhanced production technologies are expected to contribute to the fabrication chain, with the aim of reducing the time needed to process a 1.45 m optical segment for the project [39]. In this context, the objective of the RGP is not only to remove local grinding marks and errors introduced by a CNC grinding machine during the grinding process but also to remove sub-surface damage from grinding and to control the surface texture, surface accuracy and edge-profiles in the process (the details will be discussed in Section 4.2). This will serve to enable a superior quality surface to be passed to the Zeeko

polishing machine, and thus to reduce the polishing time and further improve overall efficiency.

This grolishing development was initially demonstrated on Zeeko IRP machines, showing that mid-spatial artefacts left from CNC grinding machines take a long time to polish-out, unless a family of hard tools are used (e.g. pitch, cast iron or brass tools). Several papers have demonstrated that grolishing using the Zeeko IRP 600 and 1200 machines can remove these mid-spatial errors [40-42]. "Grolishing" has therefore been recognised to be a promising means of speeding up the smoothing process.

The contribution of this research is to migrate the grolishing process from the IRP machines on which it has thus far been demonstrated to robots (e.g. Fanuc/ABB). Robotic grolishing is shown to offer the following advantages [43-45]: firstly, although it has been established that the positioning accuracy of a robot is approximately 1/10 that of an IRP machine, the maximum speed of a similar scale robot is at least 10 times faster than a similar scale Zeeko IRP machine. Secondly, the capital expenditure entailed for a similar scale robot is approximately 15 times less than an IRP machine, thus making such a hybrid process competitive in the market. Thirdly, many optical centres separate the different fabrication processes to avoid the risk of cross-contamination, since the platforms are different (e.g. cross-contamination of different slurries use in grolishing and polishing respectively); the robot provides this inherently. Fourthly, the robotic grolishing process can preserve excellent surface topography and edges from grinding (please refer to Chapter 4), and the optical surface can then be finished to the desired specification

by the subsequent polishing process. Hence, a robot has been demonstrated as a suitable machine to perform grolishing. Details underpinning this contention are introduced from Chapter 3 to Chapter 6.

The research presented here includes a proposed candidate specification for the process, the design of appropriate robotic tools, the creation of supports for the glass, the invention of new methods for alignment and measurement, and the application of statistical methods to control and optimise the process, as well as programming to adjust the robots and to analyse experimental data. All these investigations are introduced in this thesis, as summarised in Figure 1-3.

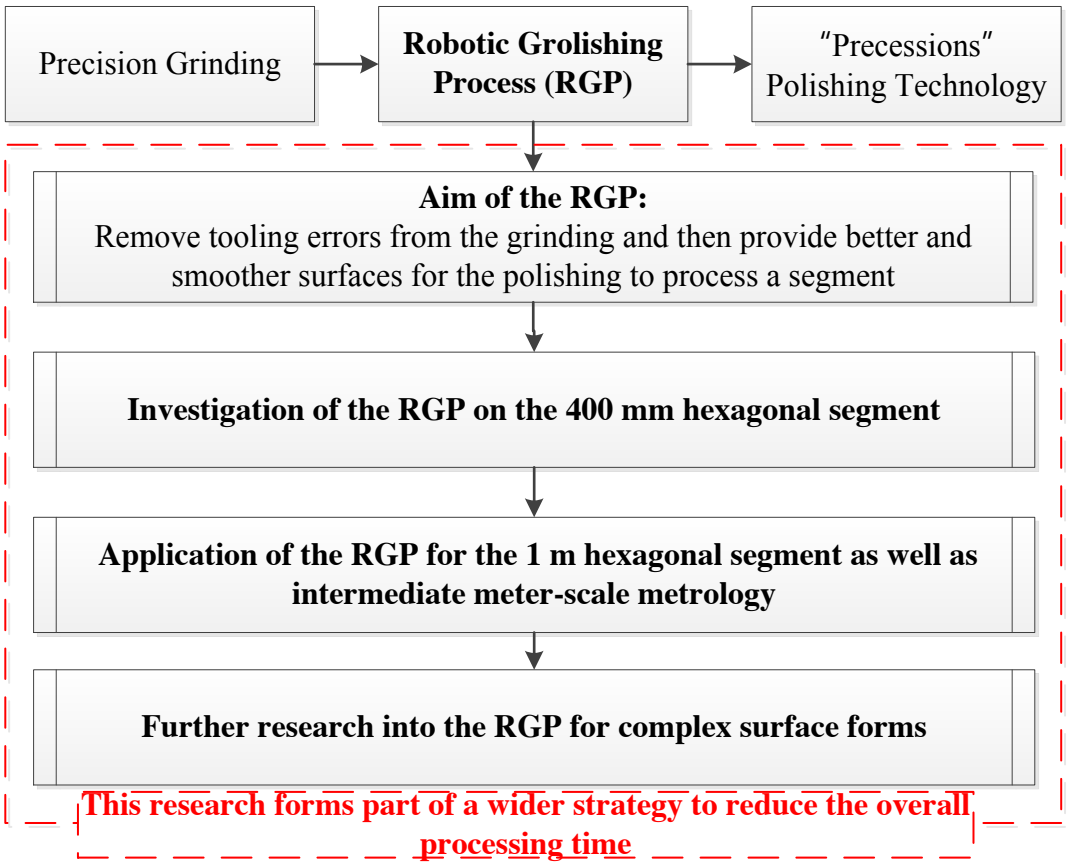

Figure 1-3: The robotic grolishing process

RGP is not only of benefit for the E-ELT project; it can also be applied to other optical industries to fabricate optical elements, as shown in Figure 1-4, Figure 1-5 and Figure 1-6.

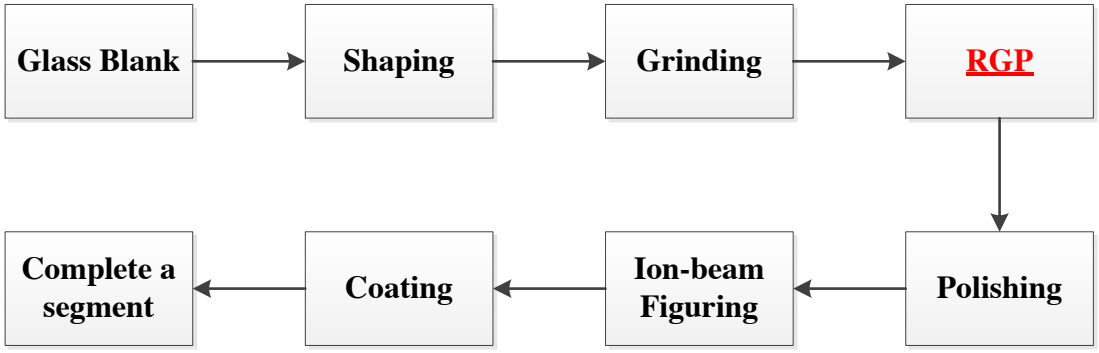

Figure 1-4: The Role of the RGP in large optical fabrication

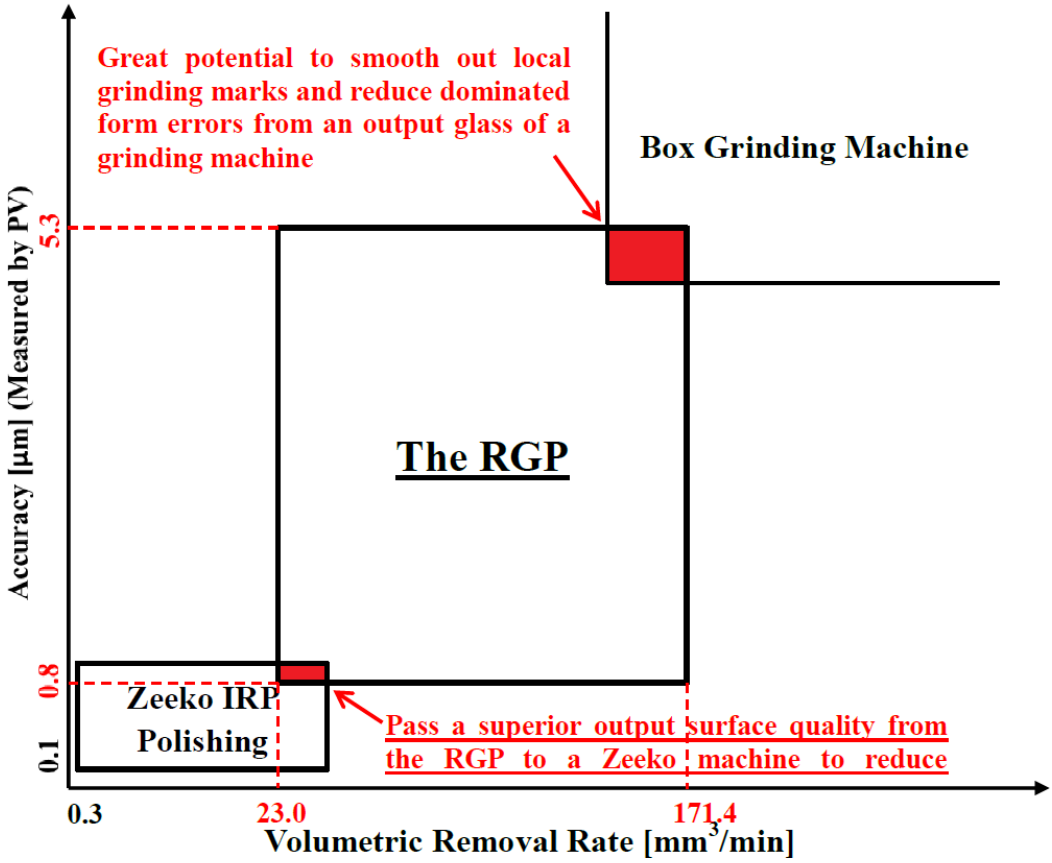

Figure 1-5: The role of RGP for the E-ELT project is to smooth the process from grinding to polishing to accelerate the overall processing time. Grinding and polishing data can refer to [89, 167]

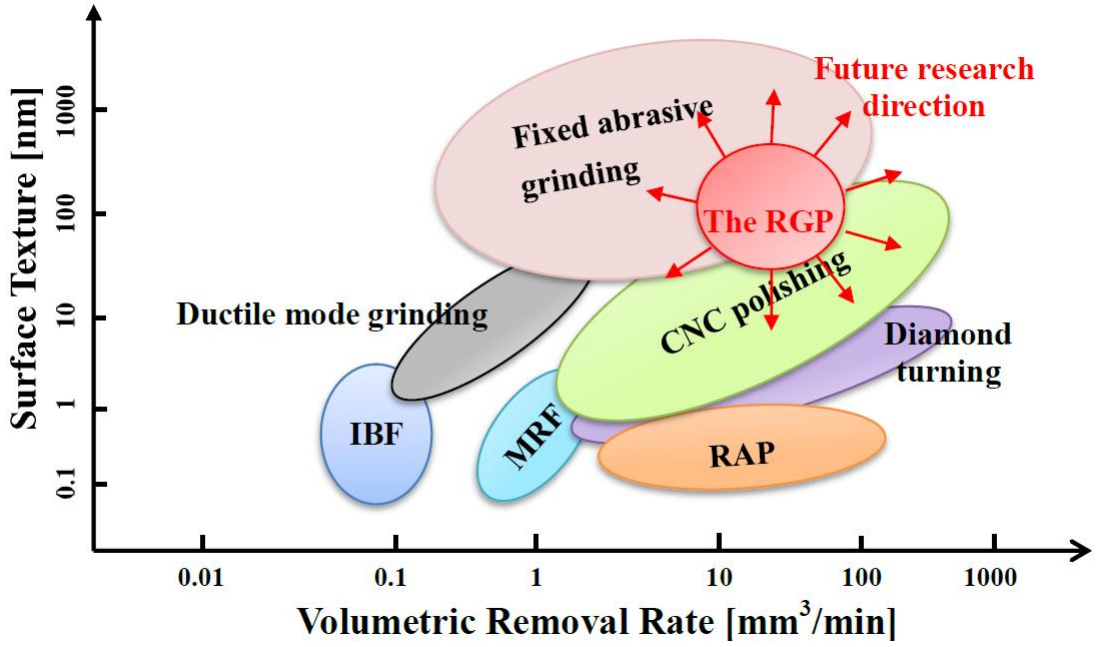

Figure 1-6: Future research directions in respect to the RGP (Data collected from [46, 47])

Although the size, mass and the required specification of the E-ELT segments, and similar projects, make the fabrication processes challenging, the RGP has been based on an initially proven demonstration. The robotic grolishing technology will require little or no further significant research and development to be applied to future processing chains in respect to large optics.

1.5 Outline of this thesis

Chapter 1 provides an introduction to the current development of extremely large telescopes and predicts the role of the RGP in the field of future optical fabrication.

Chapter 2 provides an overview of the optical designs, optical fabrication, optical measurements and other issues (such as glass material, CCD and CMOS sensors, and

active/adaptive optics) to construct a ground-based telescope. Several new techniques to process optical glasses are also discussed in this chapter.

Chapter 3 describes the RGP, which includes describing the novel grolishing work achieved by operating ABB/Fanuc robots, the working principles of the RGP, and advanced information regarding the use of the Zeeko TPG (tool path generator) to manipulate the robots used to conduct the RGP. Statistical experimental designs and analysis to optimise the outputs of the RGP (e.g. removal rate, surface texture, MSF, surface profiles and edges) are discussed at the end of this chapter.

Five experimental RGP outputs, called "responses", are evaluated as follows:

(1) Volumetric removal rate (VRR): is a response to evaluate the manufacturing efficiency in the RGP.

(2) Surface texture (texture): is a response to determine the process efficiency of removing a grey grolished surface into a specular polished surface.

(3) Edge: is a response to evaluate stray lights and diffractions into a system.

(4) Surface accuracy: is a response to determine output image quality.

(5) Mid-spatial frequencies (MSF): is a response to determine stray light and diffraction. MSF has to be controlled in the RGP.

"VRR" and texture are related to the efficiency of the RGP. "MSF", "edge control" and "surface topography" are the responses of optical performance. The

specifications for all the five responses are defined, optimised and controlled in **Chapter 4**. As shown in the third row of Figure 1-3, these investigations are extremely important to demonstrate that the RGP is a robust process (i.e. with a repeatability > 95%, two sigmas) to process high-quality surfaces efficiently.

Based on the experience in Chapter 4, the next challenge is to increase the efficiency of the RPG in respect to a 1 m hexagonal segment. This work is achieved by improving the grolishing tool, constructing a novel metrology method, and using Matlab programming to operate the prototype metre-scale measurement system and to analyse the measured results. All the research work aims to demonstrate that the RGP is able to process metre-scale optical segments, as shown in the fourth row of Figure 1-3. The investigation is undertaken in **Chapter 5.**

Manufacturing of complex surface forms is an extremely important element in the field of astronomy, imaging and defence. The scientific focus in the final stage can be described as “making any arbitrary optical surface we desire” (i.e. freeform or complex surfaces). For the RGP, the most challenging aspect is to explore the effects of errors in the fit between the rotating robotic grolishing tools and the glass. In addition, the research is facilitated by creating a glass-bending mechanism that can create an arbitrary and continuous complex surface form in a much more efficient way than the conventional method to generate a surface. This study achieves the last row of Figure 1-3. The concept and process are described in **Chapter 6**.

Chapter 7 summarises the work described in this research and provides suggestions for future work.

In summary, the objective of this thesis is to realise a new processing method (i.e. RGP) lying between CNC grinding and CNC polishing in order to speed up overall manufacturing efficiency. The contributions are summarised in Table 1-2.

Table 1-2: The author's contribution to the work of each chapter

	Contributions
Original aim	Introduce the RGP to speed up the connection between grinding and polishing.
Chapter 1	Indicate the role of the RGP in the current processing chain.
Chapter 2	Review all the current processing processes to show the importance of the RGP.
Chapter 3	Develop the principle of the robotic arm, examine the fundamentals of the experimental preparations, and propose the statistical experimental design and analysis to conduct a series of systemic experiments.
Chapter 4	Realize the RGP. Propose specification and control for all responses so as to achieve the requirement of more than 95% repeatability.
Chapter 5	Demonstrate that the RGP can process metre-scale surfaces and show that the prototype metrology can be used to measure the processed results.
Chapter 6	Develop a method to create complex surfaces and demonstrate that the RGP can be used to process any arbitrary forms.
Chapter 7	Summarise the achievements, indicate future work and propose potential applications for the techniques used in this thesis in other related areas.

Chapter 2 Overview of large optics and their manufacture

2.1 Introduction

Metre-scale optical systems have characteristics which are defined by customers to meet their specific requirements. The optical design of a telescope system, the processing methods to produce high accuracy mirrors, the metrology to examine outputs, and the active/adaptive optics to maintain sharp images are all examples of the type of characteristics that customers wish to define to meet their specific requirements.

The quality of metre-scale optical systems is measured in terms of these characteristics, and finally determined by one true evaluator: the customer, who can be astronomers, optical designers and project investors. Figure 2-1 helps to illustrate the circle of developments in optical engineering. For example, customers can vote with their funding on which products would satisfy their requirements, e.g. on price, delivery and performance risk. Optical designers take information from the customers' requirements to define specifications, which include devices, dimensions, materials, processes and tooling. Optical fabricators use this information to machine the segmented telescope (for example, the E-ELT primary segments and specification are discussed in section 2.3.3). The segments are then examined by measurements and, finally, delivered to the customers. The customers provide feedback to the optical designers and the designers listed requirements for the optical fabricators who come in terms of the number of segments, and make sure that each

segment arrives at a scheduled time in the right place to satisfy the customers. While it is challenging to meet the requirements of each phase in the development cycle, a new idea within any part of this circle may sometimes stimulate its own new market.

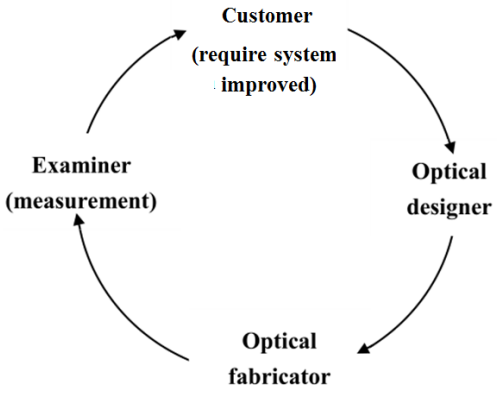

Figure 2-1: Circle of developments in optical engineering

As shown in Figure 2-1, "optical design", "fabrication" and "measurement" are three related keys to the manufacture of excellent optical surfaces, and therefore each element must be discussed in this chapter. In addition, in order to build powerful metre-scale optical systems in the future (e.g. the E-ELT and TMT), the concepts of active and adaptive optics are required and these are therefore also introduced at the end of this chapter.

2.2 Background theory of the optical telescope

2.2.1 Benefits of a larger telescope

A powerful ground-based telescope is determined by the "size" and the "surface forms" of its primary mirror. More light can be captured by a larger primary mirror, and a brighter image allows the observation of fainter and more distance objects; surface forms, meanwhile, can provide high contrast output images to detect more details in the observations. Solutions to achieve the required mirror forms are processed by various manufacturing machinery techniques (Section 2.4), and facilitated in service by active and adaptive optics (Section 2.6). Optical designs for astronomical telescopes are introduced in Section 2.3.

2.2.2 Size and resolution

There are a variety of reasons why no optical system can capture all the details of an object into its image. The first reason is diffraction. According to the Huygens-Fresnel principle of light wave propagation, the movement of light across corners, edges and obstructions results from the fact that the light does not act only as a straight-line ray, but travels as a wave motion to bend the light ray in a small but finite angle. This diffraction limits the performance of an optical system. Secondly, most objects are not absolutely planar, but are three-dimensional objects that are not in focus. Any point on the object may focus into the image plane, but the other out-of-focus mapping points result in finite spot sizes that degrade image quality. This issue is relevant for a camera or for a microscope but not an astronomical

telescope since, in most cases, the objects are so far away. Thirdly, optical aberrations within lenses or mirrors result in an imperfect preservation of the ideal image shape. One important goal for optical designers is to balance the aberrations caused by different surfaces against one another (the theory of optical aberrations is well-understood and can be referenced to [48]). Finally, a number of secondary effects contribute to degrading image quality; these include scattering and stray light from the environment, non-homogeneity and the thermal characteristics of optical materials, and machinery, alignment and support errors in respect to each surface in an optical system.

Even if a perfect optical surface were achievable, without the aberrations, lens or mirror form errors and the secondary effects mentioned above, the fundamental maximum to observe an object from an optical system would still be limited by the instrument's theoretical limit, namely its diffraction limit [49]. Although a diffraction-limited optical system is not perfect, it can act as the ideal reference against which the performance of systems can be compared. The closer the real optical system is to the diffraction-limited system, the better the image quality it can produce. Fresnel's diffraction theory is the fundamental principle to describe the limitations imposed by diffraction within an ideal optical system [50]. A fuller account of his theory is provided by Goodman [51] and Gaskill [52].

For a circular aperture of an ideal segmented telescope, without considering any gap and edge effects between and within each segment, and only considering the diffraction from the aperture, incoming light waves may interfere with the finite circular aperture to result in diffraction. The resulting diffraction pattern has a series

of concentric bright and dark rings of decreasing intensity around it, and a central bright area called the Airy disk.

The Airy disk is very important because it determines the resolution and contrast of the image in an optical system. The size of the Airy pattern is defined by the distance (*Z*) from the central disk to the first dark ring, given by:

$$Z = \frac{0.61\,\lambda}{n' \sin U'} = \frac{0.61\,\lambda}{NA} = 1.22\,\lambda\,(f/\#) \tag{2-1}$$

where λ is the wavelength, NA is the "numerical aperture" that characterises the maximum angle of incident light accepted by the system, n' is the index of refraction in which the image lies, $\sin U'$ is the half angle of the cone of illumination, and f/# is the "f-number" (the focal ratio, described by the ratio of the focal length to the clear aperture of a telescope to determine the amount of light passing through the system). It is worth noting that the illumination of an image is determined by the f-number and exposure time of the system.

As shown in Equation (2-1), both the numerical aperture and f-number are two methods to characterise an optical system. If a system is operating for infinite object distances and is corrected for coma and spherical aberration (i.e. aplanatic systems), the relationship between the two quantities is:

$$f/\# = \frac{1}{2NA} \tag{2-2}$$

Please refer to the work in [53-55] for a more rigorous mathematical development of the Airy diffraction pattern and the concept of f-number and numerical aperture.

That diffraction limits the optical performance of a telescope is to be expected, even with the best design. In order to evaluate the optical performance of a telescope, given the existence of diffraction, the "angular separation (α)" of an optical system is appropriate to describe an instrument whose object distance is extremely long [55].

In respect to angular separation (α), a conversion exists between Z and α. If one assumes that a telescope is an aberration free system (i.e. a diffraction limited system) and that it is not affected by gravity and atmospheric disturbance, as shown in Figure 2-2, then:

$$\mathrm{l}' = \frac{-\omega}{2\sin U'}$$

When α is small, the equation can be written as a close approximation as:

$$\mathrm{Z} = \frac{\mathrm{l}'\alpha}{\mathrm{n}'} = \frac{-\alpha\omega}{2\mathrm{n}'\sin \mathrm{U}'} = \frac{-\alpha\omega}{2\ \mathrm{NA}} \qquad (2\text{-}3)$$

By rearranging Eq. (2-1) and (2-3), the angular separation is

$$\alpha = \frac{1.22\,\lambda}{\omega}\ \text{radians} \qquad (2\text{-}4)$$

For a determined observation wavelength of an ELT, the limited resolution is determined by increasing the aperture. Moreover, the light collecting power is proportional to the square of the primary size. New generations of larger telescopes are therefore able to observe much fainter objects in much more detail from extremely distant parts of the universe.

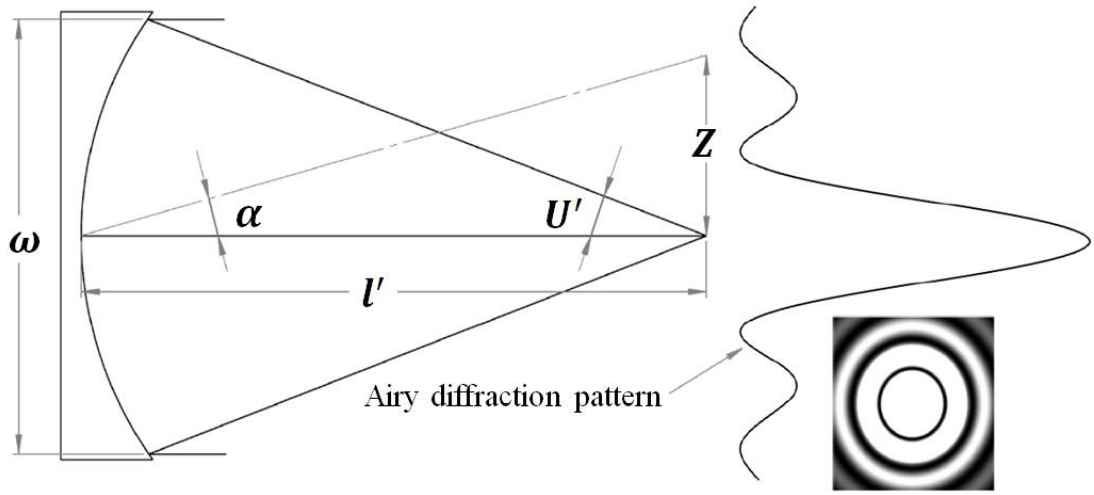

Figure 2-2: The relationship between α, U', Z, l' and ω

2.3 Optical Design

2.3.1 Aspherical surface

The advantages of aspherical surfaces, or aspheres, in optical systems have been known for many years [56]. The main problems that aspherical surfaces seek to correct are spherical aberrations (such as parabolic surfaces) and off-axis aberrations (such as the Schmidt telescope). Other benefits of using aspherical surfaces are to reduce optical elements, to reduce total weight and, in some cases, to reduce the overall cost of fabrication. Although spherical surfaces are used for the Maksutov telescope, aspherical surfaces have been widely used on large numbers of modern-day telescopes.

An aspherical surface can be described by continuous mathematical functions. According to standard ISO 100110-Part 12 [57, 58], aspherical surfaces functioning with axial symmetry are described by:

$$\text{Surface sag} = S(z) = \frac{Cr^2}{1+\sqrt{1-(1+k)C^2r^2}} + \sum_{n=2}^{\infty} \alpha_{2n} * r^{2n} \qquad (2\text{-}5)$$

where the optical axis is assumed to be the z-axis, S is surface sag – the displacement of the surface from its vertex (as shown in Figure 2-3), C is the curvature, r is the radial aperture component in the lens units, k is the conic constant, and $\sum_{n=2}^{\infty} \alpha_{2n}$ is higher order aspheric coefficients. For the mathematical proof, one can refer to [47].

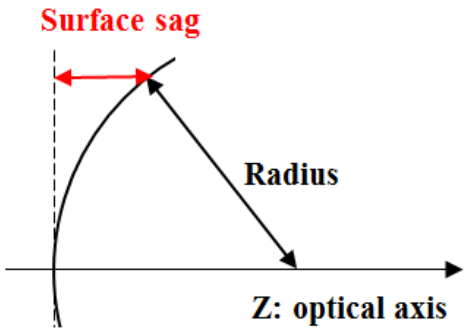

Figure 2-3: Surface sag

Since not all manufacturing equipment supports the use of α_2 in the aspherical equation, it is safer to let α_2 equal 0, even though many commercial optical software packages (e.g. Zemax, Code V, OSLO) can optimise α_2.

A conic surface can be generated by a plane intersecting through the base of a cone [59]. As shown in Figure 2-4 and Figure 2-5, various conic surfaces can be designed

in an astronomical telescope to improve its optical performance. Historical examples of the use of various combinations of conic constants to remove optical aberrations are introduced in the following subsections.

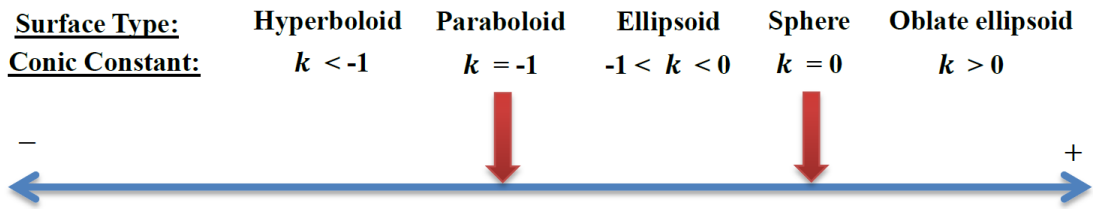

Figure 2-4: Conic constants and their related surface types

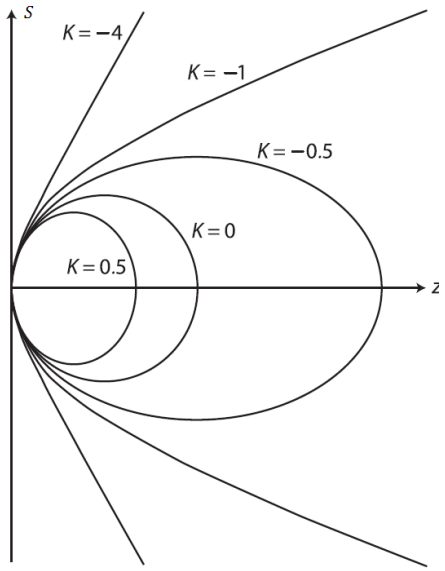

Figure 2-5: Conic constants and surface types

2.3.2 Design forms of the ground-based reflective telescope

In 1668, Isaac Newton built the first reflecting telescope, composed of a single spherical mirror with a fold mirror, namely the Newtonian telescope [60]. His telescope avoided chromatic aberrations (CAs), but the image was severely affected

by spherical aberrations. In 1721, John Hadley solved many of the problems of making a parabolic mirror, and the spherical primary mirror of the Newtonian telescope was changed to a parabolic mirror, resulting in less spherical aberrations (zero in theoretical calculation) on the axis, but with an observing field limited by off-axis optical aberrations, such as coma, astigmatism and field curvature [61, 62]. As shown in Figure 2-6, the Cassegrain telescope further improved the fold mirror, compared to the Newtonian telescope, by making it a negatively powered hyperbolic secondary mirror. Both the positive parabolic primary and the negative hyperbolic mirrors share a common focus point, resulting in an excellent correction of both the on-axis image and the field curvature [63]. The Cassegrain telescope's equivalent focal length can be much longer than the physical length.

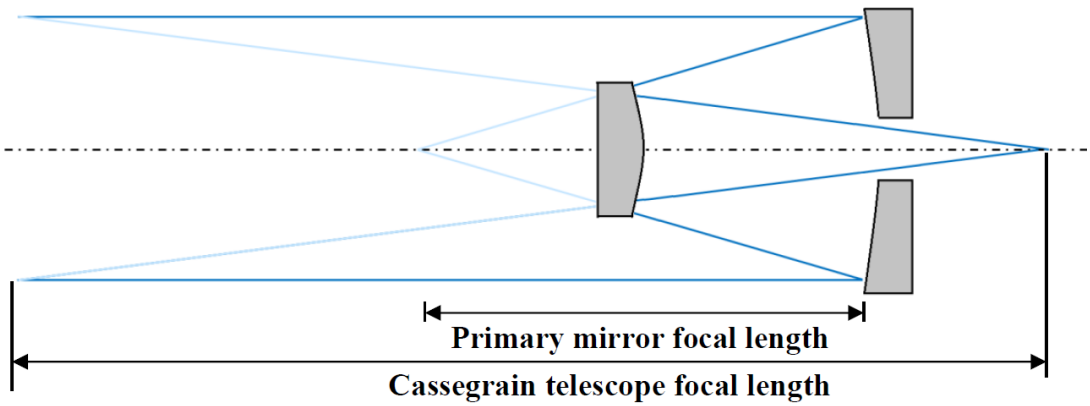

Figure 2-6: Configuration of the Cassegrain telescope

In the 1910s, George Willis Ritchey and Henri Chrétien redesigned the Cassegrain telescope to comprise two hyperbolic mirror surfaces [64]. The Ritchey-Chrétien telescope has no three-order coma and spherical aberration, resulting in wide field astronomic observation [65]. The configuration of the Ritchey-Chrétien Cassegrain

type has been applied to the current astronomical telescopes, such as the Hubble space telescope, the Keck telescopes [66], the VLT telescope, as well as the E-ELT.

2.3.3 Optical design of the E-ELT

The evolution of the telescopes has been introduced in Chapter 1 and, further, in the preceding section. This section aims to discuss details of the E-ELT project. The E-ELT will be operated in visible and near infrared wavelength ranges from 0.3 – 24 μm, with a maximum field-of-view as wide as 10 arc minutes to the Nasmyth focus. Based on the Cassegrain telescope, the Nasmyth focus is introduced by adding fold-mirrors to shift a focus position to have easier accessibility.

For the optical design, the quinary mirror system of the giant E-ELT will be composed of three aspherical mirrors and two fold flat mirrors. This configuration is based on the Ritchey-Chrétien Cassegrain telescope [67]: firstly, the primary mirror is a near hyperbolic surface; secondly, a third aspherical mirror is added. The first three reimaging mirrors are used to correct and balance off-axis aberrations, while both the folding flats transmit the image to a Nasmyth focus. There is no benefit to be had in using spherical mirrors because the three aspherical mirrors are the best composition to achieve a diffraction-limited E-ELT with the minimum optical surface and lowest overall weight [32].

The optical layout and mirror data of the E-ELT are shown in Figure 2-7, Table 2-1 and Table 2-2 respectively.

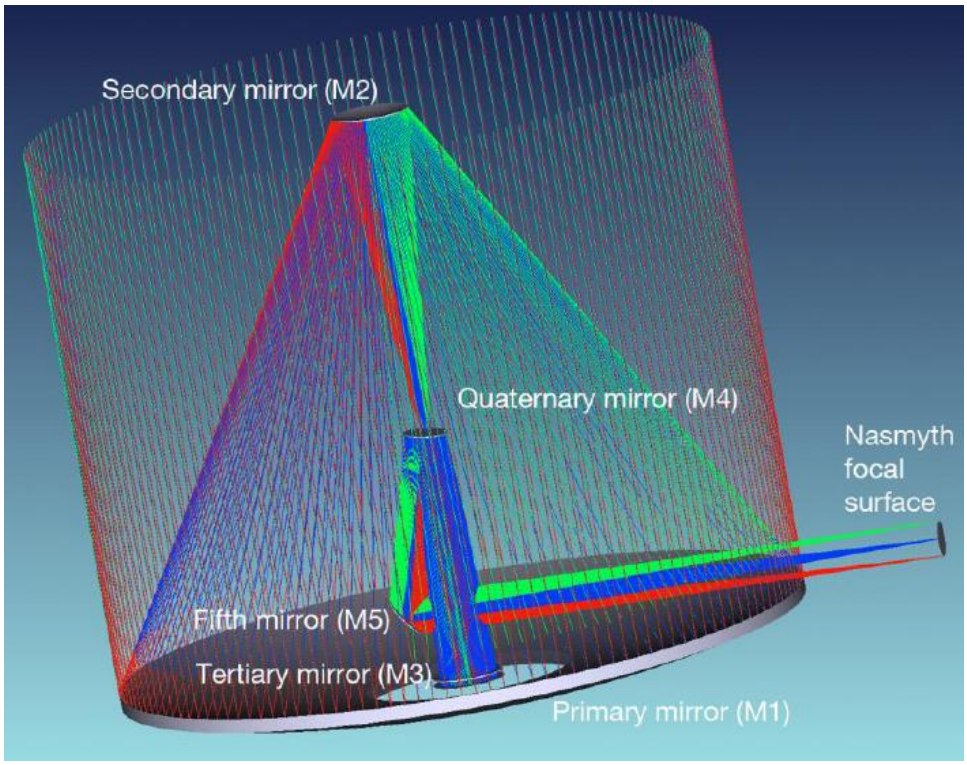

Figure 2-7: E-ELT: quinary mirror system [12]

Table 2-1: Mirror characteristics of the E-ELT [68]

Surface	Shape	Inner Radius (mm)	Outer Radius (mm)
M1	Segmented, quasi circular	4708.7	19573.2
M2	Circular	454.5	2045.3
M3	Circular	67.3	1878.6
M4	Elliptical	289.3*287.3	1190.7*1171.1
M5	Elliptical	57.6*46.9	1308.6*1038.9

Table 2-2: Mirror data of the E-ELT [68]

Surface	Radius of curvature (mm)	Thickness (mm)	Conic	Aspheric Coefficients	
				4^{th}	6^{th}
M1	-69000.000	-30830.00	-0.995882	-	
M2	-9313.000	30509.40	-2.28962	4.79584E-14	
M3	-21067.947	-13200.00	0	8.25713E-13	0
M4	Infinity	10000	-	-	-
M5	Infinity	-29172.38	-	-	-
Image	11223.000	0	-	-	-
1. The sign of the thickness is changed after reflection 2. Tilt angle of M4 is 7.75° 3. Tilt angle of M5 is 37.25°					

2.3.3.1 Modern segmented primary mirrors

Four significant reasons for using segmented primary mirrors for current and future ground-based/space telescopes are: (1) a segmented mirror can greatly reduce the weight of the mirror, (2) mirror segments can be folded up to occupy a smaller volume for transportation, (3) a segment can be manufactured more cost-effectively (e.g. ease and speed), and (4) machining a 39 m monolithic piece of glass to be

homogeneous is beyond the state-of-the-art. Hence, segmented telescopes represent the trend for future metre-scale large telescopes.

Three kinds of pupil geometries for segmenting a primary mirror are summarised in Figure 2-8. The first one is petals, also called keystones, in which a primary is sliced in azimuthal and radial directions. This segmented technique was demonstrated in the 1980s to indicate that a metre-scale primary could be segmented and controlled to achieve the required image quality [69]. The petal segmented mirror is still used today for designing metre-scale telescopes [70]. The second configuration is to use seven circular mirrors to compose the primary mirror. This arrangement is used for Giant Magellan Telescope (7 × 8.4 m apertures) [71]. The third geometry for segmented mirrors utilises close-packed hexagons. This pattern was used with the two Keck telescopes (two 10m aperture), the Southern African Large Telescope (11m aperture), GranTeCan (10.4m), and will also be used to construct the primary mirror for the E-ELT.

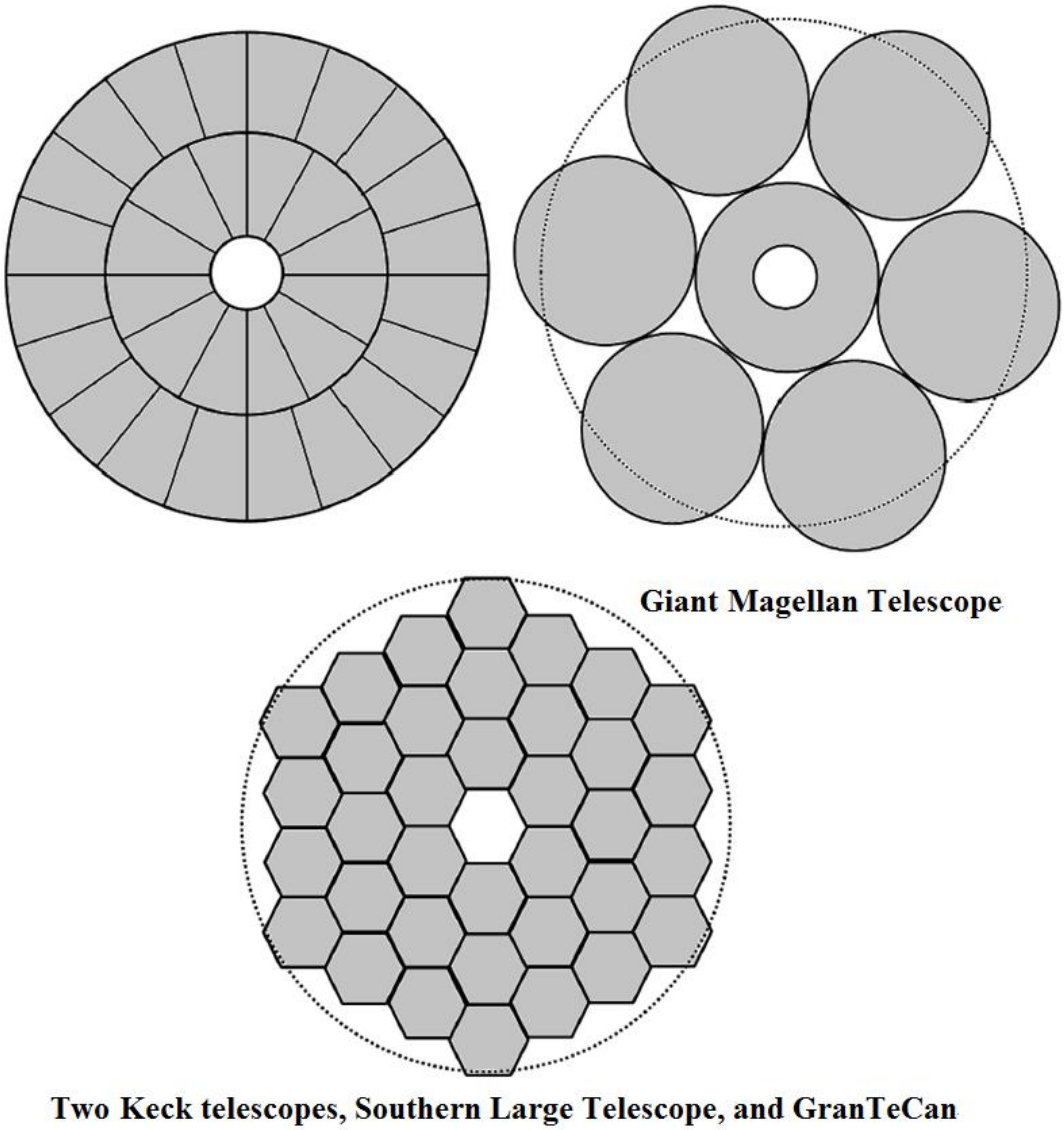

Figure 2-8: Three kinds of segmented telescopes

The common element in the three mirror geometries is the omitted central segment. This is because the centre hole is prepared for obstructions in the telescope system, such as a secondary mirror, folding mirrors or CCD /CMOS cameras for an imaging plane, or all of these.

For the hexagonal segmented telescope, the total number of required segments $K_{segments}$ within total K rings (K_{rings}), without considering the central segment, can be calculated by:

$$\mathrm{K_{segments}} = 3\mathrm{K_{rings}}(\mathrm{K_{rings}} + 1) \tag{2-6}$$

When the diameter of a circular aperture has been decided as D, the side length (L) of every same-sized hexagon to separate the equivalent circular area is given by [72]

$$\mathrm{L} = \mathrm{D}\sqrt{\frac{\pi}{6\sqrt{3}\,\mathrm{K_{segments}}}} \tag{2-7}$$

From the above two equations, and Table 2-1, it can be seen that the dimension of each hexagonal segment for the E-ELT is about 1.45 m, and the total hexagonal segments needed for the M1 are approximately 798. Note that the surface shapes of the hexagonal segments are required to be different if the gaps between segments are to be equal.

2.3.3.2 Specifications of M1 of the E-ELT

The f/0.93243 M1 mirror of the E-ELT is 39 m in diameter and composed of 798 hexagonal segments. Each hexagonal segment is approximately 1.45 m, measured from corner to corner, but only 50 mm thick. As shown in Figure 2-9, six families (133 segments for each family) are installed in the primary mirror, and a seventh family is required in order to exchange any of these for maintenance operations, such

as recoating, so as to ensure continual maximum light-throughput for the E-ELT. Hence, there will be a total of 931 segments for the M1 mirror [73-76].

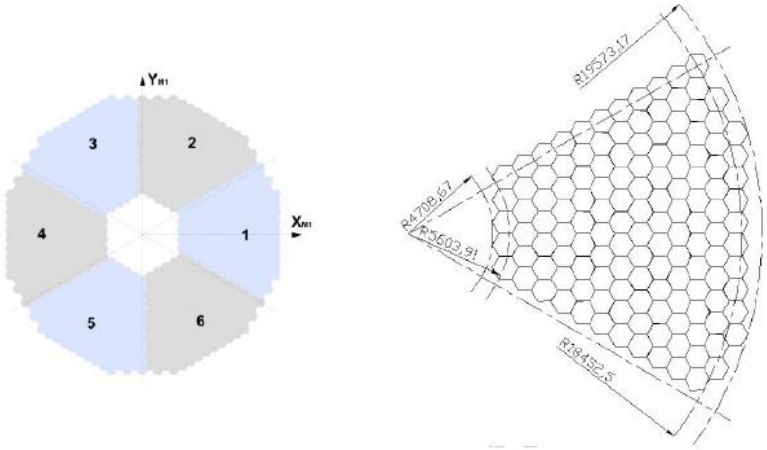

Figure 2-9: M1 of E-ELT (reference from [32])

Each segment is supported by a warping harness to compensate some low-order form-errors, such as defocus and trefoil. The residual requirements of the specification per segment are still stringent, however.

As shown in Figure 2-10, the specification of an E-ELT segment comprises two parts:

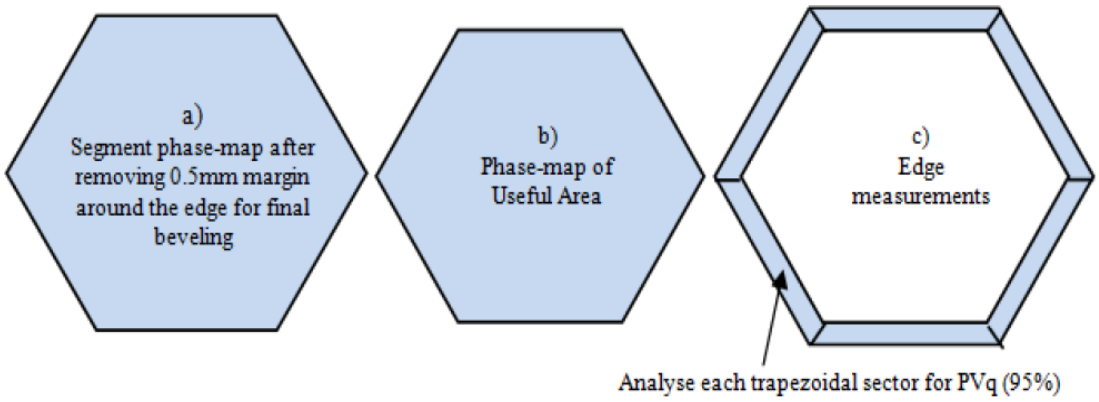

Figure 2-10: Useful area and edge zone [77]

- Useful area: The whole part excluding a 10 mm wide peripheral zone.

  - It has to have < 50 nm RMS wavefront error (WFE), and < 3 nm (requirement) and 2 nm (goal) for the texture.

  - It has to have < 15 nm RMS WFE for the residual requirement, which corresponds to removing tilt, defocus and astigmatism (these errors can be compensated by adjusting the positions between each segment and the focus point).

- Edge zone: A strip at the edge of the bulk required to be no more than 10 mm, with a goal of 6 mm.

  - The maximum WFE is < 400 nm peak to valley wavefront (PVW), and the average of six edges < 200 nm PVW. This is equal to < 200 and < 100 nm surface misfiguring, respectively.

More details of the M1 specifications are presented in [77-79]. Since different tools have different tooling spot sizes to fabricate a surface, it is very important to define the edge zone of a process, although this is highly dependent on the application. The definition of the edge zone in Figure 2-10 is related to polishing spot sizes, and this principle has also been used to define the edge zone of the RGP in Chapter 4.

2.3.3.3 The challenges in manufacturing the M1

The construction of the E-ELT poses the greatest challenges in the optical processing industry. Compared to the current largest segmented telescope, the Keck telescopes, the diameter and number of hexagonal mirror segments for the E-ELT are approximately 3.9 and 22.2 times larger, respectively. In terms of their construction time, the Keck telescopes began from September 1985 and were completed on 23 January 1996 [80]. According to the ESO's website, the first light of the E-ELT will be in 2024. From this point of view, newer technology, such as the RGP, is required to establish manufacturing chains to reduce overall processing time.

For both the Keck I and II and E-ELT, all of the M1 segments are off-axis, thereby increasing the difficulty of making complete hexagonal surfaces in only one orientation relative to the optical axis (details have been discussed in Section 2.3.2). For example, processing, aligning and measuring require more new technologies to reduce overall processing time.

The surface condition of a segmented surface is now discussed (please refer also to Section 2.3.3.1). The E-ELT primary mirror is a nearly parabolic conic aspherical

surface. Whereas with spherical primary mirrors, all the hexagonal segments would be identical and interchangeable, the E-ELT primary mirror requires a total number of 133 different hexagonal segments. For the Keck telescopes, however, there are only six different hexagonal segments. Hence, the E-ELT project has more challenges than the Keck I and II. A comparison between the Keck and E-ELT is provided in Table 2-3.

Table 2-3: Comparisons of the Keck telescopes and the E-ELT

	Keck I and II	**E-ELT**
Processing time	1985 ~ 1996	2024 (first light)
Total hexagons	36+36	798
Different surface forms	6	133

For the E-ELT project, although the hexagonal segments needed comprise 133 different surface shapes, it will still be a challenge to complete all the segments before 2024. Not only is the E-ELT testing the boundaries of current manufacturing technology, therefore, it also requires innovative metrology methods in order significantly to reduce the measuring time. One excellent example of automatic measuring systems proposed by our group is to devise a cooperative system between robotic systems and Zeeko's polishing machines so as to greatly reduce measuring time [81].

Our goal is ultimately to build an automatic manufacturing cell so that the precise surface can be manufactured automatically with an optimised flow from design, to manufacture to measurement, in order to speed up the process. One important aspect to realise in the automation is the need to build data-cloud-based reproducible and repeatable empirical experiments so that a process can choose optimised parameters to complete a manufacturing task automatically. This idea is facilitated by statistical experimental designs, statistical data analysis and statistical inference. These theories are introduced in Section 3.5 and applied in Chapter 4.

2.4 Optical Fabrication

This section reviews different techniques to process metre-scale optics from grinding to corrective polishing to finish a process chain on a surface. Figure 2-11 shows the historical progress in the manufacture of optical surfaces. The advantages of manual processes are that they allow better control of correcting localised errors than automatic machines. On the contrary, although an automatic machine is expensive, the most significant revolution in optical fabrication has been the application of computers that are able to duplicate a process with a high assurance of quality, fast and reproducible process, as well as minimising the need for manual processes and even human intervention.

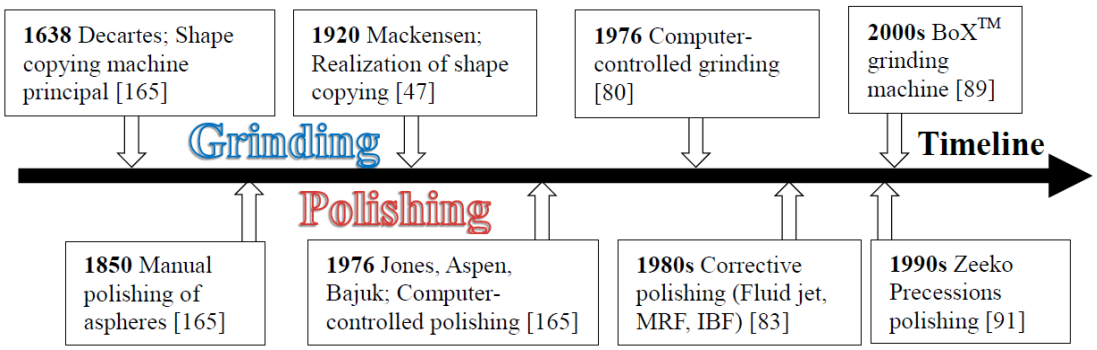

Figure 2-11: Past progress in optical fabrication

The optical surface shape is primarily machined by grinding. The role of grinding is to remove the main stock materials and to generate a required surface in the sub-micrometre range. This grinding, however, will generally leave a micro-rough surface [82, 83] that has to be removed by a subsequent polishing and corrective polishing step. The aim of polishing is to remove the roughness, subsurface damage and mid-spatial frequencies left from the grinding process, as well as to improve the surface form to as low as a few nanometres [84]. Regional surface artefacts are finally finished by corrective polishing processes, such as magnetorheological finishing, fluid jet polishing and ion beam figuring.

Since the RGP is related to grinding and polishing, it is necessary to understand both of these processes. To this end, the different CNC machines used to process large optics (diameter > 200 mm) are introduced from section 2.4.1 to section 2.4.5, and summarised in section 2.4.6.

2.4.1 Computer controlled grinding (CCG)

Disc grinding tools are commonly used by CNC grinding machines to effect stock removal with contour accuracy and high process stability, but the disc diameter may be a problem when processing a concave surface. Alternatively, cup tools and fixed abrasives are typical tool-types applied to CNC grinding machines. The angle of a cup tool is adjustable to a line or a point contact to achieve almost any surface form [85]. In Figure 2-12, A cup tool can be tilted to an angle to achieve a point contact between the tool and a lens to generate the desired surface form [86, 87]. Figure 2-13 shows an E-ELT segment that is corrected by a D25 grinding wheel with error compensation algorithms to complete the grinding process.

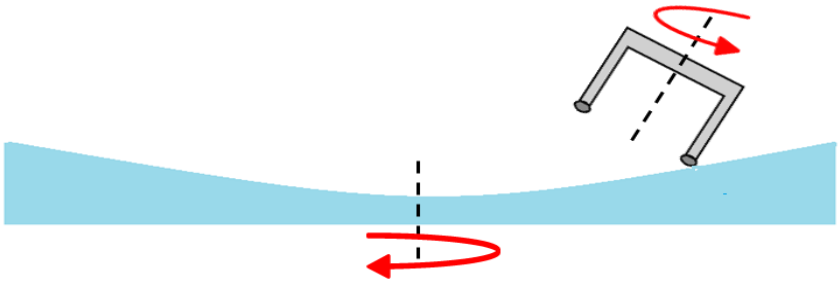

Figure 2-12: The principle of cup wheel grinding

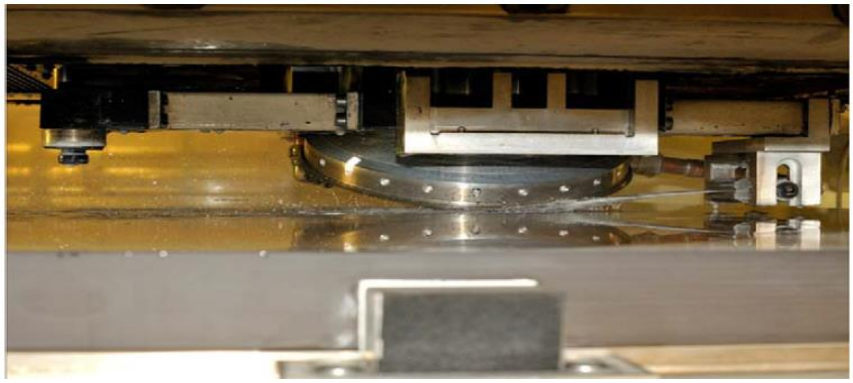

Figure 2-13: An E-ELT segment is processed using a D25 grinding wheel [88]

One significant issue for optical fabricators is to choose suitable variables at the start. Hence, information regarding significant variables for each process is summarised from section 2.4.1 to section 2.4.5 to help a researcher start their process. All the workpieces are metre-scale ceramic glasses (such as Zerodur, ULE, Astrositall, Clearceram and BK7) and SiC.

For the grinding, spindle speeds and other significant variables can be essential to determine a process. The grinding tool can be as large as radius = 242 mm [89] or more to generate a surface and as small as radius = 25 mm or less for fine grinding. Table 2-4 summarises the spindle speeds of typical grinding machines from Schneider GmbH & Co. KG, OptoTech, and Satisloh to grind a surface shape.

Table 2-4: Common spindle speeds for CCG

Variables	Minimum	Maximum
Workpiece spindle	0 rpm	2500 rpm
Tool Spindle	2000 rpm	15000 rpm

2.4.2 Computer controlled polishing (CCP)

The Preston equation [90] is fundamental for many removal algorithms used by CNC (computer numerical control) machines to process optical surfaces. The equation indicates that the volumetric removal rate (VRR) is determined by tool load, the relative velocity between the tool and a workpiece, and the processing time [90], as described by:

$$\frac{dz}{dt} = C_p \times \frac{L}{A} \times \frac{ds}{dt} \tag{2-8}$$

where $\frac{dz}{dt}$ volumetric removal rate describes thickness changes over time; C_p is the Preston coefficient, which is related to workpiece materials, tooling, slurry and temperature; L is the tool load; A is the contact area between the tool and the workpiece, and $\frac{ds}{dt}$ is the relative velocity of the tool to the workpiece.

One important issue for traditional polishing by using pitch tools is that a misfit may exist between a pitch tool and the aspherical surface. In order to improve local shape accuracy in such cases, since a full aperture is no longer able to change the local

curvature, the full aperture tool is replaced by a sub-aperture tool for local correction. Today, many CNC machines use dwell time to optimise the tool path in order to correct local deviation. Assuming that $s(x)$ is the inverse velocity, the local removal on a workpiece can be described as [47]:

$$\mathrm{R(x)} = \int \mathrm{c(x - x')s(x')dx'} \tag{2-9}$$

where $\mathrm{R(x)}$ is a target removal that depends on measurement, called the error map; $\mathrm{c(x - x')}$ is the tool function (i.e. **Influence function**), which must be experimentally measured. $\mathrm{s(x')}$ is solved by deconvolution of the desired removal and the tool function by an optimised algorithm. Although different algorithms exist for different CNC machines, equation (2-9) is the principle determining the application of local correction to achieve the overall required correction.

A bulged (inflated membrane) sub-aperture tool that adapts to a surface form by an applied pressure has been patented by Zeeko Technology [91]. The z-offset distance determines an important variable in CCP: pressure and process spot size. A polyurethane material is usually used on the polishing tool, and cerium oxide is frequently used for slurry over a workpiece for Zerodur, silicon and glasses. The R80 solid rubber tool (the polishing tool characteristics are explained in Chapter 3) is used by a Zeeko IRP600 machine to polish a segment, as shown in Figure 2-14. This kind of tool is excellent in terms of fitting multiple surface forms, and has been used to polish prototype E-ELT segments. The application of the bonnet polishing process can be referenced to [92-95]. Table 2-5 summarises common variables from Zeeko,

Schneider GmbH & Co.KG, OptoTech, and Satisloh for use when polishing optical surfaces.

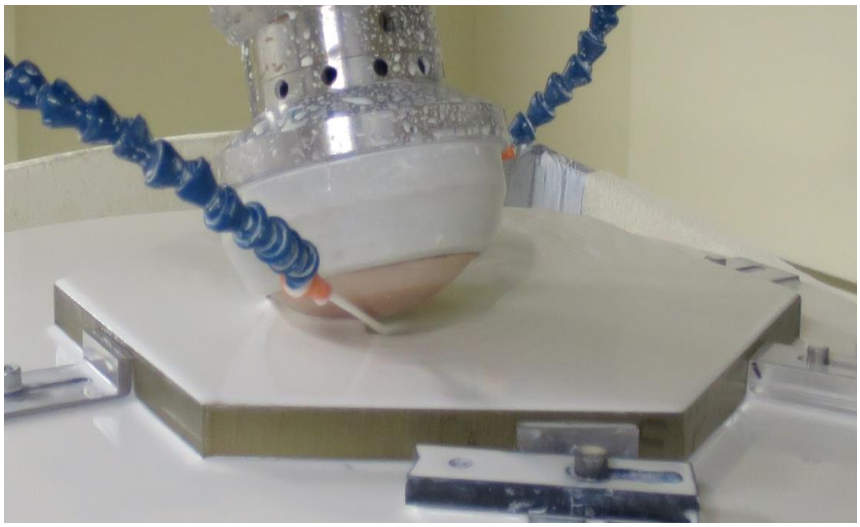

Figure 2-14: A solid rubber tool to polish a 400mm test segment

Table 2-5: Common spindle speeds for CCP

Variables	Pre-polishing		Corrective polishing	
	Minimum	**Maximum**	**Minimum**	**Maximum**
Workpiece spindle	0 rpm	2500 rpm	0 rpm	1000 rpm
Tool Spindle	500 rpm	2500 rpm	100 rpm	1000 rpm

2.4.3 Magnetorheological Finishing (MRF)

MRF is characterised by replacing the sub-aperture tool of the CCP by a wheel with a magnetorheological liquid, such that the magnetic field applied to the liquid can localise stiffness to fluid in order to assist a sub-aperture tool to correct a polished surface. There are two industrial MR fluids. The first one is composed of cerium

oxide in an aqueous suspension of magnetic carbonyl iron powder, which is suitable for low-expansion ceramics [96]. The other fluid is nanodiamond powder, which is used to machine polycrystalline ceramics [97].

The first patented MRF technique was invented in the late 1980s at the Luikov Institute of Heat and Mass Transfer in Minsk, Belarus [98]. The technique was further investigated by W. Kordonski and the Center for Optics Manufacturing (COM) in Rochester, USA, and the first commercial MRF machine was introduced by QED technologies in 1998 [99].

The disadvantages of MRF (along with other corrective polishing processes, such as fluid jet polishing and ion beam figuring) are that (1) they cannot rectify coarse form errors, (2) processing times are 50 times or more slower, and (3) they are at least 10 times more expensive than similar sized polishing machines. MRF is, therefore, not used to polish a ground surface but is an optimised process to correct regional errors in a polished surface. Hence, MRF is a 'finishing' process. The principle of the MRF system is shown in Figure 2-15. In recent years, QED has demonstrated that by combining MRF with a raster process it is possible to fabricate a polished 1.5 m diameter surface [100], as shown in Figure 2-16.

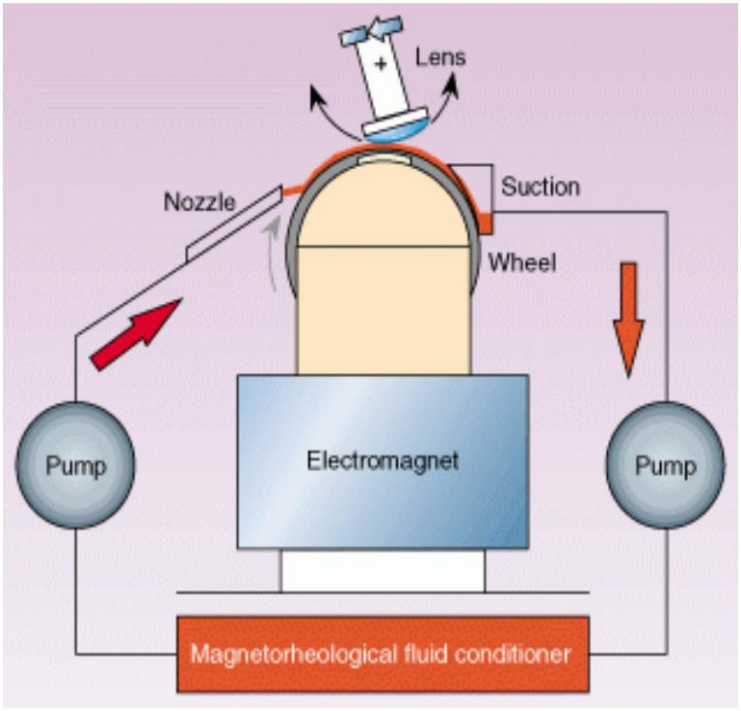

Figure 2-15: The principle of the MRF system [101]

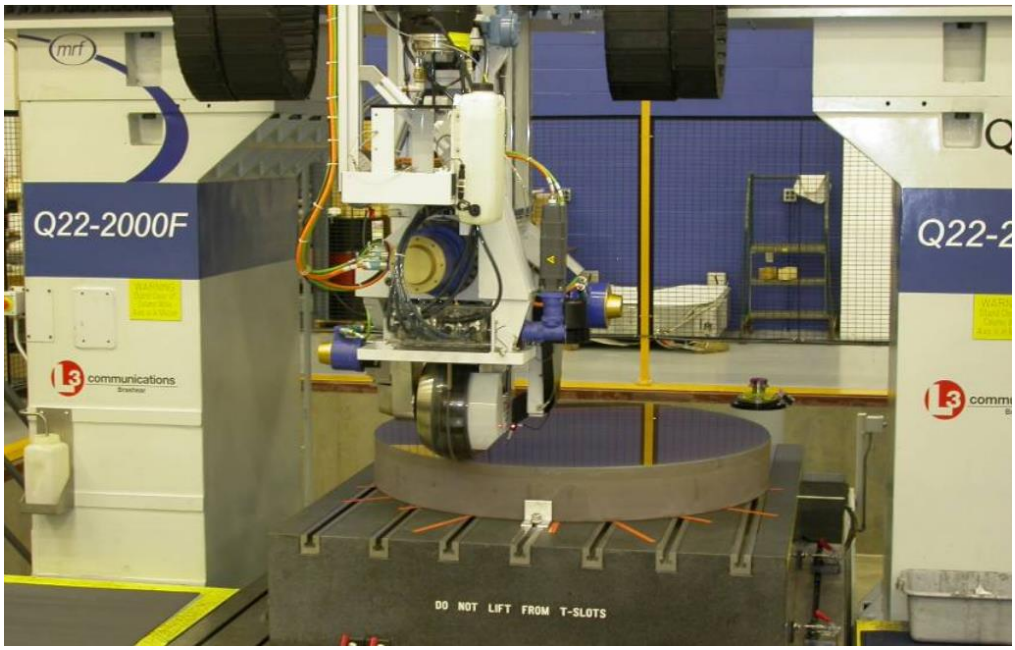

Figure 2-16: QED is used to make a 1.5 m diameter surface [102]

Compared to CCP, MRF has the advantage of avoiding the tool wear variations seen in other fabrication processes [103], and hence, has more stable material removal functions to correct a surface. Table 2-6 shows common spindle speeds required for MRF to manufacture an optical surface, taken from QED technologies Inc., Schneider GmbH & Co.KG, and the Center for Optics Manufacturing (COM). It should be noted, however, that the polishing slurry is proprietary, expensive and has a limited lifetime and hence MRF is not able to replace CCP for the scale of polishing required for projects like the E-ELT.

Table 2-6: Common spindle speed for MRF

Variables	Minimum	Maximum
Workpiece spindle	0 rpm	550 rpm

2.4.4 Fluid Jet Polishing (FJP)

The idea for FJP came from the application of abrasive slurry jets where a stream of premixed slurry is pumped through a nozzle at pressures above 70 bar, or even hundreds of bars, in order to cut metal, rock and in some cases for optical glasses [104]. Similarly, the principle of the FJP technique is to use a stream of pumped slurry passed across a small cup-wheel-like nozzle to remove workpiece materials, as shown in Figure 2-17.

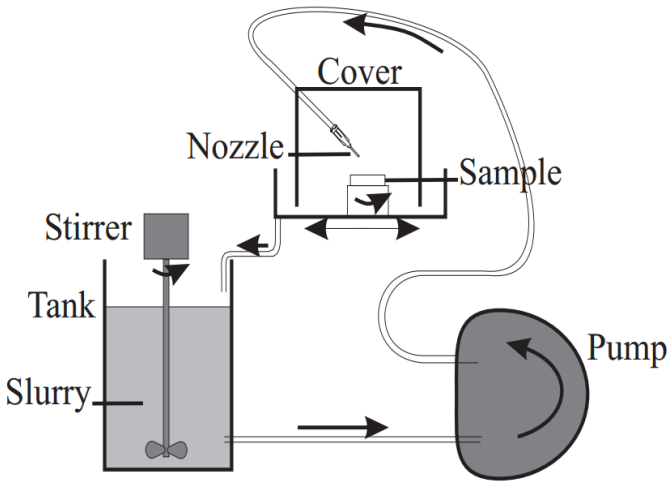

Figure 2-17: The principle of FJP [105]

Removal is decided by the collision of particles in slurry pumped through a nozzle against a working surface [106]. The desired removal profile is adjustable by several variables, as listed in Table 2-7.

Table 2-7: Variables for FJP

Variables	Minimum	Maximum
Workpiece spindle	0 rpm	500 rpm
Stand-off distance (nozzle and glass)	0.05 mm	20 mm
Pumping Pressures	5 bar	20 bar (normally < 15 bar)
Nozzle diameters	Sub-millimetre	4 mm
Footprint size	Sub-millimetre	10 mm

As a candidate process for the production of metre-scale glass segments, such as for E-ELT or TMT, FJP has been demonstrated to modify the residual edge defects of an optical segment on a Zeeko IRP polishing machine [107]. In addition, FJP has been applied with bonnet polishing to fabricate an X-ray mirror with 27 nm PV and 0.28 nm RMS surface texture [108], as shown in Figure 2-18.

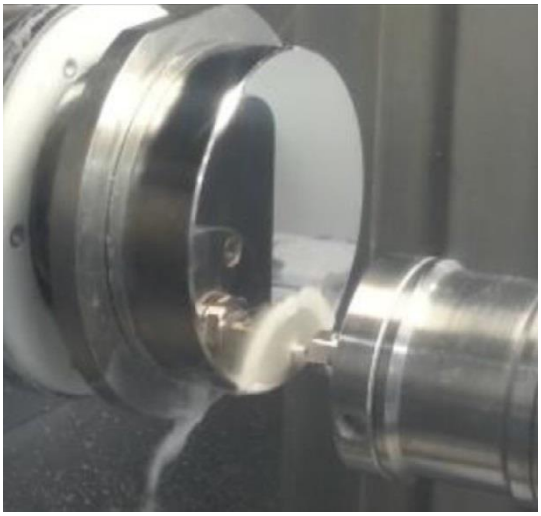

Figure 2-18: FJP on an X-ray mirror [108]

2.4.5 Ion Beam Figuring (IBF)

As shown in Figure 2-19, the sub-aperture IBF tool is an ion gun. This needs to be operated in a vacuum chamber, however. The removal function is shaped like a Gaussian beam, and the tool footprint is determined by a full width at half maximum of a Gaussian-like shape [109]. The removal rate can be accurately calculated based on laws of elastic and inelastic scattering [110].

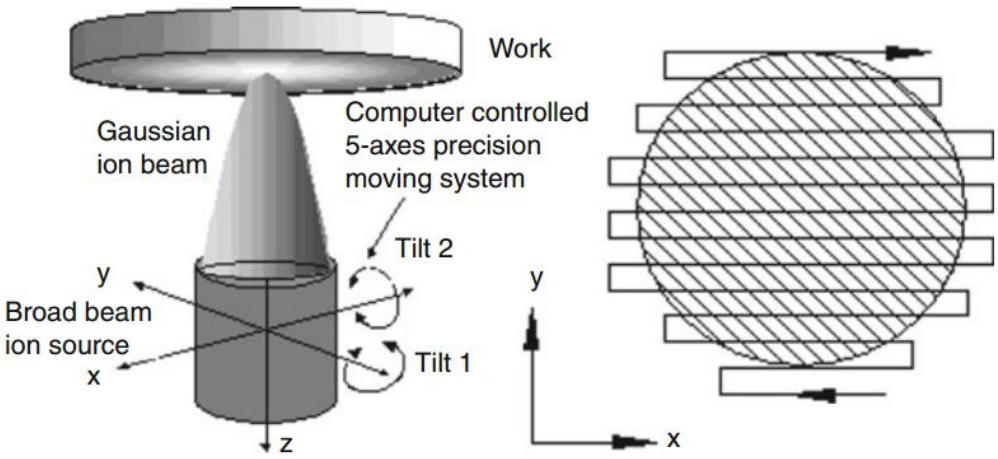

Figure 2-19: Principle of IBF (left) and process with a raster tool path (right) [110]

The absence of a chemical reaction during the process makes the IBF process stable, but the process is limited by slow manufacturing times. Its typical removal rate (response variables) and other significant variables (from Sagem and Nikon) are listed in Table 2-8.

Table 2-8: Typical variables from IBF

Variables	Minimum	Maximum
FWHM	few mm	200 mm
Ion beam current	few mA	Some 100 mA
Removal rate	~ 1 nm/min	Some 100 nm/min
Nozzle diameters	Sub-millimetre	4 mm
Footprint size	Sub-millimetre	10 mm

IBF removes materials on a molecular level to derive a minimum surface deviation, and this process may, therefore, be used after a CCP process to achieve a desired specification. Figure 2-20 shows a 1 m corner-to-corner hexagonal Zerodur segment that was polished by a Zeeko polishing machine at OpTIC before being processed using IBF in the Brera Astronomical Observatory.

Figure 2-20: A 1 m corner-to corner hexagonal segment processed by IBF [111]

2.4.6 Summary of the fabrication processes

A comparison of the five different fabrication processes discussed in the above sections is summarised in Table 2-9. The table indicates that there is a huge gap between grinding and polishing, and that the RGP represents a suitable process to fill this gap in order to speed up the overall process. Details of the RGP are introduced in Chapter 3.

Table 2-9: Summary of different fabrication process. A segment was typically generated by CCG, polished by CCP and finally finished by MRF, FJP or IBF. It is obvious that RGP can fit a gap between CCG and CCP to accelerate the overall process.

Process	Typical output surface deviation [nm)	Typical output texture [rms nm]	Advantages	Limitations	Will it polish?
CCG	PV < 1000	5-1000	High speed to generate an accurate surface	Surface texture Sub-surface damage Mid-spatial frequencies Part radius < tool radius	No
CCP	PV < 20 RMS ~ 1	0.5	Very low surface texture	Tool wear Edge roll-off Stability of chemo-mechanical reaction	Yes
MRF	PV < 10	0.3	No edge roll-off No tool wear	Part radius < tool radius	No
FJP	30	0.5	No edge roll-off	Jet stability Pumping systems Nozzle shape	Some-times
IBF	5 RMS: ~0.1	0.2	No edge roll-off Stability of footprint	Low removal rate Surface texture is limited by a determined polished surface High investment and maintenance for a vacuum chamber	No

2.5 Metrology

Precision fabrication needs to be closely integrated with metrology in order to examine a processed surface shape. When measuring the quality of an individual surface (for example, surface shape, MSF errors and texture), the techniques and equipment used depend on the desired target quality and equipment limitation. Furthermore, the need for repeated metrology is essential to close a process-loop.

The aim of the RGP is to improve regional surface errors from grinding and thus to reduce the extra corrective time needed for polishing. Hence, the goals of a grolished surface for metrology are (1) micron accuracy surface forms and edges < 3 μm (Section 4.2.3), (2) surface texture < 400 nm (Section 4.2.1), and (3) MSF < 40 nm (imaging quality simulations are demonstrated in Section 4.2.4). To this end, the measuring methods and equipment used in this thesis are introduced in this section. More details of other metrology techniques can be found by referring to [112-114].

A surface can be characterised in the domains of spatial frequency and surface height by applying a Fourier analysis [115]. The most common method to analyse the topography of an optical surface is to classify the spatial frequency domain into three spatial regions: separating surface form (a low spatial frequency, LSF), from mid-spatial frequencies (MSF), and from surface texture (a high spatial frequency, HSF) [116, 117]. The form has many terminologies, for example, shape, geometry, or figure, but is related to a general macroscopic shape. MSF and texture, meanwhile, relate to microscopic defects in a surface. Generally, there is no clear definition to

distinguish when the spatial period shifts from “LSF” into “MSF” or “MSF” into “HSF”, with the definition depending on the application.

One method for specifying a surface profile is the power spectral density (PSD), which is a method to transfer surface information in the frequency domain. The amplitude relative to the spatial frequency of a surface can be computed and represented in the Fourier spectrum [118, 119]. The PSD has been applied to optics for quantifying the scattering light of a surface [120].

Given that the E-ELT project at OpTIC uses Zeeko polishing technology, the MSF has been defined as the region of 0.02 mm^{-1} < MSF < 1 mm^{-1} [41]. Hence, when the spatial region is higher than the MSF it is described in this thesis as form, and when it is lower it is described as surface texture. In the previous experience at OpTIC, more than 160 hours of polishing hours using R80 bonnets is still not sufficient to remove the signature errors originating from a CNC grinding machine [37], and this grinding artefact is referred to as the “MSF errors”. From Chapter 4 to Chapter 6, it is shown that the RPG process can help the polishing process to remove these MSF errors left over from grinding, so that a hybrid process of grolishing and polishing can improve the overall processing speed when manufacturing a segment (Section 7.3).

Many methods and equipment can measure a grolished surface. The following subsections introduced contact and non-contact measurement techniques that have been used in the RGP.

2.5.1 Surface form measurement

An interferometer can be used to measure a grolished surface. When the texture of the surface is greater than S_a = 250 nm [121], however, the surface may be too grey to be detected by an interferometer with a wavelength of 632.8 nm. Given that the surface textures of the grolished surface discussed in this thesis are greater than S_a = 300 nm, an alternative measurement approach is to use a stylus instrument.

Although a stylus instrument can be used to measure surface form, MSF and surface texture, care needs to be taken when using the stylus instrument [122]. Measurement data can be the convolution result of a measuring surface and a tip surface function (i.e. the tip radius); that is, the tip acts as a low-pass filter, so that signals in higher spatial frequencies are filtered out. If normal stylus equipment is not viable, therefore, other techniques, such as non-contact measurement, interferometry, or even an AFM probe, are required to measure the MSF and surface texture. Non-contact measurements can be limited by optical lenses, resolutions of imaging sensors and pixel sizes.

There are three stylus instruments (Talysurf, Talysurf Intra, and Probing arm) used to measure the grolished surface in this thesis. Details of these instruments are introduced from Chapter 3 to Chapter 6.

2.5.2 MSF determination

Apart from the stylus instrument, interferometry can be used to measure MSF on a specular optical surface (S_a > 300 nm). In section 2.4.2, it was introduced that the bonnet polishing process can achieve excellent surface shape and surface texture, but this process cannot remove the MSF errors at an acceptable speed [41]. In Chapter 4, more than 50 experiments have, however, shown that the R80 bonnet polishing tool (Figure 2-14) cannot only provide a specular surface (S_a = 30~40 nm) for a 4D simultaneous phase-shifting interferometer, but also retain information regarding MSF errors from the RGP. Hence, the R80 bonnet to remove a grey surface has been selected to measure MSF errors from the RGP.

When discussing interferometry, it is necessary to introduce Zernike polynomials, which were first introduced by Zernike for measuring a circular mirror with a knife edge test in 1934 [123] and then extensively studied by Nijboer for rotationally symmetric systems with circular pupils [124]. It has been recognised that the reconstruction of a real surface is achievable given enough polynomial terms [125], and, today, Zernike polynomials are frequently used in metrology because they are convenient for fitting wavefronts to minimise variance. Additionally, Zernike polynomials can also be transformed to describe Seidel aberrations (e.g. spherical aberration, astigmatism, coma, distortion and field curvature, which are commonly used to describe aberrations in the field of optical design), and hence Zernike polynomials have been widely used by designers [126].

Zernike circle polynomial expansions are extremely important because most optical systems are rotationally symmetrical with circular pupils [127]. Moreover, a 4D interferometer with a 180 mm circular aperture is used in this thesis for MSF measurement, and therefore the circular polynomials are introduced. Please note that other expressions for noncircular apertures, such as hexagonal, square, or elliptical shapes, would have to be amended and are not suitable in this case.

Circular Zernike polynomials can be described as:

$$W(\rho,\theta) = \sum_{i=1}^{n} a_i Z_i(\rho,\theta) \tag{2-10}$$

where $W(\rho,\theta)$ is the wavefront; $Z_i(\rho,\theta)$is the i^{th} Zernike polynomial expressed in polar coordinates; a_i is the coefficient. The first 15 terms through the 4^{th} order are listed in Table 2-10 and Figure 2-21.

Table 2-10: first 15 terms of circular Zernike polynomial [128, 129]

Order	$Z_i(\rho, \theta)$	**Name**
0	1	Piston
1	$2\rho \sin\theta$	Vertical tilt
1	$2\rho \cos\theta$	Horizontal tilt
2	$\sqrt{6}\rho^2 \sin 2\theta$	Oblique astigmatism
2	$\sqrt{3}(2\rho^2 - 1)$	Defocus
2	$\sqrt{6}\rho^2 \cos 2\theta$	Horizontal astigmatism
3	$\sqrt{6}\rho^3 \sin 3\theta$	Oblique trefoil
3	$\sqrt{8}(3\rho^3 - 2\rho) \sin\theta$	Oblique coma
3	$\sqrt{8}(3\rho^3 - 2\rho) \cos\theta$	Horizontal coma
3	$\sqrt{6}\rho^3 \cos 3\theta$	Horizontal trefoil
4	$\sqrt{10}\rho^4 \sin 4\theta$	Oblique quatrefoil
4	$\sqrt{10}(4\rho^4 - 3\rho^2) \sin 2\theta$	Oblique secondary astigmatism
4	$\sqrt{5}(6\rho^4 - 6\rho^2 + 1)$	Spherical aberration
4	$\sqrt{10}(4\rho^4 - 3\rho^2) \cos 2\theta$	Horizontal secondary astigmatism
4	$\sqrt{10}\rho^4 \cos 4\theta$	Horizontal quatrefoil

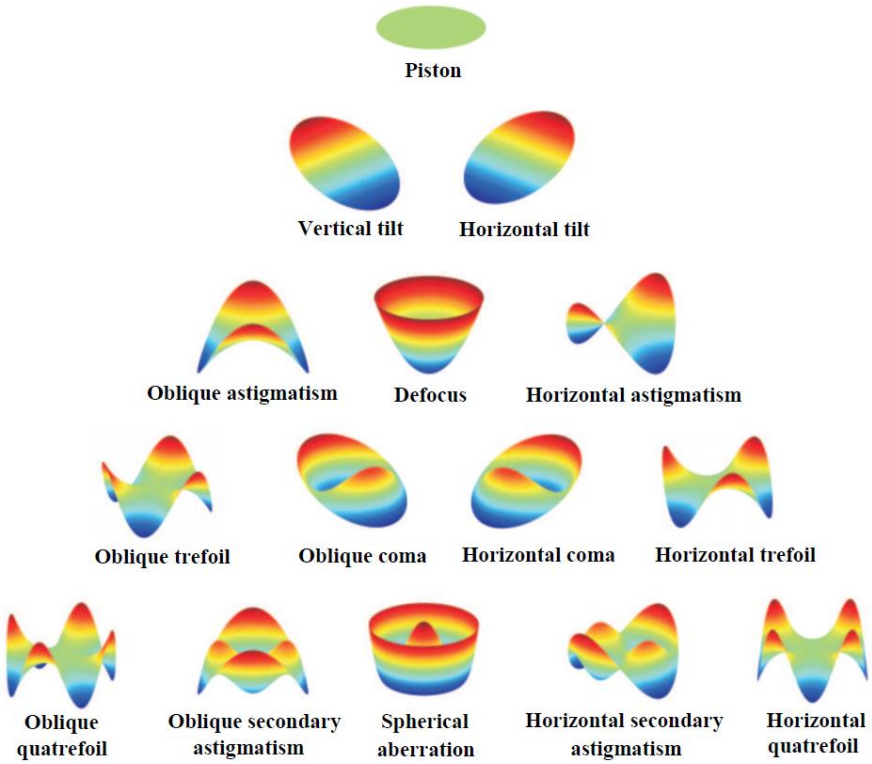

Figure 2-21: First 15 terms of circular Zernike polynomials [130]

Care must be taken when removing Zernike terms from data to avoid an oversimplified result when measuring the MSF errors. If too many Zernike terms are removed, some important information may be filtered out. On the other hand, if too few terms are removed, the target signals may be overshadowed by the data such that the MSF errors may not be readily apparent. For the RGP, extensive experimental testing (as reported in Chapter 4) has shown that the first 35 terms belong to lower order aberrations, and can be removed without affecting the measurement of the MSF errors.

2.5.3 Surface texture measurement

When measuring surface texture, R_a and S_a usually refer to descriptions of the average of the absolute surface height (z) over a measured length (L), and area (A) across a surface, respectively [131, 132]. The two terms can be defined by the following form [133]:

$$\mathrm{R_a} = \frac{1}{\mathrm{L}}\int_0^{\mathrm{L}} |\mathrm{z(x)}|\mathrm{dx} \tag{2-11}$$

$$\mathrm{S_a} = \frac{1}{\mathrm{A}}\int_0^{\mathrm{Ly}}\int_0^{\mathrm{Lx}} |\mathrm{z(x,y)}|\mathrm{dxdy} \tag{2-12}$$

Compared to a 2D measurement, 3D areal images: (1) are an area assessment, and thus can show the relationship between surface finish and function that is sometimes limited in 2D stylus measurements; (2) can recognise pits or valleys, peaks or ridges (3) are far more comprehensive and informative than a 2D surface [134]. Figure 2-22 and Figure 2-23 show different surface finishes in nature, but with identical $\mathrm{R_a}$ and $\mathrm{S_a}$ values. It can be observed that 3D results are more informative for the 3D areal images than 2D scanning.

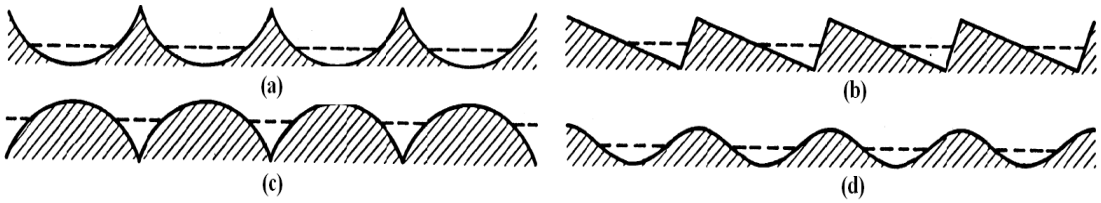

Figure 2-22: Four different surface types with the same $\mathrm{R_a}$ value [135]

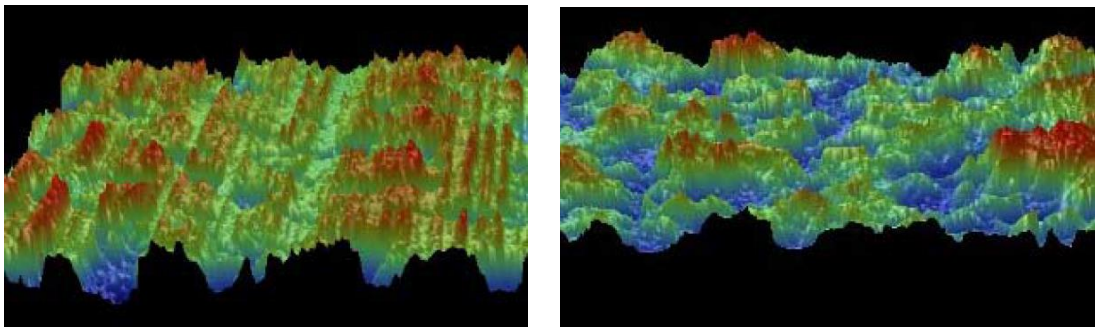

Figure 2-23: Two different surface finishes with the same S_a value [136]

Since 3D scanning is more informative, 3D measurement is adopted in this thesis to measure the surface texture of a processed surface. An ADE Phase Shift MicroAXM white-light texture interferometer with a sub-nanometre resolution is used to measure the surface texture of a grolished surface. The instrument is based on a microscope with a 250 mm lateral measurement range, as shown in Figure 2-24.

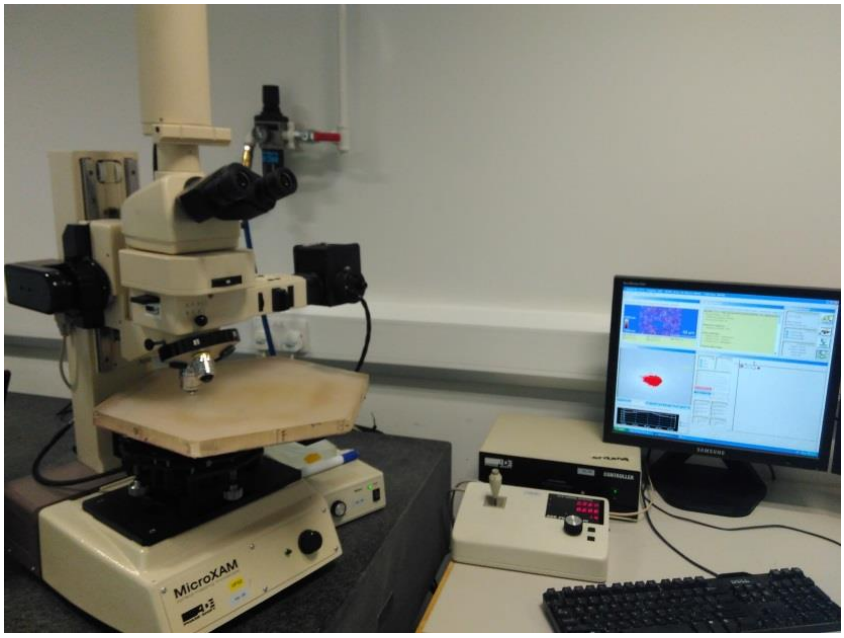

Figure 2-24: Surface texture measurement

2.6 Active/Adaptive optics and other criteria for future ELTs

Compared to a heavy monolithic telescope, a lightweight segmented telescope requires fewer materials (such as steel) to support each mirror element. There are two methods to avoid a bulky telescope structure: using (1) lightweight mirrors, or (2) thin mirrors. The lightweight ZERODUR® mirror developed by Schott is the state-of-the-art, removing 88% of mirror materials by means of deep pockets and 2 mm thick ribs, and this technology has been demonstrated to > 4 m diameter mirror [137]. This kind of technology has been applied to many mirror shapes, including hexagonal, oblong and off-axis unobscured telescopes [137].

For the E-ELT, each meniscus mirror is 50 mm thick and mirror surfaces are adjustable by means of its supports. When adjusting a segmented telescope, each single mirror is independently controllable to shape part of an integral surface. Figure 2-25 illustrates the principle to adjust the tip, tilt and relative positions so as to shape a segment to the desired surface form. For the general mathematical concepts behind controlling segment movement, please refer to [23, 138].

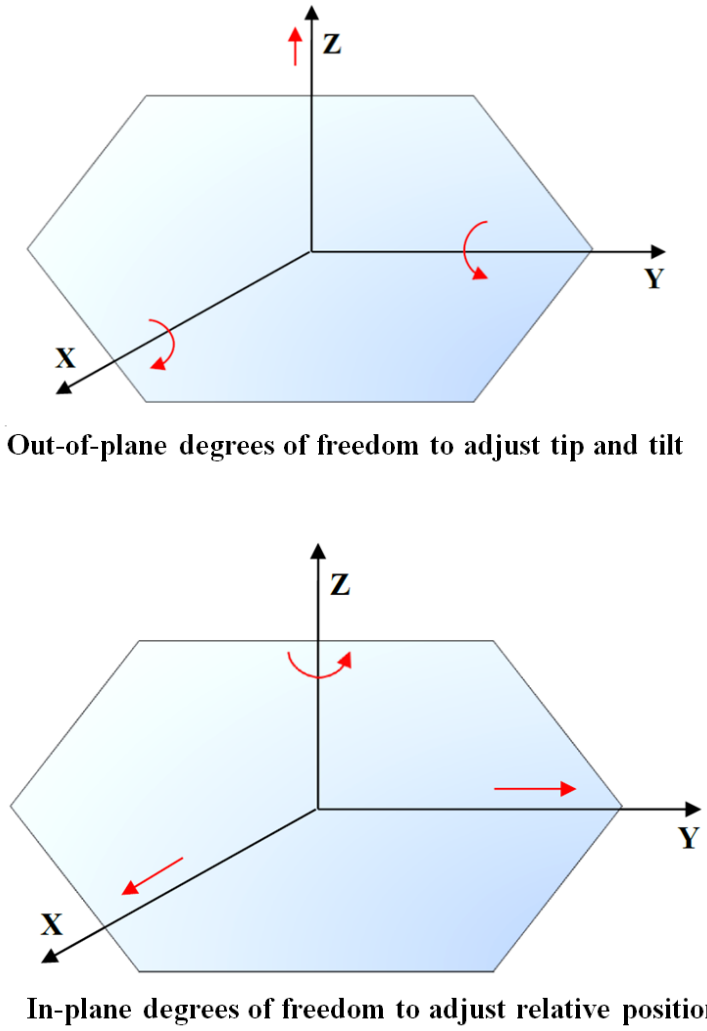

Figure 2-25: Segment adjustment

For the E-ELT, the interface of every hexagonal segment is supported and detected by segment supports and sensors, respectively. As illustrated in Figure 2-26 and Figure 2-27, 27 axial pads and six lateral pads are bonded to the reverse of each segment. The rotation of the segment is constrained by three azimuthal pads, and the segment position is controlled by a set of 12 edge sensors [139]. Together, these complicated devices are the first step to correct aberrant images due to environmental disturbances. More details of active/adaptive optics are introduced in Section 2.6.2.

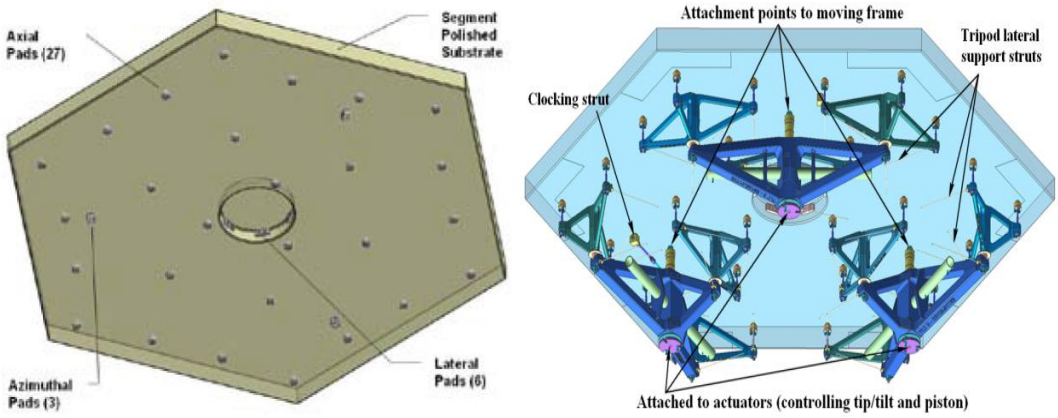

Figure 2-26: Adjustment of each segment for the M1 of the E-ELT [139-142]

Figure 2-27: Twelve edge sensors and whole adjustments for M1 segments [143]

2.6.1 The wider context: issues beyond segment fabrication

In practice, the image quality of a ground-based ELT is affected by both atmospheric and telescopic errors, creating phase errors in the formation of the resulting image. Even when the mirror surface forms have been corrected to be optically excellent (i.e. diffraction limited), a ground-based ELT without active and adaptive optics would

not be able to achieve angular separation better than a telescope of 10 - 20 cm diameter [144, 145].

Since the 1970s, therefore, the manufacturing of metre-scale optics has been greatly improved so as to minimise telescope errors: advanced mirror figuring and processing technology have been improved (Section 2.4); lighter and thinner mirrors are now devised to reduce the weight of supports needed (gravity is one important factor in inducing glass deformations); high altitude mountaintops are chosen to minimise atmospheric turbulence, noise from human activities, and light pollution.

Furthermore, special ceramic glasses and other materials with low thermal expansion characteristics ($< 0.15\times10^{-6}$/℃ at room temperature) have been used to maximize the ability to achieve mirrors free from temperature variation. For example, Zerodur (Schott) has been employed for existing large segmented telescopes (Keck and HET) [137, 146, 147]. Sitall (LZOS) has been used for the Southern African Large Telescope for its 91 segmented primary mirrors [148]. Clearceram (Ohara), which was originally used for photolithography [149], is able to produce blank glass 2 m in diameter [150]. ULE (Corning) has been adopted for the Subaru Telescopes [151] and the four secondary mirrors for the Vary Large Telescope. SiC and beryllium are the hard-to-process materials that have been used for space telescopes, such as the secondary mirror of the Herschel [152] and Infrared Space Astronomical Telescope [153]. Owing to its characteristics of low thermal expansion, making it an ideal material for a cryogenic system, SiC is now also planned for use in future ground-based telescopes [154].

Even when a telescope has been properly designed and is equipped with well-supported systems, the atmosphere and long term mechanical error effects still limit the size of the primary mirror to around 4 m in diameter. In order to prevent these inevitable errors degrading optical performance, active and adaptive optics have been introduced for monolithic primary mirrors of about 3 m or larger [155, 156], including for the Keck telescope [157] and the E-ELT.

In principle, active optics aim to deal with errors of rather low temporal frequencies (less than 0.01 Hz) and errors smaller than three wavelengths or so; adaptive optics, however, have to correct errors of about 1/50 of a micrometre every millisecond [144]. Hence, in mechanical terms, the main difference between active and adaptive optics is the speed of actuators behind an optical surface for adjusting distorted wavefronts. By using active/adaptive optics, the output image of metre-scale telescopes can be automatically optimised through constant adjustments that serve to make images approach a diffraction limited standard.

In addition, the image provided by current astronomical telescopes has gradually evolved from a recorded film to a computer-controlled instrument with digital image output. The lower noise, faster electronic processors and higher radiation tolerance of charge-coupled devices (CCDs), and complementary metal-oxide-semiconductors (CMOS), image sensors are being used for higher performance astronomical telescopes [158-160].

Although the technologies used in active and adaptive optics are changing quickly, their fundamental principles are similar. The basic operating function is shown in

Figure 2-28. Both systems consist of three principal subsystems [161, 162]: a "wavefront sensor" to detect the distortion of the wavefront coming from an observing target; an active mirror or "deformable mirror" to correct the distorted wavefront; and a "control computer", which can be very slow for active optics, but extremely fast for adaptive optics.

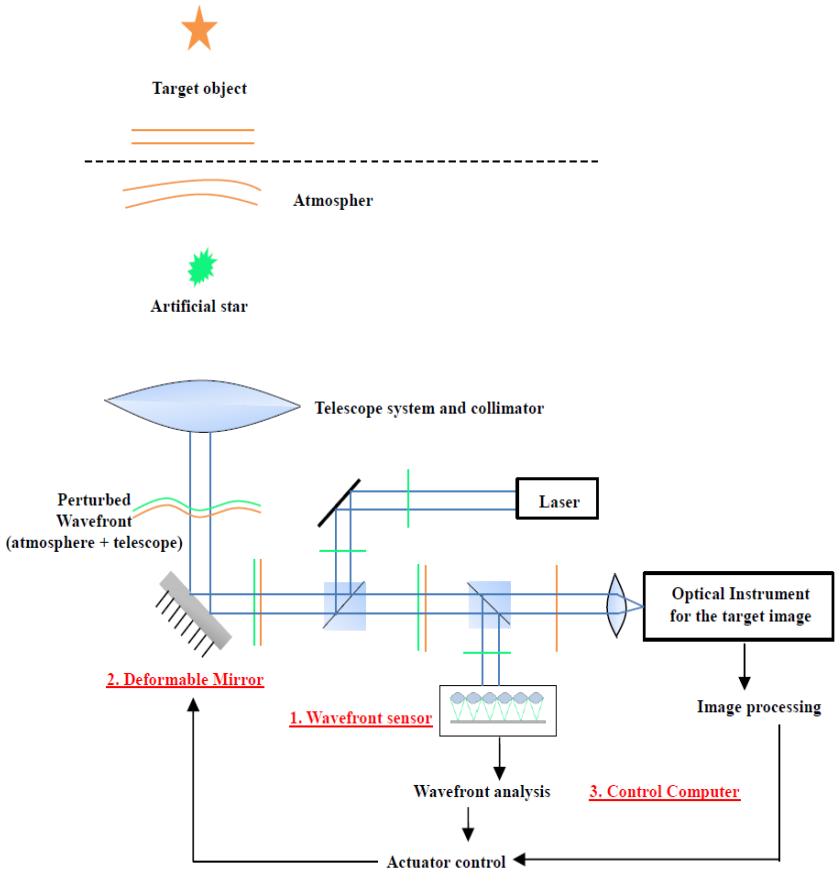

Figure 2-28: Active/adaptive optics for image stabilization

In addition, one or more artificial stars (also referred to as laser guide stars, laser probes and laser beacons) are used to facilitate image stabilization [163] and to enhance the optical resolution of a telescope to detect fainter objects in the universe [164]. All these sophisticated technologies (e.g. active and adaptive optics and the

artificial stars) aim to deliver a near-diffraction-limited image while retaining a sufficient FOV to discover the mysteries of the universe [165].

For the E-ELT project, each mirror functions diversely to correct both atmospheric and telescopic errors. Each segment of M1 weighs about 365 kg, and each segment aims to remove piston and tip-tilt and to compensate for some deflections due to temperature and gravity. The weight of M2, meanwhile, will be less than 12 tonnes, and its mechanism is not only to protect the mirror from falling down, but also to compensate for some other long terms errors, such as maintenance errors in the mirror supports and structures. The tertiary mirror is designed for refocusing in tandem with M2 and M4. The quaternary mirror is supported by about 8000 actuators to readjust a surface in real time at very high frequencies to compensate for atmospheric, wind shake and tracking errors, as well as small amplitude residual tip-tilt corrections. M5 is a very thin and ultra-lightweight mirror whose main purpose is to adjust for tip-tilt and provide field-stabilization for image motions up to a few Hz. All these up-to-date technologies have been introduced in the E-ELT construction proposal [32].

2.6.2 Active/adaptive optics for optical fabrication

For optical fabrication, an obvious advantage of active and adaptive optics is that the optical manufacturers may not have to correct all the errors on a mirror [144]. For example, astigmatic surface deformations can be compensated by mirror actuators for the E-ELT [166]. More time and resources can, therefore, be invested into removing artefacts of higher spatial frequency, such as surface texture and MSF

errors. The “RGP” is one significant technique to speed up the removal process of mid-spatial frequencies left from a CNC grinding machine, leading to an enormous reduction of time and cost in the overall process for the E-ELT project. This automatic robotic technology to process metre-scale optics is introduced in the next chapter.

2.6.3 Summary of active/adaptive optics

The challenge for future ELTs is that sensors and actuators need to align and maintain a surface to the desired form instantly. To achieve this, robust computer control is needed to adjust each mirror so as to compensate continuously for the distorted wavefront from a target object. One significant advantage of using this active/adaptive technology is to de-sensitise the telescope performance to lower-order aberrations. With these advances, large ground-based telescopes equipped with these facilities are capable of approaching diffraction-limited images.

Chapter 3 The Robotic Grolishing Process (RGP) and statistical quality control

3.1 Introduction

This chapter will be centred on the automatic robotic grolishing process (RGP). The topics covered here include the working principles of robotic arms, operating software, abrasives, and statistics for quality control. All topics are fundamental if the RGP is to be conducted successfully and will apply to the remaining chapters. In discussing these topics, the emphasis is not purely on robotic grolishing but also on the fundamental principles which are applicable to grinding and polishing, as well as the implications for the use of a broad range of other CNC machines with multi-functional processes for the fabrication of large workpiece materials.

3.2 Position and orientation

When using Cartesian CNC machines, the fundamental requirement is to guide the tooling as to its optimum position and orientation with respect to the workpiece in a processing environment. Before using commercial software (e.g. Zeeko Ltd.'s Tool Path Generator, TPG) to generate a set of points on the workpiece surface (i.e. a tool path), it was therefore important to know the operating coordinate frame. Since the Cartesian (XYZ) frame is used for many commercial machines as well as to guide robotic arms to complete a process, the following discussion is based on the

Cartesian coordinate system (a robotic arm has six axes and can therefore act within the Cartesian frame).

Defining the position and orientation of coordinates was the first step of the RGP. Figure 3-1 illustrates an example of four different coordinate frames and indicates their relative positions. The relative position between the tool frame and the user frame had to be determined in order to guide the robot to use the tool on the tool frame so as to process the objective workpiece. In order to achieve this, an orthonormal rotation matrix can be used to calculate the orientation between the coordinate frames.

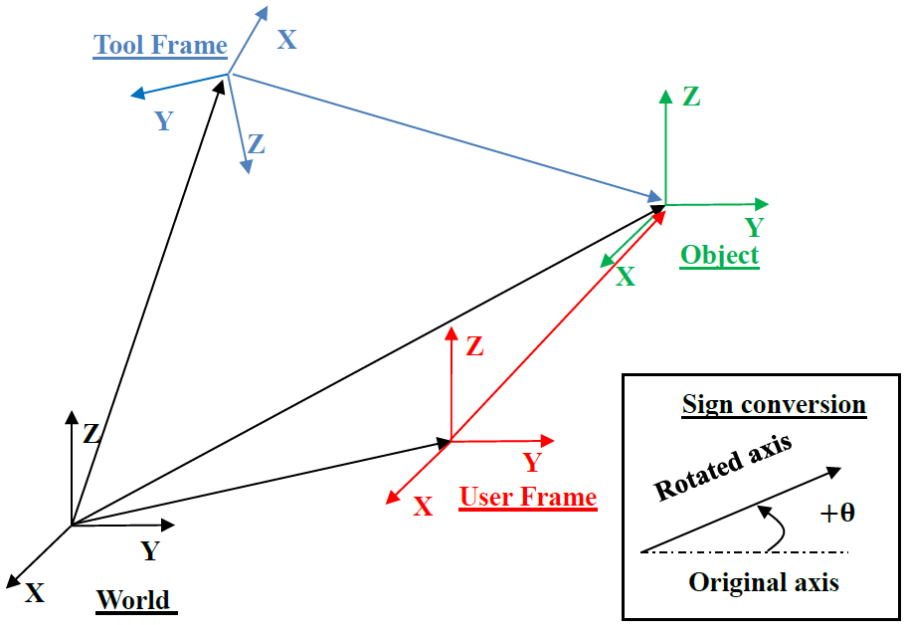

Figure 3-1: Typical frames and relative positions in the RGP

As illustrated in Figure 3-1, each frame can be described by a unit vector which is composed of three elements (i.e. x, y and z). When a vector is rotated, the vector in a new frame can be calculated by:

$$\begin{bmatrix} x \\ y \\ z \end{bmatrix} = R \begin{bmatrix} x' \\ y' \\ z' \end{bmatrix} \quad \textbf{(3.1)}$$

where R is equivalent to the rotation matrices for a rotation of θ about the three elements, and the matrix value is:

$$R_x(\theta) = \begin{bmatrix} 1 & 0 & 0 \\ 0 & cos\theta & -sin\theta \\ 0 & sin\theta & cos\theta \end{bmatrix} \quad \textbf{(3.2)}$$

$$R_y(\theta) = \begin{bmatrix} cos\theta & 0 & sin\theta \\ 0 & 1 & 0 \\ -sin\theta & 0 & cos\theta \end{bmatrix} \quad \textbf{(3.3)}$$

$$R_z(\theta) = \begin{bmatrix} cos\theta & -sin\theta & 0 \\ sin\theta & cos\theta & 0 \\ 0 & 0 & 1 \end{bmatrix} \quad \textbf{(3.4)}$$

When using the Cartesian (XYZ) frame, it is important to ensure that the correct coordinate system is selected so as to avoid accidents, such as breaking a workpiece or the equipment.

Singularities are fundamental problems when using the Cartesian (XYZ) frame. Singularities describe a situation where a machine has its own defined coordinate system and sequence of orientations, but where the sequence of frames is not

commutative. For example, it can demonstrate that $R_x(\theta)R_y(\theta)$ is not equal to $R_y(\theta)R_x(\theta)$. If an operator casually chooses the wrong coordinate system without immediately stopping the machine, a workpiece and machine will be damaged.

All these rotation matrices are important in order to examine whether a 6-axis non-Cartesian robot can follow a mathematical singularity (e.g. a Cartesian coordinate system) in order to process a workpiece at the same time as avoiding an unexpected accident. For example, using a robot guide is a health and safety strategy in a simulated environment so as to verify the movement when operating a robot. As shown in Figure 3-2, the robotic arm is conducting a grolishing process following a tool path in the User Frame 1 environment.

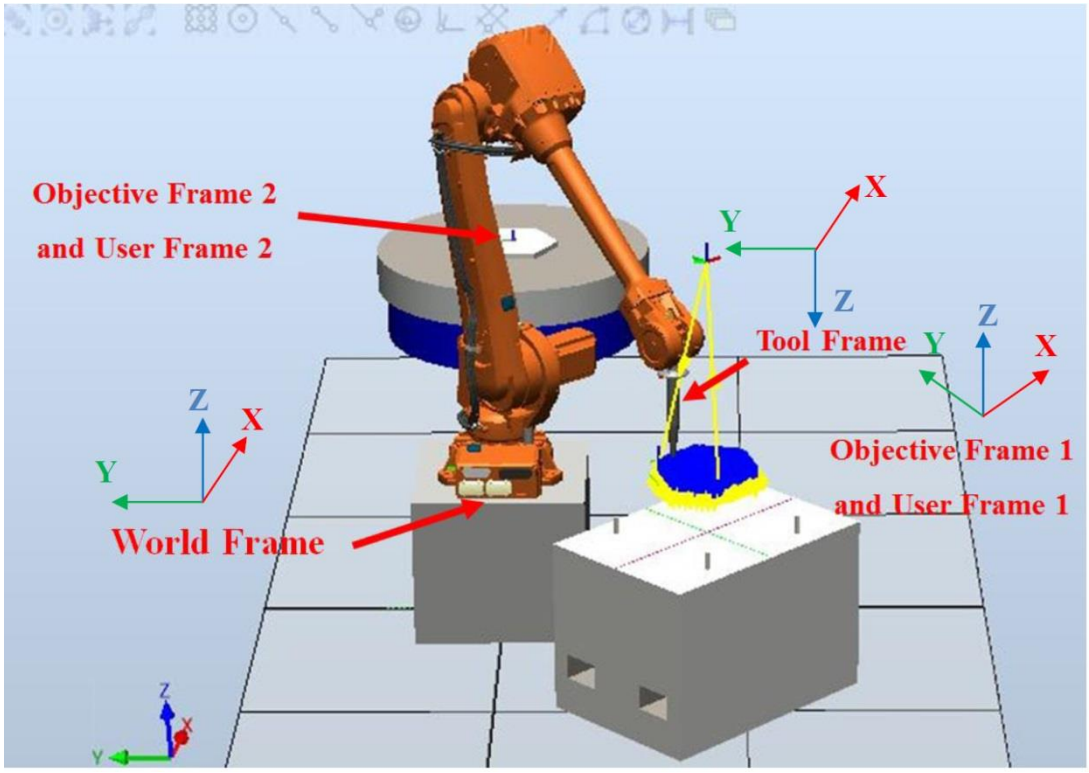

Figure 3-2: Process simulation

Please note that people were excluded from hazardous areas (e.g. the working area) during operation of the machine. In order to avoid an accident, an interlock system was successfully built by Dr Bibby and Dr Li in our group in 2015 to avoid the machine hurting a human being in the working area.

3.3 Tool Path Generator (TPG)

Tool path generation software from Zeeko Ltd. was used in this research to generate tool paths based on equations (3.1) to (3.4). As shown in Figure 3-3, the TPG is able to select from multiple machines to process optical glasses, specifically in this thesis the IRP600, IRP1200, Fanuc and ABB machines, as shown in Figure 3-4.

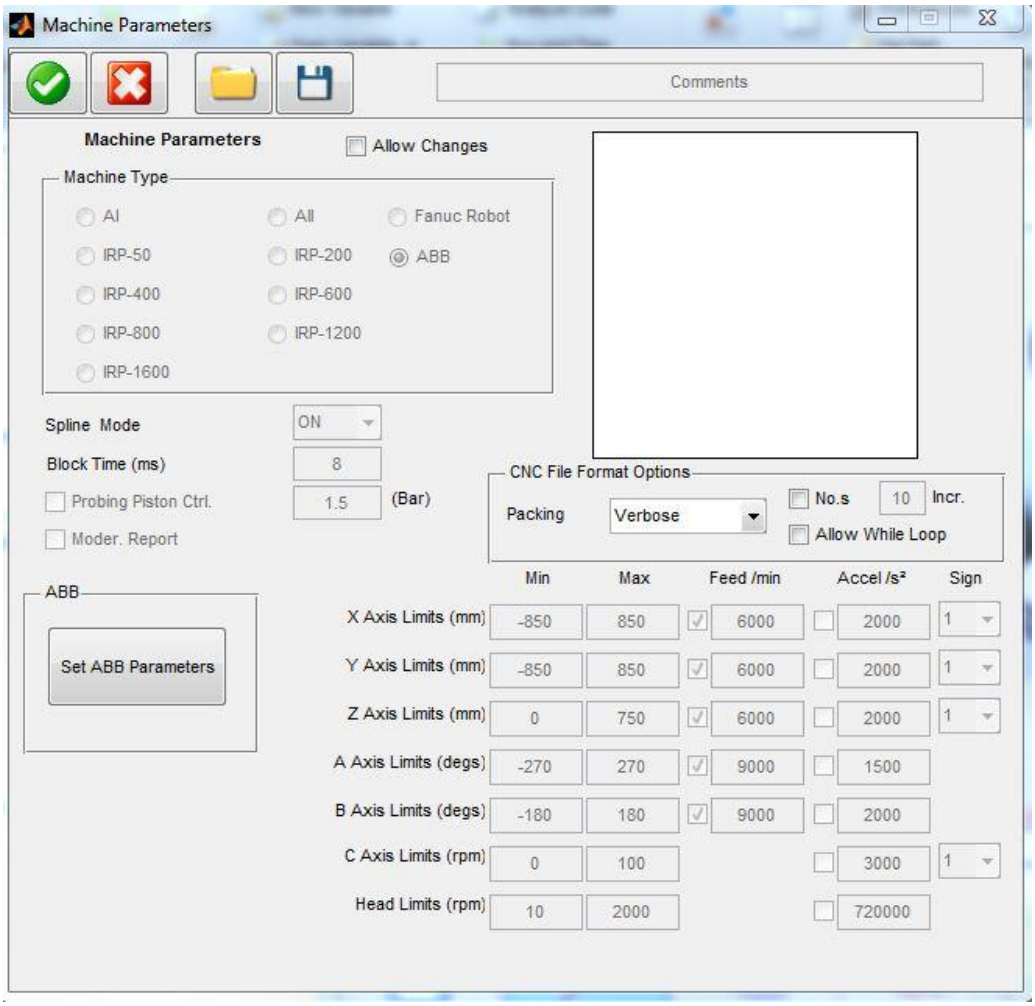

Figure 3-3: Selection of machines through TPG

Figure 3-4: Grolishing robots and polishing machines

As shown in Figure 3-5, the software used was tailored TPG software developed by Zeeko Ltd. and was designed specifically for generating tool paths for grolishing or polishing a surface. The variables defined in the TPG process included the following:

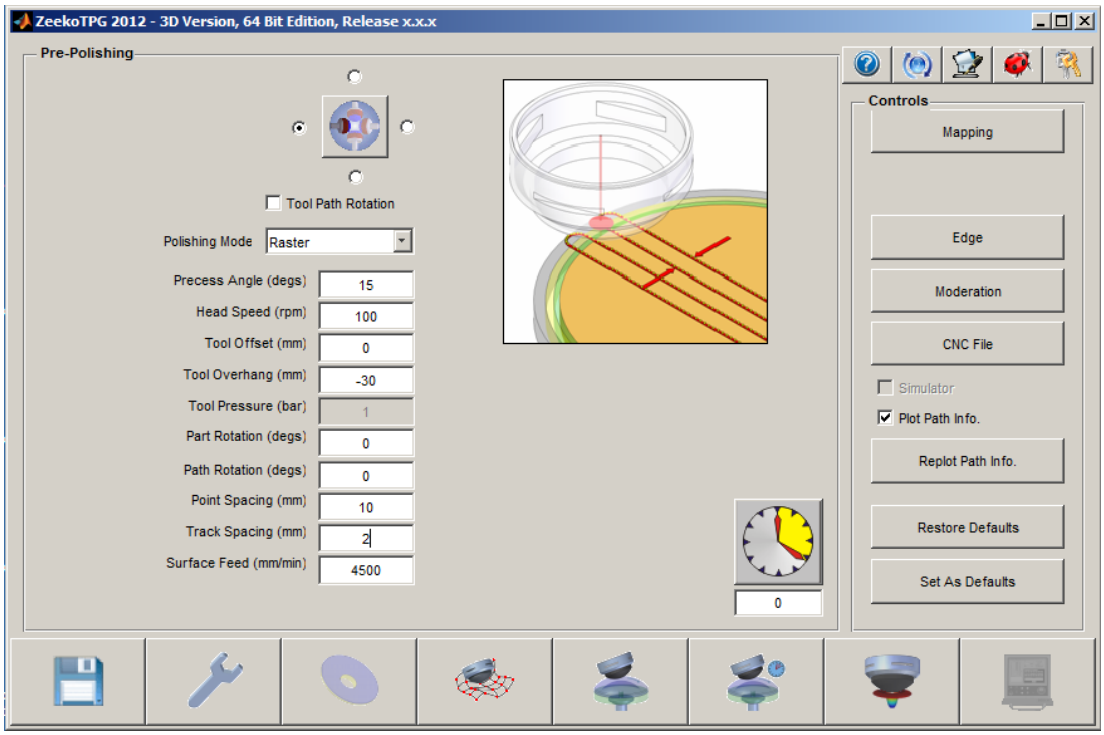

Figure 3-5: Variable settings in TPG

3.3.1 Precess Angle

The precess angle is defined as the angle of intersection between the centre line of a tool and the 90° perpendicular line, measured in degrees, as shown in Figure 3-6. When using soft tools, such as bonnet or solid rubber tools, the precess angle and the tool offset determine the spot size, which is related to the material removal rate and surface texture [167, 168]. When using the designed robotic grolishing tools the precess angle was 0°. Readers can refer to [169] for more details regarding the use of the precess angle to achieve the required removal functions in processes such as polishing.

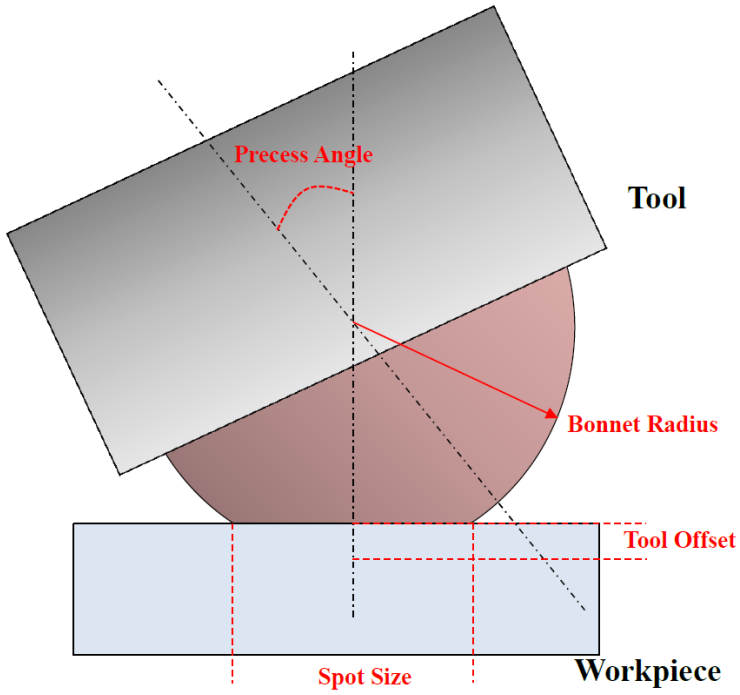

Figure 3-6: Introduction to TPG using bonnet polishing as an example

3.3.2 Spindle Speed (Head Speed)

The spindle speed is the rotational frequency of a tool on a machine, measured in revolutions per minute (rpm). Excessive spindle speed would produce extensive tool wear and breakages, as well as tool chatter, leading to poorly controlled and dangerous conditions [170]. When examining the prototype tools, one important step was to find a range of suitable spindle speeds that could manufacture high-performance surface finishes while retaining optimal conditions for the duration of the tool's life.

3.3.3 Tool Overhang (OH)

This parameter is extremely important for edge control in both the RGP and polishing. Normally, the OH describes the distance exceeding the edge. Specifically, in TPG, the OH is defined as the distance that the centre of the tool extends from the edge of a workpiece, as shown in Figure 3-7. The higher the OH value, the further the tool position will be with respect to the edge of the workpiece.

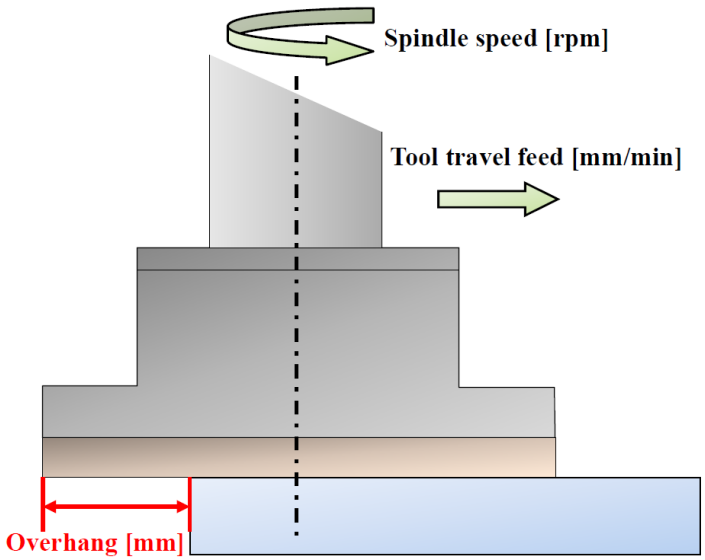

Figure 3-7: Definition of OH

3.3.4 Tool Offset

The tool offset describes the compression between a tool and a workpiece. This variable is highly important for the polishing process, but was not applicable for the RGP (since the z-axis functions to adapt to a surface inclination (Section 4.3.1)). When conducting polishing, the tool offset determines the delivered spot-size for a

chosen bonnet. Manipulating the tool offset, such as by progressively lifting a bonnet, is a critical method for controlling the edges of a segment in the polishing process [95, 171].

3.3.5 Track Spacing

The track spacing refers to creating an even space between raster lines or spirals in order to affect the density of a tool path. Track spacing is one significant variable resulting in the spacing of 'cusping' features (one source of Mid-Spatial Frequency, MSF) on optical surfaces. Due to the effects of overlapping paths, MSF artefacts can be minimised or removed by choosing a suitable track spacing, tool size and removal depth. Details will be discussed in Section 4.2.4.

3.3.6 Tool Travel Speed (Surface Feed)

Tool travel speed is the difference in relative velocity between a tool and a workpiece. In this thesis, the workpiece was static and therefore the tool travel speed simply describes the tool's speed across the workpiece in mm/min.

3.4 Mechanisms of the grolishing process

Two primary types of abrasives play a role in the RGP: "loose abrasive" and "bound abrasive" [106, 172]. The geometries of the two abrasive types are shown in Figure 3-8. In loose abrasive grolishing, abrasive grains are applied to a liquid that is supplied between the tool and the workpiece. It is believed that the loose grit slides

along the surface creating microscopic chips that separate from the workpiece into the slurry [173]. In bound abrasive grolishing, meanwhile, abrasive grains are held in place and distributed throughout a soft resin, pitch or metal. When the bound-abrasive is rubbed against a workpiece, the tips of the abrasive grains create furrows in the workpiece that serve to remove materials. Diamond is the material generally used for bound-abrasive pads, but this is extremely difficult to clean should a diamond particle contaminate the polishing slurry system. In order to avoid such cross-contamination between the grolishing and polishing processes, a loose abrasive was the primary type of abrasive used in this thesis.

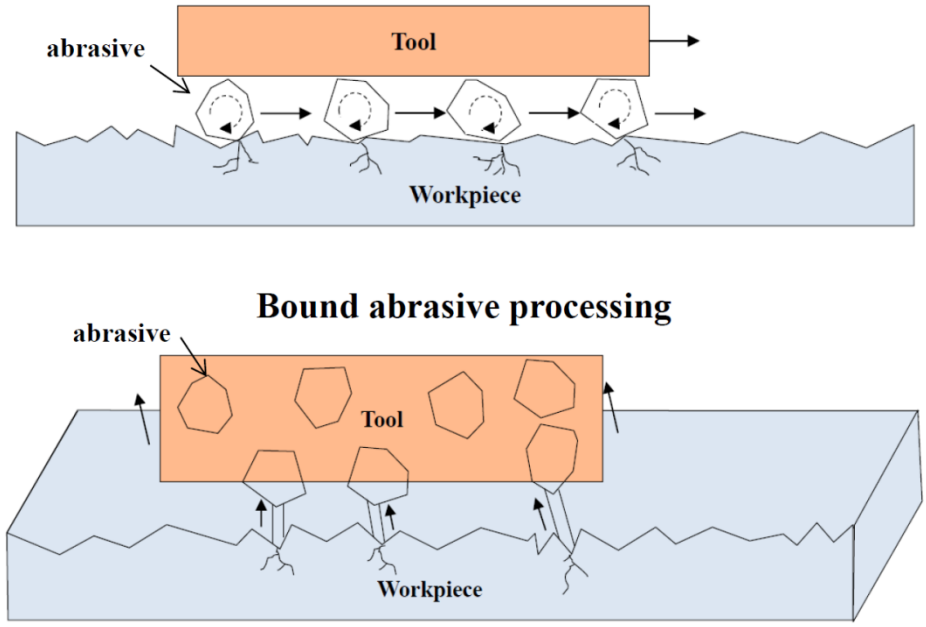

Figure 3-8: Functions of loose abrasive (top) and bound abrasive (bottom)

Aluminium oxide (9 µm, 15 µm and 20 µm) was used for the RGP while cerium oxide (3.5 µm) was used for polishing in this thesis. Both the loose abrasives were from the Microgrit WCA series. In order to assess the purchased abrasives, a

scanning electron microscope (SEM) was used to reveal the grit sizes and shapes. As shown in Figure 3-9, the abrasive sizes were normally distributed and concentrated on the purchased sizes: 9 μm, 15 μm and 20 μm. Although it is known that inconsistent grit shapes may produce substantially different wear characteristics [174], statistical techniques can catalogue the grit shape as a noise. If the noise is insignificant in the statistical analysis, it can be neglected in a process. Details of this kind of statistics are introduced in the following section.

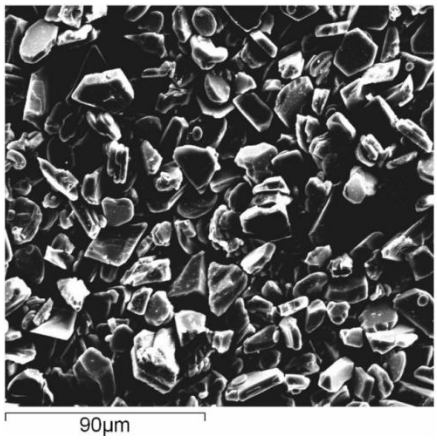

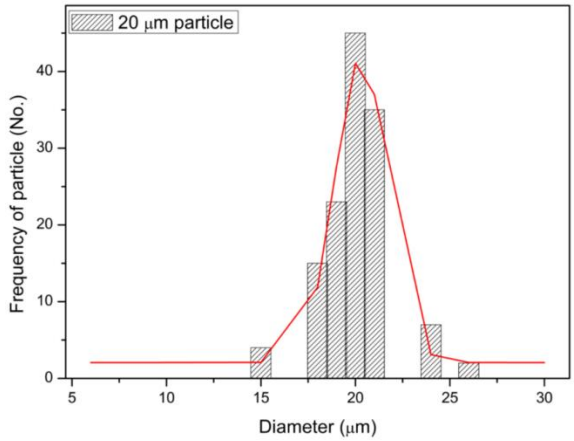

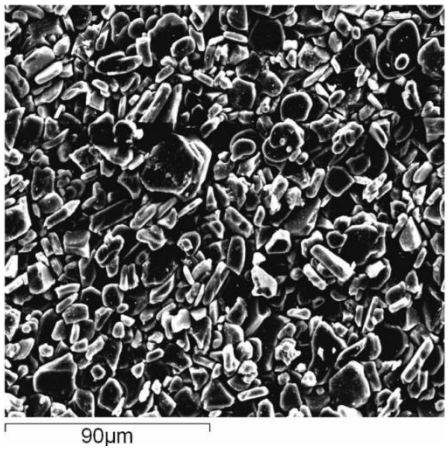

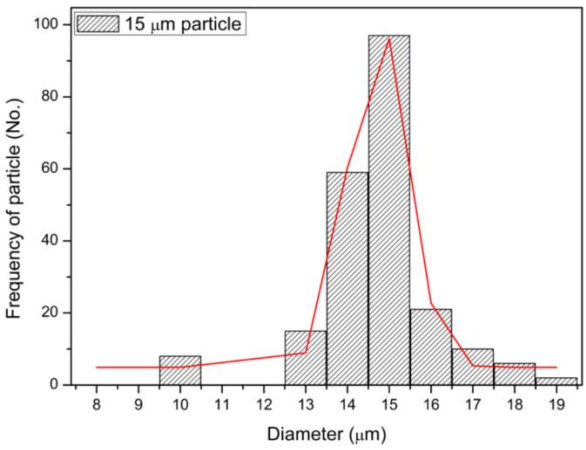

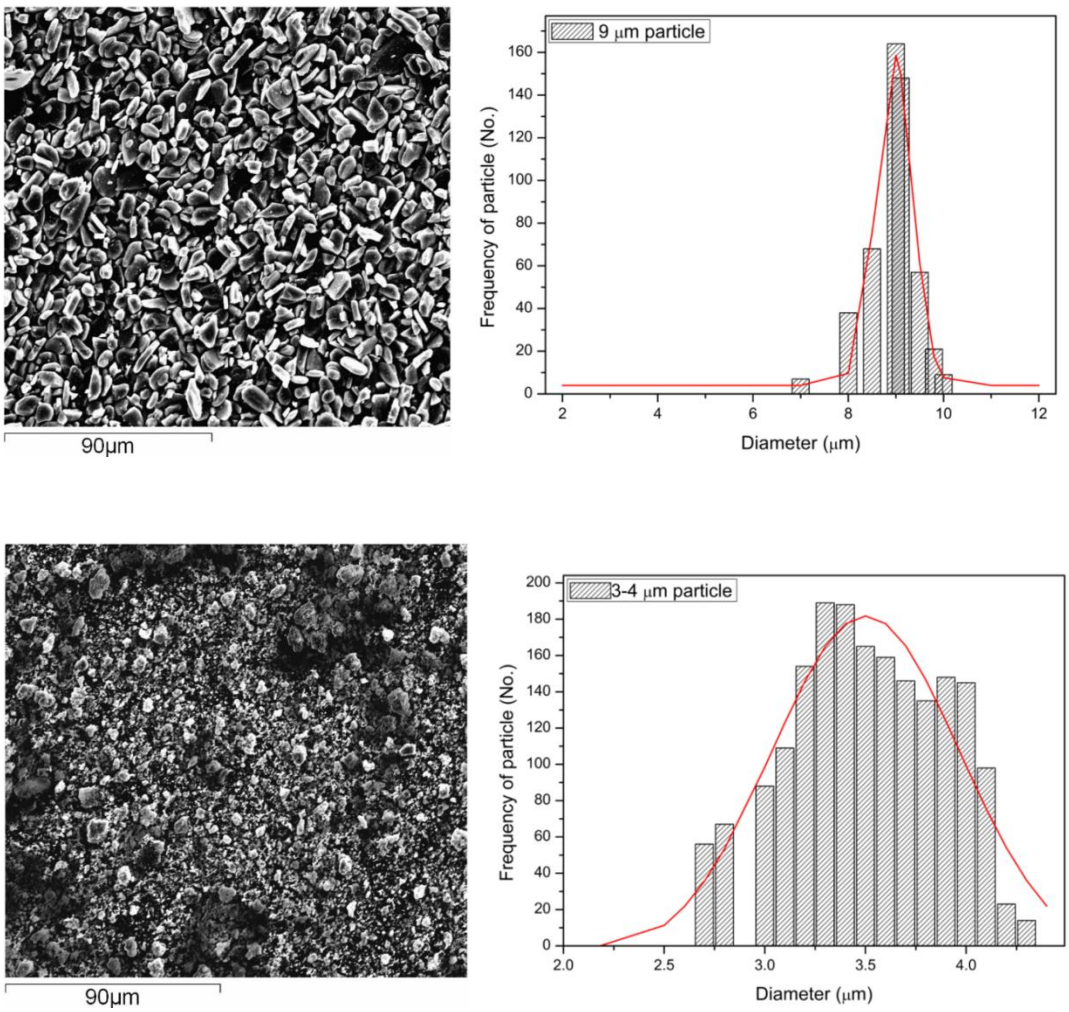

Figure 3-9: Abrasives measured by SEM[1]

3.5 Statistics

Determining the variables needed to achieve optimised outputs (e.g. removal rate, surface texture, edge, surface profile, MSF) was the next goal in respect to the RGP. This optimisation was achieved through the following process: when a target was defined, the next stages were measurement and analysis, followed by an

[1] The author acknowledges Dr Wen-Jun Lu for the abrasive measurements.

improvement stage, which aims to achieve better performance, and then by the control stage, used to monitor and sustain uniform outputs.

Since it is time-consuming and impossible to evaluate all variables, the statistical experimental designs and analysis techniques described in this section are proposed as a reliable way of evaluating significant variables, insignificant variables and noise. Some examples of inherent noises (i.e. the variables that were not controlled) in the RGP in this thesis were temperature, humidity, machine vibration, abrasive shape, chemical interaction between slurry and workpiece, and measurement and alignment errors. In order to determine optimised outputs, the statistical techniques described in this section can be used to control significant variables to achieve uniform outputs (e.g. < 5% output deviations). The 5% significant level is approximately equivalent to the 2 sigmas interval, and this value is recommended to establish a process [175]. In practice, however, this value can be adjusted after a process has been established, and Section 7.2 will explain the reasons for seeking to improve the 5% level to a 1% level (i.e. 3 sigmas).

Chapters 4 and 5 in this work provide some examples to demonstrate that these statistical methods may be an ideal approach to investigate large optical fabrication. The proposed statistical methods are not only able to reduce experimental trials and overall time, but can also summarise results in a systemic format for further optimisation so as to achieve deviations of less than 5%. Using multiple statistical methods to achieve robust (e.g. reliable) results is surprisingly complex, however, and discourages many scientists and engineers, although a 2014 study from the

Fraunhofer Institute for Production Technology IPT, Germany, also sought to utilise this kind of statistics to process optics [173].

The following subsections are devoted to a fuller exploration of these issues. These theories are mainly summarised from four textbooks about experimental designs and analysis as well as statistical quality control [176-179]

3.5.1 Statistical experimental designs

In general, there are three types of strategy to conduct an experiment: (1) best guess, (2) a single variable experiment, and (3) statistical design of experiments (DoEs). The three methods are introduced in the following paragraphs.

Firstly, the experimental method of best guess, as shown in Table 3-1, uses prior experience to modify more than one variable at a time under expected conditions to give the best outputs. This strategy is useful in an intermediate experiment to find a new reference point for discovering a new locally optimised region.

Table 3-1: Change several variables all at the same time

	Variables				
Trial	A	B	C	D	Test results
1	-	-	-	-	*
2	+	+	+	+	*

The * symbolises response variables that would be obtained in the experiment. – and + represent low and high levels of a variable respectively.

Secondly, the experimental strategy of changing one variable at a time consists of modifying one variable while keeping the others fixed. Table 3-2 shows the test plan for this approach. When using this method, only two variables are used for comparison; the remaining variables are temporarily ignored. For example, if A and B are chosen to be compared, C and D are ignored for the moment. This type of method is the most common experimental method in today's scientific approach. Since this experimental method is not orthogonal (Section 3.5.1.1), however, the limitation is that no interaction term can be observed. For instance, A_- to A_+ is not a fair comparison if all the response variables are averaged and compared. The orthogonal exists only when trial 1 is compared to other trials, one at a time. This method is applicable, therefore, when an experimenter only considers the main effect and has confidence that the interaction effect is negligible.

Table 3-2: One variable experiment

	Variables				
Trial	A	B	C	D	Test results
1	-	-	-	-	*
2	+	-	-	-	*
3	-	+	-	-	*
4	-	-	+	-	*
5	-	-	-	+	*

Finally, the DoE method may be the most effective experimental strategy for solving complex problems with many variables and interaction effects. A full-factorial design (FFD), as shown in Table 3-3, is orthogonal, meaning that there are an equal number of data points under each level of each variable. Under the variable A_-, for

example, the variable B has two data points so that the estimate of A (A_- and A_+) is not influenced by the variable B. Hence, an FFD can be treated as a balanced design.

Table 3-3: Full-factorial design

	Variables		
Trial	A	B	Test results
1	-	-	*
2	-	+	*
3	+	-	*
4	+	+	*

When using an FFD, however, there might be too many experimental trials at the beginning of an experiment. Partial factorial designs (such as 1/2 FFE, 1/4 FFE and 1/8 FFE), single replication of FFE and the Taguchi method can be used to reduce the number of experimental trials; but these DoE approaches may reduce their power to resolve interaction effects [177, 180, 181]. Among these DoEs, the Taguchi Method can be described as an extensively fractionated factorial design that has been of interest in industry and among academics. Although the results of peer review indicate that there are problems (e.g. loss of accuracy) when using the Taguchi's method for experimental strategy and data analysis [182-185], it has been widely used for improving output quality [176, 186-188]. For example, even though using the Taguchi method will extensively reduce experimental trials so as to reduce experimental resolution (i.e. accuracy), the result can provide a general overview that can be evaluated by subsequent confirmation experiments. The Taguchi method is an efficient method to determine significant variables used in Chapter 4 and, therefore, this method must be reviewed.

Before exploring the use of the Taguchi Method in more detail, the Taguchi's loss function [189] is worth discussing. The loss function is a function that presents some "cost" associated with a process. Its response has three different characteristics: higher is better (HB), normal is better (NB) and lower is better (LB). For example, in the RGP, the removal rate is HB to achieve an efficient process; whereas the surface texture, the MSF errors and sub-surface damages are LB to produce a good surface quality, the form and the edge controls are NB to achieve the desired value to meet a requirement.

The three mathematical models are described as follows:

$$L_{HB} = k\left(\frac{1}{\bar{y}^2}\right)\left[1 + \left(\frac{3S^2}{\bar{y}^2}\right)\right] \tag{3-5}$$

$$L_{NB} = k[S^2 + (\bar{y} - m)^2] \tag{3-6}$$

$$L_{LB} = k(S^2 + \bar{y}^2) \tag{3-7}$$

where L is the loss associated with a particular **response** value (**y**), $\bar{y}$ is the average value of y for the group, m is a nominal value of the specification (i.e., $\bar{y} - m$ is the offset of the group average from the nominal value), k is a constant depending on the cost at the specification limits, and S^2 is a variance around the average $\bar{y}$.

For the above three formulae, the lowest loss can be derived since the variation S^2 is very small and the output is close to the target ($(\bar{y} - m)^2$ or $\bar{y} \sim 0$). The function of an experiment is to discover, and thence to control, significant variables in order

to make the output satisfy the specification, as well as to eliminate the variance in order to fabricate uniform outputs. This is very similar to the concept of using DoEs to reduce variance and improve performance to achieve high-performance outputs.

3.5.1.1 Orthogonal characteristics of the DoE

An orthogonal array (OA) is a table whose entries are composed of a fixed finite set of symbols. An easy way to demonstrate any two-level OA that has orthogonal characteristics in DoEs is to set the high and low level as 1 and -1 respectively, and thus:

$$\left(\mathbf{Matrix}_{\mathbf{any\ two-level\ OA}}\right) \times \left(\mathbf{Matrix}_{\mathbf{any\ two-level\ OA}}\right)^{\mathrm{T}} = \mathrm{I} \qquad (3\text{-}8)$$

where $\left(\mathbf{Matrix}_{\mathbf{any\ two-level\ OA}}\right)^{\mathrm{T}}$ is the transfer matrix (from the experimental design matrix) of $\left(\mathbf{Matrix}_{\mathbf{any\ two-level\ OA}}\right)$, and I is a unit matrix. In the DoE, the orthogonal means that each of the vectors is statistically independent, i.e. there is no correlation between vectors. This characteristic shows that all variables, with their levels, have an equal possibility to be selected in an experiment. Hence, it can be recognised that each variable with its relative level is independent in the DoE.

3.5.1.2 Summary

Experimental designs are very important in this thesis. An overview of the experimental methods discussed in this section is provided in Table 3-4. A

comparison of various DoEs and suggested applied situations is provided in Table 3-5.

Table 3-4: Summary of current experimental methods

Strategy	Experimental Method	Advantage	Disadvantage
1	Change one variable at a time	This method can successfully evaluate which variable has the most important effect	This design cannot discover interaction effects
2	Several variables, changing one at a time	The most common test strategy in today's scientific approach	The main limitation, however, is that no interaction term can be observed.
3	Several variables, changing all at the same time	A useful method to discover a new localised optimised region	1. No clue to separate which variables contribute positive or negative effects. 2. An approach to determine a new optimised region.
4	Full-factorial design (FFD)	All interaction effects can be solved	Time consuming to complete all trials
5	Efficient test strategy (such as Taguchi method, fractional factorial designs)	These methods reduce the number of trials needed to produce a workable solution.	Higher order interaction effects cannot be solved

Table 3-5: Comparisons between DoEs

	Full Factorial Design	Fractional Factorial Design	The Taguchi Method
Experimental trials	Trials of all combinations	Reduce some trials	Extensively reduce trials
Resolution (Resolving Ambiguities)	Find the combinations of all possible interaction effects	Resolve lower-order interactions and main effects	Filter out insignificant variables and determine main effects.
Analysis method	ANOVA	ANOVA	ANOVA
Application	It is recommended to use this method in the mature stage of a process	It can be applied to an intermediate but not a well-known process	It is suggest using this method at the beginning of screening experiments.

3.5.2 Data analysis

Analysis of variance (ANOVA) is used to decide which variable effects are significant or insignificant in DoEs, followed by controlling significant variables to achieve < 5% deviation in output (discussed in Section 3.5). For example, after all trials in a DoE are completed, the ANOVA is the predominant statistical method to analyse and interpret the result. Significant effects can be determined based on the calculation of ANOVA, and after that, these significant effects can then be selected and analysed to improve the process. The purpose and calculation of ANOVA are introduced in the following subsections.

3.5.2.1 Hypothesis testing

When an experiment is conducted using a DoE approach, and the results are then analysed by a statistical method (e.g. ANOVA) to find the cause-and-effect relationships between a process and the output of that process, a statistical hypothesis is being tested. Suppose *n* samples are selected independently from their respective populations. The concept of hypothesis testing may be stated as:

$$H_0: \mu_1 = \mu_2 = \cdots = \mu_n \tag{3-9}$$

$$H_1: \text{at least one } \mu_i \neq \text{another } \mu \tag{3-10}$$

where H_0 is the **null hypothesis,** and H_1 is the **alternative hypothesis**. Since the statement would be true whether $\mu < \mu_i$ or $\mu > \mu_i$, H_1 is a two-side alternative hypothesis.

No hypothesis test is 100% certain, and two kinds of errors are possible. A type I error has occurred if the H_0 is true but rejected. If the H_0 is false but is not rejected, a type II error has been made. The concept is summarised in Table 3-6.

Table 3-6: Type I and Type II errors

Truth		
Decision	**H_0 is true**	**H_1 is true**
Not reject H_0	Correct Decision (probability=1- α)	Type II error (probability = β)
Reject H_0	Type I error (probability= α)	Correct Decision (probability=1- β)

where

$$\alpha = \mathrm{P}(\text{type I error}) = \mathrm{P}(\text{reject } \mathrm{H}_0 | \mathrm{H}_0 \text{ is true}) \tag{3-11}$$

$$\beta = \mathrm{P}(\text{type II error}) = \mathrm{P}(\text{fail to reject } \mathrm{H}_0 | \mathrm{H}_0 \text{ is fales}) \tag{3-12}$$

These two errors are inversely related because their risks are determined by the significance level α and the power (1- β) of the test. To lower both risks, it is recommended to use a lower α value or to increase sample sizes. Generally, α = 0.05 is adopted in the industry for quality control.

3.5.2.2 Sum of squares (SS)

The ANOVA is a mathematical technique to decompose total variance (or the total sum of squares) into several component parts. In an ANOVA table, total variance can be separated as:

$$SS_T = SS_m + \sum SS_c + SS_e \tag{3-13}$$

where SS_T is the total sum of squares, SS_m is the sum of squares due to the mean, SS_c is the individual variance from each column, and SS_e is the error sum of squares. These sums of squares can be calculated by the following equations:

$$SS_T = \sum_{i=1}^{N} {y_i}^2 \tag{3-14}$$

$$SS_m = \frac{T^2}{N} \tag{3-15}$$

$$SS_c = \left[\sum_{i=1}^{k_c} \left(\frac{c_i^2}{n_{c_i}}\right)\right] - \frac{T^2}{N} \tag{3-16}$$

$$SS_e = SS_T - \sum SS_c - SS_m \tag{3-17}$$

where y_i is the ith observation, N is the total number of observations, T is the sum all observations, k_c is the number of levels of a column, c_i is the ith observation in the c column, n_{c_i} is the number of observations under the c_i level.

3.5.2.3 Degree of freedom (DOF)

One other description statistic that must be considered in the ANOVA table is the degree of freedom (DOF). The number of DOF is the number of values that are free to vary; i.e. the number of independent variables. A DOF is related to each estimate of information from the data. The total DOF can be written as:

$$v_T = v_m + \sum v_c + v_e \tag{3-18}$$

where v_T is the total DOF, v_m is the DOF associated with the mean (always 1), v_c is the DOF associated with each column effect, and v_e is the DOF associated with the error.

A DOF is a technique that is used for each independent comparison. The mean is estimated from all observations and its number of DOF is 1 (i.e., there is only "1" comparison between the mean value and zero, the reference). For example, the removal rate of 30 mm^3/min has physical meaning only if a 0 mm^3/min reference point is made, and therefore, there is 1 DOF associated between 30 and 0. Each effect is associated with the mean so that the mean is subtracted from the calculation in order to clear the ANOVA table.

3.5.2.4 Variance (V)

The variance (V) is a measure of how far a set of output values is spread with respect to the mean value. Significant effects are those that are strong enough to influence the mean value and, therefore, the target value is achievable by adjusting significant variables. Hence, these significant effects have to be discovered and controlled in a process to improve output performance.

To complete the ANOVA table, the V has to be calculated from the sum of squares. The V for each effect is calculated from the sum of the squares divided by its DOF. Hence, the total variance is:

$$V_T = \frac{SS_T}{v_T} \tag{3-19}$$

It is worth remembering that the standard deviation *S* is equal to the square root of variance:

$$S = \sqrt{V} \tag{3-20}$$

The standard deviation can be used to evaluate the variation of a process. Note that a smaller standard deviation of a process indicates a higher ability to produce a uniform output in that process.

3.5.2.5 F-Test

An F-test is a statistical hypothesis test to evaluate if two population variances are equal. Hence, tan F-test can be used to examine which effects are strong enough to influence a process, and to determine significant effects. The F-test of each column F_c in an ANOVA can be defined as:

$$F_c = \frac{V_{effect}}{V_e} \tag{3-21}$$

The F_c has to compare with $F_{\alpha;v_1;v_2}$ to determine which factors are strong enough to be significant. α is the risk, v_1 is the DOF associated with the numerator, and v_2 is the DOF associated with the denominator.

An effect is significant if its value is larger than the determined $F_{\alpha;v_1;v_2}$ value, and if not, it is insignificant. The risk value α = 0.05 (i.e. 95% confidence) is generally used in the manufacturing industry at the beginning of a process, and the value is

changeable depending on applications. The concept of determining the α value has been discussed in Section 3.5.2.1.

3.5.2.6 P-value

The F-test is a fixed significance level testing because a hypothesis test is made to state that α has or has not been rejected at a specified value. When H_0 is rejected at the 0.05 level of significance, however, there is little indication as to whether the computed value of the test statistic was only just rejected or whether it was very far from the rejection criteria.

The **P-value** is a statistical hypothesis test to examine the probability of a given event. Hence, the P-value statistic is an alternative method to address the above situation. That is, a selected α is used to refer to a pre-chosen probability and the P-value statistic is used to state a probability that a calculation is made after a given study. For example, when α has been accepted at 0.05, it means that a mistake could be made once in 20 tests. A calculated P-value can convey more information. If a calculated P-value is 0.001, it means that a mistake is probably made per 1000 tests. Hence, the *P*-value statistic is informative and useful in a hypothesis testing. The P-value can be calculated as:

$$\mathrm{P} = 2[1 - \emptyset(|Z_0|)] \tag{3-22}$$

where $\emptyset(x)$ is the cumulative standard normal distribution evaluated at point x. The P-value can be derived in either statistical tables or using software, such as SPSS, Minitab or MATLAB.

3.5.2.7 Confidence Interval (CI)

The CI is preferable because the CI provides an interval within which it is known how much the means differ (i.e. the reliability of an estimate). Suppose θ is an unknown value. Two statistics L and U have to be found such that the probability statement is true:

$$P(L \leq \theta \leq U) = 1 - \alpha \tag{3-23}$$

The interval:

$$L \leq \theta \leq U \tag{3-24}$$

is called a $100(1-\alpha)$ per cent confidence interval for the value θ. The L and U are called lower and upper confidence limits. The accuracy of the estimate in a test can be derived from $\pm|(U-L)/2|$.

3.5.3 Regression analysis

In many situations, there may be more than one significant variable to influence an output from the RGP. In order to develop these results, regression analysis is a method to express experimental data in terms of an empirical model. For example,

assume that an output (e.g. volumetric removal rate) is determined by two significant variables, load and spindle speed: the goal is to build a model to include the two variables for prediction, optimization, as well as to minimise variation (Chapter 4).

A regression model can be written in matrix notation as:

$$\hat{\boldsymbol{y}} = \mathbf{X}\hat{\boldsymbol{\beta}} + \hat{\boldsymbol{\varepsilon}} \tag{3-25}$$

where

$$\hat{\boldsymbol{y}} = \begin{bmatrix} y_1 \\ y_2 \\ \vdots \\ y_n \end{bmatrix}, \quad \mathbf{X} = \begin{bmatrix} 1 & x_{11} & x_{12} & \cdots & x_{1k} \\ 1 & x_{21} & x_{22} & \cdots & x_{2k} \\ \vdots & \vdots & \vdots & & \vdots \\ 1 & x_{n1} & x_{n2} & \cdots & x_{nk} \end{bmatrix}, \quad \hat{\boldsymbol{\beta}} = \begin{bmatrix} \beta_0 \\ \beta_1 \\ \vdots \\ \beta_k \end{bmatrix}, \text{ and } \quad \hat{\boldsymbol{\varepsilon}} = \begin{bmatrix} \varepsilon_1 \\ \varepsilon_2 \\ \vdots \\ \varepsilon_n \end{bmatrix}$$

In a DoE, y_i is the observed response data, $\mathbf{X}$ is the experimental variables, $\hat{\boldsymbol{\varepsilon}}$ is random errors, and β is the regression coefficients that can be solved by the method of least squares. The estimate of regression coefficients is:

$$\hat{\boldsymbol{\beta}} = (\mathbf{X}'\mathbf{X})^{-1}\mathbf{X}'\hat{\boldsymbol{y}} \tag{3-26}$$

Then, the fitted regression model is:

$$\hat{\boldsymbol{y}} = \mathbf{X}\hat{\boldsymbol{\beta}} \tag{3-27}$$

and the residual is:

$$\mathbf{e} = \mathbf{y_i} - \hat{\mathbf{y}}_\mathbf{i} \tag{3-28}$$

For estimation of the variance in a process:

$$SS_e = \mathbf{y}'\hat{\mathbf{y}} - \hat{\boldsymbol{\beta}}'\mathbf{X}'\hat{\mathbf{y}} \tag{3-29}$$

and variance is:

$$V = \frac{SS_e}{v_T - v_e - 1} \tag{3-30}$$

More explanation and rigorous mathematical proof of regression is explored in [190, 191].

3.5.4 Response surface methodology

After the regression analysis, optimisation of the responses from the regression result may then be required. This method was first published by Box and Wilson in 1951 to attain an optimal response from DoE [192].

If the aim is to find the levels of two significant variables, say x_1 and x_2, that maximise the output (y) of a process, this function can be described by:

$$y = f(x_1, x_2) + \varepsilon \tag{3-31}$$

If the expected response is $E(y) = f(x_1, x_2) = \eta$, then the response surface is

$$\eta = f(x_1, x_2) \tag{3-32}$$

The strength of RSM is to consider all outputs and find a solution space with its respective variables. More details of MSF can be found in [193] and the informative review paper [194].

3.6 Summary

This chapter has provided an overview of the methods employed in RGP, such as coordinate systems, TPG, and the working principles of loose-abrasive and bound abrasive. In addition, since fabricating robust, uniform and repeatable optical segments is the core aim of this research, multiple statistical techniques (e.g. DoE, ANOVA, regression analysis, and RSM) were used in order to reduce variance and achieve > 95% (i.e. 2σ) repeatability in the process. All of these theories and technologies are fundamental steps in developing the processes necessary to achieve high-performance optical surfaces in the RGP.

Chapter 4 A statistical approach to process development of the robotic grolishing process (RGP)

4.1 Introduction

The previous chapters have introduced the notion that grolishing is the process of smoothing a ground surface to provide a superior surface for subsequent polishing, so as to reduce the overall manufacturing time. To achieve this goal, the requirements for grolishing are listed below:

(1) To achieve a high volumetric removal rate (VRR) while minimising surface texture (abbreviated to simply "texture" in this chapter),

(2) To control Mid-Spatial Frequencies (MSF) to be smaller than 40 nm PV (as will be discussed in Section 4.2.4), and

(3) To preserve an overall surface accuracy of PV < 4 μm or RMS < 1 μm from grinding [46, 86, 195], so as to smooth the process for polishing and to achieve (1) bulk area < 50 nm RMS and (2) edges < 200 nm PVW (as discussed in Section 2.3.3.2) [77-79].

In addition, in order to demonstrate that the robotic grolishing process (RGP) can be a stable process, another challenge is to control the repeatability of outputs to more than 95% (i.e. a standard deviation smaller than 2 sigmas).

One criterion to demonstrate process efficiency is by means of the VRR. Just increasing VRR, however, is not the only means of proving efficiency because other responses must be considered: texture, MSF and surface accuracy.[2] To this end, the specification for each response in the RGP must be determined.

To consider all responses and achieve the specification seems extremely challenging. In fact, each response can be effectively controlled by a few significant variables but the problem is how to discover these significant variables effectively.[3] The solution adopted in this research was to apply statistical designs and analysis (as introduced in Section 3.5) to reduce unnecessary experimental trials, time and cost. After determining the significant variables, the following process was to model these significant variables for further optimisation so as to realise the overall repeatability target.

This chapter is organised as follows: a specification to define a successful RGP is proposed in Section 4.2, including the proposed variables to control each response. Section 4.3 introduces the experimental preparation, as well as the grolishing tool. Section 4.4 uses a screening experiment to determine significant variables. Section 4.5 models significant variables into the equation for each response (called the resolution space) for further optimisation. Section 4.6 shows how optimised parameters can be selected from the resolution spaces, so as to evaluate the efficiency and repeatability of the grolishing. A summary is provided in Section 4.7.

[2] VRR, texture, surface accuracy, edge and MSF are called "***responses***" (i.e. outputs).
[3] Significant variables are the variables that can easily alter the response of a process. These must be identified and controlled to achieve a robust process.

4.2 Specification

This section reviews the current process chain controlling responses in grinding and polishing for the E-ELT project as a case study, so as to propose an appropriate specification for the RGP that will enhance the overall processing efficiency.

4.2.1 Surface texture (i.e. texture)

The better the input quality to CNC polishing (aspheres in particular), the less time the polishing takes, and the less residual work remain after it is finished. That is, a finer texture has a faster process. In order to improve the processing efficiency from grolishing to polishing, a grolished grey surface should ideally be polished into a specular surface in one polishing run, and then be able to be measured by an interferometer for any remaining corrective polishing. From the polishing experience evidenced in this chapter, a grey grolished surface with $S_a < 400$ nm can be polished into a specular one by removing 1.3 μm of material, which is achievable in one polishing run using the R80 bonnet. Hence, the texture in the final grolishing cut should achieve $S_a < 400$ nm.

4.2.2 Volumetric removal rate (VRR)

The minimum required VRR value in the RGP can be determined by reviewing the grinding process. Tonnellier reported that to remove 1 mm of material from a 1.45 m hexagon using the BoX^{TM} grinding machine required 13.5 hrs to achieve a 3 μm PV accuracy [195]. The residual surface errors, however, comprised not only MSF

(discussed in Section 4.2.4), but also a 10 μm thickness of sub-surface damage (SSD) [89]. The SSD is a thin layer of micro-cracks introduced on the top layer of ground glass, resulting in a weakening of the strength and lifespan of optical surfaces. SSD is not the texture, as illustrated in Figure 4-1. Minimising SSD is especially important for the high power laser and semiconductor industry. Various techniques for measuring SSD, such as (1) HF etching techniques, (2) cutting segments, and (3) using quantum dots (small semiconductor particles about nanometres in size) in the slurry excited by a 540 nm laser, are outlined in [196-200].

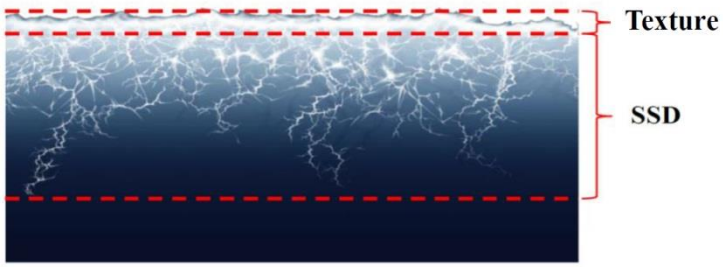

Figure 4-1: Definition of texture and SSD in optical surfaces

In this case, the required time is an overall grinding time of 13.5 hrs [195]. Hence, if the RGP succeeds in removing 10 μm of material from a 1.45 m hexagon in less than 13.5 hrs, it has attained higher removal efficiency than grinding.

The VRR is defined as:

$$\text{Removing efficiency (i.e. VRR)} = \frac{\text{required volume of removing materials}}{\text{total processing time}}$$

From the calculation, the VRR for the RGP should be greater than 16.9 mm^3/min.

4.2.2.1 Controlled methods and selection of variables

Using the Influence Function (IF) (Section 2.4.2) is one mathematical model to calculate the VRR quickly [33, 169, 201-203]. Once the IF model is built, unlimited results can be simulated in a short time. The main drawback of using the IF, however, is that the model considers only local effects (i.e. the tool area), and this means that the IF model can cause disagreement between predicted and actual results because it can easily neglect important variables. For example, Wai's PhD thesis [204] created this kind of model for the accurate prediction of removal functions for MRF (introduced in Section 2.4.3), but his model frequently omitted variables and has to be reconsidered to improve model accuracy. Building an IF model is also a tedious process that requires experimental results to verify the prediction. Since the RGP requires a more efficient method to control all responses, the IF method was not used in this thesis.

Although conducting experiments can achieve accurate results, the problem is that there is only a limited basis on which to select the right parameters. In order to avoid exhaustive experimental runs, the proposed solution was to use statistical experimental design and analysis (introduced in Section 3.5). This method has been demonstrated in manufacturing industry to be able to shorten the experimental time needed to bring products to markets, such as automobiles, coating materials on surfaces, mobile phones and metal processing [177, 179, 205, 206]. The advantages of this method are the ability to summarise and interpret experimental results systematically based on statistical science for further improvement and optimisation

at the next research stage. For these reasons, these kinds of statistical methods are used in this chapter for considering all responses (Section 4.1).

To that end, the next step is to select the potentially significant variables for VRR. The rule of thumb is to refer to input grinding variables and select input grolishing variables to control SSD, texture, MSF and surface accuracy, while ensuring that the VRR remains larger than 16.9 mm^3/min. Tonnellier [89, 195] indicated that one example of the final grinding cut can be a 50 μm depth with a 25 μm diamond grit size, 2600 rpm spindle speed, 18000 mm/min tool travel feed and a 10 N loading force. Based on this, the variables for the RGP could be: 9 ~ 20 μm abrasive sizes, 600 ~ 1000 rpm spindle speed, 1500 ~ 4500 mm/min tool travel feed, and 1000 ~ 1350 g loads to achieve a VRR > 16.9 mm^3/min [92]. Other potentially significant variables were also considered, such as track space 2~10 mm and slurry density (abrasive: water = 3:9 ~ 4:9, measured by weight).

4.2.3 Surface accuracy and edge control

Manufacturing a required surface topography is the foundation to produce high performance (i.e. diffraction-limited) optics in many kinds of imaging systems, from microscopes to telescopes [207]. The objective of this section is to define the specification and propose possible significant variables to control surfaces.

4.2.3.1 Specification of surface accuracy

In order to describe the surface fully, it was necessary to separate it into the bulk area and edge zone. According to the ESO's specification for a single hexagon, the edge zone of a segment is defined as a 10 mm wide peripheral zone. The philosophy adopted was to avoid any down-turns and to always maintain up-standing edges within the edge zone [94, 208], since these can then be easily corrected in a subsequent process step.

Actually, the achieved width of edge-misfiguring in a segment is related to the tool size. Since the tool diameter was 100 mm in this case, the 10 mm wide zone (as defined by the polishing process) [32] cannot fully describe the edge in the RGP. Hence, the edge zone was redefined to the tool size: 100 mm, as shown in Figure 4-2. The specification in the RGP, therefore, was to maintain a ground surface with RMS < 1 μm and PV < 3 μm (goal: PV < 1 μm) [195] with an up-standing edge, so that the bulk and edge zones could be corrected in the subsequent polishing process to achieve the ESO's specification.

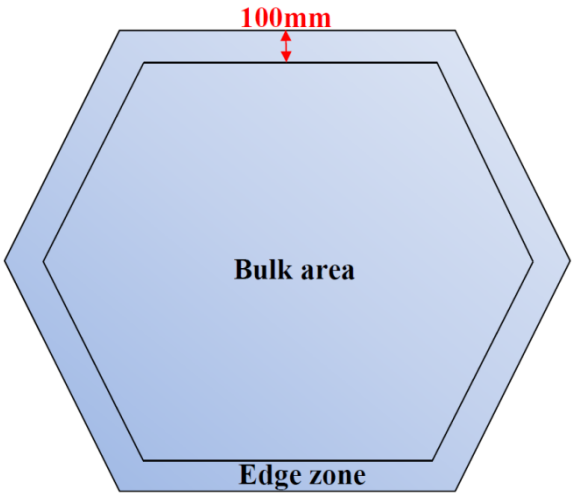

Figure 4-2: Redefinition of the bulk area and edge zone of a hexagonal segment for the RGP

Most optical techniques leave surface errors at the edges, and these serve to make the useful clear aperture slightly smaller than the fabricated optics, with the edges usually being turned down. This strategy can be used for intermediate optics for cameras or small optics for microscopes, but is not appropriate for a segmented telescope, because the whole segment is required to gather light from the universe. Although the propagation of light waves is mainly determined by the bulk area of a surface, the edge performance determines the effect of stray lights, scattering, diffraction and IR-emissivity that may degrade imaging quality [209]. For the M1 of the E-ELT, the total edge length of all the segments in the primary mirror is approximately 4.5 km. The integrated area of all the edges is therefore large, and certainly sufficient to degrade performance due to stray light effects. It is imperative, therefore, that the edge quality be controlled.

To simplify this problem, the bulk area, which is smooth and more easily controlled than the edges, will be temporarily omitted until Section 4.6. The following sub-section, therefore, focuses on methods to control the edge-misfiguring.

4.2.3.2 Review of edge control methods

The following sub-sections discuss different methods for edge control.

4.2.3.2.1 Oversize and reshape:

A segment can be manufactured to be oversized, before being cut at a later stage of the process to the required shape (such as a hexagon) once the segment meets the requirement. The risks of breakage, chipping and distortion of the surface are the main problems in the cutting process, however. For example, exterior pressure may be introduced into a segment, distorting the surface, and resulting in re-polishing or even re-grinding; all of which would increase the overall processing time. In order to avoid this, it is recommended to fabricate a segment according to its exact final hexagonal shape, so as not to introduce any adverse effects due to subsequent cutting [210].

4.2.3.2.2 Waster:

In the conventional lapping, a waster may provide extra space to support the overhanging part of a tooling [107, 211]. This method is not adopted for fabricating large optics for the following reasons: (1) the risk of pulling and distorting the

segment surfaces using waster-adhesives (2) the risk of damaging the segment due to the detachment process of the wasters (3) the risk of damaging the segment due to the accidental detachment of the wasters as a tool approaches the edge (4) handling risk. Details are described in [212].

4.2.3.2.3 Simulation and then experimental confirmations

Influence function (IF), dwell time (Equation 2-9), and finite element analysis (FEA) are a series of simulation exercises that can be used to predict local edge effects [171]. Simulations can provide a general guideline to estimate experimental results but this method cannot replace experiments. For example, a tool will experience acceleration and deceleration when changing traverse directions at the edge (Figure 4-20). Commercial software has difficulty in modelling each specific case, which points out the modelling limitations, along with the other difficulties that were introduced in Section 4.2.2.1.

4.2.3.2.4 Adjust spindle speed (SS) or tool travel feed (TF):

Manipulating SS and TF is one method to optimise rigid-tool grolishing to control edges. These two variables were related to the processing time and seem significant in the RGP and were therefore considered in the experiments.

4.2.3.2.5 Abrasive size (AS):

From a conventional perspective, a large AS can achieve high VRR when all other variables are controlled and kept constant. For this reason, the AS may be a significant influence on edges and thus needs to be examined.

4.2.3.2.6 Operating tool Overhang (OH):

Using tool overhang can be the most efficient method for edge control (a definition of OH was provided in Section 3.3.3). The philosophy of this approach is to manipulate the pressure distribution of the tool at the non-continuity and the boundary conditions during the surface processing. Since OH is a known variable to control edges [77, 95], however, in order to reduce unnecessary experimental trials, OH will not be considered in the screening experiment in Section 4.4. Please note that the function of the screening is to determine significant variables.

4.2.4 Mid-spatial frequencies (MSF)

One critical problem in the CNC manufacturing process is imprinted periodic tooling errors left behind in the surfaces. These errors are the consequence of using sub-aperture tools to follow a regular tool path to process an optical surface, resulting in the generation of periodic tooling signatures. As illustrated in Figure 4-3, these kinds of errors have a characteristic waviness, or ripples, on the surface and are referred to as “mid-spatial frequency (MSF)”, or “cusping”.

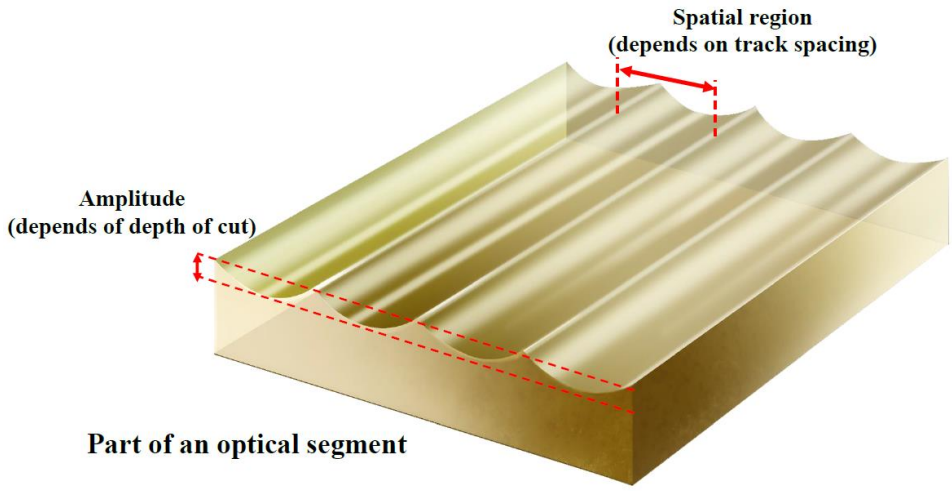

Figure 4-3: MSF (spatial region and amplitude in a surface)

In current high-resolution imaging systems, such as x-ray optics, laser optics, lithography, remote sensing, as well as telescopes [108, 213-216], controlling the amplitude of MSF errors is essential and therefore techniques are required to smooth the MSF out of the entire optical surface, without degrading the aspheric form.

MSF concerns are usually overlooked at the beginning of the optical design stage. When a fabrication chain has not been decided, designers often isolate the MSF information from the modelling. Once the surface is in the construction phase, however, the challenge for the designers is to consider the MSF modelling; e.g. when opticians measure the MSF ripples, this information can pass to the designers to incorporate it in the tolerance of their designs. For example, Rees [217] has proposed metrology requirements for polished ELT mirror segments at OpTIC.

In order to define the MSF tolerance for the RGP, a simulation based on the imaging processing was conducted, as described in Section 4.2.4.1. Variables are subsequently proposed to control MSF in Section 4.2.4.2

4.2.4.1 The specification of MSF

When using a sub-aperture rigid tool to process a surface, the challenge is to control the spatial frequency content in terms of surface and tool, especially aspherical misfits with a rigid tool (Chapter 6). As shown in Figure 4-3, when discussing the MSF specification, it is necessary to define (1) the spatial frequency content and (2) the amplitude. In Chapter 2, the MSF is defined as $0.02\ mm^{-1} < MSF < 1\ mm^{-1}$ because the MSF in this region cannot be polished out [41] and therefore must be removed in the grolishing process.

To remove MSF amplitudes is challenging for bonnet polishing [37]. Until recently, methods to reduce MSF in an optical surface, therefore, relied extensively on pitch polishing or skilful opticians who may participate in the final figuring process. To completely eliminate MSF is not necessary and impossible, however, and would increase total processing time and cost to unacceptable levels. In respect to imaging quality considerations, if the level of MSF in given a surface still allows diffraction-limited images to be achieved, then MSF amplitudes below this value can be defined as the tolerance level.

There are different commercial software available to model MSF errors, such as Zemax, CODE V, and OSLO. The method proposed in this thesis is to use processed

(grolished and then polished) surfaces and then analyse these using the 4Ssight data [218] analysis software. When determining the MSF tolerance, in order to compare with the ideal case, a theoretical zero MSF input surface was considered in the simulation. The Point Spread Function (PSF) and Modulation Transfer Function (MTF) were used to evaluate the MSF amplitudes. Goodman sets out the theory of PSF and MTF [51]. Four examining angles (0°, 45°, 90° and 135°) were considered in the 180 mm aperture to examine each field image, as shown in Figure 4-4. The PSF and MTF were automatically generated by the software, and the analysis results are shown in Figure 4-5 and Figure 4-6.

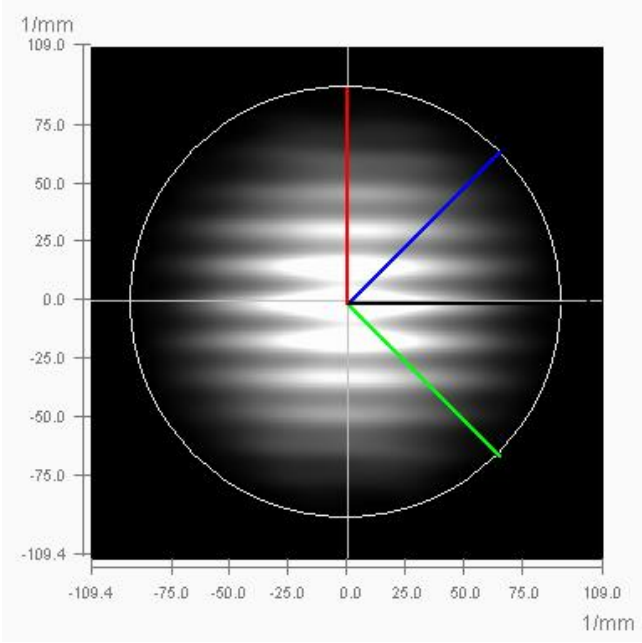

Figure 4-4: Four different examining angles for MTF

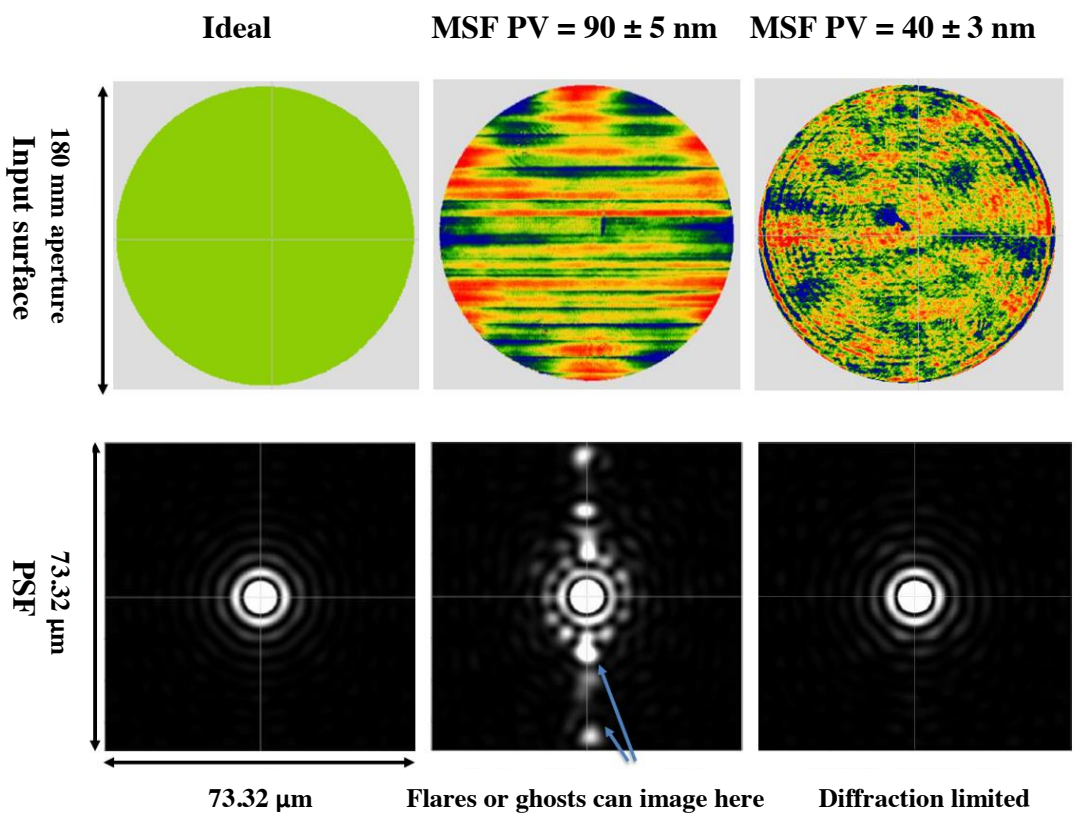

Figure 4-5: Input surfaces and their respective PSFs. MSF errors larger than PV = 40 nm can produce flares and ghosts. (532.8nm wavelength)

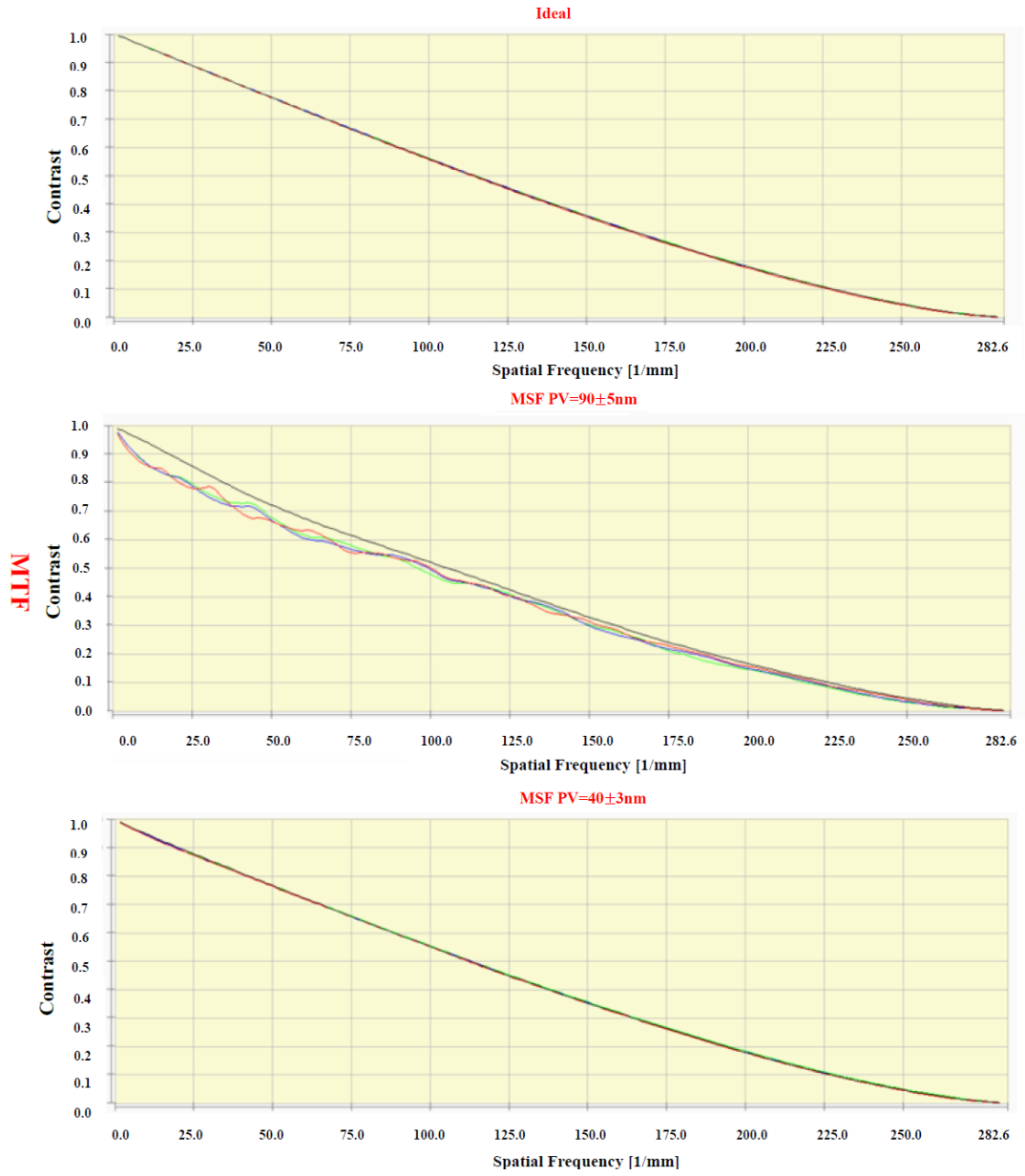

Figure 4-6: Input surfaces relative to their MTFs

The PSF result shows that MSF PV > 40 nm in the surface can introduce glare, ghosts and diffraction. Although these effects can be removed by providing an aperture located near the image plane, some amount of image energy is also filtered

out, which makes it harder to observe faint stars or other objects in the sky. This result indicates the importance of controlling MSF.

In addition, it can be seen that the image is not degraded in terms of either PSF or MTF when MSF PV = 40 nm (compared with the ideal surface). From this point, therefore, the tolerance for the MSF amplitude is PV < 40 nm, allowing the resulting image to still approach the diffraction limited state.

4.2.4.1.1 Metrology of MSF

This section serves to further discuss how to measure MSF amplitude. When measuring, the amplitude is easily swamped by background noises, with one critical noise being low order aberrations (introduced by the smoothing process, as shown in Figure 4-9). Although filtering out low order aberrations can be achieved using commercial software, the problem is that there is no evidence from which to determine the maximum terms of the Zernike polynomials (introduced in Section 2.5.2) without affecting MSF amplitudes. The following seeks to answer this question.

Thirty samples were measured with a 4D technologies interferometer (Model 6000) and then analysed using the 4Sight Data analysis software. Each data was collected by removing Zernike polynomials up to 120 terms and the results are summarised in Figure 4-7. The results demonstrated that the first 35 terms belonged to low order aberrations and were thus allowed to be removed for the purpose of measuring MSF amplitudes easily.

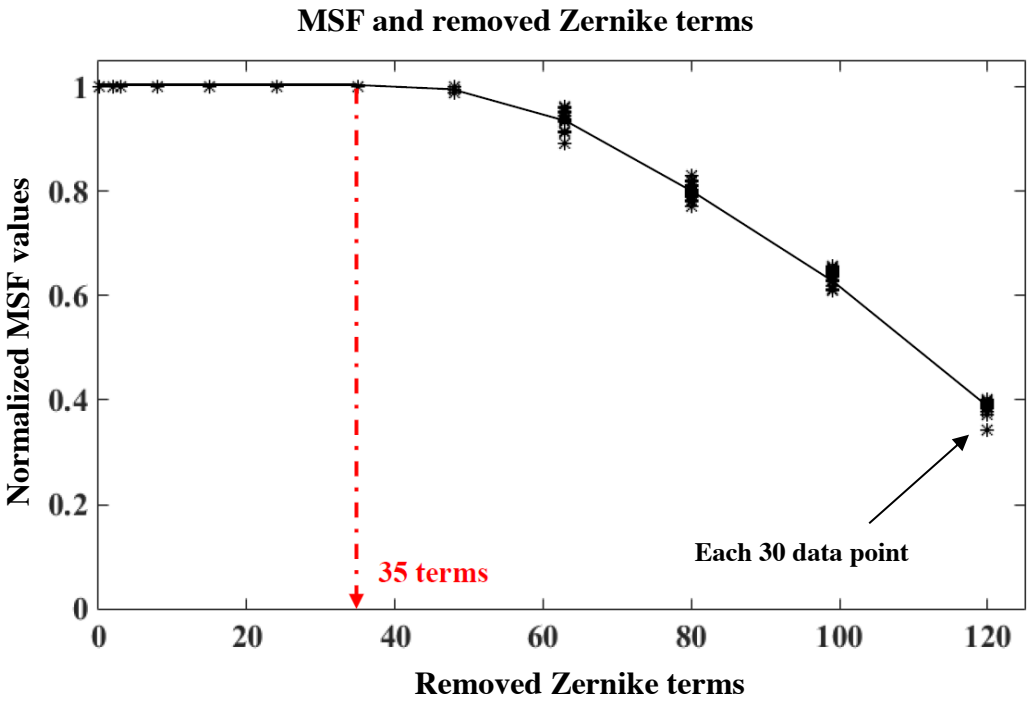

Figure 4-7: MSF amplitudes and removed Zernike terms

4.2.4.2 Proposed methods to control MSF

Researchers in the fabrication field have studied the correlation between residual MSF, the removal (i.e. depth of cut) and the tool path for more than three decades by using rigid tools for CNC grinding and polishing. The RGP is an intermediate process between the grinding and polishing, however, meaning that two processes to control MSF errors need to be reviewed.

For the grinding process, Franse [219] and Cheung et al. [220] found that the tool spindle speed was the most important variable in respect to introducing MSF. Takasu et al. [221], Sata et al. [222], and Tonnellier [89], meanwhile, investigated the relationship between the MSF and the depth of removal, showing that the removal is

affected by vibrations, tool-wear instability, overlap in the tool paths of the used tools, increase in temperature in relation to the spindle speed, as well as robotic thermal errors.

For the polishing process, Dunn and Walker [107, 223] proposed pseudo-random tool paths to remove periodic MSF structure. Yu et al. [37] used a Zeeko IRP machine to remove MSF by using loose abrasive rigid hard tools. Song et al. [224], meanwhile, discussed the relationship between MSF and tool misfits. These studies all provide useful information on how to control residual MSF in the RGP.

From this literature, it can be summarised that potential significant variables for the MSF are: (1) abrasive size, (2) spindle speed, (3) overlapping tool path, (4) tool travel feed, and (5) applied tool load. Each of these variables will be examined in Section 4.3.5.

4.2.5 Summary of the specification

The specification of each response for the RGP is summarised in Table 4-1. The potential significant variables for each response were further evaluated in the screening experiment described in Section 4.3.5.

Table 4-1: Specification for each response

	Specification
VRR	Removal efficiency > 16.9 mm^3/min (= 13.5 hrs to remove 10 μm depth materials for a 1.45 m hexagonal mirror segment (Section 4.2.2))
Texture	A final grolished surface has to be polished into a specular surface in one polishing run (S_a < 400 nm)
Surface (bulk)	Gentle and smooth (RMS< 1 μm or PV < 3 μm)
Edge	(1) Edge up-stand PV < 3 μm (2) Gentle and smooth (3) so as to be easily processed by the subsequent bonnet polishing.
MSF	PV MSF<40nm

4.3 Experimental Preparation

4.3.1 Characteristics of the grolishing tool

It is recommended that a tool used for the grolishing process should follow the design proposed in this section. For example, a 100 mm[4] diameter tool is used in this chapter to establish the grolishing process to manufacture flat borosilicate hexagonal segments with a 400 mm length measured from corner to corner, and the same tool will be employed to process complex surfaces in Chapter 6. Another 280 mm[5] diameter tool, based on the 100 mm diameter tool design, is used to process a 1 m

[4] The 100 mm diameter is limited by the 400 mm hexagonal segment.
[5] The 280 mm diameter is limited by the measuring capacity of the Talysurf.

hexagonal segment in Chapter 5. Semi-rigid pads can also be attached to this large tool for the purpose of removing MSF [225, 226].

Figure 4-8 shows the 100 mm diameter tool, which can be separated into three parts: (1) spigot, (2) holder, and (3) pad. The spigot is the element that can be dragged by a robotic arm or other CNC machines. Its function is to guide the tool to follow a tool path and to process a workpiece, with the speed of the robotic arm determining the tool travel feed. The holder is designed to link the spigot and the pad. Loose joints (i.e. a gimbal arrangement) were designed for the holder so that the tool can adjust its inclination to adapt to a surface slope, as shown in the right of Figure 4-8. The rigid pad is the surface used to process a workpiece. The total load is determined by the tool weight itself.

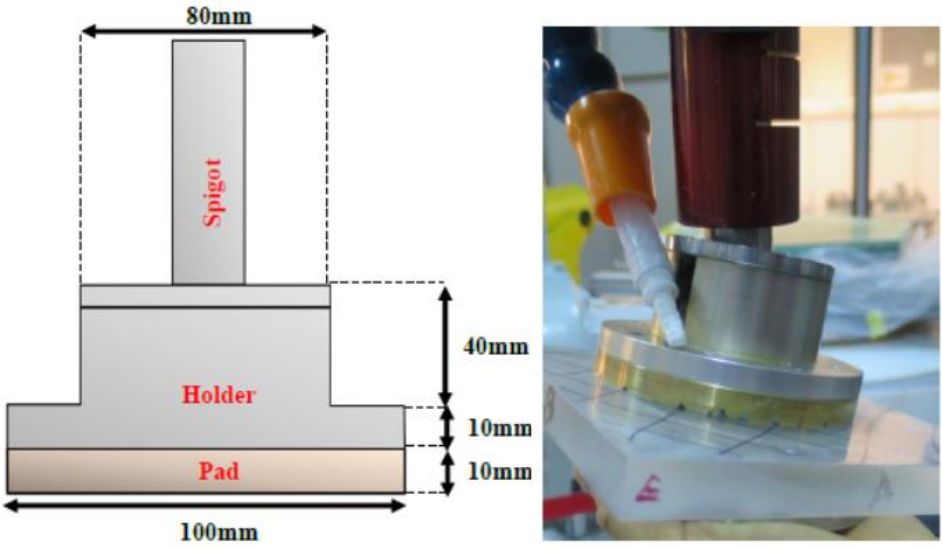

Figure 4-8: Mechanism of the grolishing tool

4.3.2 Smoothing process

The smoothing process was able to achieve a uniform starting point and was especially important to remove MSF errors in 0.02 mm^{-1} < MSF < 1 mm^{-1} (Section 2.5.2) at the beginning of an experiment. Removal of the residual processing signatures from a previous grolishing process was achieved by using a 300 mm large tool (the largest tool available), as shown in Figure 4-9. The reason for using a large tool is because its area covered all the MSF regions, helping to remove the cusping MSF features from the RGP. Even though the 300 mm tooling could produce LSF errors, these could be corrected by the polishing technique. This is an important reason why a rigid tool was used for the RGP to control MSF. An example showing a lack of the MSF cusping features following the use of this 300 mm tool is provided in the bottom section of Figure 4-9.

Smooth the surface for any remaining experiment

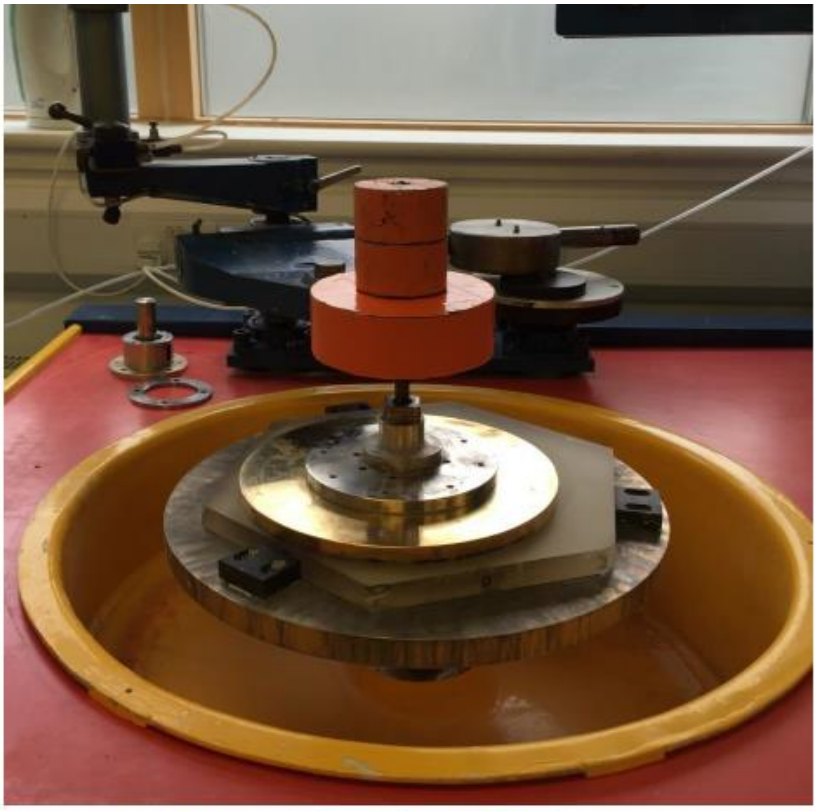

One example of removing the MSF by using the 300 mm smoothing tool

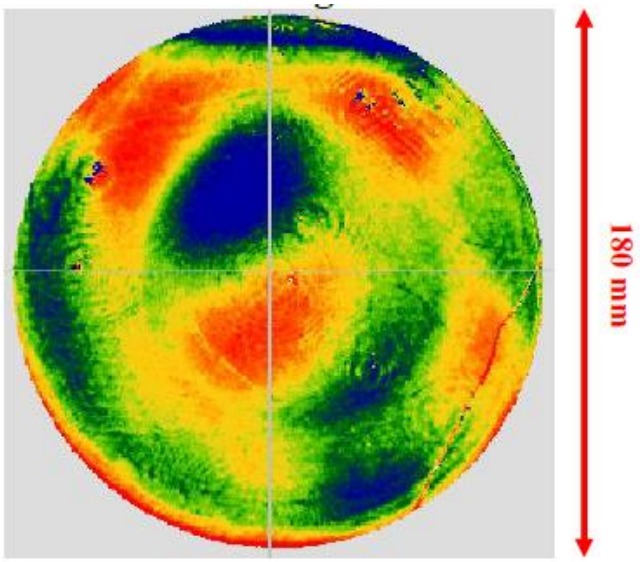

Figure 4-9: Smoothing process

4.3.3 Removal measurement

Since the maximum range for the Talysurf is 300 mm, when examining the removal depth, the grolishing dimension was a 280mm×280mm square, as shown in Figure 4-10.

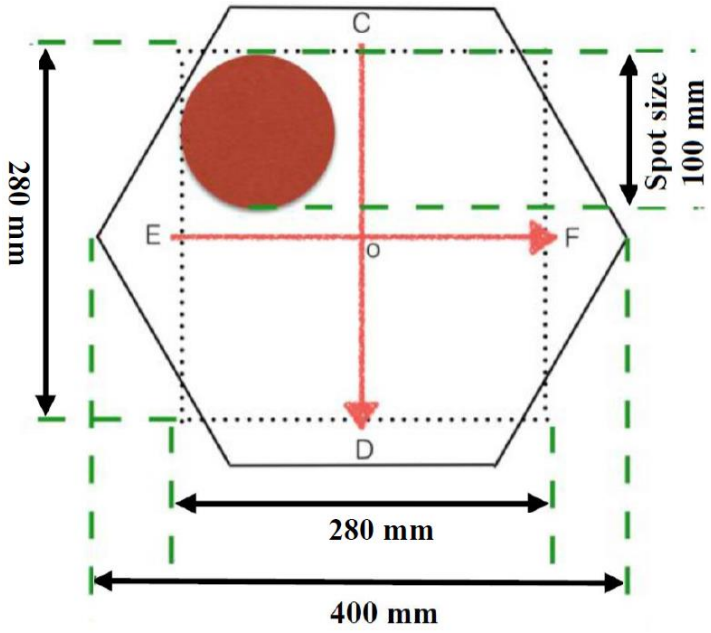

Figure 4-10: Removal measurement

4.3.4 Tool path direction

Since a circular tool path is in the development process, a raster tool path was used to control edge-misfiguring. One important task when using the raster tool path is to decide the processing direction: i.e. whether to follow perpendicular or parallel tool paths, as shown in Figure 4-11. One problem with the perpendicular raster tool path is that it can cause an intensively shaking robotic arm at the beginning and the end of

a process because a robot frequently decelerates and then accelerates to change processing directions. These kinds of momentum variations may introduce instability into the process or, in a serious case, break the glass at the corner due to the high spindle speed of the vibrating tool. The parallel raster tool path was therefore used to investigate the edge control experiment.

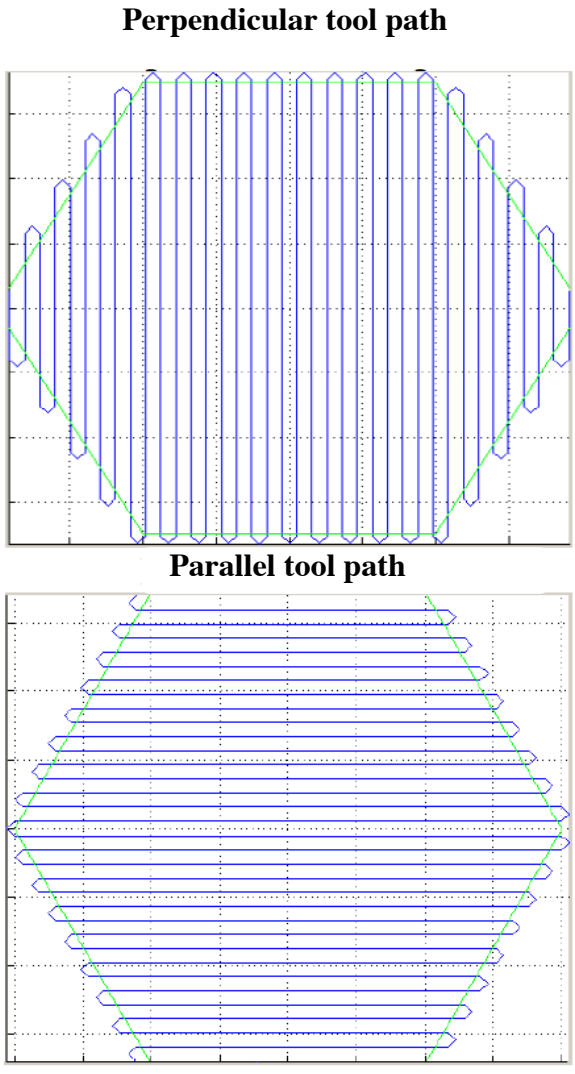

Figure 4-11: Tool path direction

4.3.5 Grolishing and Polishing

The grolishing process using the 100 mm diameter tool and then the polishing process (Section 4.2.4.1.1) using the R80 bonnet to polish a 400 mm hexagonal segment are shown in Figure 4-12. The processing machines and measurement equipment have already been fully introduced in Chapter 2 and Chapter 3.

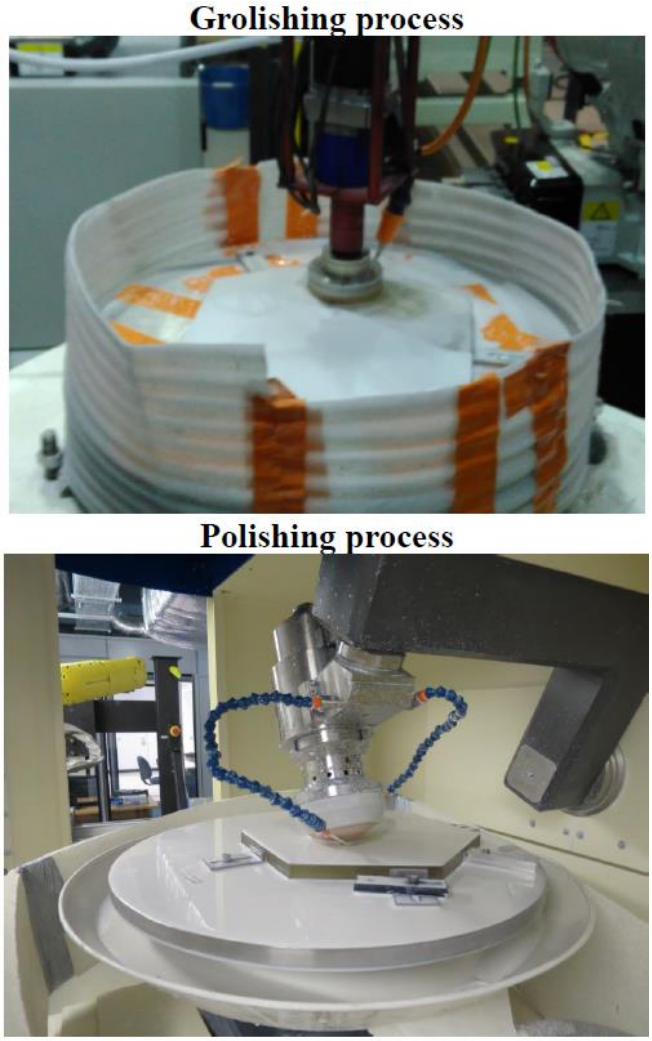

Figure 4-12: The grolishing and polishing processes on a flat 400 mm hexagonal segment

4.4 Screening experiments

The objective of this section is to determine the significant variables for each response. As discussed in Section 4.2, there are in total six potentially significant variables that need to be evaluated in this section (OH is a known significant variable and will be discussed in Section 4.5). It would be a time-consuming process to examine all the variables in detail, however. For example, if each variable has two levels,[6] the total number of experimental trials would be 64, which would require 8-10 months to complete, including metrology, data analysis and interpretation.

In Chapter 3, Taguchi's experimental design was introduced to speed up the experimental procedures, and one of his designs (L8) was used to reduce the initial 64 trials to 8. The design and results are shown in Table 4-2. Examples of these data will be shown in Section 4.5 and Section 4.6, and some in [92]. ANOVA was the statistical method used to analyse the data, with the results summarised in Table 4-3. Please refer to Section 3.5 to review ANOVA and its notation. Please also note that the edge and MSF were scaled by their respective removal depths, because if there were no removal, there would be zero edge defects and MSF on a surface. In order to determine the dominant variables, the edge and MSF must scale with their relative removal depths.

[6] Two levels are suggested for the screening experiments to determine significant variables. After that, more levels can be used to examine the effects of significant variables (Section 4.5)

Table 4-2: Screening experiment results

Trial	AS	L	S	SD	TS	TF	VRR [mm/min]	Texture [nm]	Edge/Depth	MSF/Depth ($\times 10^3$)	
1	9	1000	600	4:9	2	1500	28.1	349.7	2.10	2.3	2.4
2	9	1000	600	3:9	10	4500	23.8	348.9	2.00	4.8	4.8
3	9	1350	1000	4:9	2	4500	48.6	352.1	2.05	4.3	4.2
4	9	1350	1000	3:9	10	1500	46.0	347.1	2.08	6.2	6.3
5	20	1000	1000	4:9	10	1500	86.4	649.7	2.03	11.6	11.5
6	20	1000	1000	3:9	2	4500	89.7	658.1	2.03	8.8	8.8
7	20	1350	600	4:9	10	4500	75.7	628.7	2.07	10.0	10.2
8	20	1350	600	3:9	2	1500	80.9	644.1	2.08	7.7	7.7

AS: Abrasive Size [µm], **L**: Load [g], **S**: Spindle Speed [rpm], **SD**: Slurry Density, **TS**: Track Space [mm], **TF**: Tool Feed [mm/min]

Table 4-3: ANOVA-screening experiment

	VRR						Texture				
	dof	**SS**	**V**	**F**	**P**		**dof**	**SS**	**V**	**F**	**P**
AS	1	4333.81	4333.81	866761	0.001		1	174877	174877	11152.87	0.006
L	1	67.28	67.28	13456	0.005		1	148	148	9.43	0.200
S	1	483.60	483.60	96721	0.002		1	158	158	10.10	0.194
SD	1	0.32	0.32	64	0.079		1	41	41	2.58	0.354
TS	1	29.65	29.65	5929	0.008		1	110	110	6.98	0.230
TF	1	1.62	1.62	324	0.035		1	1	1	0.06	0.844
error	1	0.01	0.01				1	16	16		
Total	7	4916.28					7	175350			

	Edge/depth						MSF/depth				
	dof	**SS**	**V**	**F**	**P**		**dof**	**SS**	**V**	**F**	**P**
AS	1	0.5	0.5	0.03	0.895		1	105.062	105.062	4727.81	0.000
L	1	18.0	18.0	1.00	0.500		1	0.460	0.460	7.20	0.025
S	1	4.5	4.5	0.25	0.705		1	8.702	8.702	391.61	0.000
SD	1	4.5	4.5	0.25	0.705		1	0.122	0.122	5.51	0.043
TS	1	8.0	8.0	0.44	0.626		1	23.040	23.040	1036.80	0.000
TF	1	24.5	24.5	1.35	0.451		1	0.002	0.002	0.11	0.745
error	1	18.0	18.0				9	0.200	0.022		
Total	7	78.0					15	137.290			

The ANOVA result in Table 4-3 shows that the modelling of VRR, texture and MSF could explain more than 99.3% ($SS_{\text{all significant variables}}/SS_{\text{total}}$) of the variance in the data, indicating that all significant variables could be determined in the screening experiment. For the edge, however, the six testing variables were insignificant, meaning that the only significant variable was OH. This conclusion will be confirmed in the next section.

The following procedure is to determine values for the significant and insignificant variables. Since the track space is the only significant variable affecting MSF, a 2 mm track space was used to produce small MSF on a surface.[7] The next step was to decide values for insignificant variables. In order to reduce the experimental cost, the insignificant variable of slurry density was fixed to abrasive:water = 1:3 (measured by weight). Moreover, a tool feed of 4500 mm/min was determined because a high tool feed can achieve shallow MSF amplitudes per run (as demonstrated in Section 4.5.3).

The ANOVA results and decided variable values are summarised in Table 4-4 and will be further evaluated in Section 4.5

[7] The tool traverse decelerate/accelerate to produce edge-misfiguring will be discussed in Section 4.5.2.

Table 4-4: Summary of significant variables for each response

Response	Significant variables	
VRR	Abrasive size > Spindle Speed > Load	
Texture	Abrasive	
Edge	These six variables are not significant variables. OH might be the only significant variable	
MSF	Abrasive size > Track Space > Spindle Speed > Load	
Controlled variables		
2 mm track space	4500 mm/min tool feed	Slurry density = 1:3
Borosilicate glass	400 hexagon	Raster tool path

4.5 Confirmation experiment

This section is to evaluate the determined significant variables and further interprets the results by using regression analysis in order to conduct optimisation in Section 4.6.

4.5.1 VRR and texture

For VRR, there were three significant variables (abrasive size, load and spindle speed) and the controlled variable was processing time (i.e. time was constant). In order to evaluate whether any interaction effects exist, a 2^3 full factorial design

(FFD) was used. Each trial was repeated three times so as to check the repeatability of the experiment and to improve model accuracy. Since FFD is the most extensive experimental design and the measuring time for texture was short (about 10 min), the texture is evaluated in this section.

The FFD and ANOVA are shown in Table 4-5 and Table 4-6, respectively. The repeatability (goal: $< 2\sigma$ (Chapter 3)) was about $\pm 2.4\%$ for VRR and $\pm 1.3\%$ for texture, showing that VRR and texture can achieve 95% stability in a process. In addition, the result confirms the conclusion in Table 4-4, the implications of which can be summarised as follows: firstly, for the VRR, the significant variables were abrasive size, spindle speed and load, in that order, which confirms the Preston equation (Section 2.4.2) that VRR is proportional to speed $\times$ load; for texture, the significant variables were abrasive size and load in order. Secondly, the abrasive size was about 40 and 4700 times (compared with their F values for this example) larger than the second significant variable for VRR and texture respectively, indicating that abrasive size can be used to separate the process. For example, a large abrasive size could be used to perform a pre-grolishing process to achieve uniform MSF values (the effect of large abrasives will be further discussed in Chapter 6), while a smaller abrasive size could then be used for the corrective or finishing process to remove local errors (such as scratches, MSF and localised surface errors).

Table 4-5: 2^3 FFD (VRR and texture)

	Variables			VRR[mm/min]				Texture [nm]			
Trial	**AS**	**L**	**S**	**1st**	**2nd**	**3rd**	**R(±%)**	**1st**	**2nd**	**3rd**	**R(±%)**
1	9	1000	600	23.2	24.3	23.8	2.3	350.8	350.9	345.4	0.9
2	9	1350	1000	45.5	47.6	47	2.3	347.1	344.0	340.6	0.9
3	20	1000	1000	85.4	89.1	87.6	2.1	644.4	648.1	657.6	1
4	20	1350	600	78.6	78.3	81.6	2.3	643	654.3	638.6	1.3
5	9	1000	1000	42.8	41.4	41.1	2.2	356.8	351.4	352.1	0.8
6	9	1350	600	28.8	29.8	29	1.8	345.9	346.8	353.8	1.2
7	20	1000	600	73.8	73.7	71.5	1.8	653.0	659.5	647.1	0.9
8	20	1350	1000	99.8	104.4	103.4	2.4	619.9	616.8	605.4	1.2

Table 4-6: ANOVA (VRR and texture)

	VRR						Texture				
	dof	**SS**	**V**	**F**	**P**		**dof**	**SS**	**V**	**F**	**P**
AS	1	15145.4	15145.4	2170.05	0.000	**AS**	1	511029	511029	13466.41	0.000
L	1	384.8	384.8	55.13	0.000	**L**	1	1079	1079	28.43	0.000
S	1	1992.9	1992.9	285.55	0.000	**S**	1	459	459	12.08	0.003
AS×L	1	47.9	47.9	23.14	0.000	**AS×L**	1	438	438	11.54	0.003
LS×S	1	25.0	25.0	12.09	0.003	**AS×S**	1	431	431	11.36	0.004
AS×L×S	1	31.5	31.5	15.23	0.001	**L×S**	1	525	525	13.85	0.002
error	17	35.2	2.1			**error**	17	645	38		
Total	23	17662.6				**Total**	23				

Regression analysis can be used to summarise the above data into resolution space for the purpose of selecting variables effectively, yielding:

$$\text{VRR} = -16.7 + 2.84 \times \text{AS} - 0.0181 \times \text{L} + 0.0113 \times \text{S} + 0.00122 \times \text{AS} \times \text{L} + 0.000025\ \text{L} \times \text{S} + 0.00000017\ \text{A} \times \text{L} \times \text{S} \quad (4\text{-}1)$$

$$\text{Texture} = -7.34 + 34.8 \times \text{AS} + 0.133 \times \text{L} + 0.191 \times \text{S} - 0.00444 \times \text{AS} \times \text{L} - 0.00385\ \text{AS} \times \text{S} - 0.000134 \times \text{L} \times \text{S} \quad (4\text{-}2)$$

where 9 < AS (abrasive size) < 20, 1000 < L (load) < 1350, and 600 < S (spindle speed) < 1000.

It was necessary to confirm the linearity of the two equations because each variable only has two levels. Hence, another confirmation experiment had to be run in order to verify Equations (4-1) and (4-2).

The 9 μm abrasive was determined as being suitable for this experiment because this size was able to achieve the specification of VRR and texture as in Table 4-1. Since spindle speed was the second most significant variable to affect the results, five different spindle speeds (600 rpm, 700 rpm, 800 rpm, 900 rpm and 1000 rpm) were chosen to examine the two equations.

Results and statistics are shown in Figure 4-13 and Table 4-7, respectively. The experiment confirms a 95% confidence interval for the predicted data, indicating that the two equations are accurate. Moreover, both results demonstrate that the

specification defined in Table 4-1 is achievable. VRR was at least 1.67 times larger than the specification and texture was S_a < 349.2 nm, indicating that the surface could be polished to a specular condition in one polishing run.

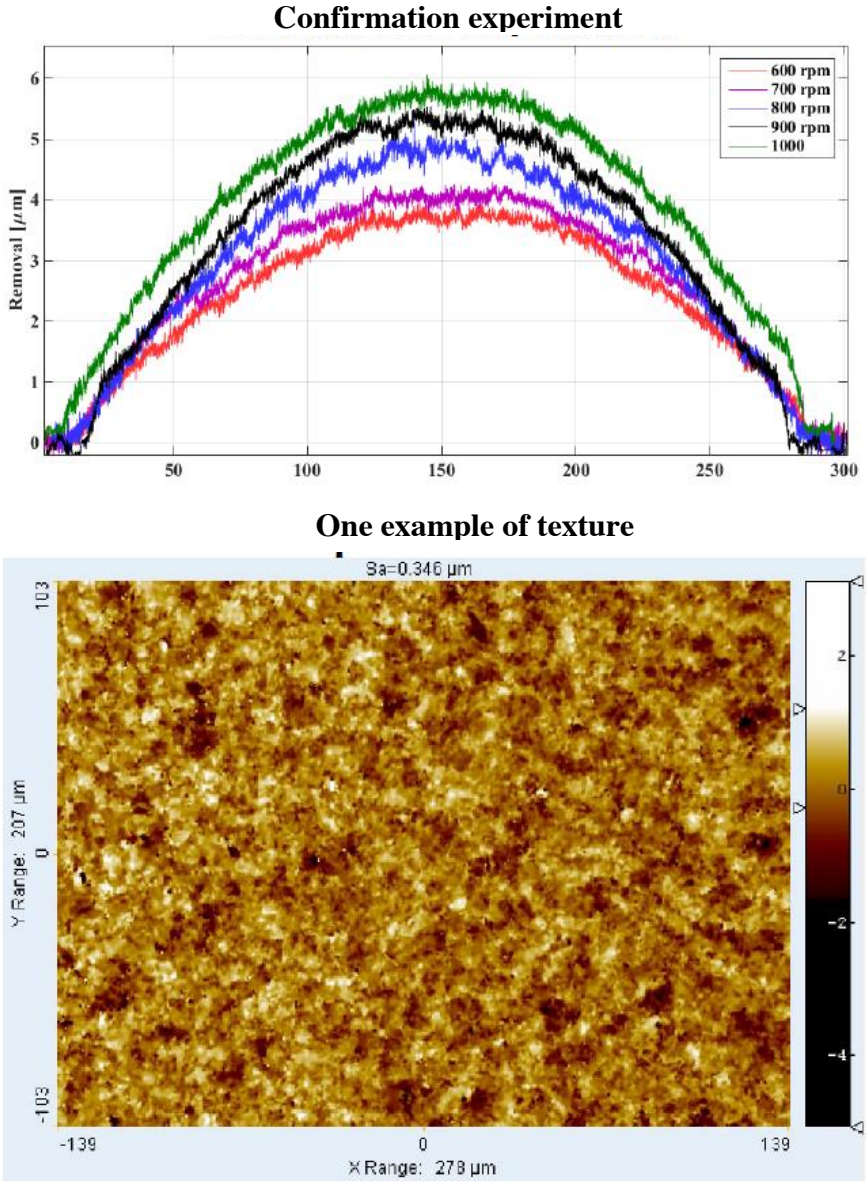

Figure 4-13: Confirmation experiment for the regression result

Table 4-7: Comparison of the predicted data (Equation 4-1) and experimental data

Spindle speed [rpm]	600	700	800	900	1000
	VRR [mm^3/min]				
Predicted from Equation (4-1)	29.2	33.6	38.0	42.4	46.4
Experiments	29.7	32.9	38.5	43.2	46.0
Error (%)	1.5	-2.1	1.3	2.0	-0.8
	Texture [S_a, nm]				
Predicted from Equation (4-2)	351.4	349	346.6	344.2	341.8
Experiments	347.2	353.3	348.3	349.2	346.5
Error (%)	-1.2	1.2	0.5	1.5	1.4

4.5.2 Edge control

There are two objectives in this section. Firstly, as demonstrated in Section 4.5.1, load, abrasive size and spindle speed were the significant variables for the control of VRR, and also appear to be a significant influence on edges. In order to verify this point of view, these three variables must be studied. Secondly, it is known that OH is a significant variable, and therefore the next step is to determine the optimised OH value.

As shown in Figure 4-14, when using a parallel raster tool path, a tool travels with a constant speed at the edge but it experiences acceleration and deceleration at the corner, resulting in a variation in the values between edges and corners (one obvious example is shown in Figure 4-20: OH 10.1 mm). In order to examine this effect, two measurements were conducted: edge-to-edge (EF, constant speed) and corner-to-corner (CD, deceleration and then acceleration), as shown in Figure 4-15.

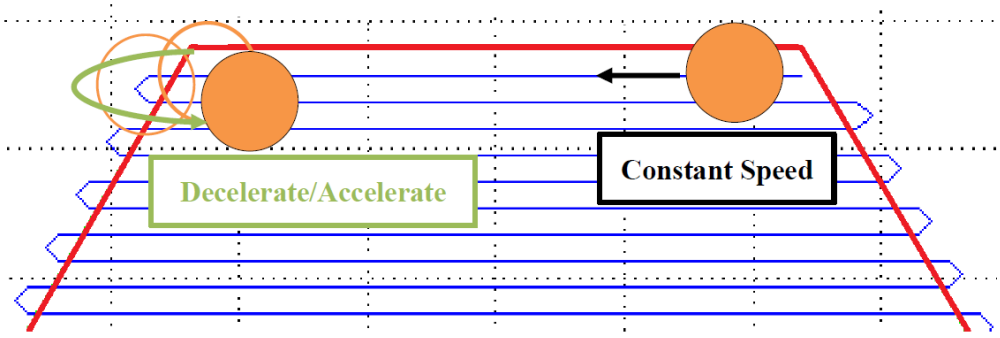

Figure 4-14: The tool speed is varied at the edge but constant at the central

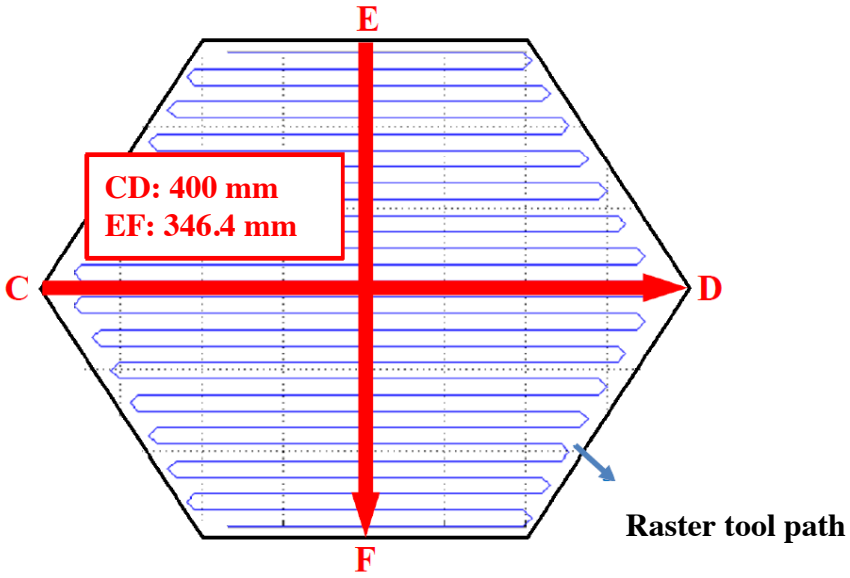

Figure 4-15: Two perpendicular measurements (corner-corner and edge-edge)

4.5.2.1 Experiment 1: testing abrasive sizes, spindle speeds and loads

As shown in Table 4-8, three levels were selected in order to test each of these variables in more detail than the two-level screening experiment in Section 4.4. In order to evaluate significant variables, the edges were normalised (rescaling the depth to achieve a comparison basis), as shown in Figure 4-16, Figure 4-17 and Figure 4-18. The experiments demonstrated that abrasive size, spindle speed and load were insignificant variables, confirming the conclusion in Table 4-4.

Table 4-8: Testing variables and controlled variables

Testing Variables			
Abrasive size	9μm	15μm	20μm
Spindle Speed	600rpm	800rpm	1000rpm
Load	1000g	1175g	1350g

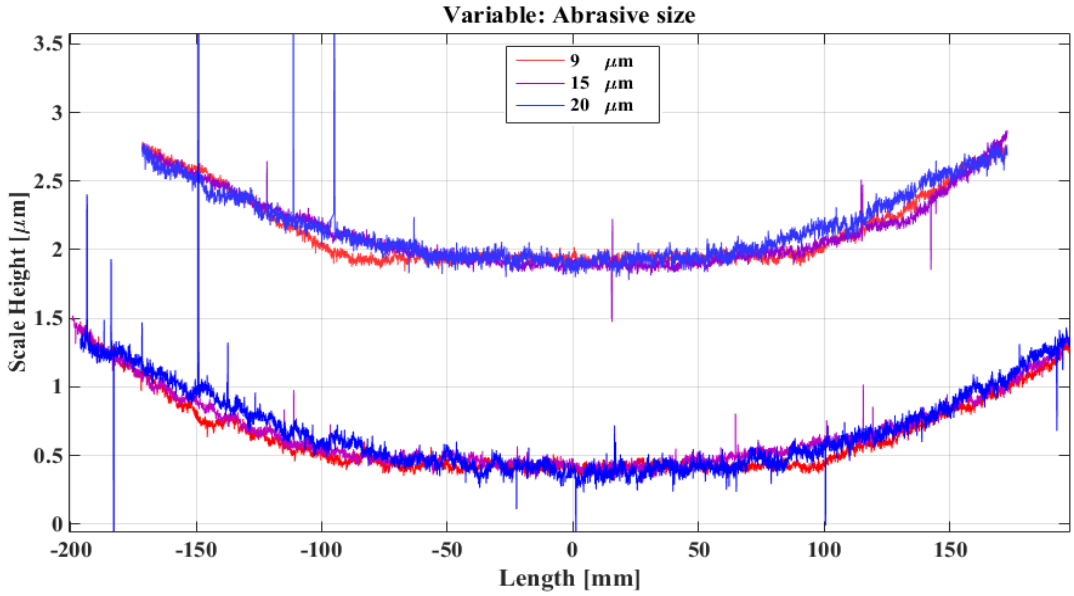

Figure 4-16: Testing variables: abrasive (Load =1175 g, Spindle speed=600 rpm)

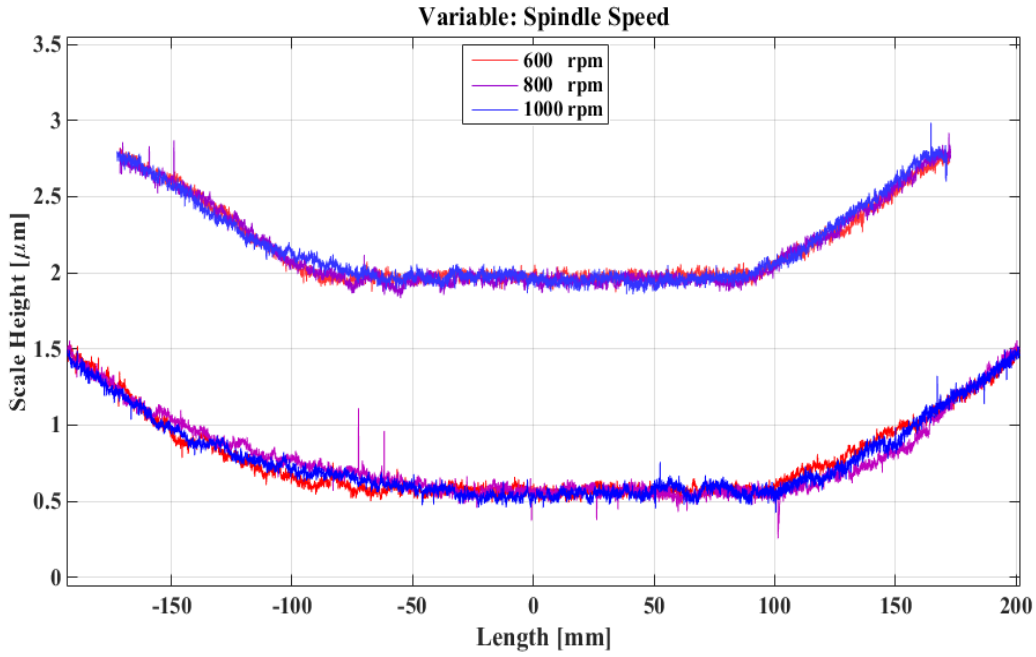

Figure 4-17: Testing variables: Spindle speed (Load=1175 g, abrasive size=9 µm)

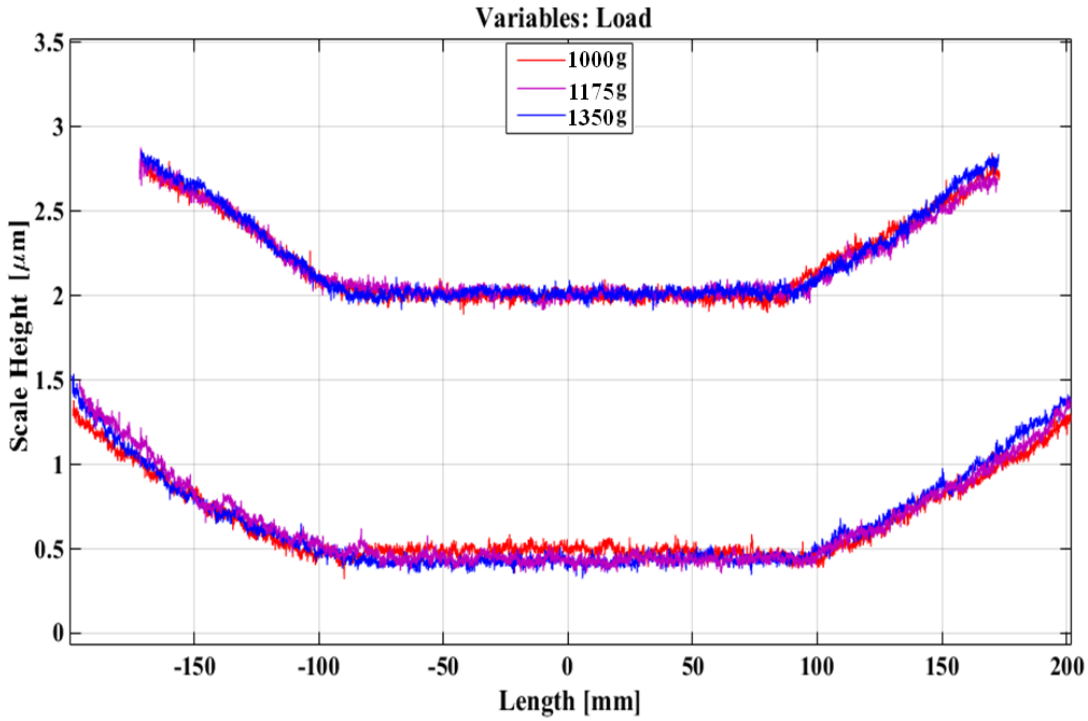

Figure 4-18: Testing variables: load (Spindle speed=600 rpm, abrasive size = 9 μm)

Since abrasive size, spindle speed and load were insignificant variables, they must be controlled to optimise the only potentially significant variable: OH. The abrasive size was set at 9 μm because this size was able to achieve the required VRR, texture, edge and MSF, as shown in Table 4-1. The spindle speed and loads were set as 800 rpm and 1175 g because of the optimization result from VRR and MSF (as will be discussed in Section 4.6).

Five different levels (9.6 mm, 11.6 mm 13.6 mm 15.6 mm and 17.5 mm) were then chosen to examine the best OH to control the edge. The results are shown in Figure 4-19.

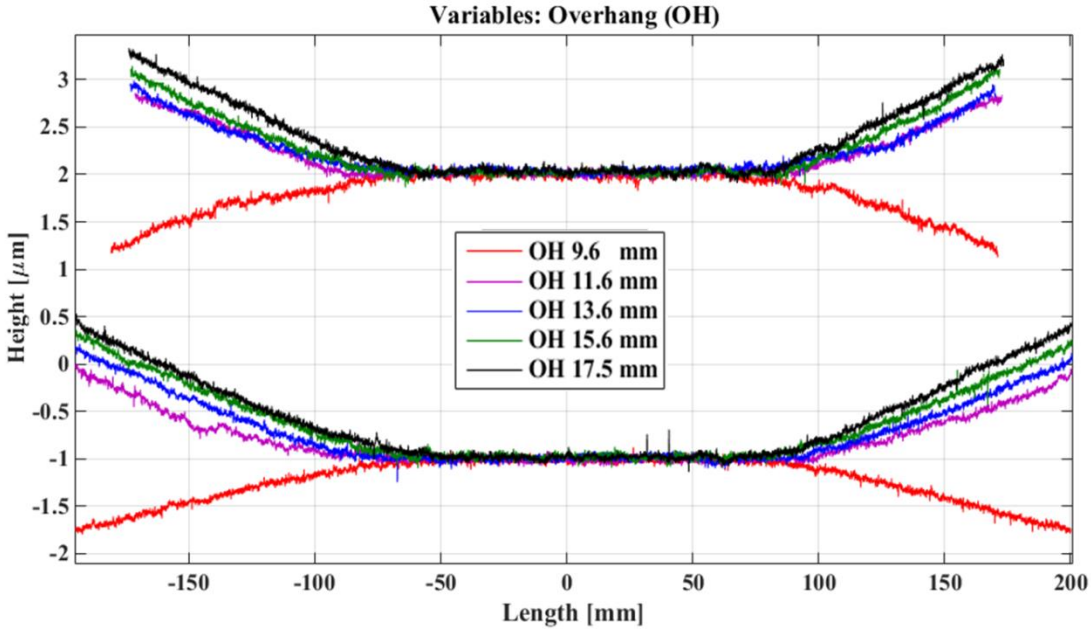

Figure 4-19: Testing OH

It can be seen that there is a huge gap between an OH of 11.6 mm and 9.6 mm, and this space is probably a critical region. In order to further evaluate this region, another experiment was conducted. The problem is that the 2 mm track space fixes the tool path. The proposed solution was to move the segment to the required OH value: 11.6 mm, 11.1 mm, 10.6 mm 10.1 mm and 9.6 mm.

The results for this are shown in Figure 4-20, and demonstrate that a critical region from an edge up-stand to a sudden down turn did indeed exist between 9.6 mm and 11.6 mm. From Figure 4-19 and Figure 4-20, the optimised OH was, therefore, 11.6 mm.

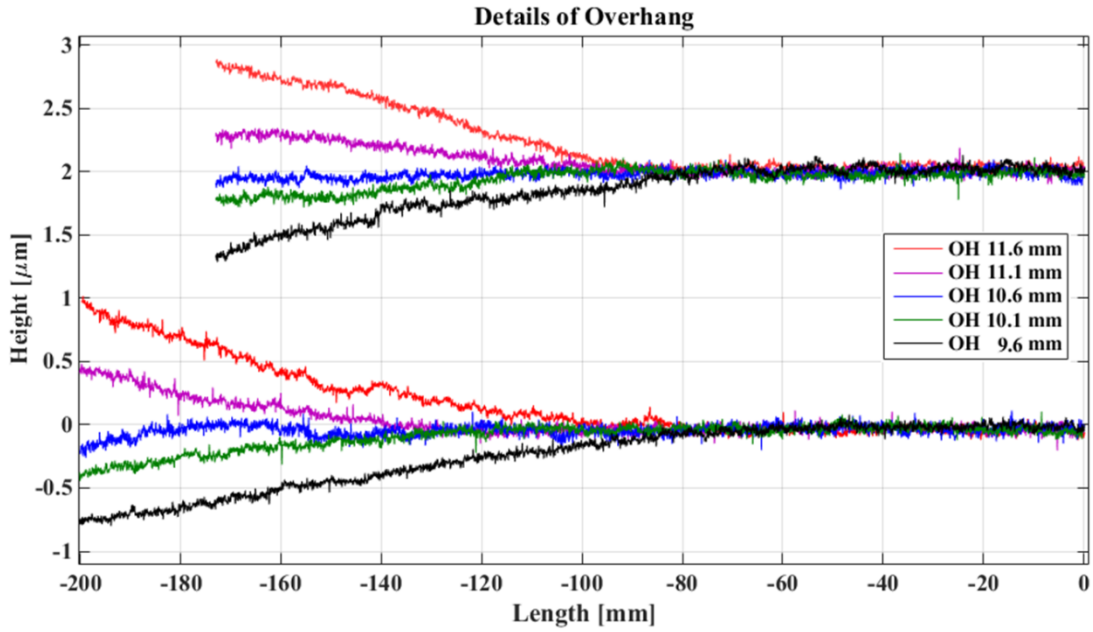

Figure 4-20: Further investigation of OH

4.5.3 Mid-spatial frequency (MSF)

The aim of this section is to investigate how to achieve an MSF amplitude below the specification (PV < 40 nm) in one grolishing run (5.9 µm > removal depth > 3.7 µm, as shown in Figure 4-13). Since abrasive size and track space overwhelm the remaining significant variables (load and spindle speed), a 9 µm abrasive and 2 mm track space was determined to minimise MSF amplitudes. Another reason for choosing the 9 µm abrasive was because this size was able to achieve the required VRR, texture and edges (as fully discussed in Section 4.5.1 and Section 4.5.2).

Although it is obvious that lower spindle speeds and loads can achieve shallower MSF amplitudes, it was still necessary to conduct another experiment to balance the

MSF with VRR in order to consider the overall process efficiency (details will be discussed in Section 4.6). For this reason, an evaluation of the load, spindle speed and tool feed values that can control removal depth or MSF amplitudes were required.

Three levels were determined in order to check the linearity of each variable. Taguchi's experimental design (L9) was used to reduce the total of 27 trials to 9. The experimental design and ANOVA are shown in Table 4-9 and Table 4-10, respectively.

Table 4-9: Investigation of variables to reduce removal depth

Trial	S [rpm]	Feed [mm/min]	Load [g]	PV MSF [nm]	
1	1000	1500	1000	80.3	82.5
2	1000	3000	1175	57.1	58.9
3	1000	4500	1350	44.1	43.7
4	800	1500	1175	73.8	74.5
5	800	3000	1350	58.4	55.4
6	800	4500	1000	22.4	21.0
7	600	1500	1350	65.7	66.1
8	600	3000	1000	37.2	35.7
9	600	4500	1175	0.0*	0.0*

Table 4-10: ANOVA for Table 4-9

	dof	SS	V	F	P
S	2	2228.1	1114.0	124.01	0.000
Feed	2	8123.6	4061.8	452.16	0.000
L	2	441.2	200.6	24.56	0.000
error	11	98.8	9.0		
Total	17	10891.8			

The result is reasonable since it shows that decreasing removal depth can achieve lower MSF amplitudes. Moreover, it can be observed that the MSF amplitude in trial 9 could be measured but recorded as zero, as shown in Figure 4-21. When considering the other results, however, it seems unlikely that the MSF amplitude in trial 9 was indeed zero. One possible reason for this apparent discrepancy is that the MSF amplitude could not be detected because the value was out of the measuring range. Alternatively, it could be that the MSF signal was too low and was thus immersed in the background noises. Hence, when the MSF amplitude becomes small and close to the diffraction limit, continuing to attempt to remove MSF can increase the overall processing time and add unnecessary cost. This conclusion again indicates the requirement to define the MSF tolerance, as in Table 4-1.

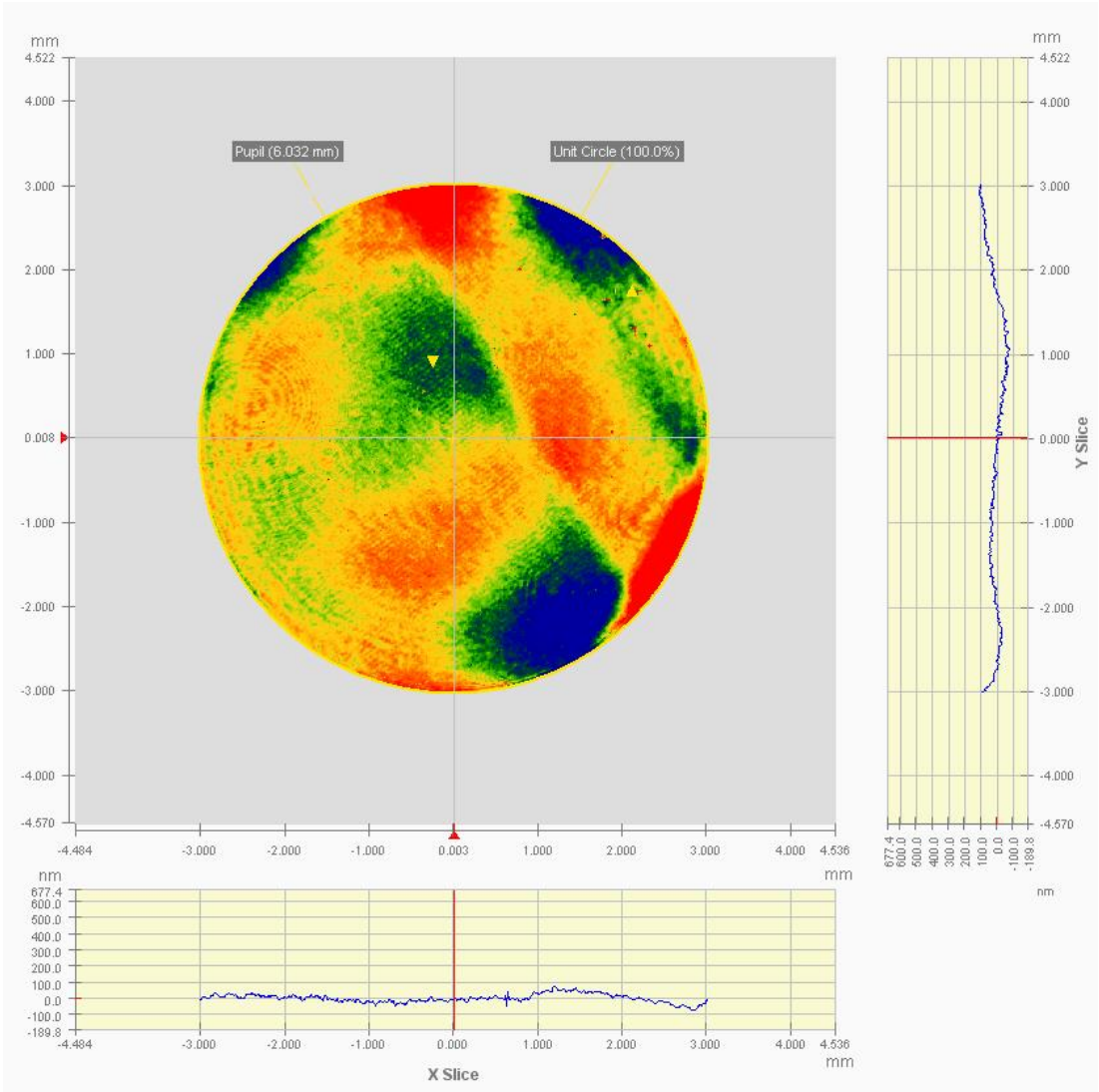

Figure 4-21: Data in the Trial 9 – low MSF amplitude

Since the three variables (spindle speed, tool feed and load) were significant variables, and the ANOVA showed that up to 99.7% of the variation in the data could be explained by this analysis, the next step was to use the regression analysis to interpret the results, yielding:

$$\mathrm{MSF} = 16.3 + 0.0675 \times \mathrm{S} - 0.0173 \times \mathrm{Feed} + 0.0259 \times \mathrm{L} \qquad \textbf{(4-3)}$$

where 600 < S < 1000, 1500 < Feed < 4500, 1000 < L < 1350

4.5.3.1 Summary

The significant variables of VRR, texture, edge and MSF were fully investigated. Each response demonstrated that the specification defined in Table 4-1 was achievable, and the resolution spaces for the five responses are thus summarised in Table 4-11. The next step was to balance these responses in order to achieve the overall optimised conditions for the grolishing process.

Table 4-11: Summary of each response

	Significant variables
VRR	$\text{VRR} = -16.7 + 2.84 \times \text{AS} - 0.0181 \times \text{L} + 0.0113 \times \text{S} + 0.00122 \times \text{AS} \times \text{L} + 0.000025\ \text{L} \times \text{S} + 0.00000017\ \text{A} \times \text{L} \times \text{S}$
Texture	$\text{Texture} = -7.34 + 34.8 \times \text{AS} + 0.133 \times \text{L} + 0.191 \times \text{S} - 0.00444 \times \text{AS} \times \text{L} - 0.00385\ \text{AS} \times \text{S} - 0.000134 \times \text{L} \times \text{S}$
Edge	OH = 11.6 mm
MSF	$\text{MSF} = 16.3 + 0.0675 \times \text{S} - 0.0173 \times \text{Feed} + 0.0259 \times \text{L}$
9 < AS < 20, 1000 < L < 1350, 600 < S < 1000, 1500 < Feed < 4500	
Controlled variables	
1:3 slurry density	2 mm Track Space

4.6 Optimisation

The objective of this section is to establish the RGP in the processing chain between grinding and polishing. In order to achieve this goal, the five responses (VRR, texture, surface accuracy, edge and MSF) were examined so as to demonstrate that the RGP was able to achieve the specification in Table 4-1. Moreover, the repeatability had to be more than 95% to show that the RGP is a robust process.

4.6.1 Determine values for each significant variable

The primary task in terms of evaluating the optimised result was to determine a set of optimised parameters. In order to simplify the problem, some significant variables that can affect the response were decided at the beginning. As shown in Table 4-11, (1) an 11.6 mm OH was set because this was the only significant variable to control the edge. (2) A 4500 mm/min tool feed and a 2 mm track space were selected because these values can control MSF amplitude in one grolishing run. (3) A 9 μm abrasive was chosen so that the grolished grey surface could be polished into a shiny one in a single polishing run in order to achieve the VRR requirement (VRR>16.9 mm^3/min).

As shown in Figure 4-22, the resolution spaces for Equation (4-1) and Equation (4-3) can be plotted to help to determine spindle speed and load values.

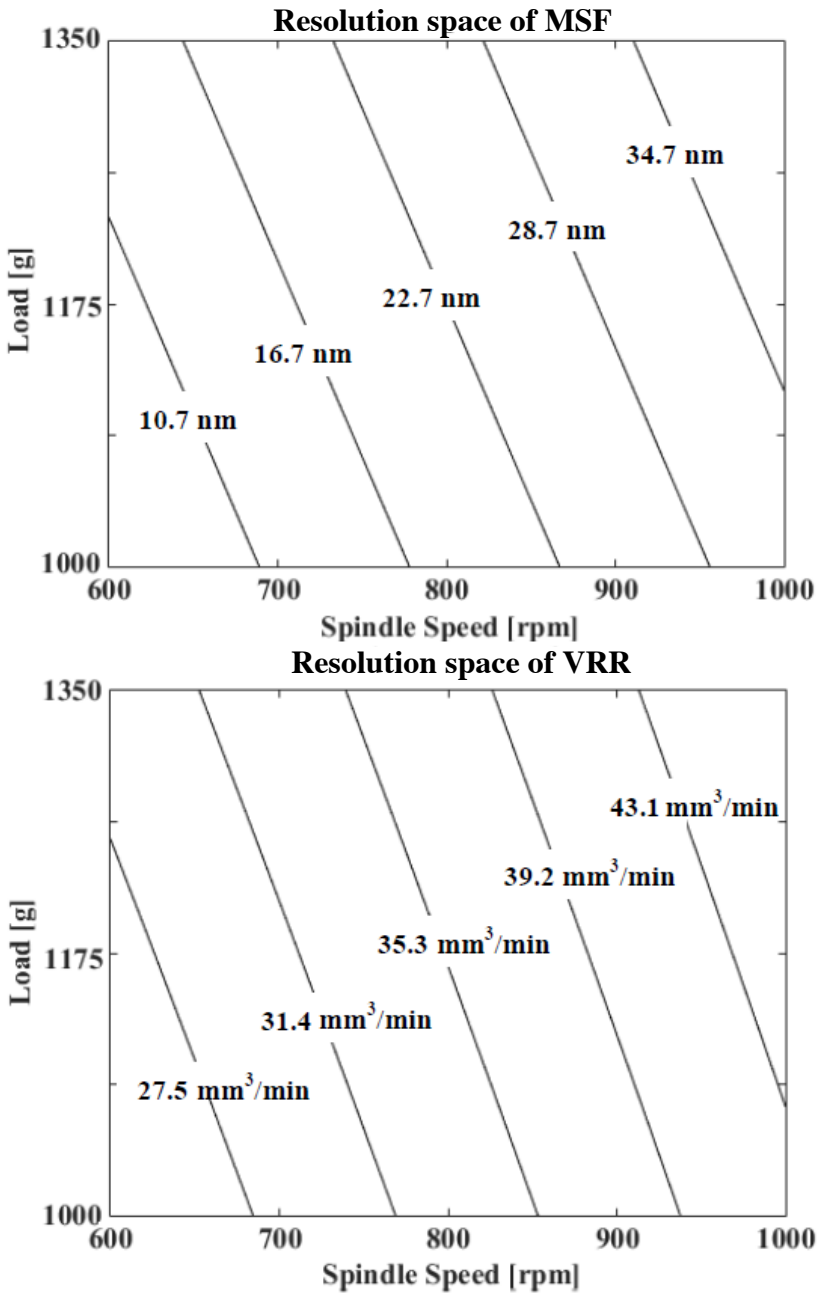

Figure 4-22: Resolution spaces of MSF and VRR respectively

One way to balance MSF and VRR is to choose the middle level of the two significant variables (i.e. 800 rpm and 1175 g). From this, all the values for

optimised variables were determined and summarised in Table 4-12. The next step was to evaluate the repeatability.

Table 4-12: Controlled variables for optimisation

Controlled variables		
1135 g load	4500 mm/min feed	800 rpm spindle speed
9 μm abrasive	2 mm track space	1:3 slurry density

4.6.2 Discussion

This section examines the repeatability of the optimised parameters shown in Table 4-12. Five repeat experiments were conducted to evaluate each response, with errors needing to be kept to less than 5% in order to demonstrate that the RGP is a robust process.

The results are shown in Figure 4-23, Figure 4-24, Figure 4-25, Figure 4-26 and Figure 4-27. Statistics for the experiments are summarised in Table 4-13. Repeatability for all responses was higher than 95.88%, indicating that the process is robust and can process uniform outputs.

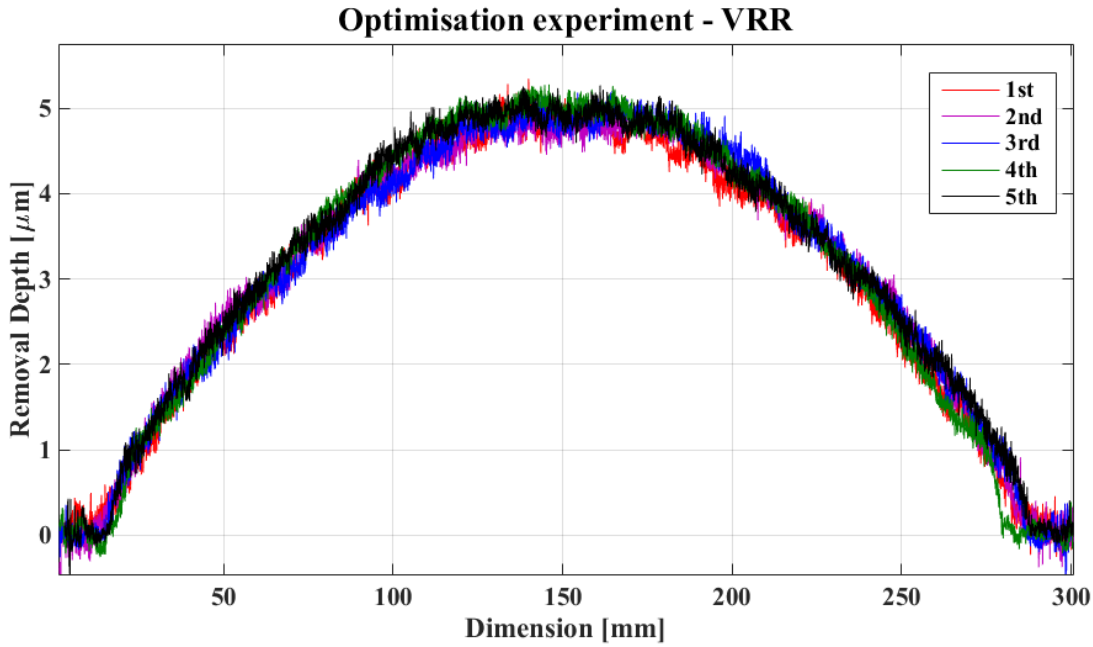

Figure 4-23: Optimisation experiment-VRR

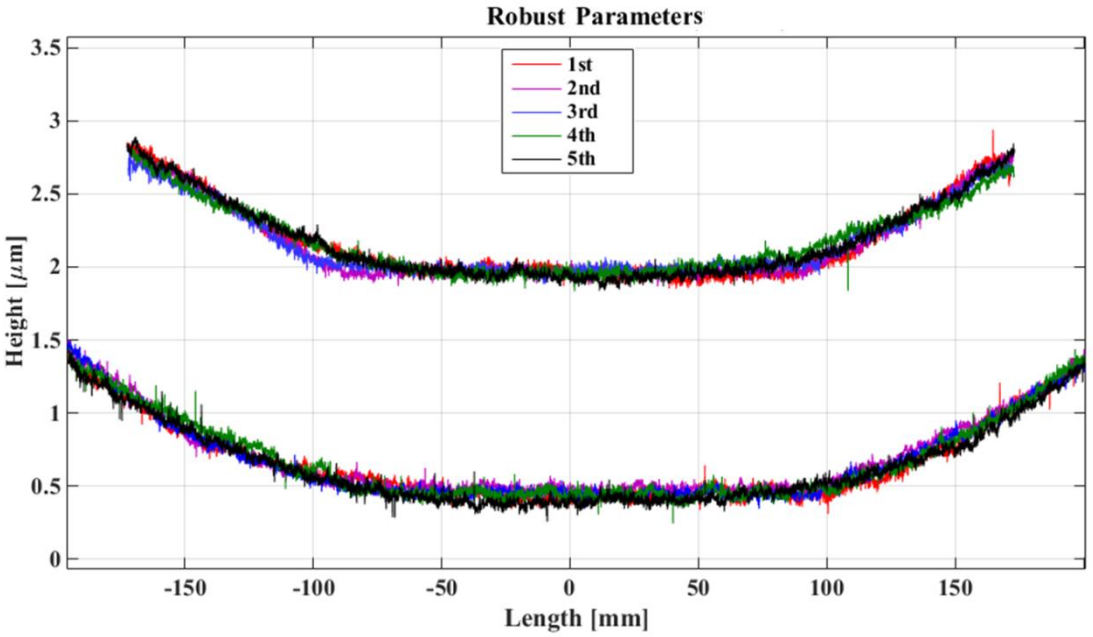

Figure 4-24: Optimisation experiment: Edge and surface accuracy

One example of 2D image

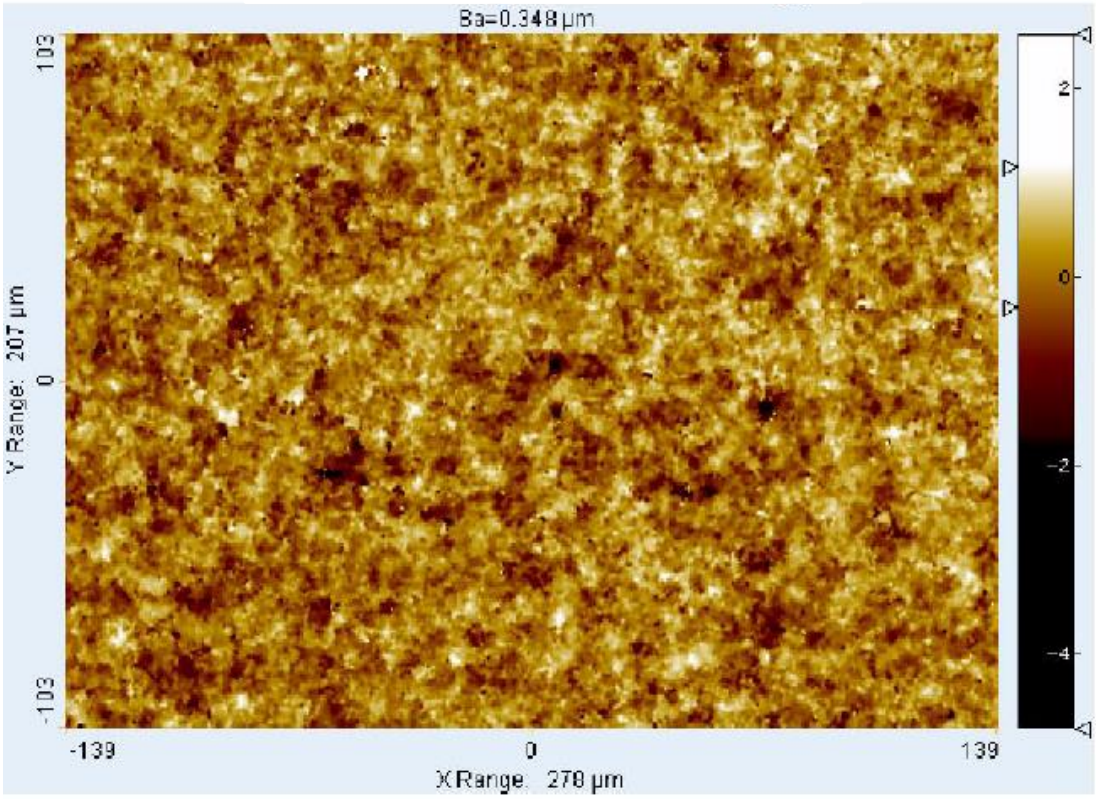

The example of 3D image

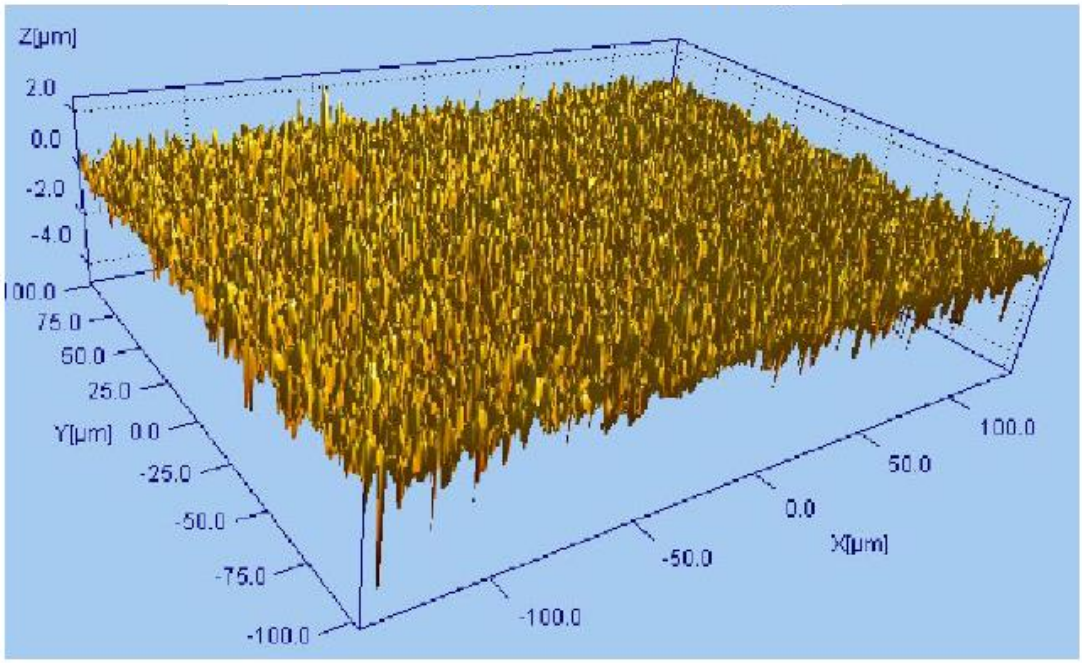

Figure 4-25: Optimisation experiment: one example of texture (S_a = 353.5 nm)

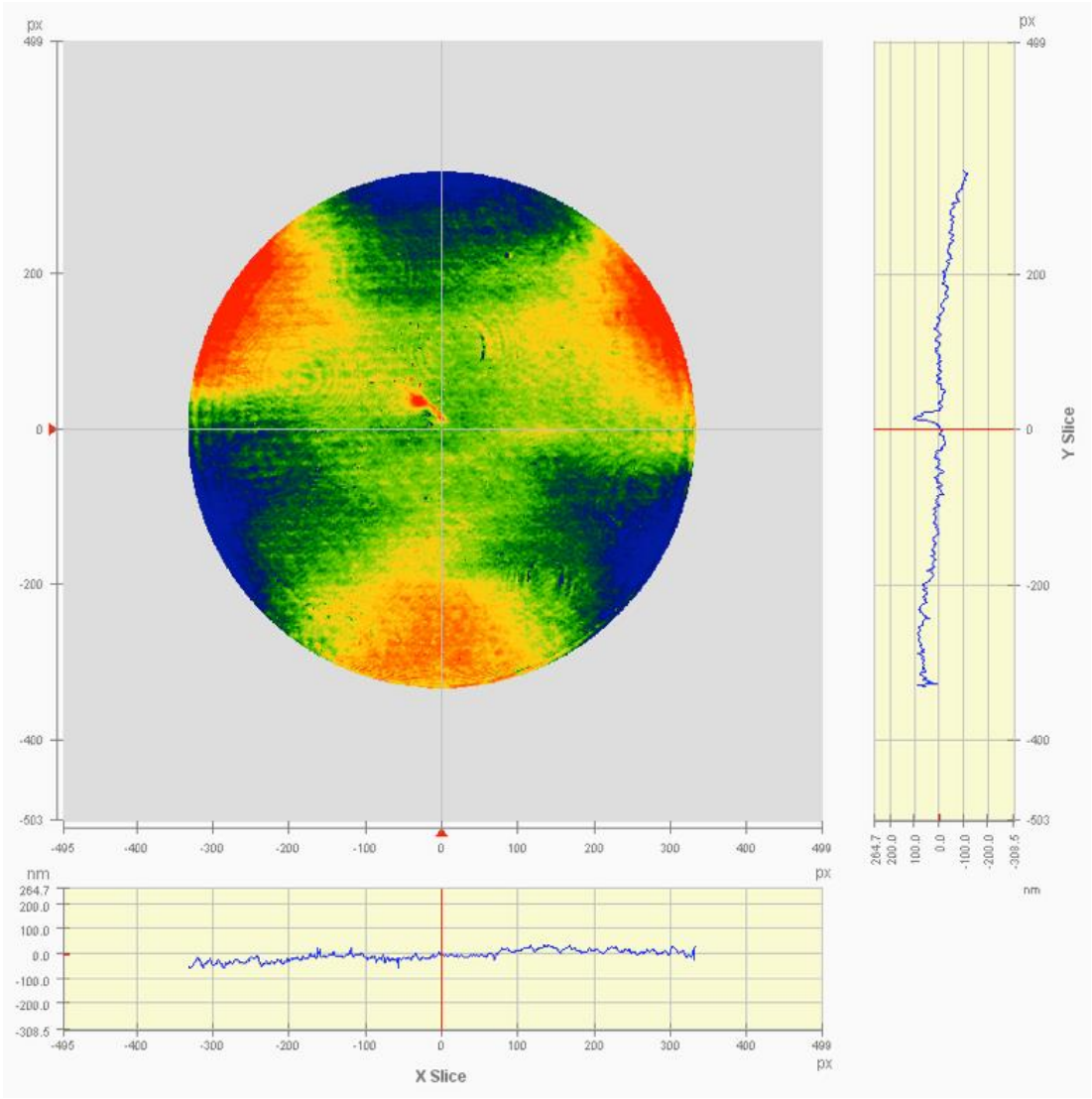

Figure 4-26: One example of optimised MSF (PV = 25.7 nm)

Table 4-13: Optimisation experiment-statistics for each response

	1st	2nd	3rd	4th	5th	Average	Error(%)
VRR [mm^3/min]	36.7	37.5	37.4	37.9	38.8	37.4	4.12%
Texture [nm]	349.7	351.1	347.5	349	353.5	348.5	1.67%
PV Edge (EF) [µm]	0.79	0.77	0.77	0.78	0.8	0.78	3.35%
PV Corner (CD) [µm]	0.81	0.8	0.82	0.79	0.79	0.81	3.51%
PV Bulk area [µm]	0.33	0.33	0.34	0.33	0.34	0.33	3.28%
MSF [nm]	24.4	24.7	25.2	24.9	25.7	24.4	4.00%

4.6.3 Error maps for the subsequent polishing process

This section further discusses the method to connect the grolishing and polishing processes. Since a grolished grey surface cannot be measured using an interferometer, the original method at OpTIC has been to remove a layer of about 1~2 μm of material by polishing (called the pre-polishing process) so as to produce a specular surface. This section aims to improve on this method.

In order to increase overall efficiency, Zeeko^{TM} Metrology software was used to stitch grolished measurements into a surface topography map (namely an error map). Based on the map, the following corrective polishing was able to replace the original pre-polishing process to improve a surface, resulting in the speeding up of the polishing process. Figure 4-27 is an example of stitching a grolished surface from the 400 mm hexagonal segment. Another advantage of using this software was that the PV = 0.81 μm and RMS = 0.17 μm (using the fifth experimental grolished surfaces in Figure 4-24 and Table 4-13) for this grolished surface can be calculated automatically.

Figure 4-27: Error maps from a grolished surface

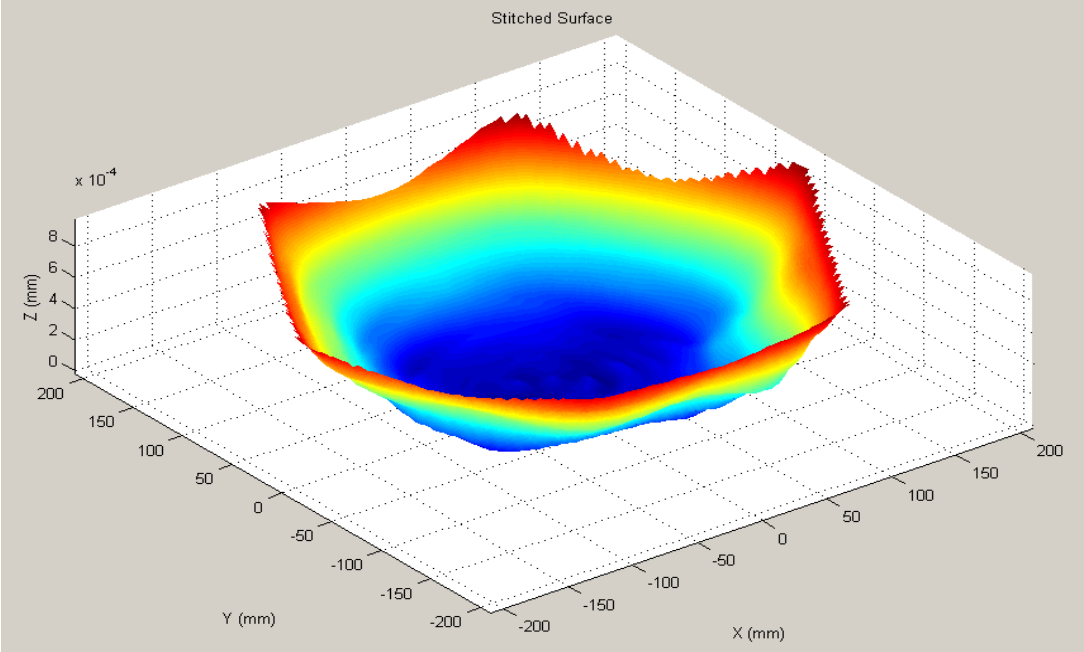

4.7 Summary

The RGP has been successfully established in this chapter. The specification for the RGP was defined and the five responses (volumetric removal rate, surface texture, surface accuracy, edge and mid-spatial frequency) were combined to achieve the requirement.

Moreover, the ultimate objective for the RGP is to participate in artificial intelligent manufacturing processes, so that a surface can be fabricated automatically across the stages of designing, manufacturing and measuring in order to speed up the process. In this regard, resolution spaces for each response were successfully built, indicating that each response can be used to build a data cloud so that any AI machines can choose optimised parameters automatically so as to realise the RGP.

Chapter 5 Robotic grolishing process for metre-scale segments

5.1 Introduction

In the previous chapter, the RGP was defined, using a 100 mm diameter tool on 400 mm borosilicate hexagonal segments. To increase the production efficiency on workpieces larger than 1 m diameter, the tool was increased to a diameter of 280 mm (as discussed in Section 5.2).

The challenges inherent in grolishing metre-scale workpieces include: investigations of (1) pad wear effects, (2) tooling marks (i.e. MSF), (3) removals, and (4) VRR from the RGP across the 1 m segment.

In respect to the first of these, a series of experiments was conducted to explore the pad wear effects, in which the pad conditions are explained by theoretical models (Section 5.3). It must first be demonstrated, however, that MSF can be removed by using the 280 mm tool, and that therefore this grolishing process can participate in the processing chain to manufacture metre-scale surfaces (Section 5.4).

The next task is to calculate the VRR for the process (Section 5.5). In order to achieve accurate measurement, a prototype metrology must be developed, including: (1) evaluation of the accuracy of the measurement, (2) development of high-speed metrology, (3) reconstruction of a 3D removal surface, and (4) calculation of the VRR from the 3D surface.

The modelling, manufacturing and measuring methodology establish a process for large tool processing for metre-scale optics. This metrology will be fundamental to non-destructive testing and non-contact measurement systems for metre-scale optics in the near future.

5.2 Tooling design and mechanism

Based on the experience of using a 100 mm tool in Chapter 4, the 280 mm tool was created as shown in Figure 5-1. The structure has been fully discussed in Chapter 4. This section, therefore, focuses on discussing the improvements.

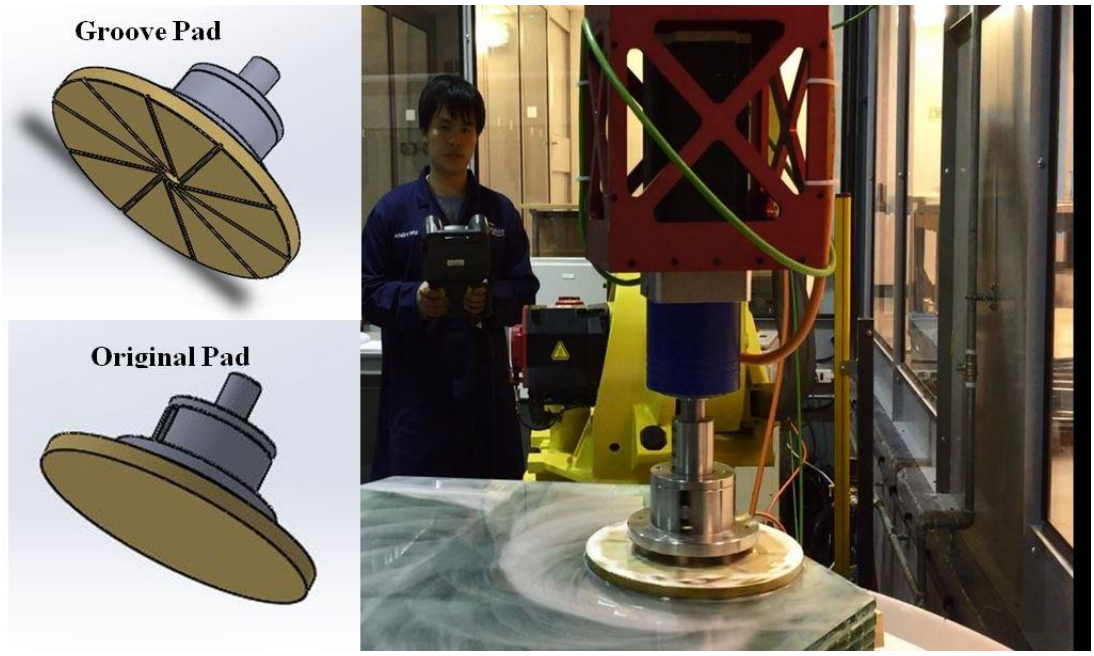

Figure 5-1: The prototype tooling and 280 mm hard brass pad (original and groove pads)

One significant difference between the tools was that whereas the small tool (1.3 kg) was used for high speed modes (600~100 rpm) the large tool (13.5 kg) was used for low speed modes (0~260 rpm). The 280 mm diameter tool was driven by the motor

and gearbox of the ABB spindle with a spindle torque of 95 Nm carried by a Fanuc R-2000IB robot. The reduction gearbox of the spindle is 10:1, and the maximum spindle speed for the whole setup was 260 rpm.

The next step was to consider pad structures (i.e. groove patterns). By comparing four different groove types (non-groove, grid-groove, annual-groove and radial-groove pads) modelling suggests that a non-groove pad was appropriate for low spindle speeds and a radial-groove pad was optimised for high spindle speeds [227]. In order to investigate which pattern provided the better surface finish, two pads with the required patterns were produced. The original pad was a pure flat brass disc, processed into intimate contact to achieve the grolishing process. When in operation, the slurry is supplied at the periphery. The modified groove pad had a 20 mm diameter central hole and radial grooves. The slurry was delivered through the central hole and spread radially to the edge.

5.3 The pad-wear effect

During the grolishing process, a pad may contribute to the generation of micrometre scale asperities, which affect accuracy, MSF, texture and other performance aspects. Since a pad surface is an important factor determining outputs, the fundamental characteristics of the two pads are investigated to optimise parameters for grolishing the 1 m part.

5.3.1 Experimental preparations

Prior to the wear experiment, the pad surface was conditioned to PV = 10±1 μm convex surfaces through smoothing (introduced in Chapter 4), following by a 30 minute match processing between the tool and the 1 m segment. After that, the experimental grolishing commenced.

The next objective was to determine optimised spindle speeds for two pads respectively. Excessive spindle speed potentially induces dangerous conditions, such as premature tool wear, breakages and tool chatter. Using the correct spindle speed greatly improves the tool life and surface quality.

The grolishing parameters are presented in Table 5-1, and the spindle speeds were the only variables in this pad wear experiment. To measure the pad wear, three grolishing runs were conducted in an experiment. Two successive experiments constitute one experiment trial. Hence, the total processing time for a trial was 90 minutes.

Table 5-1: Parameters for optimised spindle speeds

Testing variables			
Spindle Speed	0~120 rpm		
Controlled variables			
Tool Speed	6000 mm/min	**Tool Path**	Raster
Part	1 m hexagon	**Part material**	Float glass
Load	135 N	**Tool**	280 mm dia. Brass
Abrasive	20 μm Al_2O_3	**Slurry Density**	1 abrasive: 3 water
Processing time	30 min	**Track Spacing**	10 mm

5.3.2 Discussion

Figure 5-2 shows the wear on each of the two pads at the five different spindle speeds. For the original pad, 20 rpm was the optimised spindle speed to ensure a uniform pad-wear. The 30 rpm spindle speed introduced pad irregularity, and the 80 rpm speed showed undesirable sharp features. In contrast, the grooved pad allowed an optimised spindle speed that is a factor of 3.5 times faster than the original pad, indicating that it has higher removal efficiency than the original pad.

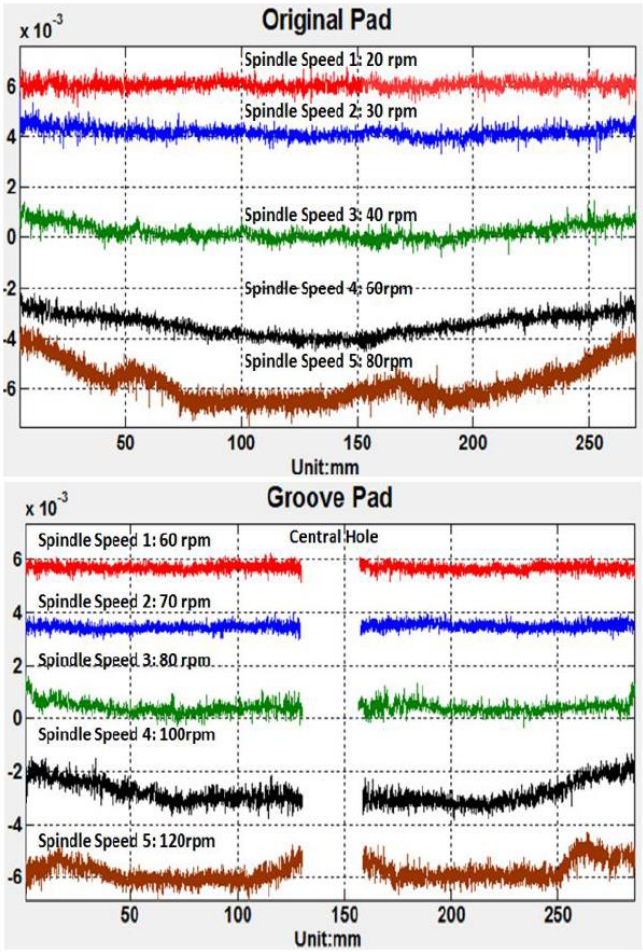

Figure 5-2: Testing optimised spindle speed. Each data was offset for comparisons.

Moreover, the pad wears in Figure 5-2 are reasonable. When the spindle speed was slow, pad wear was caused by the tool travel feed. As the spindle speed increased, however, the outer radius had a higher speed, resulting in a higher pad wear. When using the "high spindle speed modes" (e.g. 80 rpm for the original pad and 120 rpm for the grooved pad), the tool structure and slurry migration determined the pad-wear outcomes, as discussed in Section 5.3.2.1.

5.3.2.1 High spindle speed modes

In order to explain the "high speed mode", it is necessary to introduce a pad wear function (PWF), defined by:

$$\mathrm{PWF} = \mathrm{K} \times \mathrm{P} \times \mathrm{V} + \epsilon, \ (\mathrm{V} = \mathrm{R} \times \omega) \tag{5-1}$$

where K is a constant (determined by abrasive size, tool travel feed, slurry density, pad and workpiece material), P is pressure (determined by tool load and structure), V is velocity (determined by R radius and ω angular speed (i.e. spindle speed)), and ϵ is errors (determined by measurement, users and environments). This K constant can be temporary omitted to simplify the problem, however. V, meanwhile, represents known variables, and the errors are assumed to be zero for ideal conditions.

The challenge was to determine P, which can be derived from the pressure distributions of the tool structure. This can be achieved by using a finite element method (FEM). The FEM was calculated using ANSYS software in order to investigate the pressure distribution between the tool and the workpiece so as to understand pad wear in the high speed modes. The results for the two pads are shown in the top row of Figure 5-3.

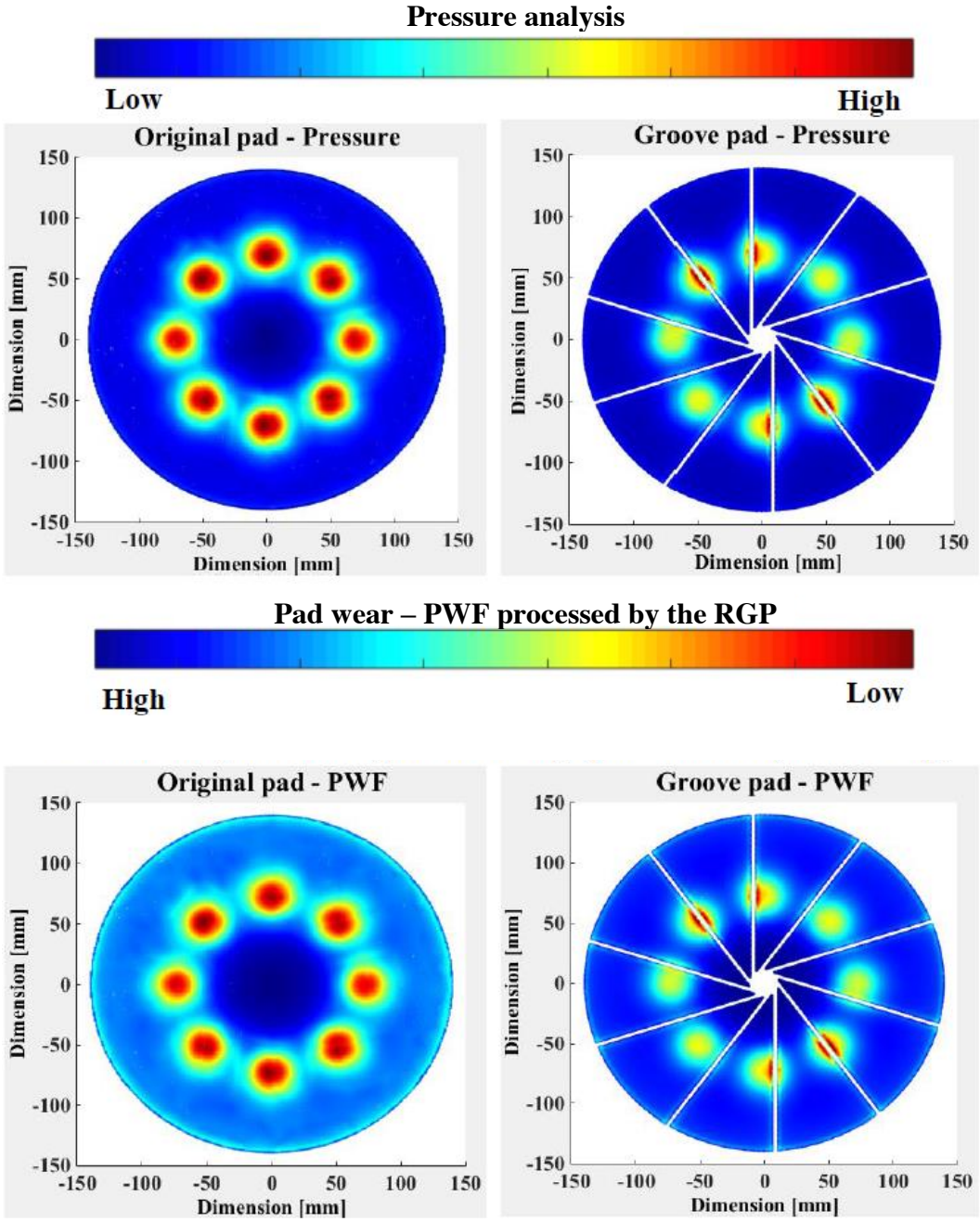

Figure 5-3: Pressure distributions (top) and PWF results (bottom): slurry migrates to the high pressure with difficulty

The figure shows that pressure distributions can reflect the tool structure, indicating that the models are correct. In order to discuss the pad wear in high speed mode, the PWFs in the bottom part of Figure 5-3 have to be studied. For the original pad, the

wear was low at the high pressure zone (i.e. the eight supporting areas), but these prevented most of the slurry migrating into the centre zone, resulting in more pad wear occurring at the edge zone and less wear at the pressure and centre zones (Figure 5-4). This argument fully explains the wear on the original pad when the 80 rpm spindle speed was used, as in the bottom left of Figure 5-2.

For the grooved pad, the slurry was supplied through the centre hole and spread to the edge through the 120 mm spindle speed and 4500 mm/min tool travel feed. Although the pressure zone disturbed the migration of slurry, the slurry could still pass through the groove to the edge zone to cause pad wear, as shown in Figure 5-4.

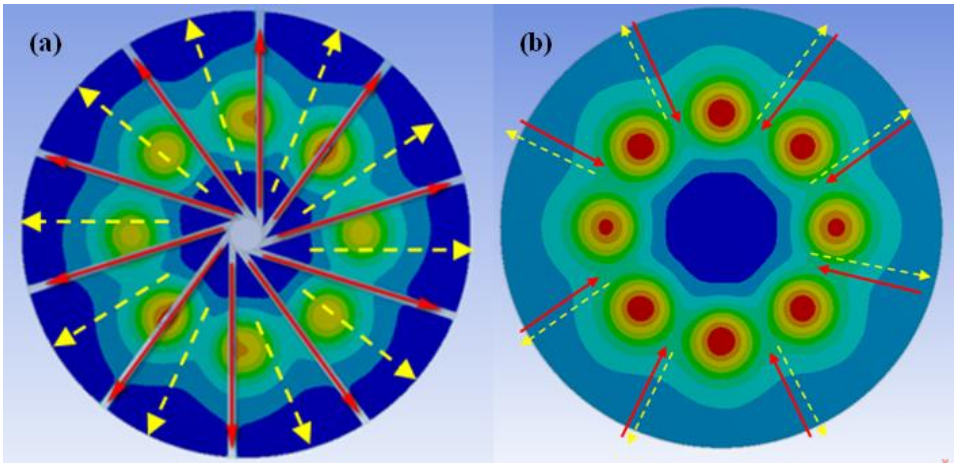

Figure 5-4: Slurry migration for (a) groove pad and (b) original pad. Red arrows are slurry supplied and yellow arrows are slurry migration between the pad and the surface.

In order to explain the wear on the grooved pad more comprehensively, the pressure zone was removed and reanalysed, as shown in Figure 5-5. In this figure, the pressure distribution is similar for the centre and edge zones, which confirms the results in the top right corner of Figure 5-3. When applying the 120 rpm spindle

speed, this model shows that the pad wear was higher at the edge than in the centre. Moreover, in the central zone, the removal was higher than in peripheral areas because higher abrasive density would cause greater pad wear. This explained the result of grooved pad used with a 120 rpm spindle speed (bottom of Figure 5-2).

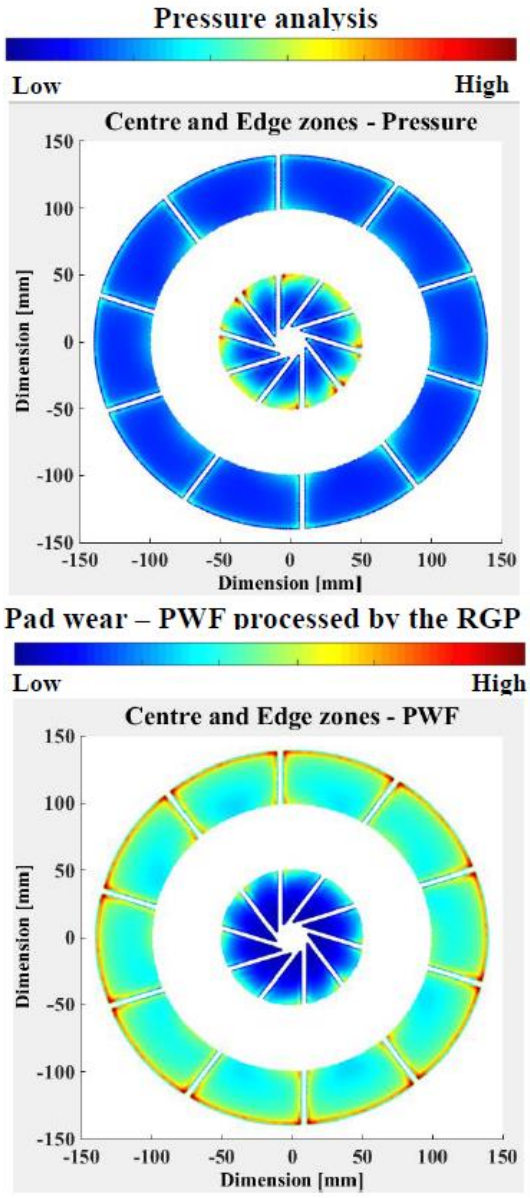

Figure 5-5: Further investigation of the groove pad

5.3.3 Pad conditions

The following task was to evaluate the stability of the two pads. Using a diamond file, the created grooves were measured to calculate accumulated wear amounts. Each trial was processed for 90 minutes and the results are shown in Figure 5-6. The groove pad applied a 70 rpm spindle speed and produced 0.407 ± 0.003 g pad wear per experiment (calculated by a brass density of 8400 kg/m^3). Supposing pad wear of 2% could affect the output (the assumption is based on the VRR model in Chapter 4), it would be expected that the pad could continue grolishing for 14 days without the need to correct the pad surface. With this assumption, there would be enough time to perform 2100 runs using the parameters in Table 5-1.

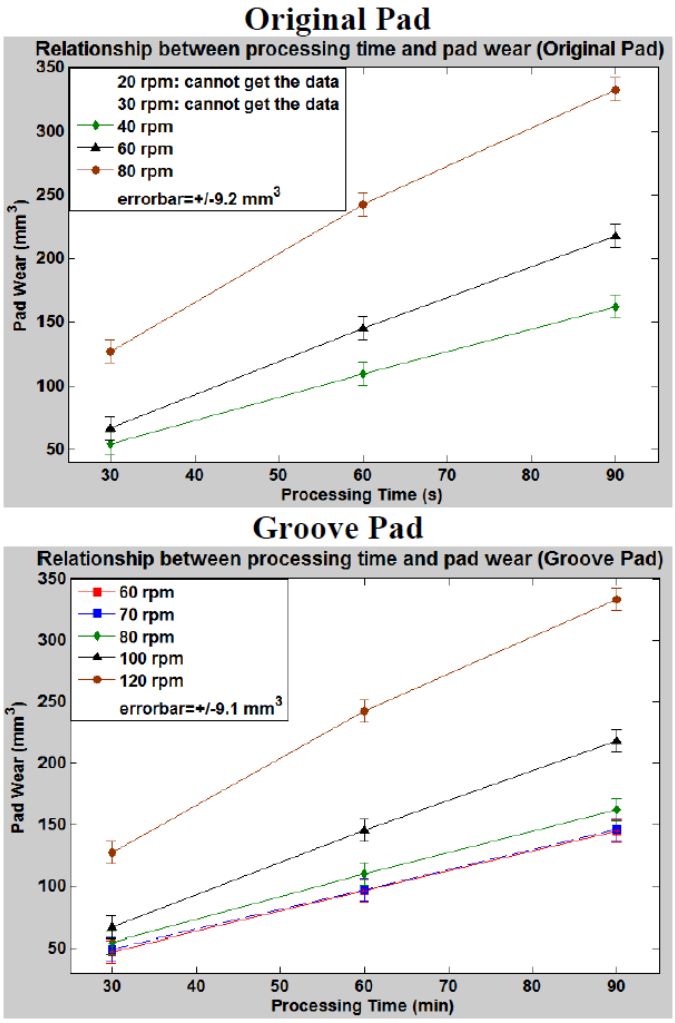

Figure 5-6: Accumulated pad wear

In Figure 5-6, the original pad driven at 20 rpm and 30 rpm spindle speeds resulted in a measurement failure. This was because the noise was too great to measure shallow removal (especially removal depths < 0.8 μm). Even when filters were applied to de-noise, it was still not possible to identify the pad wear. When measuring this kind of shallow pad wear in the future, it is suggested that the processing time be increased so that a larger amount of wear is available for measurement, since higher wear amounts can reduce measurement uncertainty compared to attempting to measure shallow levels of wear. For example, in section

5.5.2, three grolishing runs were conducted to grolish the 1 m segment to achieve accurate removal. Hence, instead of using the de-noising method and challenging the limitations of the measuring equipment, using higher removal depths can avoid measurement uncertainty.

5.3.4 Summary of the pad wear effects

In this section, the pad wear effects have been extensively explored. It is obvious that the grooved pad returned a superior processed surface and higher removal efficiency (70 rpm spindle speed) than the original pad (20 rpm spindle speed). Hence, the grooved pad, with a 70 rpm spindle was used to conduct the remaining grolishing experiments in this chapter.

5.4 MSF assessment

One core benefit of the RGP is to control MSF. The purpose of this section is to demonstrate that the MSF left by other processes is able to be removed by the RGP.

5.4.1 Experiments

The MSF were produced by a 40 μm bound-abrasive diamond KGS pad (code: 1023.0100114) cemented on a 100 mm diameter hard brass pad connected to the tool, and the Talysurf Intra was then used to measure the surface signatures, as shown in Figure 5-7. After that, one grolishing run was performed and the surface measured. Finally, the MSF data before and after the grolishing were compared to evaluate the MSF removal due to the RGP.

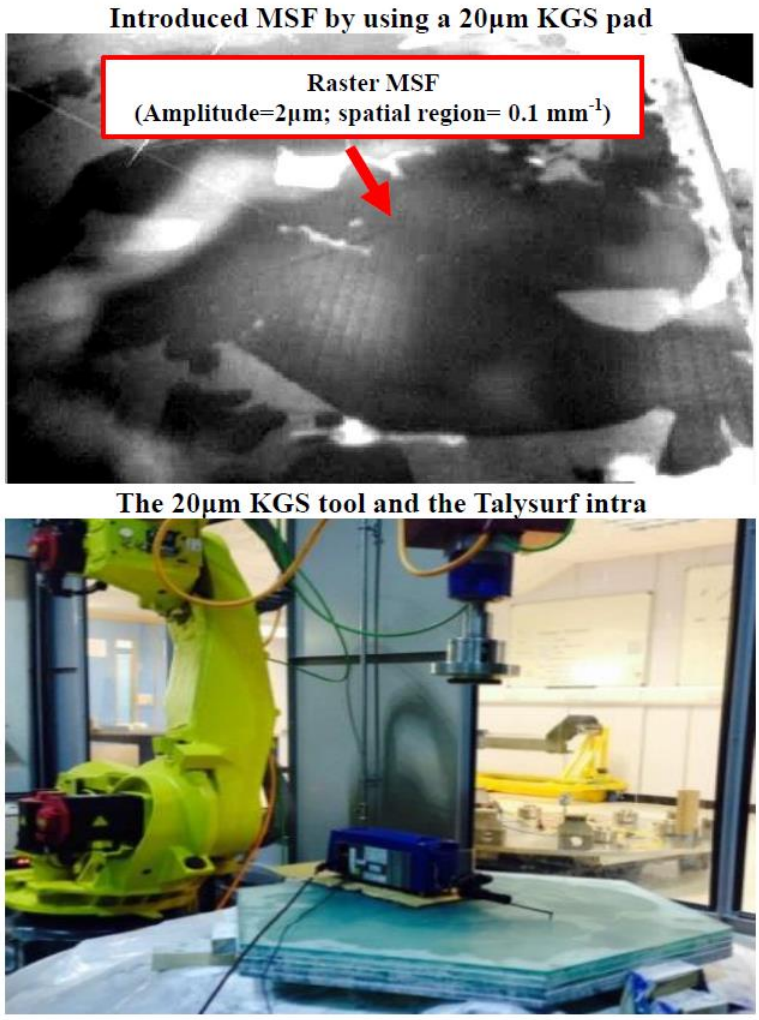

Figure 5-7: MSF measurement and the Talysurf Intra

5.4.2 Discussion

The results of using the KGS pad (i.e. before grolishing) and the grooved pad (i.e. after grolishing) are shown in Figure 5-8. The PV = 2 µm MSF is intended to be generated by the KGS pad to simulate the final cut of a ground surface (MSF left by the final grinding cut is PV < 3 µm [89, 195]). In order to evaluate the two profiles in

more detail, the data was transformed into spatial regions by PSD (introduced in Chapter 2) from the Zeeko Metrology software, and the results are shown in Figure 5-9.

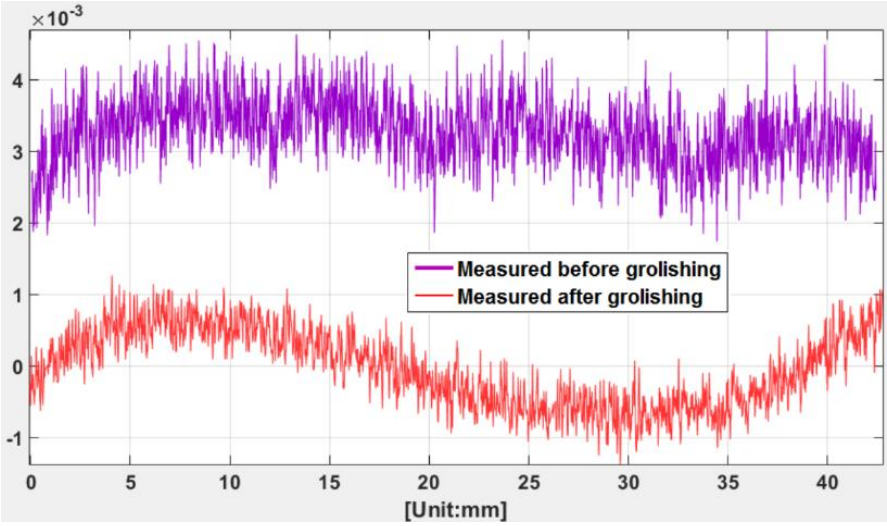

Figure 5-8: Local profiles before and after grolishing. Data was offset for comparison.

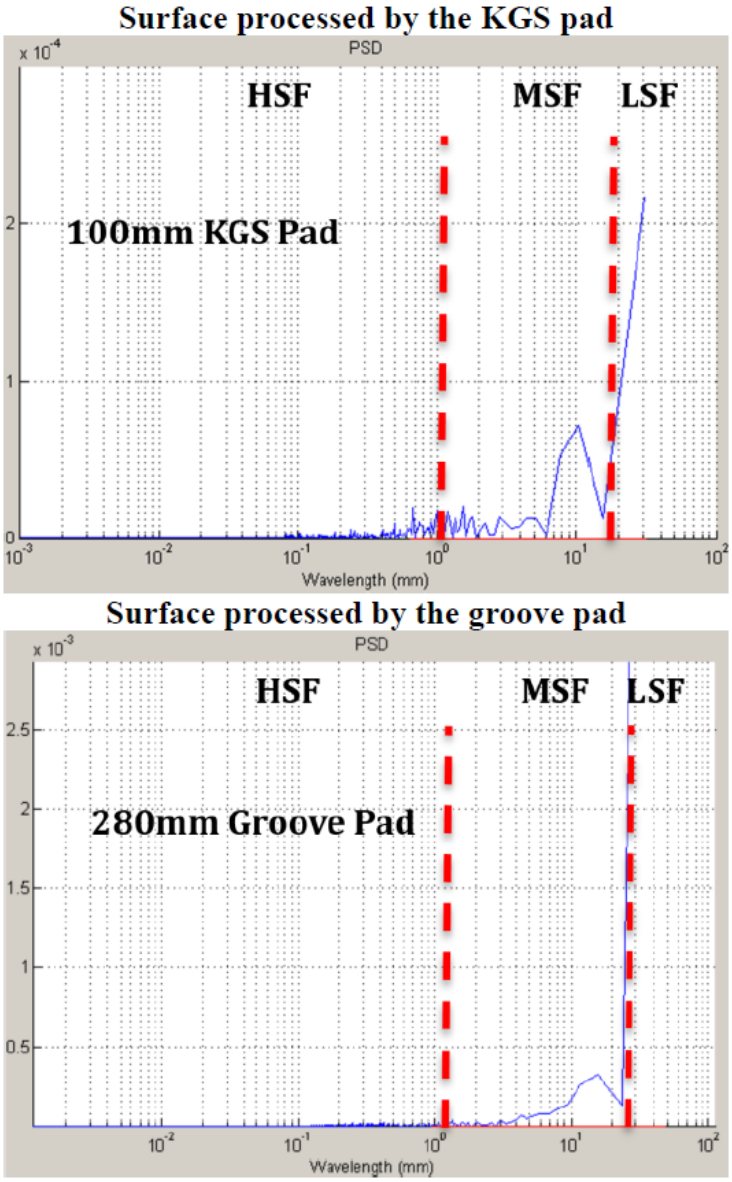

Figure 5-9: PSD results

The results show an inherent conflict between the removal of the MSF tooling marks and loss of surface form (i.e. LSF).[8] Since the Zeeko bonnet has the ability to correct both LSF and HSF to an accuracy at the scale of a few nanometres (PV LSF < 200 nm and ST about 1~2 nm [92]), a hybrid grolishing and polishing process is capable of producing high quality surfaces [39]. Hence, the result was acceptable.

[8] Please refer to Chapter 2 to review the relationship between surface errors and its spatial frequencies

Furthermore, in the previous chapter, it was demonstrated that MSF in the range 0.02 mm^{-1} < MSF < 1 mm^{-1} could be removed by using a 100 mm rigid tool. Thus, if the statistical experimental designs and analysis were applied,[9] the MSF resulting from the 280 mm grooved tool could be modelled and suppressed (as demonstrated in Chapter 4). Alternatively, hybrid tools (i.e. 100 mm and 280 mm tools) could be used to process surfaces. For example, the 280 mm tool could be used to smooth an overall ground surface, and then the 100 mm tool could be used to remove localised MSF errors on a surface. Then, the grolished surface could be passed to a polishing process to control all the errors in the spatial regions so as to achieve a diffraction limited surface.

5.5 VRR measurement

The challenges in terms of measuring VRR lie in developing a metre-scale measurement system and devising suitable algorithms to calculate removals. The following introduces a series of procedures to achieve those tasks.

The first stage was to construct a system capable of measuring at the metre-scale. To achieve this, a commercially purchased probe (DT/10/P Feather Touch, abbreviated DFT) was settled on a 1.1 m air bearing table, or any robotic arm, to achieve a measuring capacity of more than 1.45 m (the setup is shown in Figure 5-10). The accuracy of the DFT was then evaluated in comparison with the Talysurf. Thirdly, an intermediate metrology method (e.g. the grooved method in Section 5.5.1) was used to measure removal depths. Please note that the grooved method provided precise

[9] Please refer to Chapter 3 and Chapter 4 to review the statistical methods and model a response

measurements, but left features in the part. While this method is adequate for fabrication workpieces in a research context, therefore, it is not suitable for any segment for a telescope or large scale production. The final task was to reconstruct the removal surface, which was used to calculate the removal in order to derive the VRR from the grolishing process.

5.5.1 Evaluation of the new metre-scale measuring system

The Talysurf (full name: Extended Range Form Talysurf, ERFT) has been used in the UK for more than two decades, and provides a high precision micrometre scale measurement for optical segments of up to 300 mm and stitching for a 500 mm diameter segment. It is not able, however, to measure a segment larger than 1 m in diameter. In 2015, Prof Walker led our group to develop an original measurement system aimed at utilising the DFT to measure a metre-scale segment.

One important task for this setup was to increase the measurement speed since, even if the ERFT were able to measure metre-scale optics, the measuring speed would still be too slow (1 mm/s). An efficient measurement system has to complete a metre part measurement in about half a day, thus the speed must be increased to 13.33 m/s or more, enabling a 1 m segment to be measured in 1 hour.

The objective of this section is to investigate how to use the metre-scale measuring system to measure a 1 m hexagonal part. By comparison with the commercial ERFT product (Device 2), the DFT on the 1 m air bearing table (Device 1, i.e. the metre-scale measuring system) would have to show no significant difference in the

measured removal depth between the two devices in order to confirm that device 1 was able to provide accurate measurement of the 1 m segment.

5.5.1.1 Experimental design and process

As shown in Figure 5-10, a flat hexagonal borosilicate glass, measuring 400 mm from corner to corner, was used to test the two system devices. A diamond file was used to create eight grooved features on the glass surface. The depths of the grooves ranged from 31 μm to 120 μm, and the groove widths were 3.2±0.1 mm. Thirty samples were randomly selected and measured by the two devices, separately, using the same data-point collection speed: i.e. 27 points/s.

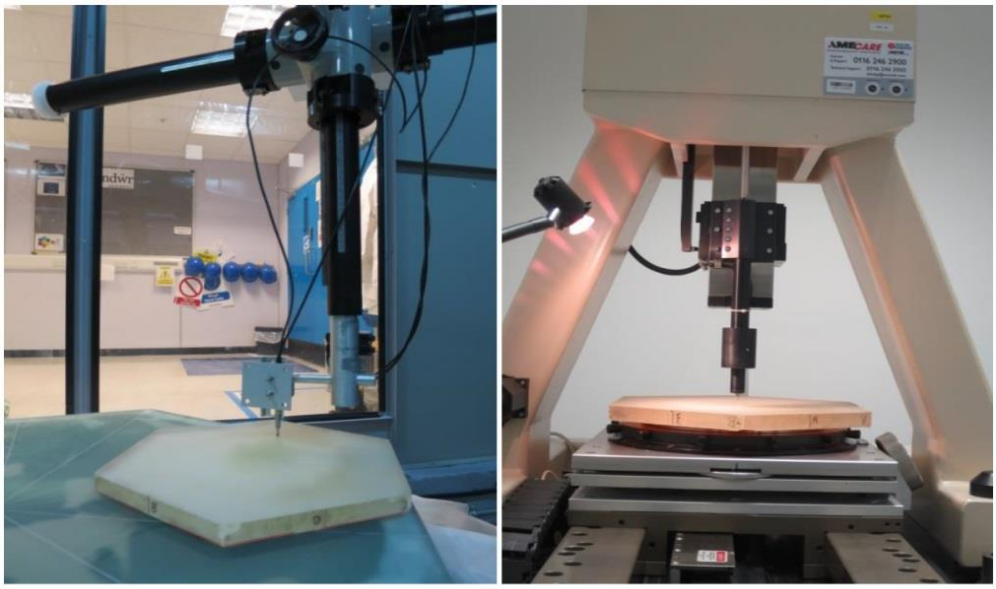

The DT/10/P Feather Touch on the supporting setup (Device 1, D1).

The Extended Range Form Talysurf, ERFT (Device 2, D2)

Figure 5-10: Comparison of the two measurement devices

5.5.1.2 Paired comparison designs

The paired t-test is the recommended method to compare the two devices in order to increase the accuracy of the comparison. The testing procedure is summarised in Figure 5-11. The lapping (or smoothing) procedure uses 40 μm aluminium oxide loose abrasive for 30 minutes. In total, 60 data points were collected from this experiment.

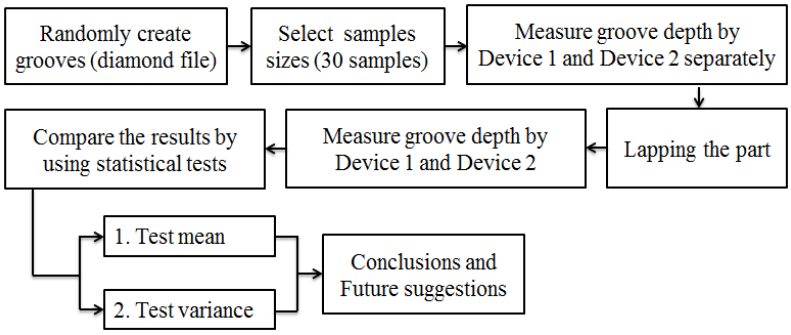

Figure 5-11: Test procedures

The following is a demonstration of the theory that using the paired t-test can increase comparison accuracy. In comparative experiments, the precision can be significantly improved by making comparisons within matched pairs of experimental samples [177, 178, 228]. A statistical model may be written as:

$$y_{ij} = \mu_i + \beta_j + \epsilon_{ij} \quad \begin{cases} i = 1,2 \\ j = 1,2,\ldots,30 \end{cases} \tag{5-2}$$

to describe the data from the experiment, where y_{ij} is the observation of the removal depth for tip i on the jth specimen, μ_i is the true mean removal depth of the ith tip, β_j is an effect caused by the specimen j, and ϵ_{ij} is a random

experimental error with mean zero and variance σ_i^2. Thus, σ_1^2 and σ_2^2 are the variance of the removal depth measurements from D1 and from D2, respectively.

The jth paired difference of the measurement can be computed as:

$$d_j = y_{1j} - y_{2j} \qquad j = 1,2,\ldots,30 \tag{5-3}$$

The expected value of d_j is

$$\mu_d = E(d_j) = E(y_{1j} - y_{2j}) = E(y_{1j}) - E(y_{2j}) = \mu_1 + \beta_j - (\mu_2 + \beta_j) = \mu_1 - \mu_2$$

If the experiment does not pair, however, and the observations are treated as two independent samples, the expected value of the variance of a two sample t-test is:

$$E(S_p^2) = \sigma^2 + \sum_{j=1}^{n} \beta_j^2$$

where S_p^2 is an estimate of the variance of the two sample t-test.

From the above demonstration, the additive effect of the specimen β_j cancels out if the measurements are paired in this manner, but β_j inflates the variance estimate in the two sample t-test. The means of the differences μ_d are therefore exactly the differences in the mean removal readings of the two devices.

One disadvantage of the paired design is that only n-1 observations are available for a paired t-test, even though there are 2n observations. When pairing, the experiment therefore effectively lost n-1 observations. One way of compensating for this is to increase the degree of freedom (DOF) so as to increase the sensitivity of the test.

5.5.1.3 Test statistic

The test statistic is to evaluate the testing accuracy, and the hypotheses of the paired comparison for the designs to be tested are:

$$H_0: \mu_d = 0$$

$$H_1: \mu_d \neq 0$$

This is a two-sided alternative hypothesis, i.e. H_1 is true if either $\mu_d > 0$ or $\mu_d < 0$ is true. Hence, when the null hypothesis H_0 is rejected, the measurements of the two devices would be determined differently.

This test statistic is a single t-test:

$$t_0 = \frac{\bar{d}}{S_d/\sqrt{n}} \tag{5-4}$$

where $\bar{d} = \frac{1}{n}\sum_{j=1}^{n} d_j$ is the sample mean differences and $S_d = \left[\frac{\sum_{j=1}^{n}(d_j-\bar{d})^2}{n-1}\right]^{1/2}$ is the sample standard deviation of the differences.

5.5.1.4 Results and Analysis

Table 5-2 shows the measurements from the two devices. Since the t-test is based on the assumption of normal distribution, the normal probability plot was assessed prior to applying a statistical test. The data show a normal distribution with a 95% confidence interval (CI), as shown in Figure 5-12.

Table 5-2: Data from the test

Specimen	D1	D2	Difference	Specimen	D1	D2	Difference
1	15.5	16.5	-1	**16**	7.9	12	-4.1
2	19.0	16.2	-2.8	**17**	15.6	13	2.6
3	18.2	14.1	4.1	**18**	15.9	12	3.9
4	10.9	13.2	-2.3	**19**	11.8	10.8	1
5	13.0	12.5	0.5	**20**	9.9	9.8	0.1
6	14.8	12.5	2.3	**21**	4.6	9	4.4
7	14.6	12.8	1.8	**22**	6.7	10.8	-4.1
8	17.3	13.5	3.8	**23**	8.6	11.5	-2.9
9	16.9	14.7	2.2	**24**	9.7	12.7	-3
10	14.9	16	-1.1	**25**	12.8	14.1	-1.3
11	18.6	16.3	2.3	**26**	9.3	13.2	-3.9
12	13.6	15.5	-1.9	**27**	12.3	12.2	0.1
13	9.5	14	-4.5	**28**	9.5	10.8	-1.3
14	10.3	12	-1.7	**29**	6.6	9.8	-3.2
15	16.3	11.7	4.6	**30**	9.1	11.5	-2.4

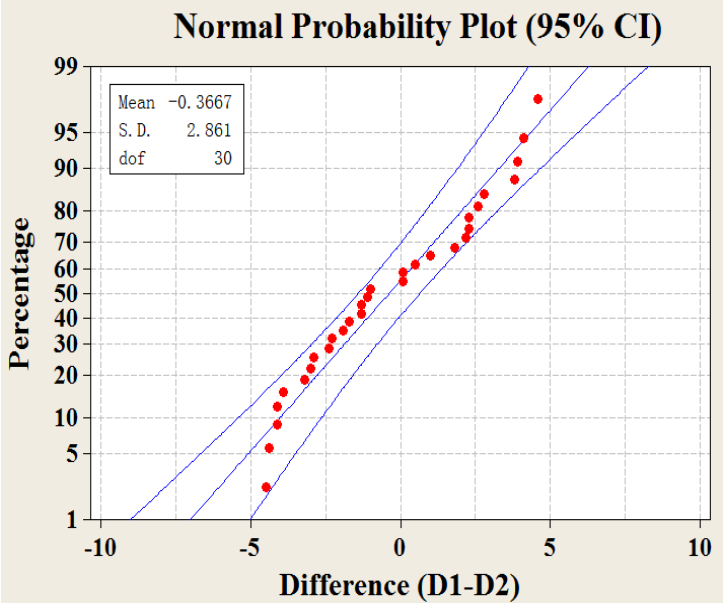

Figure 5-12: Normal distribution plot with 95% CI

Using the data in Table 5-2, three commonly used data analysis techniques[10] were applied in SPSS and then confirmed by MiniTab and finally summarised in Table 5-3. The boundaries of the critical region of the *t* distribution with 29 DOF are shown in Figure 5-13. The results showed that the null hypothesis could not be rejected (i.e. no significant difference), as there was insufficient statistical evidence to determine that the measurements were significantly different between the two device measurements, indicating that the DT/10/P Feather Touch on the arm of the metre-scale setup can achieve accurate measurement.

[10]Please refer to Chapter 2 to review the three different analysis methods and their statistical concepts, respectively.

Table 5-3: Test results on means

Paired comparison t-test		Two sample t-test	
t_0	t_0=0.702	t_0	t_0=-0.4565
P value	0.4833	P value	0.6497
CI	-0.7016~1.4349	CI	-1.9745~1.2411
Test Decision	Failed to reject H_0	Test Decision	Failed to reject H_0

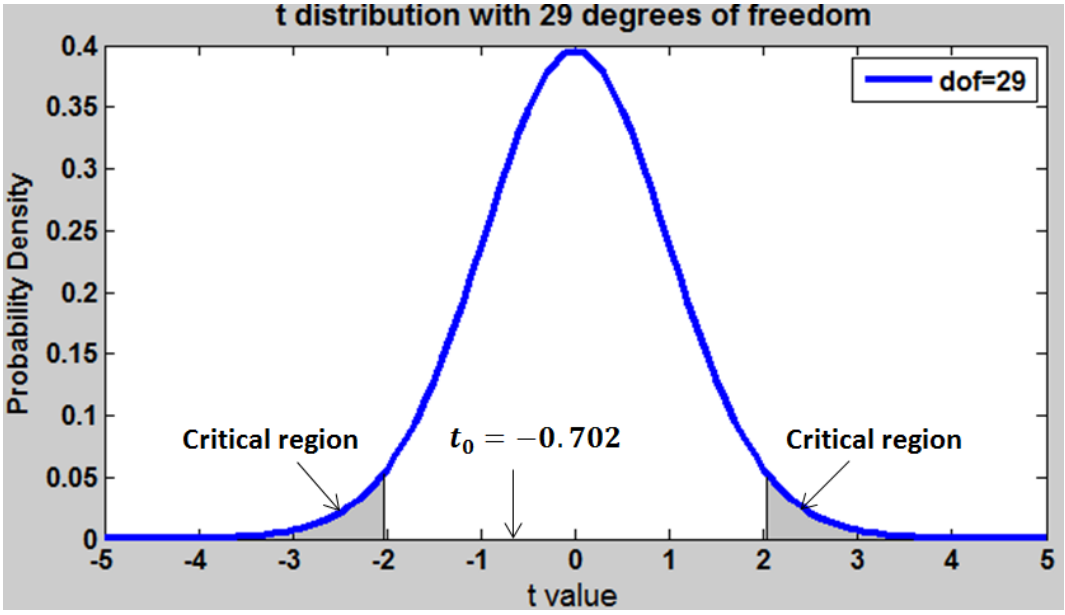

Figure 5-13: The reference t distribution with 29 DOF for the paired comparison experiment

When the paired design was used, the range of a 95% CI was 2.1365. Conversely, using the independent analysis, the range of a 95% CI was 3.2182, thereby showing the noise reduction property of a paired design to thereby achieve a real comparison between the two setups.

5.5.1.5 Inferences about the variances

In this section, the objective is to investigate the inherent variability of the two types of equipment used to measure the output of the removal depth on the 400 mm segment. In order to assess whether a difference in variation exists between D1 and D2, the hypothesis is:

$$H_0: \sigma_1^2 = \sigma_2^2$$

$$H_1: \sigma_1^2 \neq \sigma_2^2$$

Since two independent observations of size $n_1 = 30$ and $n_2 = 30$ were collected from two different normal populations, separately, the test statistic for the hypothesis is

$$F_0 = \frac{S_1^2}{S_2^2} \tag{5-5}$$

The appropriate reference distribution for the F_0 is the F distribution, with $n_1 - 1$ and $n_2 - 1$ dofs, respectively. The test statistic is a two-tailed F test, so that H_0 is rejected if $F_0 > F_{\alpha/2, n_1-1, n_2-1}$ or if $F_0 < F_{1-(\alpha/2), n_1-1, n_2-1}$, where $F_{\alpha/2, n_1-1, n_2-1}$ and $F_{1-(\alpha/2), n_1-1, n_2-1}$ denotes the upper $\alpha/2$ and lower $1-(\alpha/2)$ percentage points of the F distribution with $n_1 - 1$ and $n_2 - 1$ dof. The results of the three analysed methods are shown in Table 5-4. Two tailed critical regions for this two-tailed *f* distribution are illustrated in Figure 5-14.

Table 5-4: Test results on variances

F_0	$3.8471 > F_{0.025,29,29} = 2.1$
P value	5.1264e-04 > 0.05
95% CI	$1.8311 \leq {\sigma_1^2}/{\sigma_2^2} \leq 8.0828$
Test decision	Reject H_0

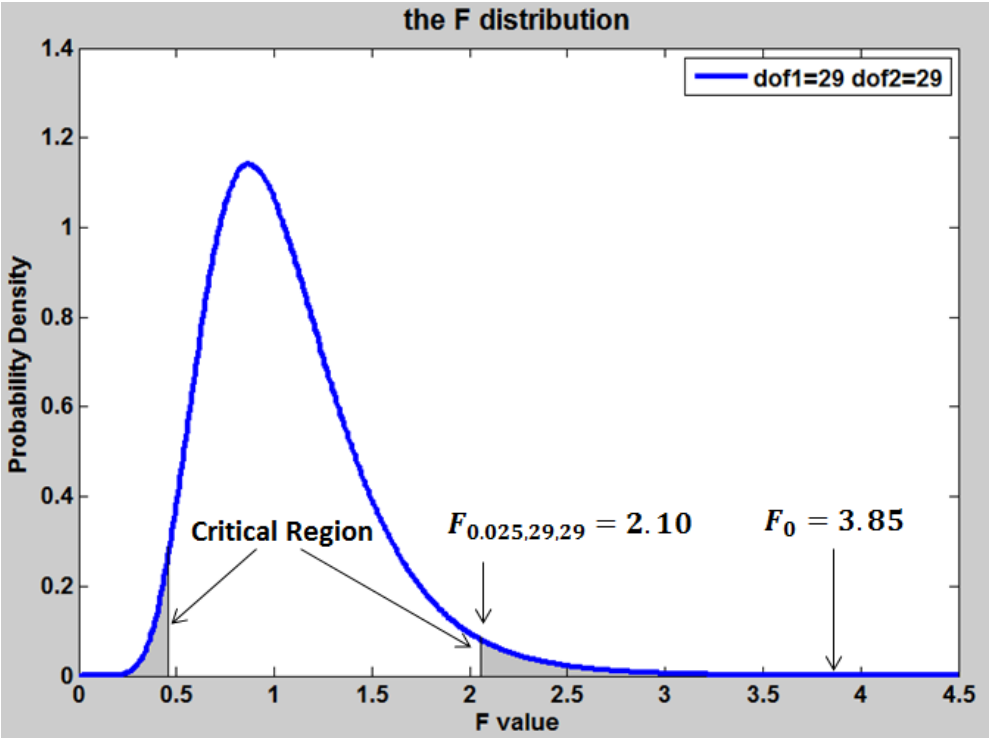

Figure 5-14: The reference F distribution with 29 numerator and 29 denominator DOF

From Table 5-4, the null hypothesis was rejected. Thus, sufficient statistical evidence is available to conclude that the variances were different in the two measurement devices. The first device had a standard deviation twice that of the second device.

From the experimental observation, the supporter and the clamper in our system were two important factors in producing the measurement deviation. The temporary supporter and clamper were made from wood, and the stiffness of this material is too low, meaning that it could easily be responsible for a few nanometres of distortion or displacement during measurement. This noise could be reduced, however, by making at least three measurements. Hence, four measurement runs were adopted to measure the 1 m part to improve measuring uncertainty (this will apply in Section 5.5.2).

Steel supporters and clampers are better material than wood to hold the segment. A new supporting system made of steel began to be used from August 2015. According to the reanalysed data in Table 5-4, the accuracy of the D2 is ± 0.15 μm peak-to-valley over the full range, and thus the ± 0.31 μm peak-to-valley accuracy of the D1 is inferred from the statistics (confirming the specification from the DFT provider: AMETEK Ltd.).

5.5.1.6 Summary of using the metre-scale measuring system

The statistical experimental designs were used to evaluate the DT/10/P Feather Touch on the metre-scale setup (Device 1) and the Talysurf (Device 2). The results and proposed methods to use this metre-scale measuring system are summarised in Table 5-5. Since the Device 1 has high measuring efficiency with acceptable

accuracy, the device was used to measure the 1 m hexagon (details will be discussed in section 5.5.2).

Table 5-5: Comparison table: Our setup and the Talysurf

	Device 1	Device 2	Suggestions for using Device 1
Tip size	2 mm	1 mm	Purchase smaller tip to increase measurement sensitivity or accuracy
Capacity	> 1 m	300 mm	Use steel to support the segment
Speed	13.3 mm/s	1 mm/s	An automatic setup can reduce time
Accuracy	$\pm$0.31 μm	$\pm$0.15 μm	Measuring more than three times can lead to great improvements in accuracy

5.5.2 Removal surface reconstruction

The objective of this section is to reconstruct a removal surface grolished by the grooved pad with the parameters in Table 5-1 and a 70 rpm spindle speed.[11] The VRR with these parameters can then be calculated from the volume of the reconstructed surface.

5.5.2.1 Data collection method

The grooved method described in section 5.5 was applied to measure the 1 m hexagonal part, as shown in Figure 5-15. Since the measurement speed is 13.33 mm/min, collecting 126 points in a measurement run would take only 1 hour. The

[11] Section 5.3 has demonstrated that a 70 rpm spindle speed is suitable for a uniform pad surface

time could be further shortened if an automatic controlling system was used to control the device.

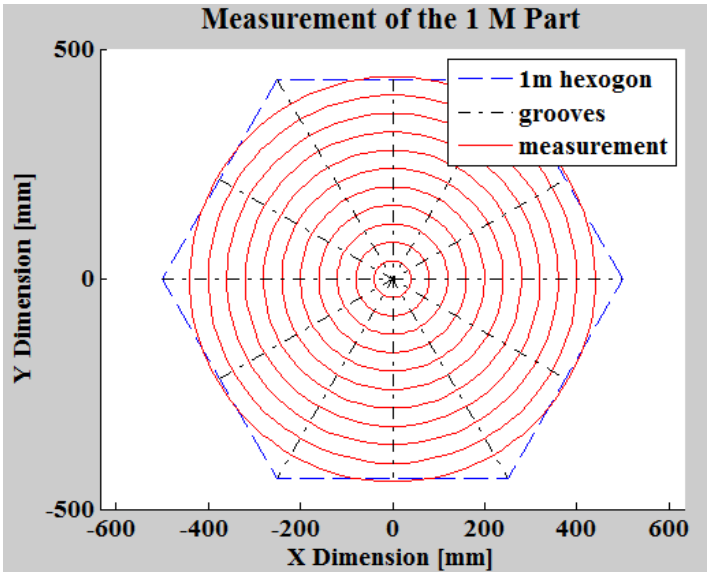

Figure 5-15: 126 collecting data points

Four runs were used to measure the 1 m surface (discussed in Section 5.5.1.5), meaning that 5 hours were used to complete the measurement. This implies that to finish a full grolishing run, with the measurement, would require about one working day. This is an important success because it means that, using the RGP, it is possible to complete a grolishing process and measurement for a 1.45 m segment each day (the aim for the E-ELT M1 is to complete one segment in an average of every two to three days), compared to the three days it normally takes to conduct surface measurement using the slow speed Talysurf (1 mm/s).

5.5.2.2 Surface reconstruction

This section introduces the methodology to reconstruct the removal surface from the collected data in Section 5.5.2.1. The innovation in this section is to introduce a new method to reconstruct the surface topography in the context of large optical fabrication. The new idea was based on a triangulated irregular network, the objective of which was to use a geographic information system to predict a stream's response to storm events, so as to optimise water storage for flood control structures, dams, and habitat improvements [229, 230]. By redesigning, reorganising and then further applying this concept, a new reconstruction method was developed here that can model surfaces in the field of metrology more accurately than those based on the conventional method of reconstructing surface topography.

In order to demonstrate this new technique, both the conventional and the new method were used to construct an ideal spherical surface, as shown in Figure 5-16. More surfaces were shown to be predicted by the new method, resulting in measured surfaces with superior 3D characteristics. The two methods will be further evaluated in Section 5.5.2.3.

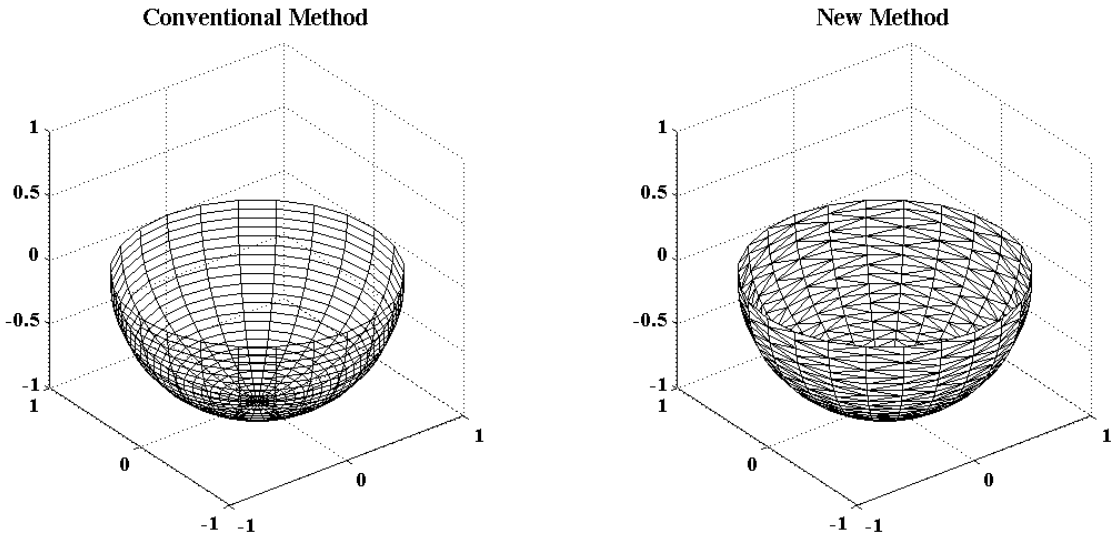

Figure 5-16: Use of conventional and new methods to reconstruct an ideal surface

5.5.2.3 Removal topography for the 1 m part

All experimental grolishing using the 280 mm diameter grooved pad and the optimum of a 70 rpm spindle speed was carried out on the 1 m hexagonal part using the parameters shown in Table 5-1. In addition, three grolishing runs were conducted and a 128 mm tool overhang was selected to control segment edges.[12] The metre-scale measuring system described in Section 5.5 was used to measure the 1 m segment. The average removal data (from four measurements) were collected by using the method in Figure 5-15, and shown in Figure 5-17.[13]

[12] The tool overhang is introduced in Chapter 3.

[13] The author wants to thank Meng Kai for the experimental cooperation to complete this experiment

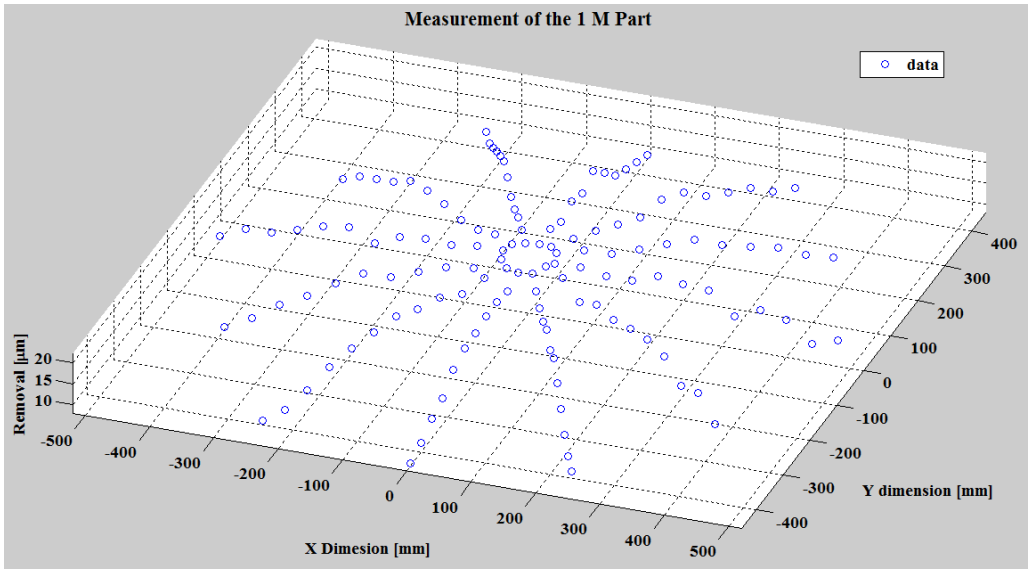

Figure 5-17: Data collection (averaged across four measurements)

The two different methods were used to reconstruct the data in Figure 5-17 (the numbers of interpolation data points are equivalent). Figure 5-18 shows that more interpolation surfaces were predicted by the new method, indicating that it is capable of achieving more surface details than the conventional method.

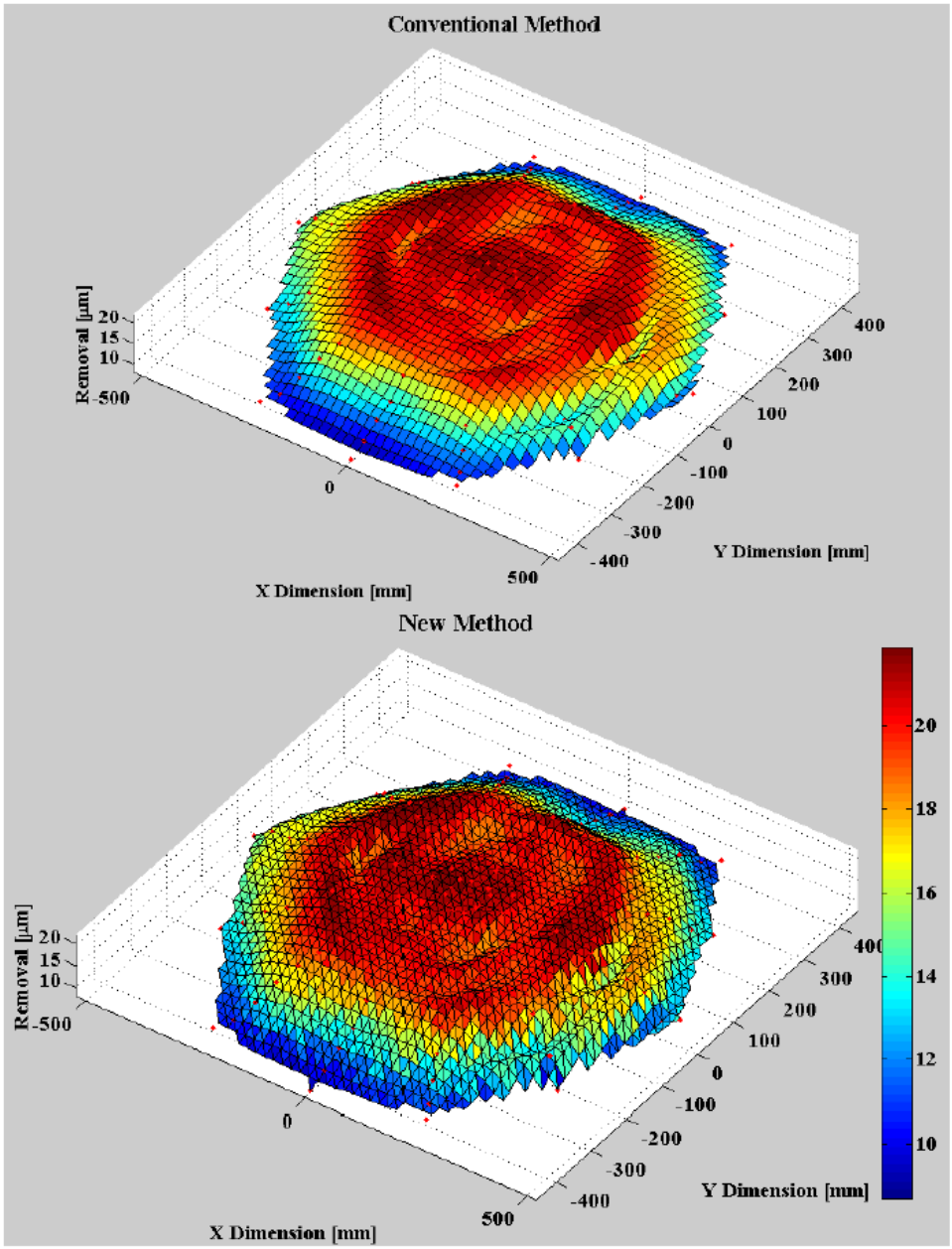

Figure 5-18: Removal surface using the conventional (top) and new methods (bottom)

After 3D reconstruction of the removal surfaces, edge, removal depth and VRR could be calculated, as summarised in Table 5-6. The results of these responses were almost equivalent, indicating the stability of the new method. Hence, this experiment demonstrated that the new method could be another approach to reconstruct a surface. Additionally, since the new method has the advantage of more interpolation surfaces,

fewer measuring points and a shorter measuring time were required to measure the surface.

Table 5-6 Measurement results for the two methods (three grolishing runs)

	VRR	Removal Depth	ST (from Talysurf Intra)	Edge up-stand
Original method	522.7 mm^3/min	21.9 μm	Ra=275 nm	15.8 μm
New Method	514.2 mm^3/min	21.9 μm		15.8 μm

5.5.2.4 VRR calculation from the removal surface

To calculate an area or volume, the usual or traditional method is to slice the target function into a number of parallel strips, such as dx, dy or dz, and then take the integral to derive the area or volume. In this section, particular consideration is given to resolving the inherent difficulties of calculating huge data for irregular shapes. This original integral method, namely triangular integral, aims to integral a complex surface. The idea was to switch the region into the spatial-frequency domain, analogous to a Fourier transform method to deal with spatial frequencies in optics [51].

An example of the use of the traditional integral to calculate the VRR=522.7 mm^3/min is provided in Figure 5-19. The traditional method was compared with the triangular integral, as shown in Figure 5-20. Using the same region as that in the middle of Figure 5-20 to separate the period, the VRR in the triangular method was

calculated as 540.2 mm^3/min. The VRR was 540.2 mm^3/min if done at half of the frequency, and the VRR was 534.6 mm^3/min if done at twice the frequency.

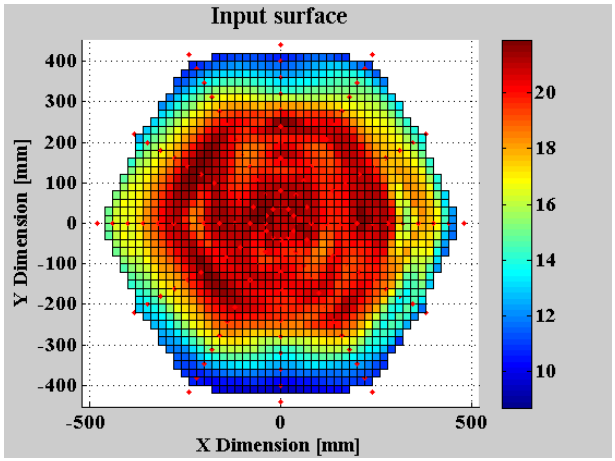

Figure 5-19: Use of the traditional integral method to calculate VRR=522.7 mm^3/min

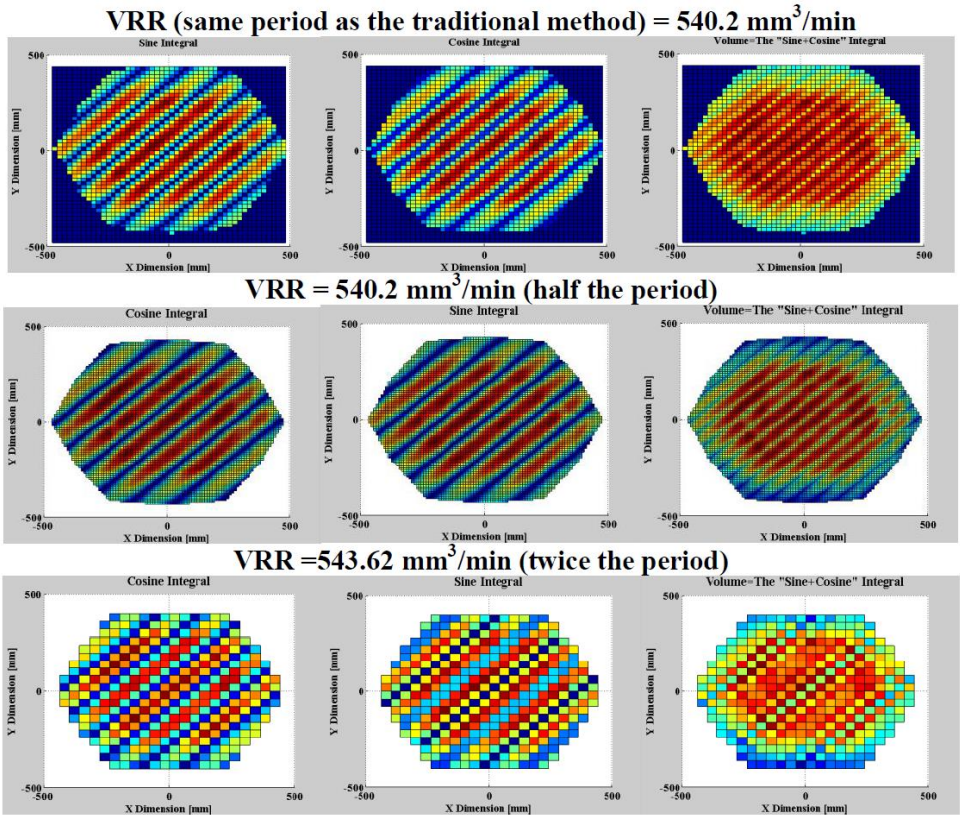

Figure 5-20: The triangular method to calculate VRR in three different spatial domains

A comparison of the two methods is summarised in Table 5-7. When switching the integral region, the errors of the two methods were as small as ±0.3 %, indicating that the triangular integral is equivalent to that of the traditional method. This method is not limited to metrology in the field of aspheres or complex surfaces, but may also be applied to other fields, such as the volume of a star in astronomy, the capacity of a human brain in life science or buildings with special structural designs in architecture and civil engineering.

Table 5-7: Comparison of the traditional and the original integral method

	Half (mm^3/min)	**Normal** (mm^3/min)	**Twice** (mm^3/min)	**Error** (±%)
Traditional Integral	517.9	522.7	524.4	0.3
Triangular Integral	534.6	540.2	540.2	0.3

5.6 Summary

The use of a 280 mm diameter tool to process metre-scale optics has been demonstrated in this chapter. The pad wear effects within the original and grooved pads have been fully understood. Tool models have been built and are able to explain all the experimental results. Furthermore, it has also been demonstrated that MSF generated by grinding (MSF amplitude < 2 μm) can be removed by the 280 mm grolishing tool. All the results demonstrate that the 280 mm tooling process has been developed.

Furthermore, a metre-scale metrology system has been established in this chapter. A novel surface reconstruction method and the triangular integral can achieve the same accuracy as the traditional method, showing the stability of the new method. The proposed new method will be used for non-destructive testing and contact measurement in the near future. The measurement method is not limited in its application to optics, but can also be applied to other relevant large-scale industries, such as aerospace, automotive and heavy equipment manufacturing.

Chapter 6 Manufacturing of complex surface forms

6.1 Introduction

The manufacturing of complex surface forms in up to metre-scale optics represents the cutting edge of optical technology in astronomy, imaging and defence. The benefits of aspheric surfaces are improved optical performance, reduced total system weight, and minimised total required surface elements, with a consequent lowering of costs, allowing the product to compete in the marketplace.

When processing aspherical surfaces, a small tool or single diamond point tool, or both, are generally used to minimise form errors by following asymmetric slopes and to process aspherical departures. These tools, however, often leave their signatures on the surface [231], and it is time-consuming for polishing to remove periodic MSF errors unless the tool size is large enough to cover the spatial period of these errors [232] (discussed in Chapter 4). In recent years, the removal of MSF in aspherical surfaces plays an important role in the area of optical fabrication. For example, one core topic of the 2015 SPIE OptiFab in Rochester USA was to remove MSF to improve surface performance.

Compared to the single point process, a large rigid tool (e.g. those of 100 mm or 280 mm diameter outlined in Chapter 4 and Chapter 5 respectively) has an advantage of a higher removal rate to smooth MSF out of the surface with a shorter processing time. As long as a significant gap (i.e. a misfit) exists between the tool and surface, MSF

errors can be created and effects such as ghosts and flares can be introduced into the optical system, reducing image contrast (please refer to Section 4.2.4 for the image simulation). When using a rigid tool to process a complex surface, the problem of residual MSF in surfaces needs to be solved.

Although the stressed-lap [233] can be used to polish aspherical surfaces, this tool requires complex electromechanical actuators controlled by computers to deform the tool surface so as to minimise the significant misfits. Alternatively, the family of non-Newtonian tools can be a cheaper way to remove MSF on an aspherical surface [225, 234], but these tools have an inherent challenge to control removal, resulting in producing low-order aberrations on a surface and the process is slow [226].

The scientific focus for the core of this chapter can be described as: to explore the effects of the misfit between a rotating rigid tool and glass, with the aim of minimising MSF errors in complex surfaces for the RGP. To date, there is no literature to discuss how to use rigid large tools to minimise the effects of MSF errors when processing aspherical surfaces. The solution proposed here aims to provide a new method to reduce MSF errors when the aspheric slope is large, specifically by using large abrasive sizes to fit the misfit between a large tool and a surface.

In chapter 4, a 100 mm tool was shown to be able to remove MSF and provide micron scale accuracy for 400 mm hexagonal surfaces. The tool used in that chapter is considered as the base starting point, however, and will be extended in this chapter to take into account the ability to process non-symmetrical surfaces (such as aspherical surfaces or even complex surface forms).

Accordingly, this chapter is structured as follows: firstly, a new glass-bending mechanism is created to bend the glass to the desired surface form. This mechanism is introduced in section 6.2. Secondly, the guidelines for using this novel mechanism are investigated in section 6.3. Then, saddle surfaces, pad conditions, removal results, and MSF errors are discussed and summarised in section 6.4 in order to demonstrate that using large abrasives is an innovative idea to minimise MSF on aspherical surfaces. Finally, a summary is provided in section 6.5.

6.2 New glass-bending mechanism

In order to investigate the technique to remove MSF in a complex surface, the primary step is to consider how to generate such a surface form. One way to create a complex surface form is to use a Zeeko polishing machine at OpTIC. By using the polishing parameters in Section 6.4.2, to remove about 1.3 μm of material from a 400 mm hexagonal borosilicate segment using the R80 bonnet requires 55 minutes (i.e. one polishing run). If the goal is to create aspherical departures of around 100 μm PV in order to evaluate the abrasive size effects using a 100 mm diameter tool, considering the polishing process and its subsequent surface measurement,[14] this process would be too slow to manufacture a complex surface larger than the desired target.

Another method is to purchase a range of fixed complex surface or variable surface forms. After these surfaces have been used to evaluate an experimental trial, the MSF

[14] Measurement time can be longer than the polishing process because of the cleaning process, transportation, and alignment.

left from the grolishing process has to be removed to avoid affecting any subsequent experiment. Although the MSF removing process can be achieved by using the 300 mm rigid tool (introduced in Chapter 4), this process would change the complex form into a symmetric surface. Each piece of glass per experiment increases the cost investment and so it is necessary to consider another way to create a complex surface.

To meet the aim set out for this chapter, therefore, requires a robust, well-maintained, well-tested and well-managed novel setup for creating complex surfaces. As shown in Figure 6-1, the designed glass bending-mechanism offers a new technique to accelerate the process of forming a complex surface.

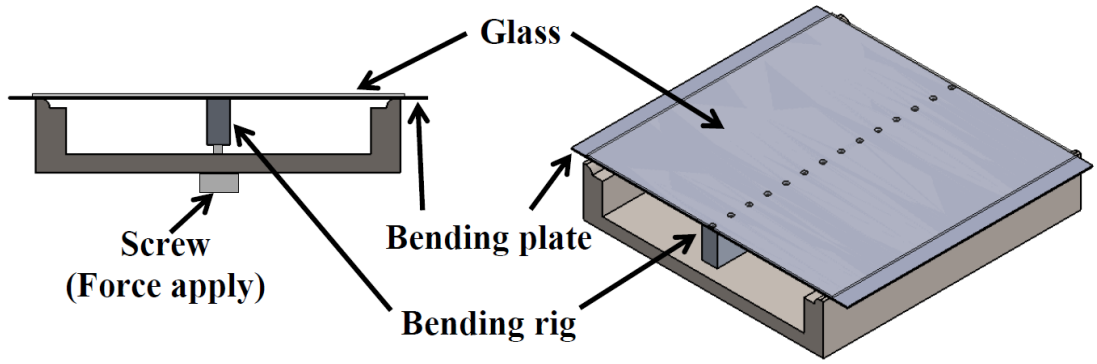

Figure 6-1: Glass-bending mechanism

A piece of thin glass was cemented on the aluminium bending plate and mounted on a stainless steel supporter. A bending rig (i.e. the cuboid bar) attached to the plate was connected with a screw and the glass was bent by turning the screw nut underneath the equipment. This mechanism is intended to bend a piece of flat glass

to provide an 'infinitely variable' non-flat surface through which to explore the effects of a poor fit between the rotating tool and glass. A better understanding of these effects will allow MSF errors to be minimised when processing such complex surfaces.

The width, length and height of the mechanism were related to the following two considerations. (1) Since the tool was 100 mm in diameter, in order to ensure that the central area was fully processed by the tool and able to be detected by the 4D interferometer (with an 180 mm clear aperture), the dimension of the glass was 400 mm x 400 mm square. (2) The glass was required to be capable of being successfully processed by the two Fanuc robots, the ABB robot, two Zeeko polishing machines (Figure 3-4), as well as being detected by the Talysurf, metrology arm (Chapter 5), and 4D interferometer. The dimensions of the bending mechanism were therefore devised to satisfy all the above conditions.

6.2.1 Problems and solutions

Many difficulties were experienced when evaluating this new mechanism to create a complex surface. The following subsections discuss the difficulties encountered and solutions adopted when using this mechanical device.

6.2.1.1 Thickness of the glass

In order to bend the glass easily, the thinnest available glass with a 400 mm x 400 mm square shape was purchased from Phoenix Optical Technologies Ltd. Due to

cost considerations, the cheapest material was Optiwhite™ float glass, with each 400 mm x 400 mm x 3 mm piece costing roughly £5.50 including VAT.

6.2.1.2 Bending plate

The function of the bending plate was to deform the glass to a useful surface configuration to determine the effects of the tooling misfit. One side of the bending plate was used to cement the glass by adhesives (discussed in the next point). As shown in Figure 6-1, the bending rig (i.e. the bar) was attached to the other side of the plate by fourteen screws, with another screw underneath the plate that could be used to apply different forces to the plate in order to bend it.

As shown in Figure 6-2, a nominally cylindrical surface with 632 μm PV can be created by setting the plate on the rig (i.e. without applying any bending force or load on the glass surface. Although this experiment showed that this device was able to create a complex surface quickly, it also shows that this surface is easily deformed in a dynamic manufacturing process and hence that support is required to strengthen the plate. Details will be discussed later.

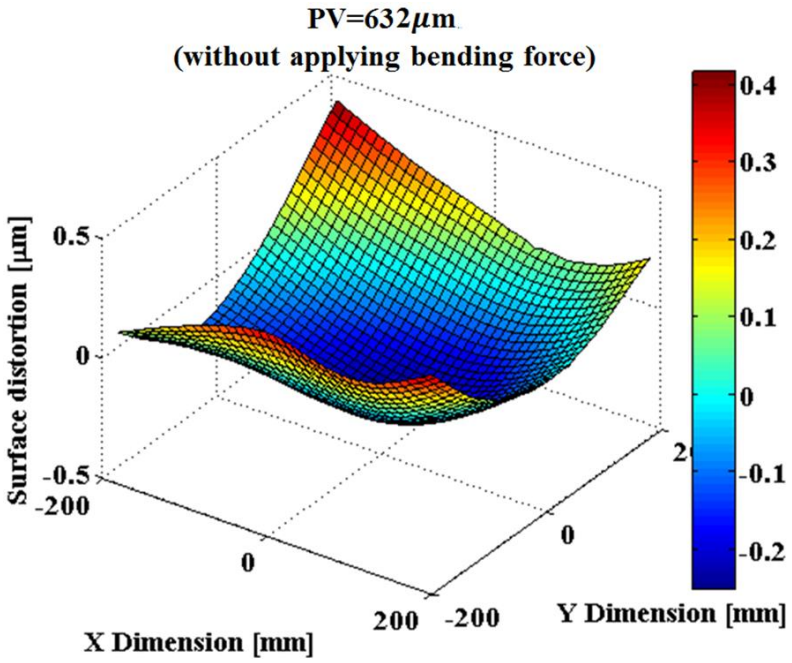

Figure 6-2: PV = 632 μm surface (created without applying bending force)

6.2.1.3 Adhesives

Adhesives were used to cement the glass to the bending rig. The adhesive had to be able to be easily removed so as to allow the glass to be detached from the mechanism. Five different adhesives were examined: (1) soft wax,[15] (2) hard wax,[16] (3) 7.36.20 Blanchard wax (from J.H Young Company Ltd.), (4) Power glue (UniBond 8081/1605193), and (5) Dow Corning 752 (i.e. silicone).

The three optical waxes have been frequently used to cement optical glass on different kinds of metal (usually stainless or aluminium) in OpTIC and therefore these three different kinds of wax were evaluated first. When using soft wax and

[15] Ingredient: 35 % paraffin wax + 35 % beeswax + 30 % resin
[16] Ingredient: 25 % paraffin wax + 25 % beeswax + 50 % resin

medium wax, the glass could be separated from the plate by applying a hand force of about 10 N. As shown in Figure 6-3, these two waxes were demonstrated not to be suitable adhesives for this experiment. Blanchard wax was found to be the strongest because it was able to allow the largest strain for bending a surface. Given Figure 6-2 as the starting point, the results of the bending tests for Blanchard wax are shown in Figure 6-4. The glass surface was bent to PV = 22.6 μm using a 25 N force. When a 30 N bending force was applied, however, the adhesive cracked on two edges. When an additional 4 N of bending force was applied, the adhesive cracked on all the edges. This experiment shows that irreversible cracks in wax adhesives could be created when more than 25 N of bending force was applied. Since this mechanism requires a bending force of more than 40 N (as discussed in the next section), all three waxes were disqualified and other adhesives with strong elastic characteristics that allow bending were sought.

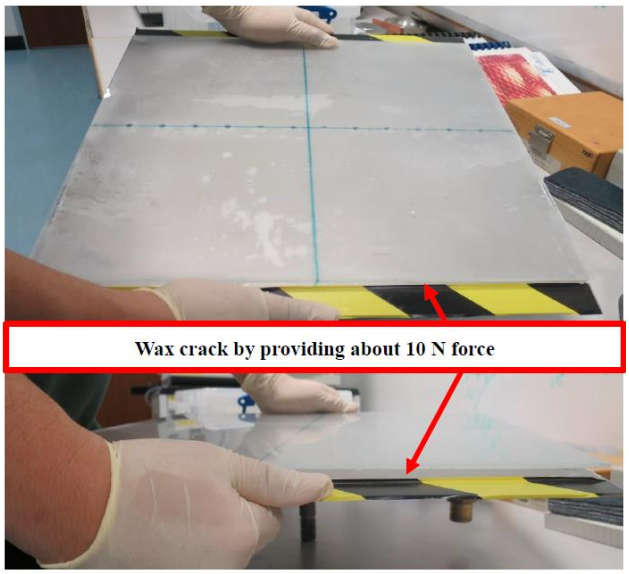

Figure 6-3: Evaluation of wax

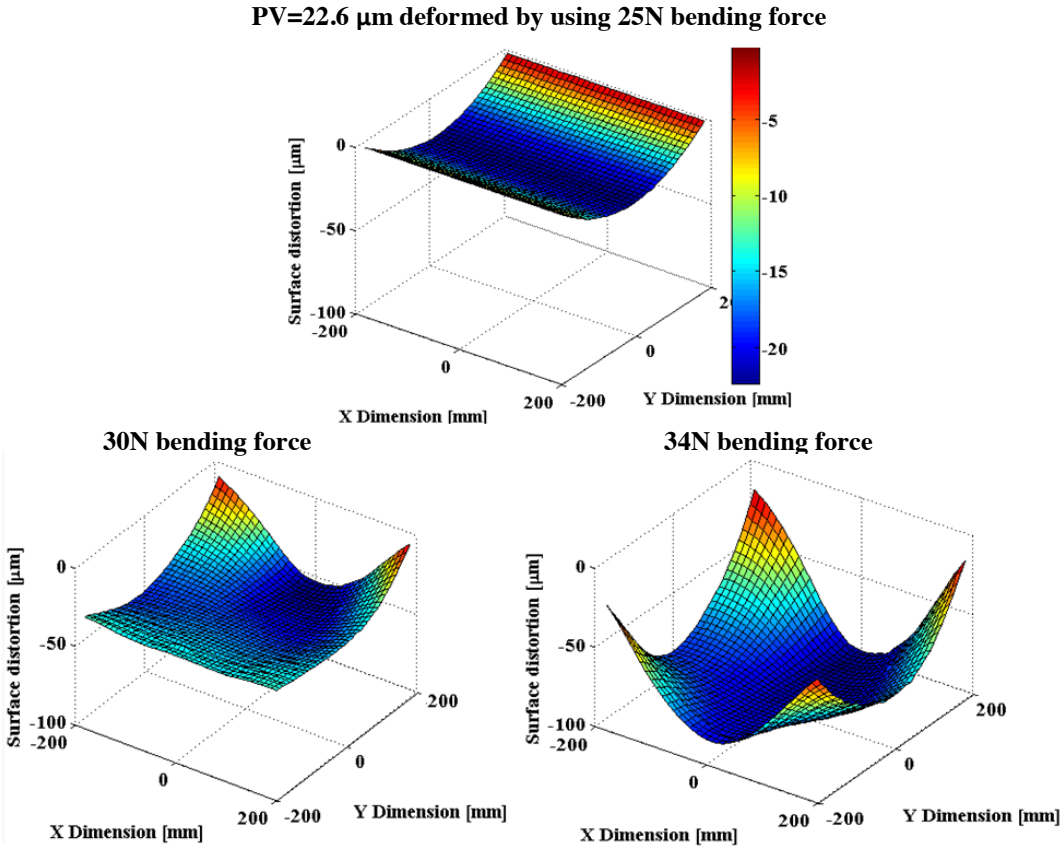

Figure 6-4: Adhesive (Blanchard wax) test

To that end, UniBond and Dow Corning 752 were tested. When testing the characteristics of UniBond and Dow Corning 752, in order to avoid damaging the bending plate, a piece of spare glass cemented with aluminium nut shims was used, as shown in Figure 6-5. From the test, the nut shims secured using UniBond were still barely able to be removed with a blade cut even after heating to 80 ℃. For Dow Corning 752, however, blades were able to separate the adhesion between the glass and the shims without the heating process. Besides, this adhesive can be cleaned by using blades to gently sweep the glass and metal surfaces. Since Dow Corning 752 has higher elastic characterises than the three waxes and is easier to remove than

UniBond, Dow Corning 752 was the adhesive used for the mechanism. Examples of the use of Dow Corning 752 to bend the plate are shown in Section 6.4.1.

Figure 6-5: Testing of adhesives by using nut shims on a spare piece of glass

6.2.1.4 Strengthening the bending mechanism

Since 12 N[17] and 75 N[18] were the two different tool loads that could be used to process the glass, and since the glass used was known to be subject to surface deformation in response to a processing force, it was necessary to test both tools in order to evaluate the surface deformation in the glass. The two tools were statically loaded on the glass, which was then measured using the probing arm, as shown in Figure 6-6. As shown in Figure 6-7, when the 12 N and 75 N tools were loaded onto the glass, the surface was distorted by 165 µm and 260 µm, respectively. In order to reduce this degree of deformation, supports were placed underneath the plate, and

[17] 12 N is the 100 mm diameter tool described in Chapter 4.
[18] 75 N is the 100 mm diameter pad attached to the large tool structure described in Chapter 5.

subsequent to this modification the deformation test results demonstrated that there was no observable surface change. Hence, this mechanism requires support to strengthen the rigidity of both surfaces during processing. The position of the supports in the glass-bending mechanism and the probing arm to measure the surface were shown in Figure 6-6.

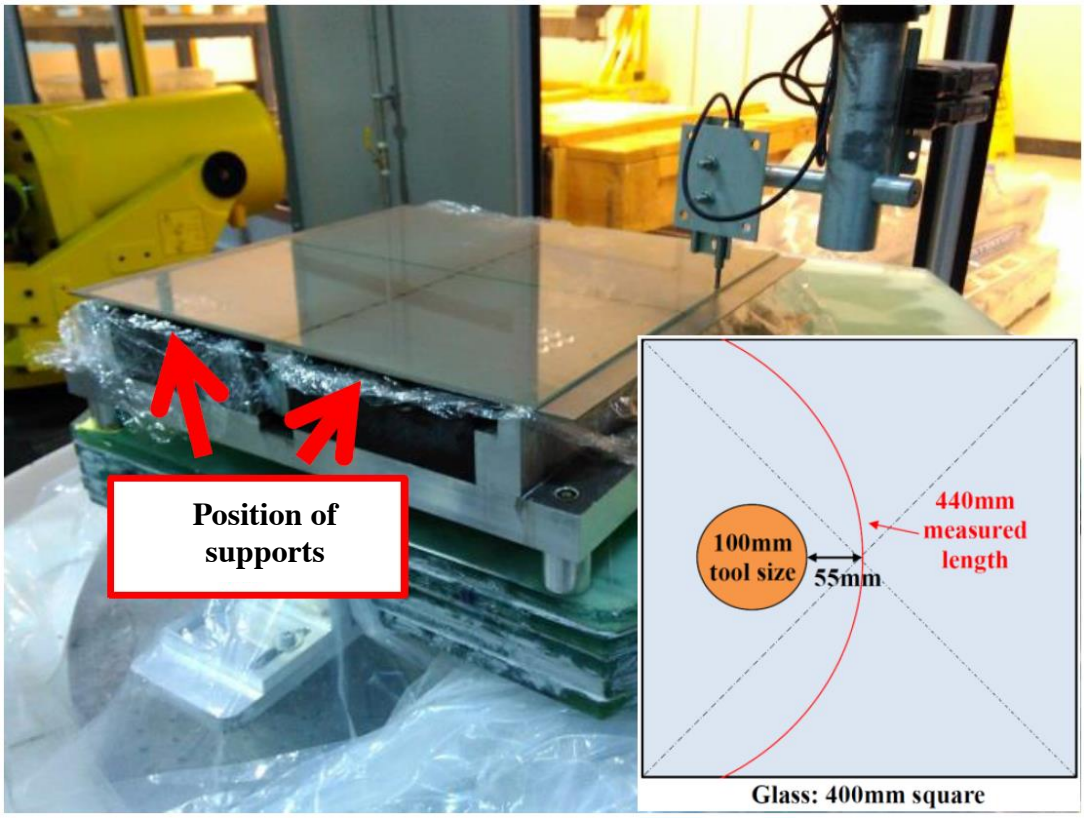

Figure 6-6: Probing arm and glass-bending mechanism

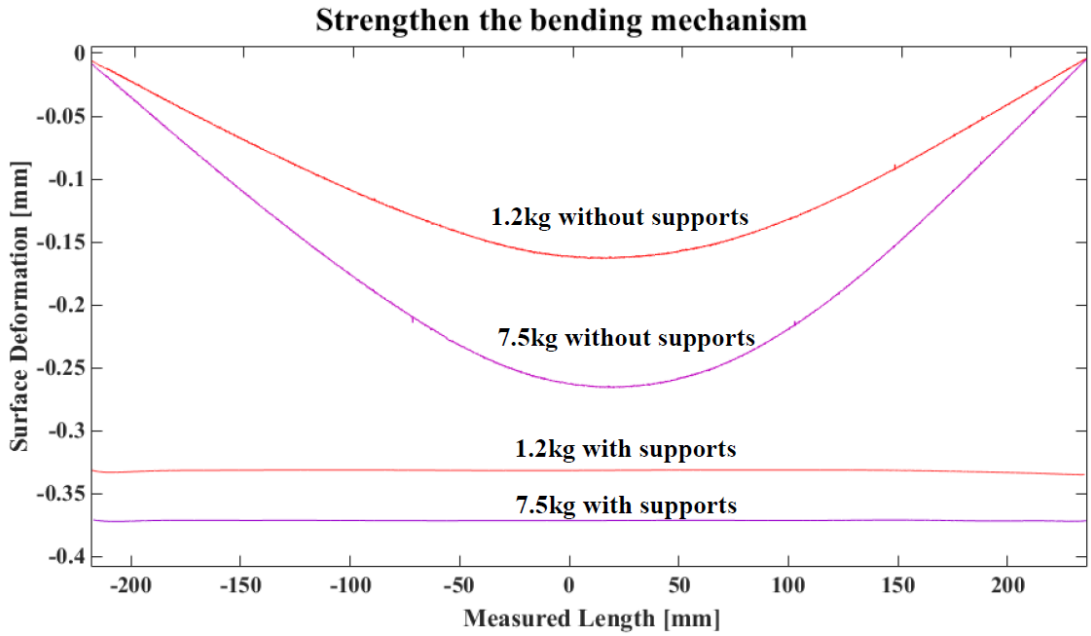

Figure 6-7: Results (with and without supports)

6.2.1.5 Support materials

Three materials were tested to strengthen the mechanism: (1) Diall expanding foam, (2) Skimfill™ (a kind of gypsum) and (3) Isopon™ (P38/1). The expanding foam was tested first. Although the foam was able to expand to fit the gap (the position shown in Figure 6-6), this material was too soft to avoid surface change when the 12 N tool was loaded. Hence, expanding foam was determined not to be appropriate for support and Skimfill was thus evaluated. In respect to Skimfill, even though the material was rigid enough to avoid surface deformation with a static tool load (12 N and 75 N), it decomposed when it was immersed in the slurry and was processed by a dynamic tool. This material might be useful for a dry process, however. Finally, Isopon was then examined. Isopon not only avoided a surface change with the two different loads, but also no decomposition was found during the RGP. Moreover, it

has a quick drying time of less than 40 minutes. Isopon was therefore used to strengthen the rigidity of the bending plate so as to avoid surface distortion during the RGP process. More information about the use of Isopon in the creation of a complex surface form will be discussed in section 6.4.1.

6.2.1.6 Arrangement of the supports

As shown in Figure 6-8, there are two geometries for using Isopon to support the bending plate: (1) localised areas of support and (2) a continuous film. For the first method, the area arrangement for the supports can be a problem. As illustrated in Figure 6-9, when a bonnet is used to polish the surface for the purpose of MSF measurement, the size of the polishing spot cannot be smaller than the distance between the supports, since this would introduce uneven removal and surface distortion or even break the glass in a serious case. The second method is therefore recommended to strengthen the glass-bending mechanism. It is important to mention that Isopon has tenacious adhesive properties, and therefore it needs to be isolated by plastic films so that the setup can be reversed.

(2) Localized areas of support

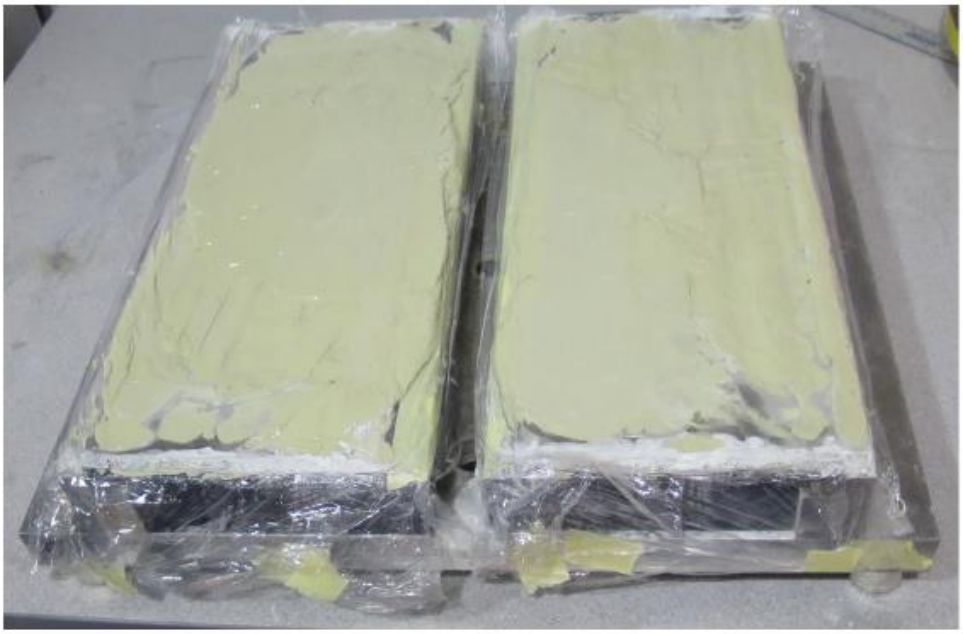

(1) Continuous film

Figure 6-8: Arrangement of the support

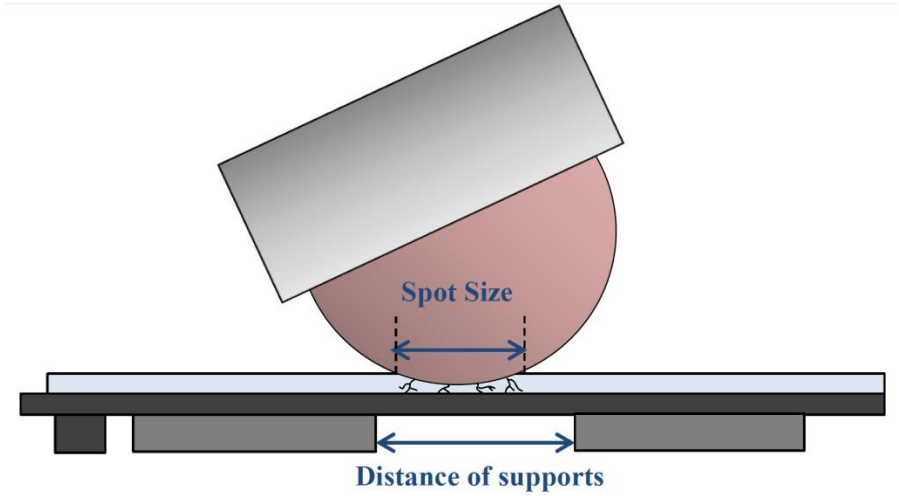

Figure 6-9: Problems of localised areas of support

6.2.1.7 MSF Measurement

In general, there are two methods to measure MSF: contact and non-contact methods (please refer to Section 2.5). When using a stylus instrument, such as Talysurf or Talysurf Intra, the two instruments are unable to resolve MSF smaller than PV 300 nm and 100 nm respectively. In the case of Talysurf, the limitation of the instrument is 300 nm so MSF smaller than that value are unable to be resolved. For the Talysurf Intra, the limitation arises from a rough surface texture in the grolished surface (usually S_a> 300 nm) which means that MSF signals can become swamped by background noise and are difficult to filter out. The proposed solution for this is to polish a grolished surface so as to reduce background noise. Notwithstanding this, the Talysurf Intra was not the main equipment used in this study to measure MSF from a polished surface. The main function of the Talysurf Intra is to confirm the MSF measured from the 4D interferometer and, in some cases, to analyse specific

areas that the 4D interferometer could not measure due to poorly localised surface topographies. Hence, the Talysurf Intra was considered as a backup solution.

This paragraph discusses two strategies to improve the image contrast when using interference fringes to calculate MSF. Firstly, it is important to avoid double reflection from the back specular surface because both the back and front surfaces can interfere with each other, which serves to increase difficulties in measurement. The purpose is to measure MSF generated by the grolishing process on the front surface. In order to remove the unnecessary signals from the back surface, it was necessary to increase the roughness of the back surface so as to avoid the double reflection effect. Secondly, it was found that the image contrast was always too low, even when the gain and power of the 4D interferometer camera (i.e. PhaseCam® Model 6000) were adjusted. This was because most of the light was absorbed by the adhesive. The solution for this was to paint the (now roughened) back surface black so as to increase the reflection rate to allow more light from the front surface back to the interferometer and thus increase the image contrast. As shown in Figure 6-10, painting the back surface black can increase fringe image contrast.

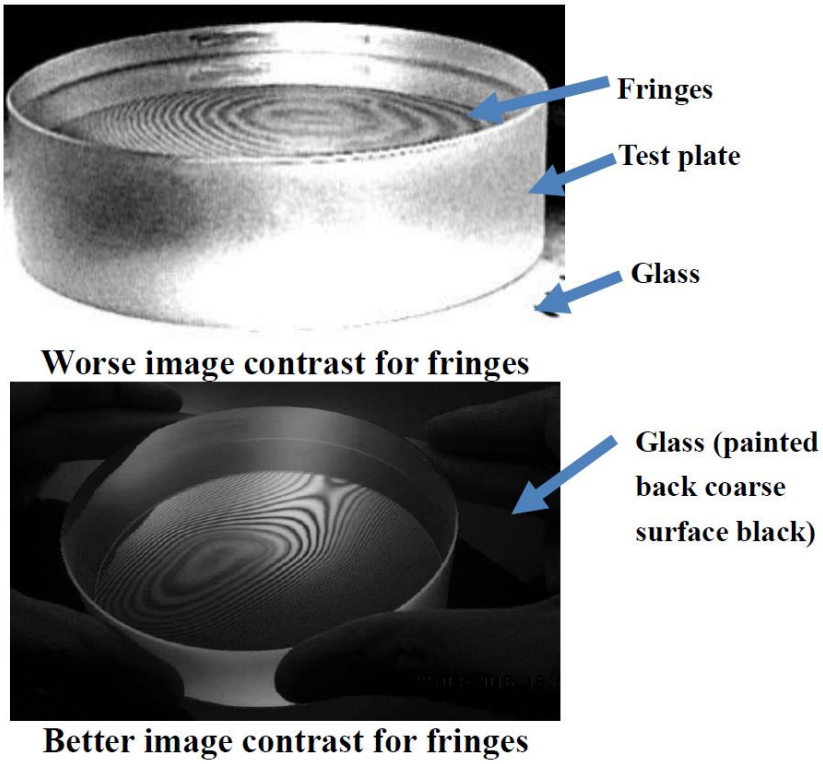

Figure 6-10: Comparison of image contrast for fringes

Before using the interferometer, a test plate was used for initial preparation in order to optimise the use of the interferometer. When using the test plate, a force of 10~60 N was used to press the test plate or bending plate, or both, so that the two surfaces (glass and test plate) were as close as possible to infinite contact with each other, meaning that there were fewer fringes for the calculation of MSF. Even so, it was difficult to measure MSF using the test plate: the lowest number of fringes observed across the 100 mm diameter test plate was 15, but these were still too densely packed to be distinguished by the naked eye and thus to calculate MSF values.

In this context, the 4D interferometer and 4Sight Data Analysis Software offer a stable method to calculate MSF from such a polished surface. The 4D interferometer is used to measure a flat surface, and therefore the glass is required to be bent to be

nominally flat in order to be measured by the 4D interferometer. Figure 6-11 illustrates the principle of reforming the localised surface to a nominally flat one so that the regional area is able to be detected by the 4D interferometer. Since the glass can be a concave form, a support underneath the bending plate would minimise the localised aspheric slope, rendering it to be close to a flat surface.

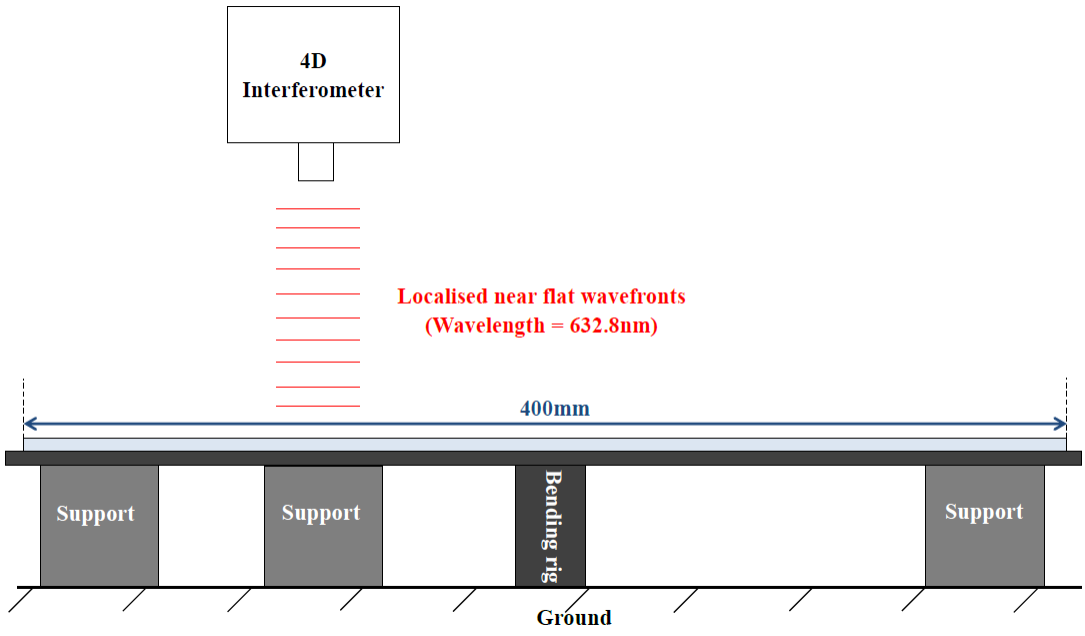

Figure 6-11: The principle of reforming the localised surface for MSF measurement

An example MSF measurement is shown in Figure 6-12. In this method, a clear aperture of up to 60 mm diameter can be used, and up to 35 Zernike terms are able to be removed to calculate MSF easily (as has been fully discussed in Section 4.2.4). The result of this measurement is shown in Figure 6-13.

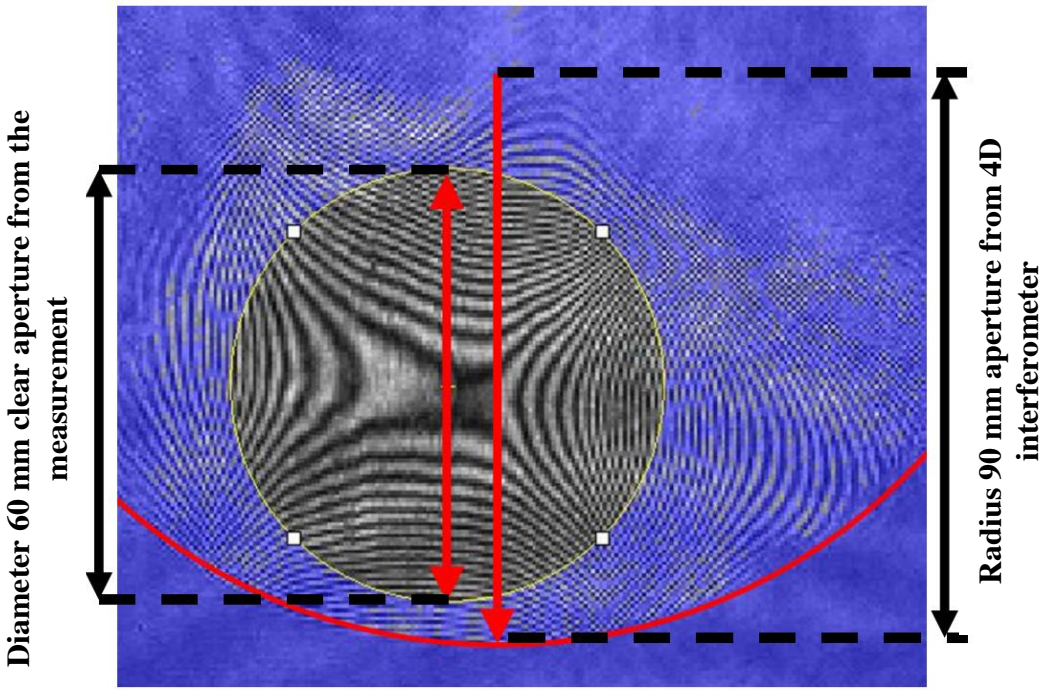

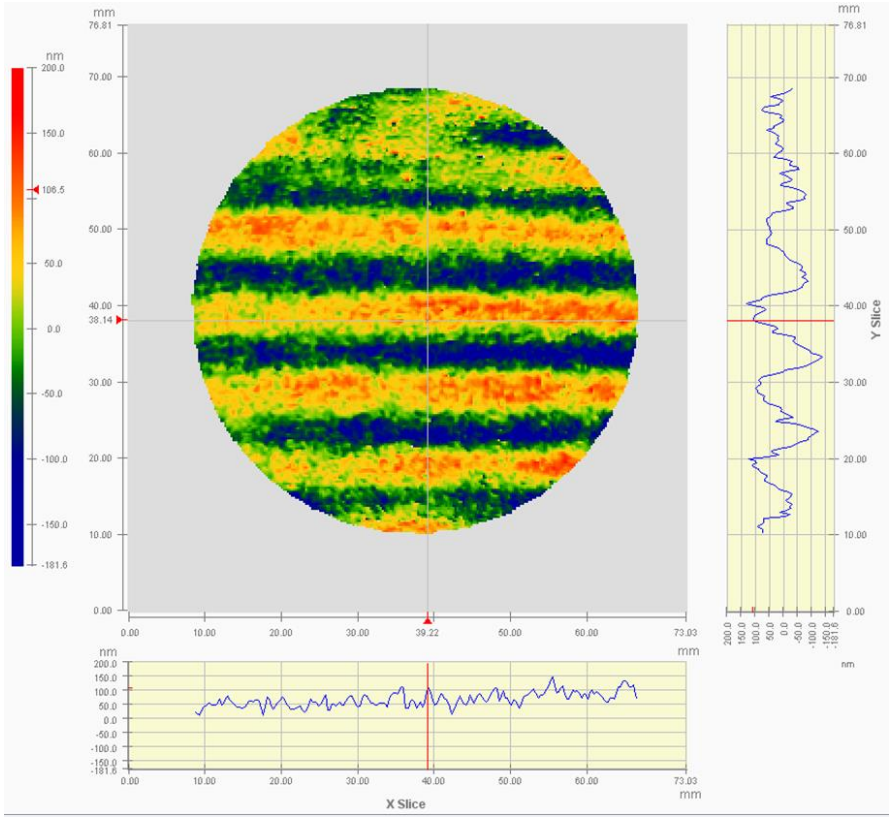

Figure 6-13: MSF measurement after removing 35 Zernike terms

6.2.2 Summary of using the glass-bending mechanism

The glass-bending mechanism aimed to create a complex surface form. To achieve the goal, adhesives were required to cement the glass and the bending plate together, as well as materials to support the bending surfaces. In addition, new techniques needed to be devised to measure aspheric surfaces for MSF calculations. The problems and solutions are summarised in Table 6-1.

Table 6-1: Summary of the problems and solutions for the glass-bending mechanism

Processing difficulties are listed in the following		
Problems	**Solutions**	**Results**
Double reflection from the thin glass	Grey one side of the glass to avoid double reflection	Problem solved
Methods to cement the glass to the bending rig	Challenge: The ideal adhesive should be easily removed to allow the glass to be removed from the glass-bending mechanism.	(1) Soft wax: breaks during the bending process (2) Medium wax: breaks during the bending process (3) Blanchard wax: 30μm is the maximum bending. If over 30μm, the wax breaks (4) UniBond: extremely difficult to remove the adhesive without breaking the glass (5) Dow Corning 752: can bend a surface up to 200μm

Distorted surfaces	Add support to the bending mechanism	Investigating: (1) Expanding foam: too soft to be an adequate support (2) SkimFill™: not suitable for wet grolishing but a potential backup material to produce other desired surfaces (3) Isopon: proven current material
Discrete areas of support	Localised areas of support	Proved not to be suitable for polishing: the gap between supports can cause uneven removal during polishing
	Continuous film	Problem solved
Measurement difficulties are listed in the following		
Measurement difficulties	**Measurement method**	**Results**
	Poor contrast under interferometer	Blacken the back surface to decrease the scattered background light
	Talysurf Intra	Backup solution. The instrument can measure MSF errors if MSF amplitudes are greater than PV=100 nm.
	Poor contrast under interferometer	Blacken the back surface to increase the intensity of the reflection light
	Test plate	Backup solution. The drawback is that the MSF value is difficult to quantify

	4D interferometer	Can be a viable method to analyse MSF errors when using regional aperture (e.g. 60 mm) and adjusting the surface by providing external pressure.

6.3 Process flow for using the glass-bending mechanism

This section introduces the experimental design and the processes for using the glass-bending mechanism in order to investigate the abrasive effects when processing a complex surface. The experimental procedures are set out in detail in Figure 6-14 but can be summarised into four main areas: (1) steps 1 to 4: preparing and creating a complex surface (discussed in Section 6.2 and conducted in Section 6.4.1); (2) steps 5 to 6: pre-grolishing (i.e. a tool-configuring process) to optimise the tool surface (demonstrated in section 6.4.3); (3) steps 7 to 11: the grolishing experiment to study the abrasive effects on the complex surface (demonstrated in Sections 6.4.4 and 6.4.5); (4) step 12: smoothing of the surface to remove MSF signatures left by the grolishing processes.

Removal of the residual MSF from a grolishing process can be achieved by using a tool larger than the MSF spatial spacing. In this study, a 300 mm tool was used to remove the MSF signatures left from the 100 mm grolishing tool. Figure 6-15 shows an example (with 35 Zernike terms removed) using a 300 mm tool to remove the residual MSF generated from the 100 mm tool. After that, the procedure had to return to step 1 for any remaining experiments.

Figure 6-14: Procedures for using the glass-bending mechanism for an experiment

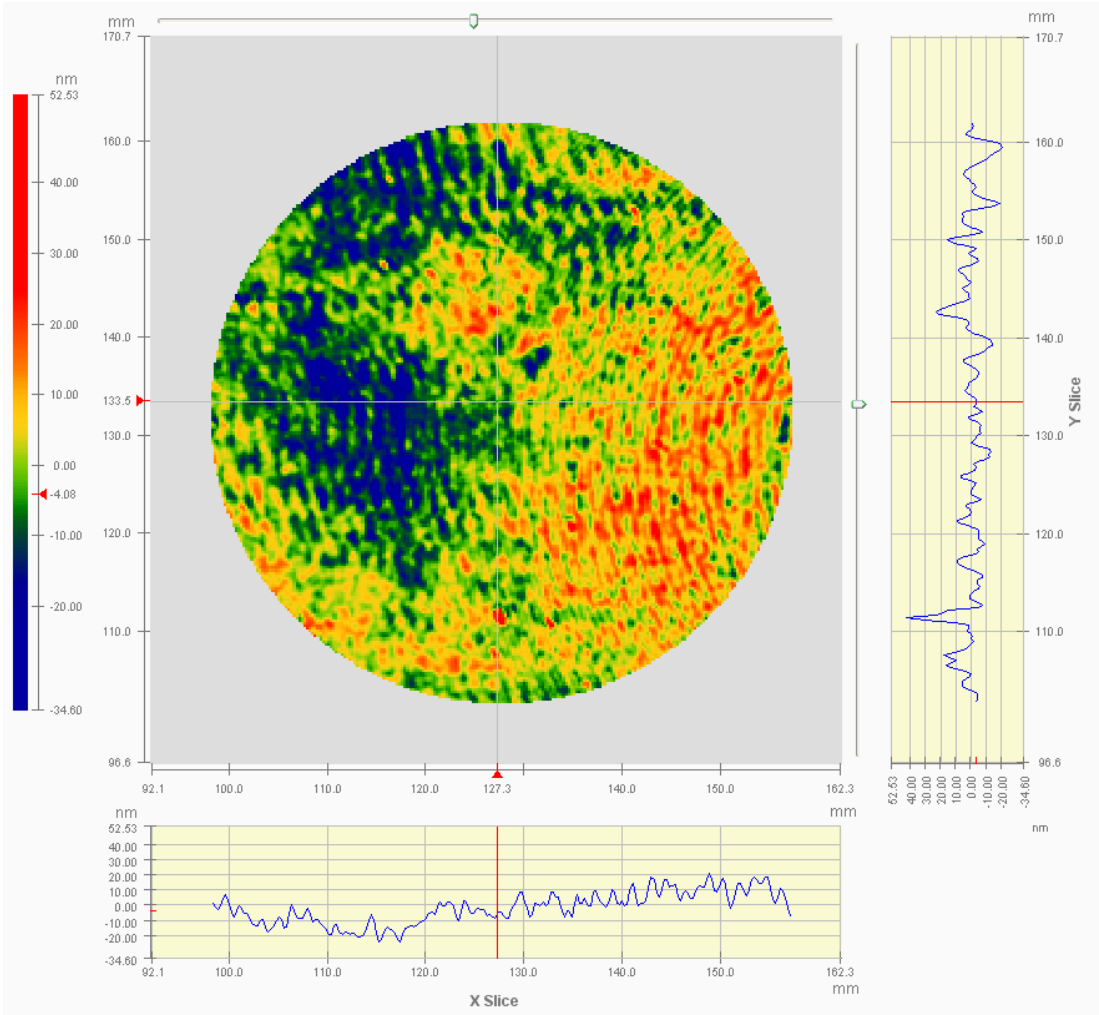

Figure 6-15: Remove cusping MSF features left from the 100 mm tool

6.4 Experiments and results

When processing a non-symmetric optical surface, such as aspherical or other complex surfaces, aspheric misfits always exist between the rotating tool and the surface; these misfits lead to MSF signatures on the surface that in turn lower the diffraction limit of the system. The proposed method to minimise the misfit and thus to achieve smaller MSF errors when processing non-symmetrical surfaces is to use

large abrasive sizes that fit the gap between the tool and the surface (conventional methods have been discussed in Section 6.1). The experiments are demonstrated in this section.

6.4.1 Creating a complex surface

The aim of this section (including the subsections from Section 6.4.1 to Section 6.4.5) is to create a complex surface. Seeking a method to produce a specific surface form is not the purpose of this section, however. The created complex surface (e.g. saddle surfaces) was used to characterise MSF on different misfits when a rotating rigid tool was used to process the complex surface.

Three significant variables were keys to creating a complex surface: the screw setting (i.e. the bending force), the amount of Isopon (about 600 ml) and the three extra loads (each weight is 1.5 kg) on the glass during the Isopon drying process. The bending force was varied to produce a near cylindrical concave surface (discussed in Section 6.2.1). The amount of Isopon and the extra load on the glass were the variables that dictated the push and adjust forces to create a complex surface, and these are discussed in the following paragraphs.

It was found that the volume of Isopon expands during its drying process. If the continuous film method is used for the support (please refer to Section 6.2.1), the expansion of the Isopon could be used to push the surface into a near cylindrical convex form. The principle of the expanding effect of the Isopon is illustrated in Figure 6-16 and the result is shown in Figure 6-17. This experiment demonstrated

that the Isopon expanding effect is a significant variable in creating a complex surface.

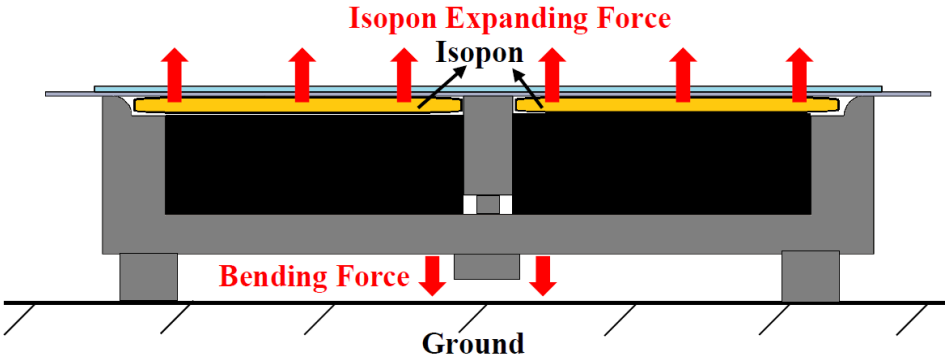

Figure 6-16: Principle of the expanding Isopon effect

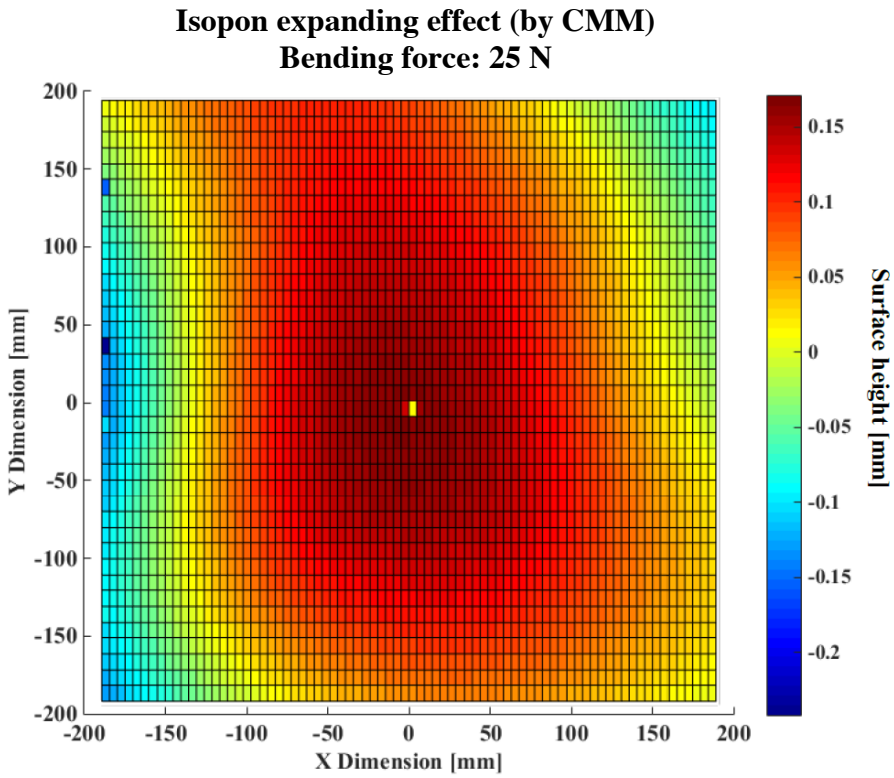

Figure 6-17: A near cylinder surface created by the expanding Isopon effect

When a 35 N bending force was combined with 3 × 15 N extra loads on the glass during the Isopon drying process, a saddle surface was created, as shown in Figure 6-18 and Figure 6-19. The two surfaces were measured after the pre-grolishing process and were used to calculate the aspheric misfit between the pad (Figure 6-21) and the glass surfaces.

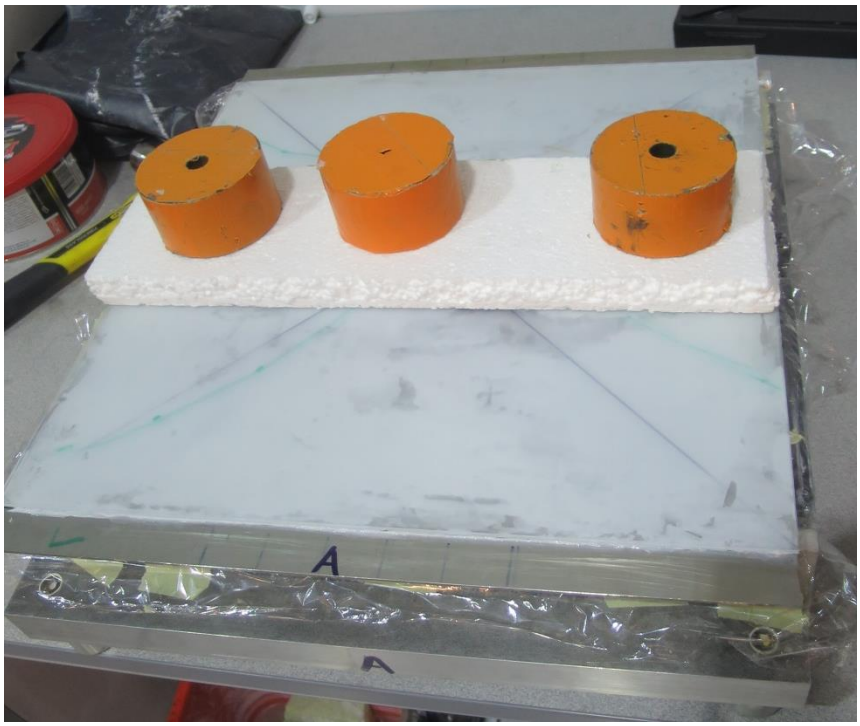

Figure 6-18: Three extra loads on the glass during the Isopon drying process

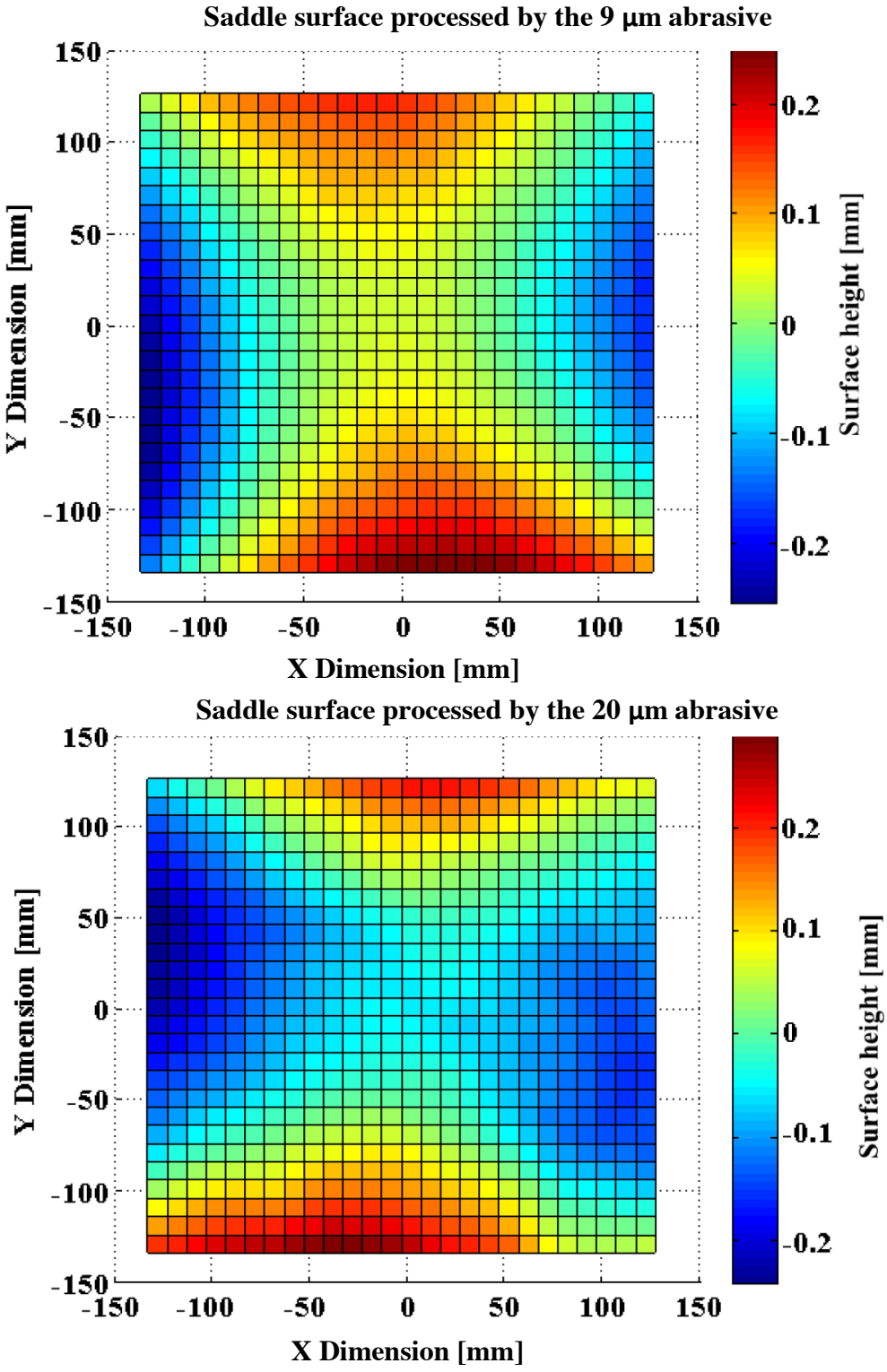

Figure 6-19: Two saddle surfaces processed by 9 μm and 20 μm abrasives (measured by the Zeeko IRP 1200 machine)

6.4.2 Parameters for grolishing and polishing

Figure 6-20 shows the grolishing and polishing processes on the glass-bending mechanism. In Chapter 4, the 100 mm diameter tool was used to process 400 mm hexagonal surfaces with a repeatability of more than 95% in respect to removal rate, surface texture, edges and MSF. To that end, this tool was further applied here to process the two saddle surfaces. The grolishing parameters also replicated those in Chapter 4 and are presented in Table 6-2, in order to allow measurement by the 4D interferometer and analysis by the 4Sight Data Analysis Software.

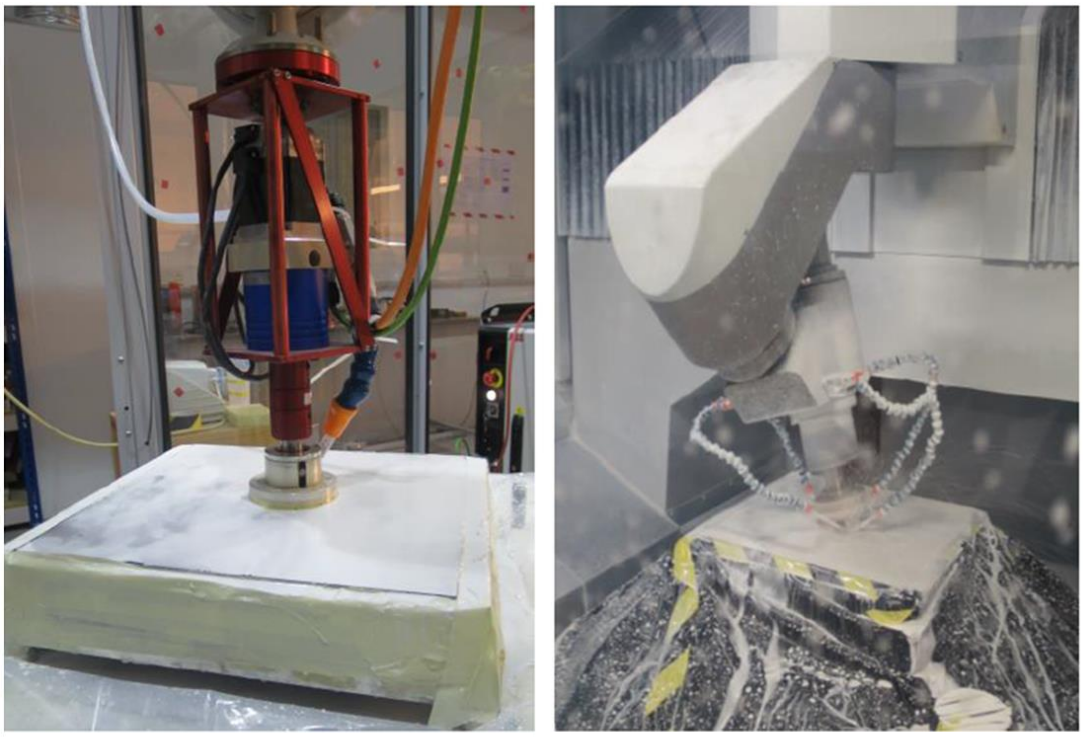

Grolishing by a robot **Polishing by an IRP 1200 CNC machine**

Figure 6-20: Grolishing and polishing for the glass-bending mechanism

Table 6-2: Variables for processing saddle surfaces

Variables		
9 μm and 20 μm Al_2O_3 abrasive		
Controlled variables		
1000 g load	10 mm track space	4500 mm/min tool feed
600 rpm spindle speed	100 mm diameter tool	400 mm square glass

After the grolishing process, the surface was polished to be specular so that it could be measured by the 4D interferometer and beam expander. The parameters shown in Table 6-3 were able to polish a grey grolished surface (S_a = 620 nm) into a shiny surface (S_a = 85nm) in one polishing run (73 minutes).

Table 6-3: Polishing parameters used

Controlled variables		
15° process angle	1 mm point spacing	7 mm tool offset
Raster tool path	1 mm track space	800 mm/min tool feed
1000 rpm spindle speed	R80 bonnet	400 mm square glass

6.4.3 Pad surface

In order to calculate the misfit between a rotating tool and surface, the tool surface was measured, as shown in Figure 6-21. The pad surface must be symmetrical as it rotates to grolish a surface. Two parallel measurements can be used to compare and contrast in order to confirm the centre measurement.

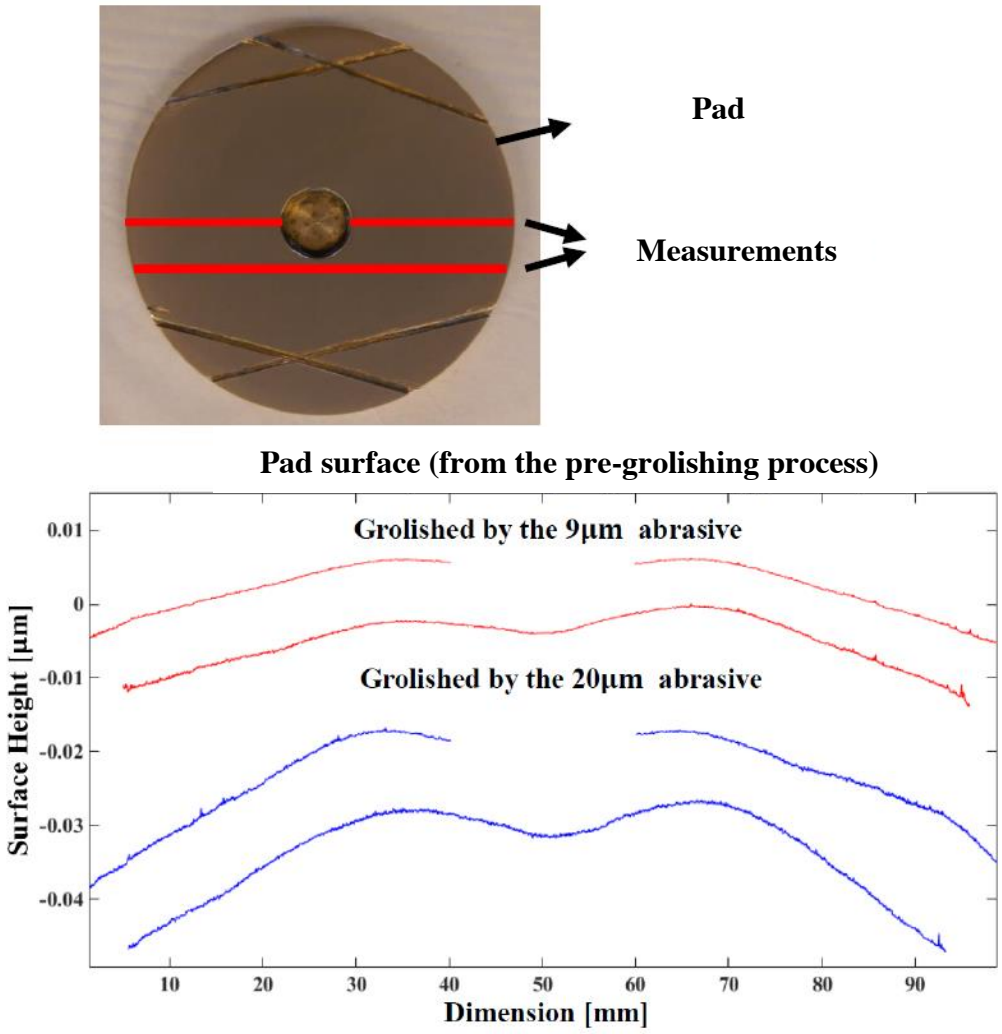

Figure 6-21: Pad surface profile measured (convex) after the pre-grolishing process

The W surface profile from the pad was reasonable: firstly, the outer part of the radius of the pad had a higher velocity, resulting in greater pad wear than the inner areas. Secondly, it can be observed that pad wear near the centre hole area was larger than that near the centre zone. This is because when the tool was dragged by a robotic arm with a tool feed, the denser slurry at the centre hole results in higher pad wears than in the surrounding area, as illustrated in Figure 6-22. For the above two reasons, and since the peripheral speed is much higher than the centre, the W form measurement in Figure 6-21 can be realised.

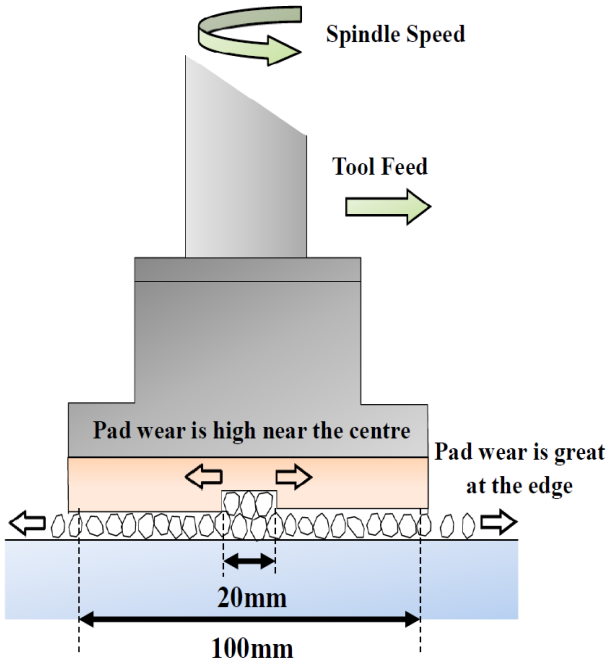

Figure 6-22: The principle of pad removal

In fact, the 'W' form is very similar to that created by pole-down-polishing using a bonnet tool with a 0° precession angle [33]. One difference is that the pressure goes to zero at the edge of the polishing spot [167], but the pressure for the grolishing spot

is not zero [227] (more detail regarding pressure distribution for grolishing tools can be found in Chapter 5 and [227]). The other difference between the two is that one W profile is measured from the pad and the other is from a workpiece. To this end, it can be furthered inferred that pad wear is the inverse of the removal function on a glass surface. Hence, investigation of the pad wear can be another new strategy to understand a grolishing process, such as slurry migration, surface removal, MSF and surface texture. The study of pad wear has been used to investigate the 280 mm diameter large tool in Chapter 5 as well as to simulate the geometry of pad grooves for use in the smoothing process in [227].

6.4.4 MSF and surface removal

When measuring MSF errors, the measurement is ideally perpendicular to the MSF direction. Moreover, it is important to confirm that the MSF has to (1) be parallel to the raster tool path and (2) that the MSF spatial region is 0.1 mm^{-1} because of the 10 mm raster track spacing. From the experiments, it was found that the MSF errors from the pre-grolishing process could be removed by the subsequent post-grolishing process (i.e. step 10 in Figure 6-14) by using the same parameters as in Table 6-2 but with a perpendicular processing direction. MSF errors generated from the post-grolishing were found on the glass surface, however: one example is shown in Figure 6-13. More data regarding the MSF measurements for the two processes can be found in [225].

The glass removal depth must be measured in order to compare the MSF errors generated by the post-grolishing process using 9 μm and 20 μm abrasives respectively. MSF had to be scaled by removal depth, instead of removal rate, because, even though the time for the experiments was exactly the same, it was still difficult to control all other factors affecting the removal rate to be equal. As shown in Figure 6-19, the surface forms for each experiment were not exactly the same, and the pad surfaces were also not equal, as demonstrated in Figure 6-21. The removal depth was therefore the correct way to scale MSF to put all the results on a truly comparative basis. Removal topographies for the two processes are shown in Figure 6-23.

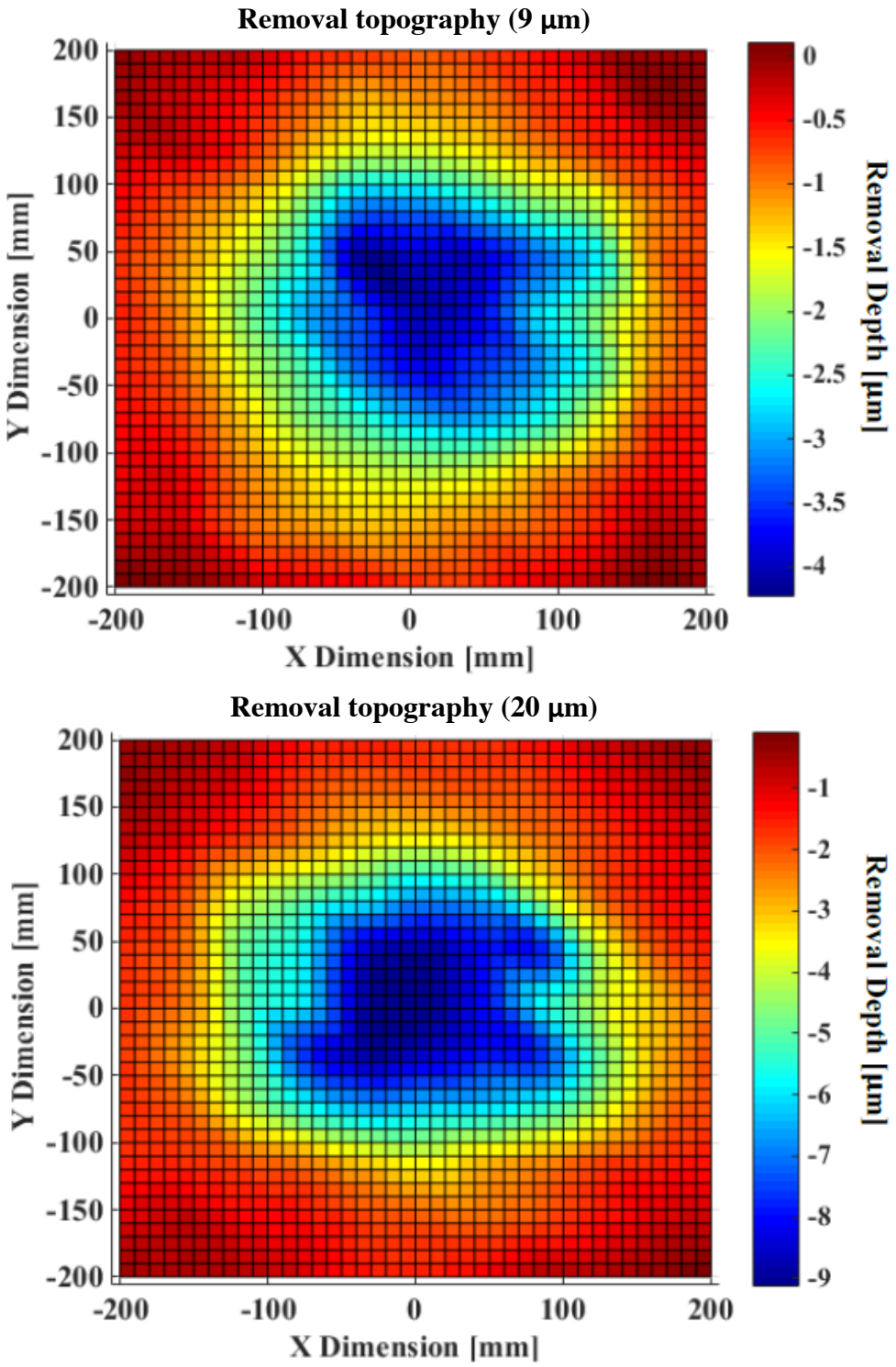

Figure 6-23: Removal topography

6.4.5 Data analysis and discussion

Conventionally, MSF errors can be suppressed by providing for reduced removal depth in a process when using a sub-aperture tool. This is the main reason why the polishing comes after the grinding, and the MRF or IBF comes after the polishing, in order to gradually improve the surface characteristics such as form and surface texture (including MSF). If the MSF generated from each process were scaled according to the relative rates of removal, however, it is obvious that the highest removing efficiency is grinding, and then polishing, and finally MRF and IBF (please refer to Section 2.4 for each specific process and process efficiency).

Instead of reducing the removal, the emphasis of this experiment is to provide a new approach to suppressing or eliminating MSF when grolishing aspheric surfaces by using larger abrasives with larger tools than the traditional methods (discussed in Section 6.1). For a like-for-like comparison, therefore, MSFs should be scaled according to the removal depths.

The data from section 6.4.1 to section 6.4.4 are summarised in Figure 6-24. Since misfits would exist when processing the two complex surfaces (RMS misfit > 6.2 μm), in order to verify the starting point conditions of this experiment, seven data points (1.8 μm > RMS misfit > 1.0 μm) for each abrasive process were selected from Chapter 4 and are considered in Figure 6-24.

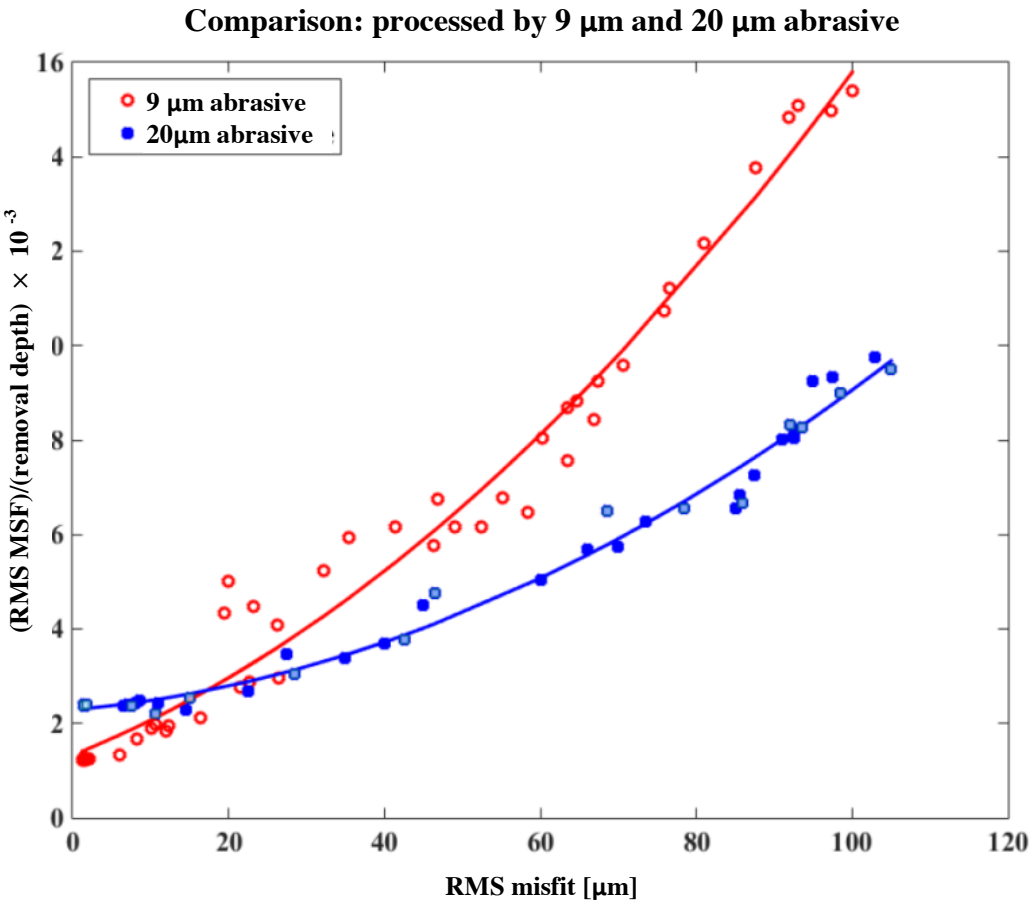

Figure 6-24: Comparison: processed by the 9 μm and 20 μm abrasives, respectively

When misfits are small, the data from both the symmetric surfaces (i.e. nominally, with zero misfit) and the complex surfaces have similar MSF values, indicating that the experimental result is reasonable. When processing symmetric surfaces, small MSF values can be achieved by controlling the removal function. This can be determined by load, spindle speed, travel feed, overlapping tool path, small abrasive size, shape, material and density, as well as the tools used. Controlling these variables to achieve small MSF in nominally flat surfaces has been demonstrated in Chapter 4.

When an aspheric departure becomes obvious (i.e. misfits increase), the MSF value increases, indicating difficulty in controlling MSF. The traditional method to remove MSF in a CNC process is to use a small tool applied with small abrasive sizes. The removing efficiency decreases, however, since the tool and abrasive are both small, resulting in increased overall processing time. In summary, this experiment provides a new solution for processing large aspheric departures: showing that a large abrasive size can fill the misfit between the tool and glass surfaces to achieve small MSF whilst also having the advantage of a high removal rate, as shown in Figure 6-23.

6.4.5.1 **Overlapping track space**

This section further investigates the conventional method to reduce MSF errors when the aspheric misfit is large. Traditionally, one frequently used method to control MSF is to overlap track space. This section discusses this overlapping track space method for use to suppress MSF in a large aspheric departure surface.

Since one traditional method to control MSF is to use a small abrasive, the abrasive size was controlled to 9 μm, instead of 20 μm. The examined variable was the raster track spaces, which were 10 mm and 5 mm, respectively. Experimental results are shown in Figure 6-25.

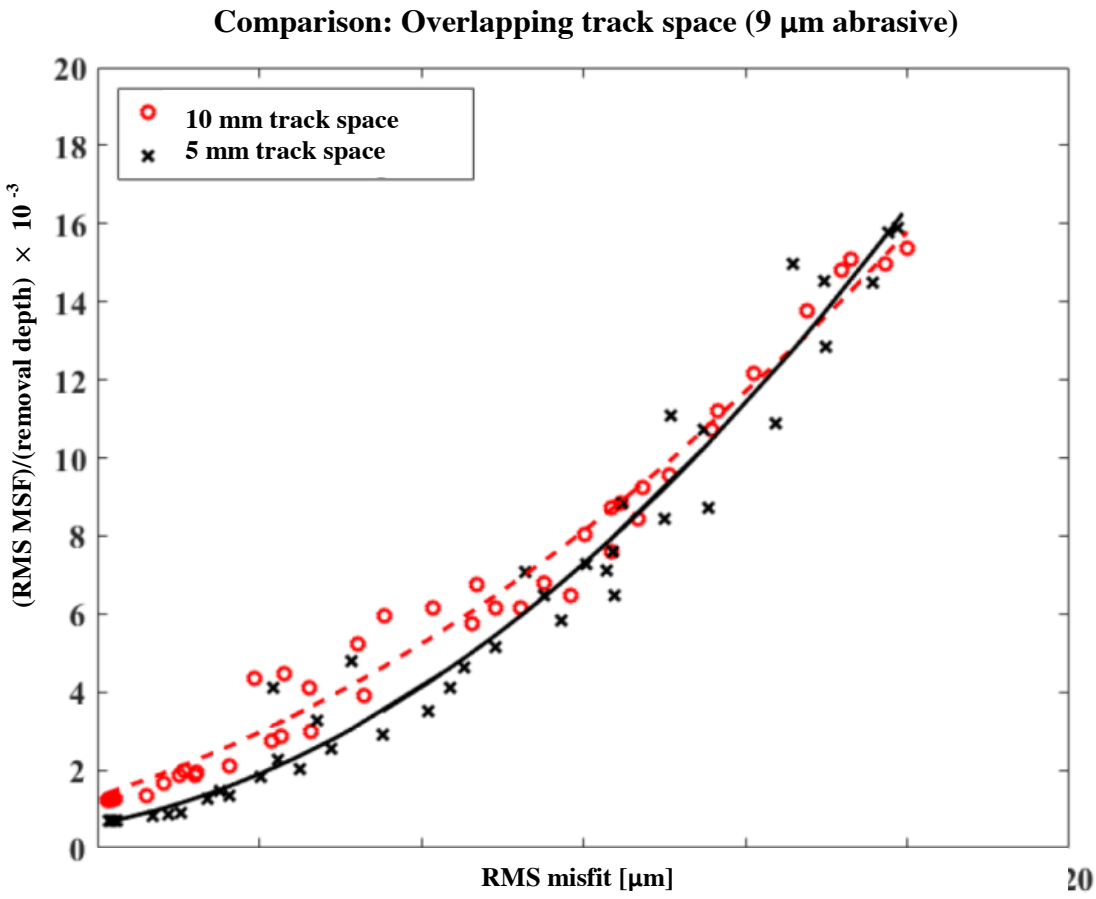

Figure 6-25: Comparison: Overlapping track space

The result shows that using overlapping track space to control MSF can be a useful method when the misfit is small. For example, as demonstrated in Chapter 4, the MSF can be reduced by using overlapping track space. When the asymmetric slope is significantly increased (e.g. aspherical surfaces), however, the overlapping track space cannot achieve smaller MSF. This summary can also explain the reason why MSF is usually found in those localised areas where there has been the greatest aspheric departure in the surface. To solve this problem, (1) a large abrasive size (as demonstrated in Figure 6-24), (2) small tool diameter, and (3) added flexibility to the

tool (e.g. stressed-lap or Non-Newtonian tools) can be optimised methods to control MSF effectively when processing aspherical surfaces.

6.5 Summary

In this chapter a novel glass-bending mechanism has been demonstrated that is able to create a complex surface form in a new way encompassing various manufacturing machines (such as two Fanuc and one ABB robot arms, Zeeko IRP 600 and 1200 machines) and testing equipment (such as CMM or probing arm, 4D interferometer and test plate). In addition, the experiment has successfully demonstrated that large abrasive sizes cannot only reduce the misfit between the tool and surface to achieve smaller MSF but also decrease the time to remove MSF because of the high removal rate. This result shows that the RGP is an ideal process to smooth the transition from grinding to polishing for aspheric surfaces as well as providing a new solution to process metre-scale large aspherical departures in the future.

Chapter 7 Conclusion and future work

7.1 Conclusion and future applications

The significant problem compromising the overall processing efficiency of glass grinding and polishing processes is that the hard contact between CNC grinding and glass produces sub-surface damage and texture that CNC grinding will never remove. Even though polishing can improve such a ground surface, the process is very slow. The aim of this thesis has been to introduce a new processing method lying between CNC grinding and CNC polishing in order to speed up overall manufacturing efficiency. During the course of the thesis, the novelty of the developed RGP using loose abrasive has been demonstrated. Firstly, the proposed specification for the grolishing has been demonstrated to be achievable and repeatable, showing that the process has been reliably established. Secondly, the relationship between the grolishing outcomes and metrology has been demonstrated on a flat metre-scale prototype hexagonal segment. Lastly, an innovative method to investigate the use of hard tools to control MSFs on complex surfaces has been realised.

7.1.1 The RGP development

The hard contact between CNC grinding and glass can produce SSD and texture that CNC grinding will never remove. The successful development of the RGP is mainly attributed to three key features that allow it to provide superior surface quality than

grinding before passing on to a polishing process to figure the optical segments and improve textures.

The first key feature was the establishment of the proposed role (i.e. the specification) of the RGP in the whole processing chain from grinding to polishing and then the clear definition of IBF or MRF, as shown in Figure 7-1. There were a total of five responses that had to be controlled in the RGP: (1) VRR > 16.9 mm^3/min was required to achieve better efficiency than grinding in respect to the removal of the required materials. (2) an S_a < 400 nm had to be polished into a specular surface and then measured by an interferometer in one polishing run based on the current bonnet polishing technology (3) Form and edges had to be PV < 3 μm, gentle and smooth, allowing for improvement by the subsequent polishing processes. (4) MSF in the spatial region of 0.02 mm^{-1} < MSF < 1 mm^{-1} was required so as to be controlled to be lower than the diffraction-limit (i.e. MSF amplitude < 40 nm)

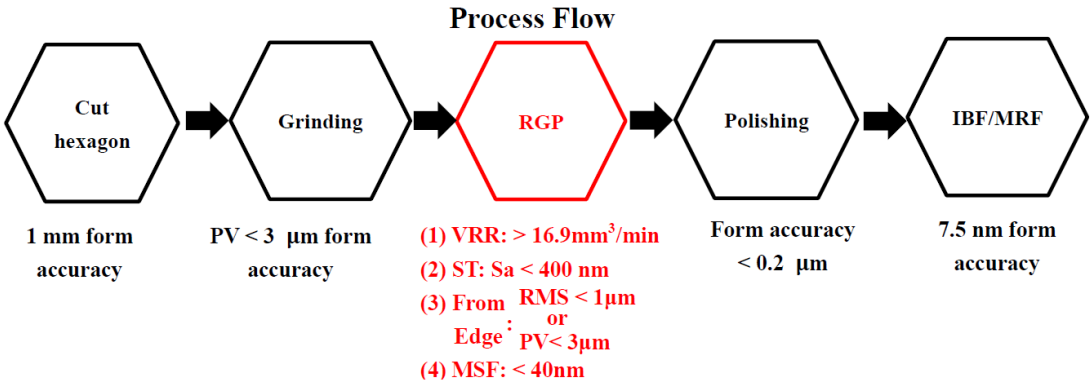

Figure 7-1: The role of RGP in the process flow

The second key element was the construction of empirical models using statistical experimental designs and analysis to demonstrate that the reliable RGP had been

established. The principle is summarised in Figure 7-2. The first step was to review potential significant variables, which were then evaluated by the subsequent screening experiments and analysed by ANOVA. After determining the significant variables, the next step was to conduct confirmation experiments to evaluate the significant variables. The following process used regression analysis to transform the experimental data into empirical models for optimisation (optimised parameters can be determined from this stage). Finally, it was necessary to assess the repeatability and evaluate outputs to prove that the final RGP was a stable and robust process. In the future, data clouds will be created by using this method for process automation, so that an artificially intelligent machine can choose parameters from this data cloud without human intervention.

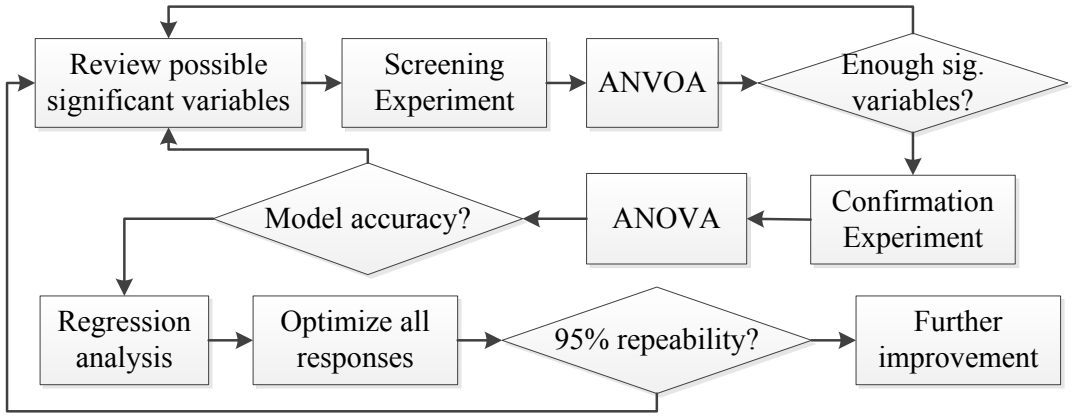

Figure 7-2: Principle of the statistical experimental design and analysis

The third key element was to determine the pivot mechanism of the grolishing tool. This kind of tool is able to alter its angle so as to adapt to any local slope and to remove regional surface errors, such as scratches, defects and MSF. In this thesis, a

100 mm diameter tool was used to meet the specification in Figure 7-1 and thus to demonstrate control of MSF in complex surfaces. A 280 mm diameter tool, based on a similar tooling mechanism, was also used to process the 1 m hexagonal segment. Semi-rigid pads were applied to this tool to remove MSF.

7.1.2 Processing a 1 m hexagon and metrology methods

Having established the process and advantages of the 100 mm diameter tooling, the additional 280 mm grolishing tool was devised and used to process the 1 m hexagonal segment so as to assess the pad wear effects, removability of MSF, and removal efficiency, with this being measured by a novel prototype metre-scale measuring system.

Firstly, the simulation model showed that the original pads (i.e. a pure disc with any pattern) and grooved pads were recommended for slow and high spindle speeds, respectively, by comparing with four different grooved patterns [227]. The experimental results confirmed the simulations, showing that the optimised spindle speed for the grooved pad was 70 rpm, which was higher than that for the original pad by a factor of 3.5. Specifically, the principle of pad-wear effects could be understood from the models. When spindle speeds were higher than the optimised values, the irregular pad surfaces could be fully explained by the models, showing that all the simulations were correct and could be guidelines for future processes.

Secondly, with the selected parameters, the 280 mm tool was able to (1) remove the MSF left over from the grinding, (2) achieve an accurate surface with a PV = 5.3 μm,

up-stand, smooth and gentle surfaces, which could be easily processed by the following processes (such as the 100 mm grolishing tooling or polishing), and (3) attain the required efficiency of VRR = 174.2 mm^3/min in (4) 30 minutes. All these results have demonstrated that the RGP has been developed to process metre-scale optical surfaces.

Thirdly, the prototype metre-scale measuring system was constructed.[19] By using the proposed method, the maximum measuring time per run for the 1 m segment was 1 hr, showing that a 1.45 m hexagon would be able to be fully measured in a day. Moreover, two different (conventional and proposed) algorithms were used to construct surfaces and calculate their volumes. These helped to substantiate the development of non-destructive testing.

7.1.3 Controlling MSF in complex surfaces

A new glass-bending mechanism was created to shorten the time needed to produce complex surfaces. Multiple technologies were evaluated in this mechanism, such as the use of Dow Corning 752 to cement the bending plate and glass, the use of Isopon to support the glass, and the blackening and reforming of the glass to allow it to be measured using an interferometer. The achievement of this mechanism is not limited to the production of surfaces, but could also be applied to test material characteristics, such as stress performances. Stress is an obvious guideline to understand the amount of loads and velocity that can be used for tooling to avoid glass breakage, which is

[19] The author acknowledges Peng Zhang's contribution in developing the hardware.

important so as to be able to process the thin glass segments needed for light-weight telescopes.

Secondly, the established metre-scale metrology and the use of the 100 mm tool were further evaluated. For metrology, distorted surfaces and removals were measured by the newly developed metre-scale metrology system. Complex surfaces and removal topographies were reconstructed by the proposed algorithms. For processing, the 100 mm tool with the optimised parameters was used to process complex surfaces. These demonstrated a new method to control MSF: using large abrasive sizes to fit the misfit and thus to control the MSF in complex surfaces.

7.2 Future work

The RGP has been developed in this thesis. Novel processes to control MSF, edges, surface accuracy and ST with the required VRR have been established, as well as a prototype metre-scale metrology system. The work presented can be expanded upon in the following ways.

Wherever the performance, speed and reliability of the RGP are essential, outputs from the RGP have further to eliminate potential variations (e.g. measurements, equipment improvement, processing temperature, vibration, and humidity) from the requirements. The current probability of reliability in the RGP is 95.45% of outputs within the specification (in respect to the current ± 2 sigma standard). In order to further reduce the variance, there is a need to focus on improving the current ± 2

sigma standard to a ± 3 sigma (i.e. 99.73% of outputs within the specifications). The following, therefore, discusses potential improvements to achieve this future goal.

The experimental results in this thesis have shown that controlling abrasives in the RGP should further reduce the process variation. In fact, the abrasive is not limited to size or slurry density, but also refers to its distribution and migration, which are related to the slurry supply and tool structure for use in a process. The proposed improvements are provided as follows:

It has been demonstrated that to supply slurry to the centre pad hole would achieve uniform pad wear and the required surface finishes. The current slurry supply method is shown in the top of Figure 7-3. The problem with this setup is that slurry will spread radially to the edge if the slurry cannot pass through the centre hole. In order to avoid this, the slurry can be supplied directly through the centre, as shown in the bottom of Figure 7-3. From this improvement, all slurry would pass through the hole and thus reduce variation in the RGP.

Moreover, it has been demonstrated in both experiments and models that the tool structure is one major factor in the determination of the pressure distribution, which can further decide slurry migration and surface finishes. The proposed solution is to amend the tool structure (i.e. change the pressure distribution), so as to improve slurry migration underneath the pad, as shown in Figure 7-3

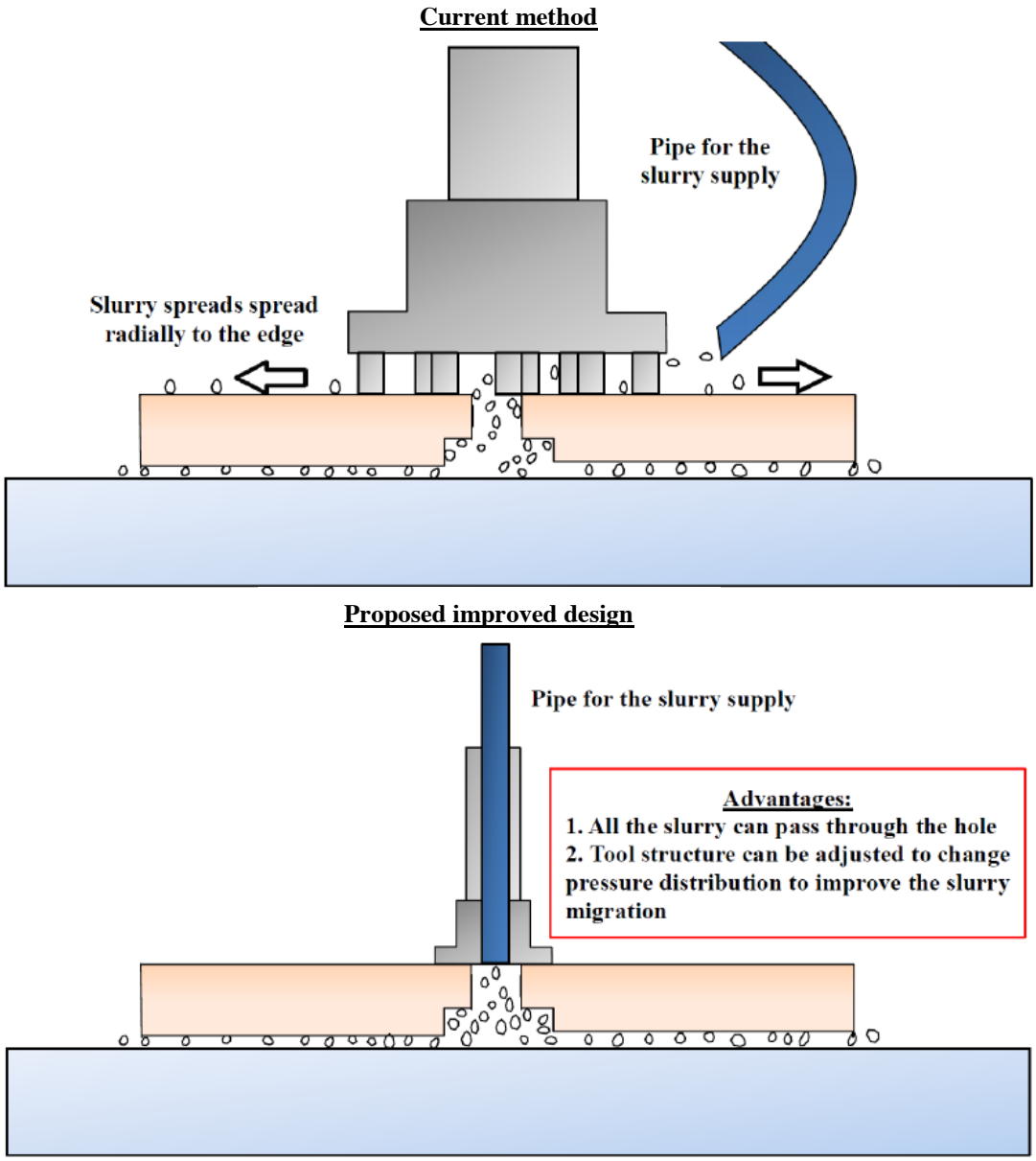

Figure 7-3: Current setup and proposed improved design

Lastly, several other variables can be considered to reduce variation in the RGP. These include reducing the non-uniform distribution of abrasive sizes, investigating grolished outputs by using similar abrasive sizes (8 µm, 9 µm and 10 µm, or finer, for example), or to investigate whether it is possible to achieve better performances

by using different abrasive materials. All these variables would imply a significant increase in complexity in the following experiments. The proposed statistical experimental designs and analysis can be efficient methods to assess these potentially significant variables and reduce the experimental times needed to control variation in the process.

7.3 Summary

The RGP proposed here represents an advance on the state-of-the-art in several respects. It offers several advantages over classical lapping machines using big tools and loose abrasives, and a simple motorised orbital mechanism to move the tool over the part, while still yielding predictable surface performance. Compared to the conventional methods, the RGP is faster, able to control the VRR, surface accuracy, edge, surface texture and MSF more predictably, and more adaptable to the working environment. Hence, the RGP blurs the lines between grinding and polishing technologies to increase the overall efficiency.

In addition, the results have shown that the benefits of using a robot over a Zeeko machine to conduct the grolishing process are (1) the 6-axis degrees of freedom of the robotic arm can adjust itself to different part sizes, shapes and forms, (2) the specification listed in Figure 7-1 is achievable, (3) the capital expenditure when comparing similar machine sizes is more competitive in the market since, and (4) avoidance of the risks of cross-contamination between grolishing and polishing when

the platforms are different. These indicate that a robotic arm is an ideal CNC machine to conduct the grolishing process.

Additionally, the use of RGP combined with the Zeeko polishing technique would stimulate market growth. In respect to smoothing and polishing, some of the market competitors in the half metre to metre scale optical manufacturing community are Schneider GmbH & Co.KG, OptoTech, Satisloh, Nikon, Canon, QED, Sagem, among others. The proposed hybrid process can not only remove errors in all spatial regions to achieve diffraction-limited optics in a short processing time, but also have the advantages of competitive capital expenditure by using a robotic arm with a Zeeko machine. This combination of techniques is not limited only to the processing of large segments, but may also be applied to the manufacture of high quality imaging systems for defence and laser physics.

Chapter 8 References

1. Unrue, J., *Life of a Star*. ISBN-13: 978-1936194001, 2010.

2. Brecht, B., *Life Of Galileo*. 2015: p. ISBN: 9781472538048.

3. Dougherty, J.P., *Finocchiaro, Maurice. the Trial of Galileo: Essential Documents*. The Review of Metaphysics, 2015. 68(3).

4. Sandage, A., *Edwin Hubble 1889-1953*. Journal of the Royal Astronomical Society of Canada, 1989. 83: p. 351-362.

5. Hubble, E.P., *Extragalactic nebulae*. Astrophysical Journal, 1926. 64(321-369).

6. Hubblb, E., *A relation between distance and radial velocity among extra-galactic nebulae*. Proceedings of the National Academy of Sciences of the United States of America, 1929. 15(3): p. 168-173.

7. Cho, A., *Universe's High-Def Baby Picture Confirms Standard Theory*. Science, 2013. 339(6127): p. 1513-1513.

8. Turner, M.S., *Origin of the Universe*. Scientific American, 2013. 22: p. 36-43.

9. Survey, U.S.G., *The age of the Earth*. Scientific American, 1996, Retrieved 2006-01-10: p. 474.

10. Guo, J., et al., *Probability distribution of terrestrial planets in habitable zones around host stars*. Astrophysics and Space Science, 2009. 323(4): p. 367-373.

11. Hickson, P., *A Technical Comparison of the TMT and the E-ELT*. The University of British Columbia, Physics and Astronomy, 6224 Agricultural Road, Vancouver, 2010.

12. *The E-ELT Construction Proposal*. ESO, 2013.

13. Martin J.S. Rudwick, E.E.D., Victor E. Thoren, *Notes on Contributors*. The British Journal for the History of Science, 1974. 7(03): p. 305-305.

14. John Gribbin, M.G., *From Here to Infinity: A Beginner's Guide to Astronomy*. 2009: p. Ch4_1: Introduction.

15. Schroeder, D.J., *Astronomical Optics, Second Edition*. ISBN: 978-0-12-629810-9, 1999.

16. Cunningham, C., D. Melotte, and F. Molster. *The OPTICON technology roadmap for optical and infrared astronomy*. 2010.

17. Cheng, A.Y.S., *Design apects of future very large telescopes (Honeycomb mirrors)*. PhD thesis, The University of Arizona., 1987.

18. Marker Iii, A.J., Fuhrmann, H., Tietze, H., Froehlich, W. *Lightweight large mirror blanks of zerodur*. 1986.

19. Hofferbert, R., et al., *LINC-NIRVANA for the large binocular telescope: setting up the world's largest near infrared binoculars for astronomy.* Optical Engineering, 2013. 52(8): p. 081602-081602.

20. Martin, H.M., et al. *Manufacture of the second 8.4 m primary mirror for the Large Binocular Telescope*. 2006.

21. Martin, H.M., et al. *Manufacture of 8.4-m off-axis segments: a 1/5-scale demonstration*. 2004.

22. Kitchin, C.R., *Types of Telescopes*, in *Telescopes and Techniques*. 2013, Springer New York. p. 3-30.

23. Mast, T.S. and J.E. Nelson, *Figure control for a fully segmented telescope mirror*. Applied Optics, 1982. 21(14): p. 2631-2641.

24. Nelson, J.E., et al., *Stressed mirror polishing. 2: Fabrication of an off-axis section of a paraboloid*. Applied Optics, 1980. 19(14): p. 2341-2352.

25. *The European Extremely Large Telescope (E-ELT) project: www.eso.org/e-elt*.

26. *The Thirty Meter Telescope (TMT) project: http://www.tmt.org*.

27. *The Giant Magellan Telescope (GMT) project: http://www.gmto.org*.

28. Gilmozzi, R. *Science and technology drivers for future giant telescopes*. 2004.

29. *Science with a 30-meter telescope: A 30-meter telescope, operating in wavelengths ranging from the ultraviolet to the mid-infrared, is an essential tool to address questions in astronomy ranging from understanding star and planet formation to unraveling the history of galaxies and the development of large-scale structure in the universe*. available from http://www.tmt.org/science-case.

30. Hook, I.M. *Highlights from the science case for a 50- to 100-m extremely large telescope*. 2004.

31. Hook, I.a.t.O.E.S.W.G., *Science with Extremely Large Telescopes*. The Messenger 121, 2005.

32. *The E-ELT Construction Proposal*. ESO, 2014.

33. Walker, D., Brooks, David King, Andrew Freeman, Richard Morton, Roger McCavana, Gerry Kim, Sug-Whan, *The Precessions tooling for polishing and figuring flat, spherical and aspheric surfaces*. Optics Express, 2003. 11(8): p. 958-964.

34. Walker, D.D., et al. *Recent developments of Precessions polishing for larger components and free-form surfaces*. 2004.

35. David Walker1, Anthony Beaucamp1, Christina Dunn2, Richard Freeman1, Andreas Marek1, Gerry McCavana1, Roger Morton1, David Riley1, *First Results on Freeform polishing using the Precessions Process*. *CD-Rom*. 2004.

36. Walker, D.D., et al., *Use of the 'Precessions'™ process for prepolishing and correcting 2D & 2½D form*. Optics Express, 2006. 14(24): p. 11787-11795.

37. Yu, G., H. Li, and D. Walker, *Removal of mid spatial-frequency features in mirror segments*. 2011. Vol. 6. 2011.

38. D. Walker, G.D., T. Fox-Leonard, C. Gray, J. Mitchell, P. Rees, H. Y. Wu, A. Volkov, G. Y. Yu, *Advanced Abrasive Processes For Manufacturing Prototype Mirror Segments For The World's Largest Telescope.* Advanced Materials Research, 2014. 1017: p. 532-538.

39. Lu, D.W.C.D.G.Y.M.B.X.Z.H.Y.W.H.L.C., *The role of robotics in computer controlled polishing of large and small optics*. SPIE Proceedings, 2015. 9575.

40. Yu, G., D. Walker, and H. Li, *Implementing a grolishing process in Zeeko IRP machines*. Applied Optics, 2012. 51(27): p. 6637-6640.

41. Yu, G., D.D. Walker, and H. Li. *Research on fabrication of mirror segments for E-ELT*. 2012.

42. Walker, D.D., et al. *A quantitative comparison of three grolishing techniques for the Precessions process*. 2007.

43. *Zeeko IRP specification: http://goo.gl/GpyHGV*.

44. *ABB robotic arm (specification): http://goo.gl/Huz7d9*.

45. *Fanuc Robotic Arm: Specification: http://goo.gl/IswsaV*.

46. P. Comley, P.M., P. Shore, X. Tonnellier, *Grinding metre scale mirror segments for the E-ELT ground based telescope*. CIRP Annals, 2011. 60(1): p. 379-382.

47. Tiziani, R.H.B.B.H.J., *Advanced Optics Using Aspherical Elements*. ISBN: 9780819467492, 2008.

48. Sasián, J., *Introduction to Aberrations in Optical Imaging Systems*. Cambridge University Press, 2013(ISBN:9780511795183).

49. Smith, W., *Modern Lens Design*. McGraw-Hill Professional Engineering Press, 2004(ISBN-13: 978-0071438308).

50. Schwiegerling, J., *Optical Specification, Fabrication, and Testing*. Spie Press Book, 2014. PM252(ISBN: 9781628413663).

51. Goodman, J.W., *Introduction to Fourier optics*. 2005: Roberts and Company Publishers.

52. Gaskill, J.D., *Linear Systems, Fourier Transforms, and Optics*. John Wiley & Sons, New York, 1978.

53. Hecht, E., *Optics (4th Edition)*. ISBN-13: 978-0805385663, 2002: p. pp467-470.

54. Robert Fischer, B.T.-G., Paul R. Yoder, *Optical System Design, Second Edition*. ISBN-13: 978-0071472487, 2008.

55. Smith, W., *Modern Optical Engineering, 4th Ed*. ISBN-13: 978-0071476874, 2008: p. pp194.

56. Wagner, R.E. and R.R. Shannon, *Fabrication of Aspherics Using a Mathematical Model for Material Removal*. Applied Optics, 1974. 13(7): p. 1683-1689.

57. 10110-12:2007, I., *Optics and photonics -- Preparation of drawings for optical elements and systems -- Part 12: Aspheric surfaces*. 2007 (last review in 2010).

58. *Introduction to ISO 10110*. Avaialbe from: http://fp.optics.arizona.edu/optomech/files/ISO%2010110.pdf.

59. *Conic Sections (Conics)*. Mathematics, available from: http://math.ucsd.edu/~barnold/math4c/4C%20Lessons/Additional%20Material/Conics.pdf.

60. Wilson, R.N., *Reflecting Telescope Optics I: Basic Design Theory and its Historical Development*. Springer Berlin Heidelberg Press, 2007.

61. Cheng, J., *The Principles of Astronomical Telescope Design*. Book: Astrophysics and Space Science Library, 2009. 360(ISBN: 978-0-387-88790-6 (Print) 978-0-387-88791-3 (Online)).

62. Garstang, R., *Hadley, John*, in *Biographical Encyclopedia of Astronomers*, T. Hockey, et al., Editors. 2014, Springer New York. p. 877-877.

63. John T. McGraw, P.C.Z., *An Overview of Wide-Field-Of-View Optical Designs for Survey Telescopes*. SPIE, 2011.

64. Sacek, V., *Classical and aplanatic two-mirror systems*. Notes on Amateur Telescope Optics, 2006.

65. Olson, J.B.C., *Field Guide to Lens Design*. eISBN: 9780819491657 | Print ISBN13: 9780819491640, 2012.

66. David Sprayberry, P.A., Randy Campbell, Bob Goodrich, Grant Hill, Barbara Schaefer, Greg Wirth, *Keck Telescope and Facility Instrument Guide*. 2002.

67. Zimmer, M.R.A.J.T.M.P.C., *Alternative design for extremely large telescopes and options to use the VATT for ELT design demonstration*. Advanced Optical Technologies, 2013. 2(5-6): p. 423–432.

68. Cayrel, M., *E-ELT optomechanics: overview*. SPIE 8444, Ground-based and Airborne Telescopes IV, 84441X (17 September 2012); doi: 10.1117/12.925175, 2012.

69. Lillie, C.F. *Large deployable telescopes for future space observatories*. 2005.

70. Lei, C., L. Zheng, and Y. Che. *Study of the impact of petal-shape mirror segmentation on 2 m segmented telescope*. 2015.

71. J. H. Burge, W.D., H. M. Martin, C. Zhao, *Development of surface metrology for the Giant Magellan Telescope primary mirror* SPIE, 2008. 7018.

72. Bely, P., *The Design and Construction of Large Optical Telescopes (Astronomy and Astrophysics Library)*. Springer, 2003. ISBN-13: 978-1441930323.

73. Rodolfo, J., et al. *Prototype segments polishing and testing for ELT M1*. 2012.

74. Walker, D., *Faster production of high-quality telescope mirrors*. SPIE Newsroom. DOI: 10.1117/2.1201304.004794, 2013.

75. Tamai, R. and J. Spyromilio. *European Extremely Large Telescope: progress report*. 2014.

76. A. Bosa , R.H., P.C.J.N. Rosiellea, M. Steinbucha, *Nanometre-accurate form measurement machine for E-ELT M1 segments*. Precision Engineering, 2015. 40: p. 14-25.

77. Walker, D., et al., *Edges in CNC polishing: from mirror-segments towards semiconductors, paper 1: edges on processing the global surface*. Optics Express, 2012. 20(18): p. 19787-19798.

78. Swat, E., *ESO prototype segment specification*. . E-SPE-ESO-300–0150, 2009.

79. Walker, D., et al. *Edge-control and surface-smoothness in sub-aperture polishing of mirror segments*. 2012.

80. Swanson, M.L.a.R., *Astronautics and aeronautics: a chronology, 1996-2000*. NASA History Division 2009.

81. Bibby, M., *The development of Automatic On-Machine Metrology*. UCL PhD Thesis, 2015.

82. Chinn, R.E., *Grinding and Polishing: Preparation and Analysis of Ceramic Microstructures*. ASM International, 2002. ISBN: 0-87170-770-5.

83. F. Klocke1, A.G., D. Hollstegge1, C. Voelker1, O. Dambon1, M. Herben1, B. Bulla1, D. Czarlay1, J. Riegel1, *Polishing-Grinding – an innovation for manufacturing of high precision optics*. American Society for Precision Engineering (ASPE Annual Meeting), 2008.

84. Raimondi, L., *X-ray telescope mirrors From surface profile to Point Spread Function: a new approach*. PhD thesis UNIVERSITA DEGLI STUDI DELL'INSUBRIA, 2015.

85. H. Buchenauer, M.H.-P., *Processing Technologies*. SPIE, 2008: p. 211-216.

86. Paul Shore1, X.L., Tan Jin1, Xavier Tonnellier1, Paul Morantz1, David Stephenson1, Roger Collins1, Andy Roberts1, Richard May-Miller2, Roger Read2, *Grinding mode of the "BOX" ultra precision free-form grinder*. SPIE, 2005.

87. Guang Feng, F.H., Dongming Guo, Renke Kang and Zhuji Jin, *Ultra-precision grinding of asymmetric curved surfaces by line contact with cup wheel*. Mechanical Engineering Science, 2012.

88. P. Comley , P.M., P. Shore, X. Tonnellier, *Grinding metre scale mirror segments for the E-ELT ground based telescope*. CIRP Annals - Manufacturing Technology, 2011. 60: p. 379-382.

89. Tonnellier, X., *Precision Grinding for Rapid Manufacturing of Large Optics*. PhD Thesis, 2010.

90. Preston, F.W., *The Theory and Design of Plate Glass polishing Machines*. Journal of Glass Technology, 1927. 7: p. 124.

91. Bingham, R.G., Walker, D. D., Kim, D-H., Brooks, D., Freeman, R. and Riley, D. , *A Novel Automated Process for Aspheric Surfaces*. . Proc. SPIE: 45th Annual Meeting, the International Symposium on Optical Science and Technology, 2000. 4093: p. pp. 445-448.

92. David Walker *, G.D., Tony Fox-Leonard, Caroline Gray, John Mitchell, Paul Rees, Hsing Yu Wu, Andy Volkov, Guo Yu Yu, *Advanced Abrasive Processes for Manufacturing Prototype Mirror Segments for the World's Largest Telescope*. Advanced Materials Research, 2014. 1017: p. 532-538.

93. Walker, D., et al. *Technologies for producing segments for extremely large telescopes*. 2011.

94. Gray, C., et al. *Fast manufacturing of E-ELT mirror segments using CNC polishing*. 2013.

95. Li, H., et al. *Active edge control in the precessions polishing process for manufacturing large mirror segments*. 2014.

96. L. Jiaoa, Y. Wub,, X. Wanga, H. Guob , Z. Liang, *Fundamental performance of Magnetic Compound Fluid (MCF) wheel in ultra-fine surface finishing of optical glass*. International Journal of Machine Tools and Manufacture, 2013. 75: p. 109-118.

97. Bongsu Jung, K.-I.J., Byung-Kwon Min, Sang Jo Lee, Jongwon Seok, *Magnetorheological finishing process for hard materials using sintered iron-CNT compound abrasives*. International Journal of Machine Tools and Manufacture, 2009. 49(5): p. 407-418.

98. W. Kordonski, e.a., *magnetorheological polishing devices and methods*. US Patent, No. 5 449 313, 1995.

99. Golini, D., et al. *Magnetorheological finishing (MRF) in commercial precision optics manufacturing*. 1999.

100. Messner, W., et al. *Manufacturing meter-scale aspheric optics*. 2007.

101. Don Golini, M.D., William Kordonski, and John Bruning, *MRF polishes calcium fluoride to high quality*. Laser Focus World, 2001.

102. Piché, F. and A.R. Clarkson. *One Year of Finishing Meter-Class Optics with MRF®at L-3 IOS Brashear Optics*. in *International Optical Design Conference and Optical Fabrication and Testing*. 2010. Jackson Hole, Wyoming: Optical Society of America.

103. Kordonski, W.I., et al. *Magnetorheological-suspension-based finishing technology*. 1998.

104. O.W. Fahnle, H.v.B., *Finishing of Optical Materials Using Fluid Jet Polishing*. 14th ASPE Annual Meeting, 1999: p. 509-512.

105. Booij, S.M., *Fluid Jet Polishing*. PrintPartners IPSKamp B.V., Enschede, 2003. ISBN:: 90-9017012-X.

106. Williamson, R., *Field Guide to Optical Fabrication*. Spie Press Book, 2011. ISBN13: 9780819486769.

107. Walker, D.D., et al. *Active control of edges and global microstructure on segmented mirrors*. 2008.

108. Anthony Beaucamp, Y.N., *Super-smooth finishing of diamond turned hard X-ray molding dies by combined fluid jet and bonnet polishing*. CIRP Annals - Manufacturing Technology, 2013. 62(1): p. 315-318.

109. Biskup, H., A. Haberl, and R. Rascher. *Surface errors in the course of machining precision optics*. 2015.

110. Xie, X. and S. Li, *Ion Beam Figuring Technology*, in *Handbook of Manufacturing Engineering and Technology*, A.Y.C. Nee, Editor. 2015, Springer London. p. 1343-1390.

111. Ghigo, M., et al. *Ion figuring of large prototype mirror segments for the E-ELT*. 2014.

112. Whitehouse, D.J., *Handbook of Surface and Nanometrology*. CRC Press, ISBN-13: 9781420082012, 2010.

113. Malacara, D., *Optical Shop Testing 3rd Edition*. Wiley Press, 2007.

114. Leach, R.K., *Fundamental Principles of Engineering Nanometrology* Elsevier Press, 2010.

115. Davies, A.D., L. He, and C.J. Evans. *Mid-spatial Frequency Specification and Characterization for Freeform Surfaces*. in *Renewable Energy and the Environment*. 2013. Tucson, Arizona: Optical Society of America.

116. *ISO 11562, 2.6, 3.2*. 1996.

117. *ISO 3274, 4.4*. 1996.

118. Sidick, E., *Power Spectral Density Specification and Analysis of Large Optical Surfaces* SPIE, 2009. 7390.

119. Harvey, J.E., *X-ray optics*. in Handbook of Optics, 2nd Edition, Optical Society of America, Washington, D.C., 1995. 2, Chapter 11.

120. Elson, J.M. and J.M. Bennett, *Calculation of the power spectral density from surface profile data*. Applied Optics, 1995. 34(1): p. 201-208.

121. Bernhard Braunecker, R.H., Hans J. Tiziani, *Chapter 6: Metrology*. SPIE PRess, 2008.

122. Leach, R.W., A.; Coupland, J. & Hartmann, W., *Interpreting the probe-surface interaction of surface measuring instruments, or what is a surface?* Surface Topography: Metrology and Properties, 2014.

123. Zernike, F., *Diffraction theory of the knife-edge test and its improved form, the phase-contrast method*. Monthly Notices of the Royal Astronomical Society, 1934. 94: p. 377-384.

124. Mahajan, V.N., *Zernike annular polynomials for imaging systems with annular pupils*. Journal of the Optical Society of America, 1981. 71(1): p. 75-85.

125. Qi, B., H. Chen, and N. Dong, *Wavefront fitting of interferograms with Zernike polynomials*. Optical Engineering, 2002. 41(7): p. 1565-1569.

126. Mahajan, V.N., *Zernike Circle Polynomials and Optical Aberrations of Systems with Circular Pupils*. Applied Optics, 1994.

127. Dai, G.-m. and V.N. Mahajan, *Orthonormal polynomials in wavefront analysis: error analysis*. Applied Optics, 2008. 47(19): p. 3433-3445.

128. Z80.28-2004., A., *Method for reporting optical aberrations of eyes*.

129. 24157:2008, I., *Ophthalmic optics and instruments — Reporting aberrations of the human eye*.

130. Bastaits, R., *Extremely large segmented mirrors: dynamics, control and scale effects*. . PhD Thesis, University Libre de Bruxelles (ULB). 2010.

131. Petropoulos, P.G., N.C. Pandazaras, and P.J. Davim, *Surface Texture Characterization and Evaluation Related to Machining*, in *Surface Integrity in Machining*, P.J. Davim, Editor. 2010, Springer London: London. p. 37-66.

132. Leising, C., *Paper Surface Roughness With 3D Profilometry*. NANOVEA: technical report, 2010.

133. STANDARD, A.A.N., *Surface Texture (Surface Roughness, Waviness and Lay*. American Society of Mechanical Engineers, 2009.

134. Blunt, P.L., *Why use areal surface texture measurement?* DMAC Meeting,University of Huddersfield, 2006.

135. Raia, T.V.V.a.J., *Surface Finish Metrology Tutorial*. National Institute of Standards and Technology (USA), 1990.

136. Novak, M., *Surface Texture: Non-contact Metrology for Industrial Applications*. Bruker Nano Surfaces Division, 2015.

137. Hull, T. and T. Westerhoff. *Lightweight ZERODUR: a cost-effective thermally stable approach to both large and small spaceborne telescopes*. 2014.

138. Nelson, J., T. Mast, and G. Chanan, *Segmented Mirror Telescopes*, in *Planets, Stars and Stellar Systems*, T. Oswalt and I. McLean, Editors. 2013, Springer Netherlands. p. 99-136.

139. E-ELT, A.M.P., *E-ELT Opportunities for Civil & Mechanical Engineering Companies*. ESO-E-ELT Programme, 2010.

140. Nijenhuis, J., R. Hamelinck, and B. Braam. *The opto-mechanical performance prediction of thin mirror segments for E-ELT*. 2012.

141. Cavaller, L., et al. *Design of the primary mirror segment support system for the E-ELT*. 2008.

142. Nijenhuis, J., et al. *Meeting highest performance requirements for lowest price and mass for the M1 segment support unit for E-ELT*. 2010.

143. *ESO Awards Contracts for E-ELT Primary Mirror Segment Support System Units*. Available from: https://www.eso.org/public/unitedkingdom/announcements/ann15003/, 2015.

144. Hubin, N. and L. Noethe, *Active Optics, Adaptive Optics, and Laser Guide Stars*. Science, 1993. 262(5138): p. 1390-1394.

145. G Love, A.S., *active and adaptive optics for the new generation of large telescopes*. Current Science, 1995. 66(5): p. 349-355.

146. Döhring, T., et al. *Properties of Zerodur mirror blanks for extremely large telescopes*. 2006.

147. Dohring, T., et al. *ZERODUR mirror blanks for ELTs: technology and production capacity at SCHOTT*. 2004.

148. Ponin, O.V., et al. *Demonstrating the suitability of Sitall for the SALT primary mirror*. 2003.

149. *OAHARA CRS Report*. available from: file:///G:/PhD%20thesis/Chapter%201/reference/Oahara%20CRS%20Report%202013.pdf, 2013.

150. Kishi, T., et al. *Material characteristics of CLEARCERAM-Z HS for use in large diameter mirror blanks*. 2010.

151. Sabia, R., et al. *Corning 7972 ULE material for segmented and large monolithic mirror blanks*. 2006.

152. Bougoin, M. and J. Lavenac. *From Herschel to Gaia: 3-meter class SiC space optics*. 2011.

153. Smiljanic, R., *Stellar abundances of beryllium and CUBES*. Astrophysics and Space Science, 2014. 354(1): p. 55-64.

154. Onaka, T., et al. *Cryogenic silicon carbide mirrors for infrared astronomical telescopes: lessons learnt from AKARI for SPICA*. 2013.

155. Creedon, J.F. and A.G. Lindgren, *Control of the optical surface of a thin, deformable primary mirror with application to an orbiting astronomical observatory*. Automatica, 1970. 6(5): p. 643-660.

156. Merkle, F., Beckers, Jacques M. *Application of adaptive optics To astronomy*. 1989.

157. *W. M. Keck Observatory*. Avaialbe from: http://goo.gl/7Fhhds, 2015.

158. Waltham, N., *CCD and CMOS sensors*, in *Observing Photons in Space*, M.E. Huber, et al., Editors. 2013, Springer New York. p. 423-442.

159. Litwiller, D., *CCD vs. CMOS: Facts and Fiction*. Photonics Spectra, 2001.

160. Brandl, C.U.K.R.N.B.R., *Field Guide to Astronomical Instrumentation*. eISBN: 9781628411782 | Print ISBN13: 9781628411775, 2015.

161. Frazier, R.K.T.B.W., *Field Guide to Adaptive Optics, Second Edition*. Spie Press Book, 2012.

162. Restaino, S.W.T.S.R., *Introduction to Image Stabilization*. spie Press Book, 2006(ISBN: 9780819464347).

163. R Foy, A.L.a.A.A., *Letter to the editor feasibility of adaptive telescope with laser probe*. Astronomy and Astrophysics, 1985. 152: p. L29-L31.

164. Max, C.E., et al., *Image Improvement from a Sodium-Layer Laser Guide Star Adaptive Optics System*. Science, 1997. 277(5332): p. 1649-1652.

165. Breckinridge, J.B., *Basic Optics for the Astronomical Sciences*. SPIE Press Book, 2012(eISBN: 9780819483676 | Print ISBN13: 9780819483669).

166. Emmanuel Hugot, G.R.L., and Marc Ferrari, *Active optics: single actuator principle and angular thickness distribution for astigmatism compensation by elasticity*. Applied Optics, 2008. 47(10): p. 1401-1409.

167. Li, H., *Research on Manufacturing Mirror Segments for an Extremely Large Telescope*. 2012.

168. S. Zeng, L.B., X. Jiang, P. Bills, *Investigation of the material removal characteristic for polishing CoCr alloy* Computing and Engineering Researchers' Conference,, 2010.

169. Walker, D.D., et al. *Zeeko/UCL process for polishing large lenses and prisms*. 2002.

170. Atul Kumar, S.K., Rohit Garg, *A review of optimization of process parameters for material removal rate and surface roughness in end milling of stir cast al 2024-SICP metal matrix composite*. Proceedings of 47th IRF International Conference, 2016.

171. Li, H., et al., *Edge control in CNC polishing, paper 2: simulation and validation of tool influence functions on edges*. Optics Express, 2013. 21(1): p. 370-381.

172. II, J.B.J., *Characterization of optical surface grinding using bound and loose abrasives*. PhD thesis, The University of Arizona., 2011.

173. Evans, J., Paul, E., Dornfeld, D., Lucca, D., Byrne, G., Tricard, M., Klocke, F., Dambon, O., and Mullany, B., *Material Removal Mechanisms in Lapping and Polishing*. CIRP Annals, 2003. 52(2): p. 611-633.

174. De Pellegrin, D.V.S., Gwidon *Simulation of three-dimensional abrasive particles*. Wear. 258: p. 255-270.

175. Goh, T.N., *The Role of Statistical Design of Experiments in Six Sigma: Perspectives of a Practitioner*. Quality Engineering, 2002. 14(4): p. 659-671.

176. Kackar, R.N., *Off-Line Quality Control, Parameter Design, and the Taguchi Method*. Journal of Quality Technology, 1985. 17: p. 176-188.

177. Montgomery, D.C., *Design and Analysis of Experiments, 8th Edition International Student Version*. 2012(ISBN: 978-1-1-118-09793-9).

178. Montgomery, D.C., *Statistical Quality Control* ISBN-13: 978-1118146811, 2009.

179. Oh, H.-S., *Introduction to Linear Regression Analysis, 5th edition by MONTGOMERY, DOUGLAS C., PECK, ELIZABETH A., and VINING, G. GEOFFREY*. Biometrics, 2013. 69(4): p. 1087-1087.

180. Pridmore, A.B.J.D.W.A., *Taguchi methods : applications in world industry*. FS Publications ; Berlin : Springer-Verlag, Bedford, U.K, 1989., 1989.

181. Ross, P.J., *Taguchi Techniques for Quality Engineering*. ISBN-13: 978-0070539587, 1996.

182. Box, G.E.P., *Signal-to-Noise Ratios, Performance Criteria, and Transformation*. Technometrics, 1988. 30: p. 1-40.

183. Box, G.E.P., S. Bisgaard, and C. A. Fung, *An Explanation and Critique of Taguchi's Contributions to Quality Engineering*. Quality and Reliability Engineering International Biometric Society, 1988. 4: p. 123-131.

184. Hunter, J.S., *Statistical Design Applied to Product Design*. Journal of Quality Technology, 1985. 17: p. 210-221.

185. Myers, R.H., D. C. Montgomery and C. M. Anderson-Cook, *Response Surface Methodology: Process and Product Optimization Using Designed Experiments*. 3rd edition. Wiley, New York, 2009.

186. Taguchi, G., and Y. Wu, *Introduction to Off-Line Quality Control*. Central Japan Quality Control Association, Nagoya, Japan, 1980.

187. Taguchi, G., *System of Experimental Design: Engineering Methods to Optimize Quality and Minimize Cost*. UNIPUB, White Plains, NY, 1987.

188. Taguchi, G., *Introduction to Quality Engineering*. Asian Productivity Organization, UNIPUB, White Plains, NY., 1991.

189. Gray, C.T., *Introduction to quality engineering: Designing quality into products and processes, G. Taguchi, Asian productivity organization, 1986. number of pages: 191. price: $29 (U.K.)*. Quality and Reliability Engineering International, 1988. 4(2): p. 198-198.

190. Douglas C. Montgomery, E.A.P., G. Geoffrey Vining, *Introduction to Linear Regression Analysis, Praise for the Fourth Edition*. John Wiley & Sons, New York, 2012.

191. Myers, R.H., *Classical and Modern Regression with Applications, 2nd edition*. . PNS-Kent, Boston, 1990.

192. Box, G.E.P.a.W., K.B., *On the Experimental Attainment of Optimum Conditions (with discussion)*. Journal of the Royal Statistical Society. Series B13(1), 1951: p. 1-45.

193. Khuri, A.I., and J. A. Cornell, *Response Surfaces: Designs and Analyses*. *2nd edition*. Dekker, New York., 1996.

194. Myers, R.H., D. C. Montgomery, G. G. Vining, C. M. Borror, and S. M. Kowalski, *Response Surface Methodology: A Retrospective and Literature Survey*. Journal of Quality Technology, 2004. 36: p. 53-77.

195. Tonnellier, X., et al. *Precision grinding for rapid fabrication of segments for extremely large telescopes using the Cranfield BoX*. 2010.

196. Lee, Y., *Evaluating subsurface damage in optical glasses*. 2011. Vol. 6. 2011.

197. Blaineau, P., et al., *Relations between subsurface damage depth and surface roughness of grinded fused silica*. Optics Express, 2013. 21(25): p. 30433-30443.

198. Hongjie, L., et al., *Subsurface defects of fused silica optics and laser induced damage at 351 nm*. Optics Express, 2013. 21(10): p. 12204-12217.

199. Neauport, J., et al., *Subsurface damage measurement of ground fused silica parts by HF etching techniques*. Optics Express, 2009. 17(22): p. 20448-20456.

200. Wesley. Williams, B.A.M., Wesley C. Parker, Patrick J. Moyer, and Mark H. Randles, *Using quantum dots to tag subsurface damagein lapped and polished glass samples*. Applied Optics, 2009. 48(27): p. 5155-5163.

201. Walker, D.D. and P.R. Shore. *Manufacture of segments for extremely large telescopes: a new perspective*. 2004.

202. Li, Z., et al., *Optimization and application of influence function in abrasive jet polishing*. Applied Optics, 2010. 49(15): p. 2947-2953.

203. Walker, D.D., et al. *Novel CNC polishing process for control of form and texture on aspheric surfaces*. 2002.

204. Wai, K.C., *Process and media development of an MR fluid-based finishinh for high efficiency material removal*. PhD Thesis, 2016.

205. Team, R.D.C., *R: A language and environment for statistical computing*. *Vienna, Austria: Foundation for Statistical Computing*. Retrived from http://www.R-project.org, 2010.

206. Myers, R.H., et al., *Linear Regression Models*, in *Generalized Linear Models*. 2012, John Wiley & Sons, Inc. p. 9-76.

207. Mimura, H., et al., *Breaking the 10[thinsp]nm barrier in hard-X-ray focusing*. Nat Phys, 2010. 6(2): p. 122-125.

208. David Walker, G.Y., Hongyu Li, Wilhelmus Messelink, Rob Evans, and Anthony Beaucamp, *Edges in CNC polishing: from mirror-segments towards semiconductors, paper 1: edges on processing the global surface*. Opt. Express 2012. 20(18): p. 19787-19798.

209. Pascale, E., et al., *The Balloon-borne Large Aperture Submillimeter Telescope: BLAST*. The Astrophysical Journal, 2008. 681(1): p. 400.

210. Ruch, E., *The Challenge of Optics in Future Extremely Large Telescopes*, in *Astronomy at the Frontiers of Science*, J.-P. Lasota, Editor. 2011, Springer Netherlands. p. 229-241.

211. Wang, W., et al. *Research on edge control in the process of polishing using ultra precise bonnet on optical elements*. 2010.

212. Walker, D.D., *The internal report: The draft on the investigation edge asymmetry*. 2011.

213. Li, H., et al., *Modelling and measurement of polishing tool influence functions for edge control*. 2011. Vol. 6. 2011.

214. Chow, M.T.C., Hafiz, A.M.K. ; Tutunea-Fatan, O.R. ; Knopf, G.K., Chow, M.T.C., *Experimental statistical analysis of laser micropolishing process*. IEEE, 2010.

215. Ohmura, Y., et al. *Studies of high index immersion lithography*. 2008.

216. Tinker, F. and K. Xin. *Fabrication of SiC aspheric mirrors with low mid-spatial error*. 2013.

217. Rees, P.C.T. and C. Gray. *Metrology requirements for the serial production of ELT primary mirror segments*. 2015.

218. Technology:, D., http://www.4dtechnology.com/products/4sightsoftware.php.

219. Franse, J., *Manufacturing techniques for complex shapes with submicron accuracy*. Reports on Progress in Physics, 1990. 53(8): p. 1049-1094.

220. Lee, C.F.C.a.W.B., *Modelling and simulation of surface topography in ultra-precision diamond turning* Proceedings of the Institution of Mechanical Engineers, Part B: Journal of Engineering Manufacture, 2000. 214: p. 463-480.

221. Shuhei Takasua, M.M., Takashi Nishiguchia, Akira Kobayashib, *Influence of Study Vibration with Small Amplitude Upon Surface Roughness in Diamond Machining*. CIRP Annals - Manufacturing Technology, 1985. 34(1): p. 463-467.

222. T. Sataa, M.L., S. Takatac, H. Hiraokaa, C.Q. Lib, X.Z. Xingb, X.G. Xiaob, *Analysis of Surface Roughness Generation in Turning Operation and its Applications*. 1985. 34(1): p. 473-476.

223. Dunn, C.R. and D.D. Walker, *Pseudo-random tool paths for CNC sub-aperture polishing and other applications*. Optics Express, 2008. 16(23): p. 18942-18949.

224. Song, C., D. Walker, and G. Yu, *Misfit of rigid tools and interferometer subapertures on off-axis aspheric mirror segments*. Optical Engineering, 2011. 50(7): p. 073401-073401-6.

225. Hsing-Yu Wu, G.Y., David Walker, Xiao Zheng, Hongyu Li, Christina Dunn , Caroline Gray, *Optimisation of Grolishing Freeform Surfaces with Rigid and Semi-rigid Tools*. SPIE (accepted), 2016.

226. Walker, D., et al. *The role of robotics in computer controlled polishing of large and small optics*. 2015.

227. Hsing-Yu Wu, K.M., *Investigation of four classical groove patterns with three typical tool types for use in the rigid tool smoothing process*. SPIE 2016. Paper Number: 9912-273 at SPIE Astronomical Telescopes + Instrumentation.

228. Shier, R., *Paired t-tests*. Mathematics Learning Support Centre, 2004.

229. Andrew T. Silfer , G.J.K.a.J.M.H., *A Geographic information system utilizing the triangulated irregular network as a basis for hydrologic modeling*.

230. Simonovic, D.S.a.S.P., *Water Resources Research Report*. City of London: Vulnerability of Infrastructure to Climate Change, Background Report #2 Hydraulic Modeling and Floodplain Mapping, 2009.

231. Xin, F.T.K., *Fabrication of SiC aspheric mirrors with low mid-spatial error*. SPIE, 2013. 8837.

232. David, A. and B. Jim, *Optical Fabrication*, in *Handbook of Optical Engineering*. 2001, CRC Press.

233. West, S.C., et al., *Practical design and performance of the stressed-lap polishing tool*. Applied Optics, 1994. 33(34): p. 8094-8100.

234. Kim, D.W. and J.H. Burge, *Rigid conformal polishing tool using non-linear visco-elastic effect*. Optics Express, 2010. 18(3): p. 2242-2257.